Wegener Center for Climate and Global Change
University of Graz

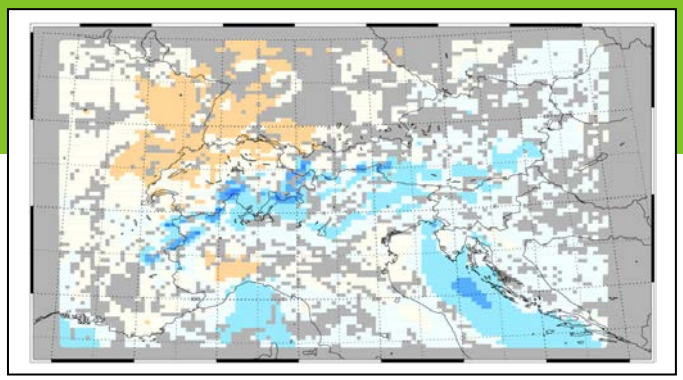

Scientific Report No. 32-2010

High resolution wind field modelling over complex topography: analysis and future scenarios

Heimo Truhetz

April 2010

The **Wegener Center for Climate and Global Change** combines as an interdisciplinary, internationally oriented research center the competences of the University of Graz in the research area „Climate, Environmental and Global Change“. It brings together, in a dedicated building close to the University central campus, research teams and scientists from fields such as geo- and climate physics, meteorology, economics, geography, and regional sciences. At the same time close links exist and are further developed with many cooperation partners, both nationally and internationally. The research interests extend from monitoring, analysis, modeling and prediction of climate and environmental change via climate impact research to the analysis of the human dimensions of these changes, i.e., the role of humans in causing and being effected by climate and environmental change as well as in adaptation and mitigation.

The present report is the result of a PhD thesis work completed in March 2010.

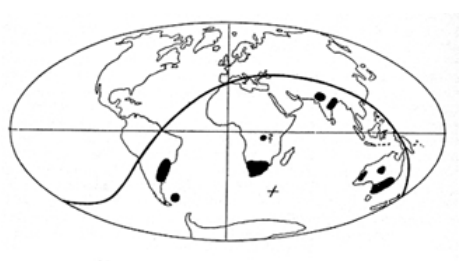

Alfred Wegener (1880-1930), after whom the Wegener Center is named, was founding holder of the University of Graz Geophysics Chair (1924-1930) and was in his work in the fields of geophysics, meteorology, and climatology a brilliant, interdisciplinary thinking and acting scientist and scholar, far ahead of his time with this style. The way of his ground-breaking research on continental drift is a shining role model — his sketch on the relationship of the continents based on traces of an ice age about 300 million years ago (left) as basis for the Wegener Center Logo is thus a continuous encouragement to explore equally innovative scientific ways: *paths emerge in that we walk them* (Motto of the Wegener Center).

Wegener Center Verlag • Graz, Austria

ISBN 978-3-9502940-0-2

April 2010

Contact: Heimo Truhetz.
heimo.truhetz@uni-graz.at

Wegener Center for Climate and Global Change
University of Graz
Leechgasse 25
A-8010 Graz, Austria
www.wegcenter.at

High resolution wind field modelling over complex topography: analysis and future scenarios

Dissertation

zur Erlangung des akademischen Grades

Doktor der Naturwissenschaften

vorgelegt von

MAG. HEIMO TRUHETZ

an der Naturwissenschaftlichen Fakultät
der Karl-Franzens-Universität Graz

Betreuer:

Univ.-Prof. Mag. Dr. Gottfried Kirchengast

Mitbetreuer:

Mag. Dr. Andreas Gobiet

Wegener Zentrum für Klima und Globalen Wandel
und
Institutsbereich Geophysik, Astrophysik und Meteorologie
Institut für Physik
Karl-Franzens-Universität Graz

GRAZ, MÄRZ 2010

Acknowledgments

I wish to express my gratitude and respect to the supervisor of this PhD thesis, Prof. Gottfried Kirchengast, for his excellent scientific advice. In his position as founder and head of the Wegener Center (WegCenter) he built up the proper open-minded surrounding conditions for writing this thesis.

I am deeply indebted to the co-supervisor, Dr. Andreas Gobiet, for his excellent, inspiring and time-consuming scientific and personal support. Although he was occupied by building up the Regional and Local Climate Modelling and Analysis Research Group (ReLoClim) at the WegCenter and establishing ReLoClim as an internationally recognised group, he had time enough for long-lasting discussions over the last years that encouraged me and helped me to improve the quality of this thesis and its underlying analyses.

The thesis's investigations required a huge amount of computational resources. This demand was covered by the high-performance computing facilities of the European Centre for Medium-Range Weather Forecasts (ECMWF), the Information Service (ZID) of the University of Graz, and the Institute for Geophysics, Astrophysics, and Meteorology (IGAM) / Institute of Physics of the University of Graz. Special thanks are expressed to the system administrators, Wim de Geeter (WegCenter), Carsten Maass (ECMWF), Ing. Roland Maderbacher (IGAM), and Dr. Ursula Winkler (ZID) for their professional and unbureaucratic support and to the Austrian Central Institute for Meteorology and Geodynamics (ZAMG) for offering parts of their computing time allocated at the ECMWF. Many thanks are also expressed to Dr. Georg Mayr, Institute for Meteorology at the University of Innsbruck, and ZAMG for the provision of high-quality observational data.

I gratefully acknowledge the financial funding from the Austrian Research Centers systems research GmbH (ARC-sys) via the project "Research for Climate Protection: Model Run Evaluation (reclip:more)" and from WegCenter's startup support for ReLoClim in the beginning of my doctoral programme. Furthermore, I really appreciate ReLoClim's financial support over the last years, since apart from reclip:more this PhD thesis stood outside of any project-related funding.

My thanks also go to my colleagues at WegCenter, particularly to the members of ReLoClim, for fruitful discussions and support. Due to its interdisciplinary composition, WegCenter provides an inspiring scientific and personal environment, I am proud to be able to contribute to. I wish to thank my room mates, Dr. Michael Borsche, Mag. Bettina Lackner, Mag. Susanne Schweitzer, and Mag. Martin Suklitsch for the excellent working atmosphere flavoured with a whiff of humour.

Finally, my heartfelt thanks go to my parents and close friends for constantly accompanying me with their openness and honesty through these years.

Abstract / Zusammenfassung

The present thesis focuses on investigating and improving a hybrid dynamic-diagnostic downscaling method for near surface wind (based on the dynamic PSU/NCAR model MM5 and the diagnostic California Meteorological model CALMET), which enables to provide wind climatologies over complex topography on the 100 m scale. A second objective is to conduct climate simulations and to identify climatological main processes affecting the long-term behaviour of averaged near surface wind conditions in the European Alpine region and the Vienna Basin under increasing greenhouse-gas concentrations. Questions of wind gusts and extremes are set aside.

Several variants of the method were applied (driven by the reanalysis dataset ERA-40) in two study regions, the Hohe Tauern region and the Vienna Basin. Comparisons to observations show that the steady-state flow concept and the orographic speed-up effect are the most dominant climatological mechanisms. The quality of the modelled climatologies is mostly affected by the ability to capture synoptic- and regional-scale processes. In the Vienna Basin the steady-state flow concept is more valid and leads to an enhanced systematic overestimation of wind speed (biases from 0.9 m/s to 2.1 m/s).

The method has been successfully applied to the output of the climate model ECHAM5 (periods 1981 to 1990 and 2041 to 2050, IPCC scenario IS92a). The climate change signals show decreasing annual wind speeds (up to -20.8 %, i. e., -1.2 m/s, in the inner Alps) and it can be concluded that a) changes of synoptic- and large-scale processes are affecting gradient-forced synoptic- and regional-scale air flows, particularly during DJF, b) the orographic speed-up effect amplifies changes of wind speeds in mountainous areas, and c) interactions between the atmosphere and the earth's surface lead to regionally varying climate change effects. There exists strong evidence for a robust model-independent reduction of wind speed during MAM and JJA in the inner Alps.

Das Ziel der vorliegenden Arbeit ist die Untersuchung einer kombinierten dynamischen-diagnostischen downscaling Methode für bodennahen Wind (basierend auf dem dynamischen Modell MM5 und dem diagnostischen Modell CALMET), welche es ermöglicht Windklimatologien in komplexer Topographie auf der 100 m Skala zu erstellen. Ein zweites Ziel ist die Durchführung von Klimasimulationen zur Identifikation klimatologischer Prozesse, die das Langzeitverhalten von mittleren Windverhältnissen in den Europäischen Alpen und dem Wiener Becken bei steigenden Treibhausgaskonzentrationen bestimmen. Böen und Extremereignisse werden nicht betrachtet.

Mehrere Varianten der Methode (angetrieben vom Re-Analysedatensatz ERA-40) wurden in den Hohen Tauern und dem Wiener Becken eingesetzt. Vergleiche zu Beobachtungsdaten zeigen, dass die Konzepte der Stationären Strömung und der Strömungsüberhöhung die dominantesten Klimamechanismen sind. Die Qualität der Windklimatologien wird hauptsächlich von der Fähigkeit, synoptische und regionale Prozesse abzubilden, beeinflusst. Im Wiener Becken hat die Stationäre Strömung mehr Validität und führt zu einer verstärkten systematischen Überschätzung der Windgeschwindigkeiten (Bias zw. 0,9 m/s und 2,1 m/s).

Die Methode wurde erfolgreich auf eine Klimasimulation des Modells ECHAM5 (Perioden 1981 bis 1990 und 2041 bis 2050, IPCC Szenario IS92a) angewandt. Die Klimaänderungssignale zeigen rückläufige Jahreswindgeschwindigkeiten (bis zu -20.8 %, das sind -1.2 m/s, in den Alpen) und es kann gefolgert werden, dass a) Änderungen der synoptischen und regionalen Prozesse gradientenbedingte Strömungen beeinflussen, insbesondere im Winter, b) die Strömungsüberhöhung Änderungen der Geschwindigkeiten im Gebirge verstärken und c) Wechselwirkungen zw. Atmosphäre und Erdoberfläche zu regional unterschiedlichen Effekten führen. Unabhängig von der Wahl der Modelle werden saisonale Windgeschwindigkeiten im Frühling und Sommer in den Alpen zurückgehen werden.

Contents

Introduction

The present thesis contributes to the scientific activities in the broad field of climate research. It is focused on near surface wind and it is concerned with both, the current climate and the climate's future behaviour under increasing greenhouse-gas concentrations. The motivation of the thesis is partly basic research-oriented and partly application-oriented. The former lies in a better understanding of the climate-relevant processes for near surface wind over complex topography, the latter lies in the development of a numerical modelling approach to provide wind climatologies on the 100 m scale.

Since the early 1990s much effort has been put on climate research, increasingly gaining knowledge and understanding about the climate system and its possible developments throughout the 21st century. By now, four assessment reports summarising the work of thousands of honourable scientist concerning the physical science basis, impacts, adaptation, vulnerability, and mitigation of climate change have been published by the Intergovernmental Panel on Climate Change (IPCC). In advance to the recent United Nations Climate Change Conference in Copenhagen, December 2009, the Climate Change Research Centre at the University of New South Wales, Australia, synthesised together with partners the most policy-relevant recent science activities. In their report, "The Copenhagen Diagnosis" (*Allison et al.*, 2009), the authors provide a climate change science update starting from the 4th IPCC assessment report. Some of the most important all-agreed key-findings indicating the urgent need for climate protection are:

- Based on observational data the Earth's climate is changing with increasing speed. *"The linear warming trend [of global near surface temperature] over the last 50 years is nearly twice that for the last 100 years"* (*Solomon et al.*, 2007).

- Ongoing global warming leads to irreversible damage. *"Several vulnerable elements in the climate system (e. g., continental icesheets, Amazon rainforest, West African monsoon and others) could be pushed towards abrupt or irreversible change if warming continues in a business-as-usual way throughout this century"* (*Allison et al.*, 2009).

- The probability that the observed increase in anthropogenic greenhouse gas concentrations is the cause for most of the observed increase in global temperature since the mid-20th century has changed from *"likely (>66 % probability)"* (*Houghton et al.*, 2001) in the 3rd IPCC report to *"very likely (>90 % probability)"* (*Solomon et al.*, 2007) in the 4th IPCC report. Based on most recent analysis of other possible causes for global warming, *Allison et al.* (2009) finally conclude that *"the greatest part of the century-scale warming is due to human factors."*

Depending on greenhouse-gas emission scenarios the best estimates for the global temperature increase derived from climate simulations are expected to lie within a range between 1.8 °C and 4.0 °C by the end of this century (*Solomon et al.*, 2007). However, while there is a broad agreement throughout the involved climate models about the temperature increase and an expansion of the Hadley Circulation together with a pole-ward shift of the mid-latitude storm tracks (*Yin*, 2005) in general, the regional climate change effects of near surface wind in the European Alps are largely unclear. Due to the complexity of the climate system and due to model-limitations only some few robust key-findings on global and regional scales can be identified from multi-model multi-scenario simulations: e. g., the role of the global atmospheric circulation, the relation between changes of mean sea level pressure gradients and shifts of cyclon-tracks (*Solomon et al.*, 2007), and constant or weakly reducing annual wind speeds (up to -5 %) across the Alpine region by the end of this century depending on the used climate model (*Rummukainen et al.*, 2004).

In the face of this wide range of uncertainties, the present thesis focuses on investigating and improving a modelling approach for near surface wind, which enables to provide spatially distributed wind climatologies on the 100 m scale as they are required in numerous climate impact studies and other applications, like the exploitation of wind energy. This is an increasingly upcoming field in climate protection since near surface wind is one of the most prominent renewable energy carriers (*Zervos et al.*, 2009).

The applicability and the limitations the modelling approach, the steady-state flow concept, are investigated by means of two study regions with differently complex topography, the Hohe Tauern region and the Vienna Basin. A further objective of the thesis is to apply the modelling approach to climate simulations and to identify climatological main processes in the European Alpine region which are affecting the long-term behaviour of near surface wind under changing climate conditions.

The thesis is structured into five chapters. Chapter 1 is focused on Planetary Boundary Layer (PBL) processes and gives an overview of near surface air flows. Starting on planetary scale, the main driving phenomena for near surface wind are subsequently analysed ending up with local-scale flow patterns in the European Alps. Observation-based climate change effects of near surface wind and the essential outcome of modern climate simulations are discussed as well. In Chapter 2 the basic concepts of state-of-the-art models for near surface wind including their advantages and limitations are presented and the modelling approach favoured in this thesis, the hybrid dynamic-diagnostic downscaling method, is introduced. Various modifications and improvements of this method are designed in Chapter 3. Chapter 4 provides a thorough evaluation of the downscaling method and its variants and isolates the method's inherent downscaling errors. In order to reduce these errors statistical correction functions based on the quantile mapping method are derived. The influence of these correction functions on simulation-based climate change effects is discussed at the end of this chapter. In Chapter 5 statistically significant climate change effects for near surface wind and their causes in the Alpine region and in the Vienna Basin are derived by applying the hybrid downscaling method on a global climate simulation representing the current climate (period 1981 to 1990) and a future climate scenario (period 2041 to 2050).

1 Air Flows in the European Alps and the Effects of Climate Change

The Alps, an 800 km, arc-shaped mountain range with an average width of ∼200 km and an average height of ∼2500 m (highest summit: Mont Blanc 4810 m) resides in Central Europe between Vienna (Austria), Munich (Germany), Lion (France), Marseille (France), Milano (Italy), and Maribor (Slovenia). This amazing mountain range is spread over numerous European countries and is lying in a transition zone influenced by the European continent and two oceans, the cool Atlantic farther to the west and the warmer Mediterranean Sea close to the south.

The Alpine climate as an ensemble effect of different atmospheric and oceanic processes on a wide range of spatial and temporal scales has always been of interest for the resident population. It was Horace Bénédict de Saussure (1740–1799) from Switzerland who built the foundations for scientific exploration of mountain meteorology in the second half of the 18$^{\text{th}}$ century (*Schär et al.*, 1998). The longest-lasting climate records from systematic observations originate from that era (*Auer et al.*, 2007). About 100 years later, first national-wide observation networks were established based on initiatives by leading scientists, like the Austrian Julius Ferdinand von Hann (1839–1921) and the Swiss Heinrich von Wild (1833–1902) (*Wanner et al.*, 1997). In the ongoing course of the scientific, technological, and economic progress over the last centuries new observation techniques, analysis-methods, and knowledge from interdisciplinary cooperations have been developed and applied in order to reveal the underlying processes of Alpine climate. During the last decades another aspect (of global dimension), the global climate change and its sources from anthropogenic activities, appeared. Much effort has been put on the investigation of the impacts of anthropogenic greenhouse gases on the global climate system and its feedbacks. Nowadays, more than 2000 scientist from 154 countries typically participate in the climate assessment process of the Intergovernmental Panel on Climate Change (IPCC). The presented work focusses on near surface wind affected by climate change on a regional and local scale to contribute the knowledge about the Alpine climate under changing conditions.

1.1 Main Driving Phenomena from the Global to the Local Scale

In modern climatology the global climate system represents a four-dimensional (three coordinates in space and one in time) physical system that is described by observable

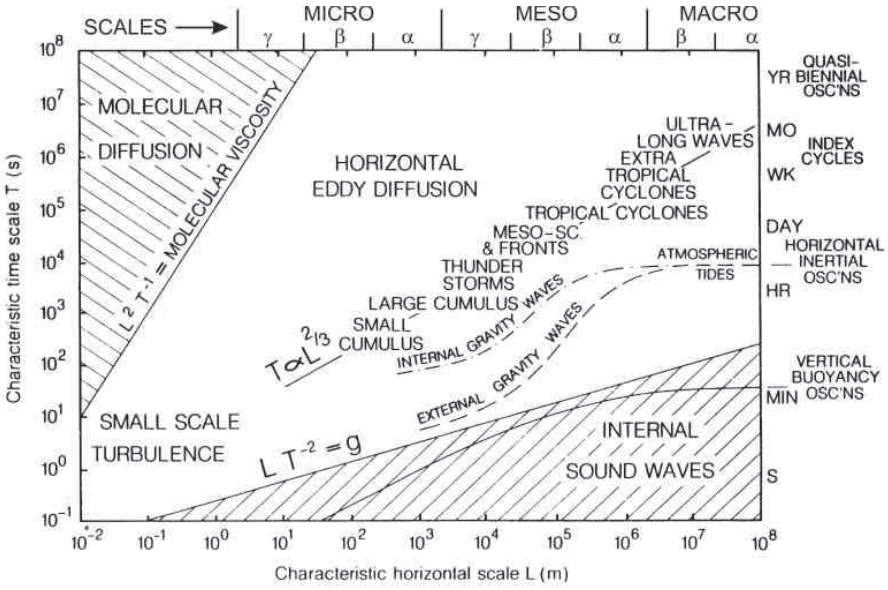

Figure 1.1: Definition of length-scale classes (micro, meso, and macro) (*Orlanski*, 1975) and correlation between time- and length-scales for characteristic atmospheric phenomena. From *Barry and Carleton* (2001), modified.

physical quantities (e. g., temperature, precipitation, wind speed, wind direction, etc.), called "climate variables" (ger. "Klimaelemente"), and their behaviour in space and time (*Barry and Carleton*, 2001; *Hantel*, 2001). The climate system is divided into its (climate) components: the atmosphere, the hydrosphere, the cryosphere, the lithosphere, the biosphere, and eventually the anthroposphere. Single (climate) phenomena (such as cyclones, planetary waves, cumulus convection, etc.) are resulting from the interplay of physical, chemical, and biological mechanisms within and between the climate components and occur on a wide range of time and length scales. Thereby, the phenomena on smaller scales are embedded into phenomena on larger scales generating a chain of interdependency from larger to smaller scales (downscale) and vice versa (upscale) (cf. Figure 1.1): e. g., the genesis, track, and strength of synoptic-scale (100 km to 1000 km) weather phenomena are causally depending on the general circulation of the atmosphere which is induced by the zonal distribution of the earth's surface temperature. However, the temperature distribution is significantly influenced by the weather phenomena in turn (*Schär et al.*, 1998).

Based on the differences of scales and/or the most active mechanism the atmosphere can further be separated into major sub-systems. One commonly used division results from the vertical thermal stratification leading to the definition of the troposphere, stratosphere, mesosphere, and thermosphere.

Another well-known separation defines the free atmosphere in which the effect of the earth's surface friction on the air motion is negligible (*AMS*, 2000) and the Planetary Boundary-Layer (PBL) which is characterised by its turbulent transfer of mass (*Pielke*, 2002) and *"[...] is directly influenced by the presence of the earth's surface, and responds to surface forcings with a timescale of about an hour or less."* (*Stull*,

1988). Note, the PBL is the lowest boundary of the troposphere and usually reaches heights below 2 km and 3 km. During night, it might reach a depth of no more than 50 m and 100 m and is strongly influenced by internal gravity waves. However, under strong convective conditions the PBL grows much deeper into the troposphere (up to 5 km) (*Garratt*, 1992) and might extent into the stratosphere in exceptional cases when thunderstorms occur (*Pielke*, 2002). Moreover, all the incoming and outgoing global energy fluxes at the earth's surface are transmitted through the PBL resulting into its high variability in space and time and its complex structure: Firstly, at the lower-most level there is the surface layer (Prantl layer) where Monin-Obukhov theory is valid and Coriolis turning of the wind is not evident. It is subdivided into the inter-facial sub-layer dominated by molecular viscosity and diffusivity and the inertial layer where turbulent motions exist on scales much smaller than the PBL depth. Secondly, there is the outer layer (transition layer) where turbulent motions occur on scales comparable to the PBL depth (*"large eddies"*) and which is often capped by an entrainment zone or a stable inversion layer. It changes into free convection layer, mixing layer, stable layer, and the residual layer (remaining from a mixed layer of the previous day) depending on static and dynamic instabilities (cf. Figure 1.2). Moreover, due to the diversity of surface conditions (e. g., radiative properties, surface drag, moisture availability, thermal conductivity, etc.) an Internal Boundary-layer (IBL) is induced, which separates distinctive areas of turbulence. Depending on the heterogeneity the mean horizontal air flow is accelerated or decelerated at the IBL and/or the stability of the entire PBL might change (cf. Figure 1.3). *Savelyev and Taylor* (2005) report over more than 20 empirical formulae to estimate the IBL's height. Note, based on different sets of balanced forces the outer layer is also defined as Ekman layer, advective layer, or Stokes layer (*Pielke*, 2002). However, due to static (convective or Rayleigh-Benard) and dynamic (shear and Kelvin-Helmholtz) instabilities laminar PBLs like the Ekman layer cannot be observed in the atmosphere. Since the PBL couples the free atmosphere with the remaining climate components, it plays a central role in the climate system. More than a half of the atmosphere's kinetic energy loss occurs in the PBL (*Garratt*, 1992).

Due to the chain of interdependency, time series of wind speed and wind direction at a certain point in the PBL depend on phenomena over all scales, even in the case of local wind systems at the micro-β-scale (10 m to 100 m) which are nearly independent from meso-scale (synoptic) weather patterns (autochthonous wind systems): it is up to the synoptic patterns to allow such wind systems. Hence, in order to generate a highly resolved wind-climatology phenomena on all scales have to be considered.

1.1.1 On Planetary and Large Scales

On the planetary scale ($>10^4$ km) a circulation in the free atmosphere (the general circulation) can be derived from time-related statistics of wind observations (cf. Figure 1.4a). Because of the earth's curvature the incoming solar radiation results in a meridional distribution of heat. This imbalance between the poles and the equator is compensated by a poleward heat-transfer which is accomplished by the general circulation and a circulation of the global ocean (cf. Figure 1.4b). Both circulations are interacting with each other and with the global landmasses through their boundary layers via friction and the exchange of energy. The circulations are perturbed by the global land-sea

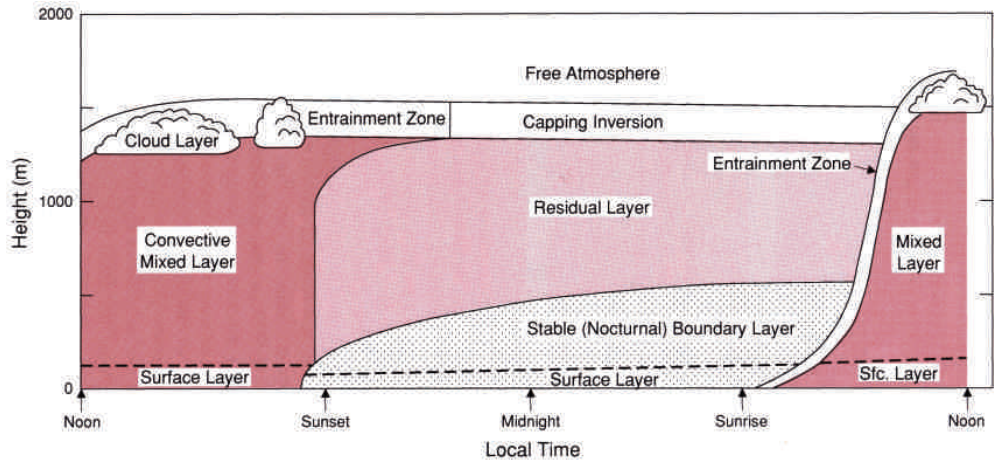

Figure 1.2: Schematic of the diurnal cycle of the inversion-capped PBL over land without disturbance from the free atmosphere. Based on hydrostatic stability and type of turbulence the PBL is divided into the surface layer, the convective layer, the mixed layer, the stable layer, and the residual layer. From *Stull* (1988).

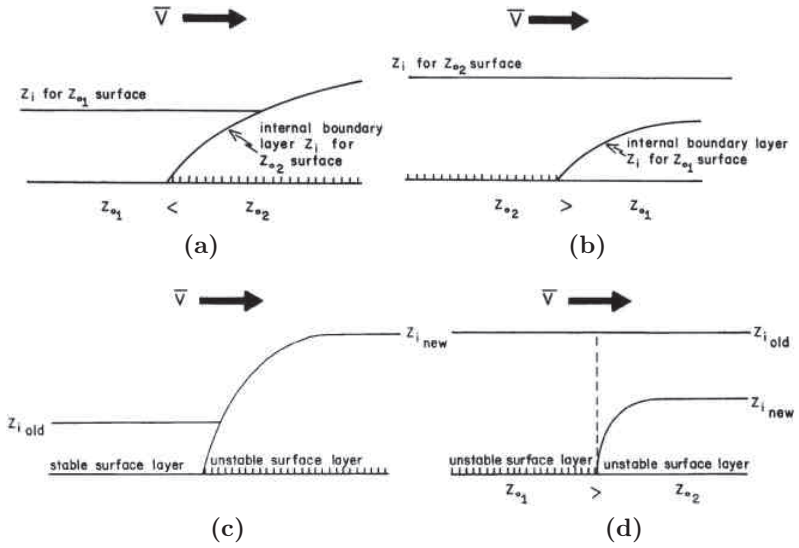

Figure 1.3: Schematics of the IBL from *Pielke* (2002). Upper panels: an airflow advects under neutral conditions (a) from a smooth (small roughness length z_0) to a rough (large z_0) surface; and (b) vice versa. The IBL appears at boundaries of adjacent regions of distinctive turbulence. Lower panels: (c) a stable stratified airflow becomes unstable as it advects from a smooth to a rough surface; (d) an unstable flow becomes stable as it advects from a rough to a smooth surface.

distribution inducing fluctuations and waves.

Looking into detail, the Alpine region (44° N to 48° N) lays in the southern part of the mid-latitude westerly wind belt of the Ferrel Cell (30° N to 60° N) and between the subtropical high pressure and the sub-polar low pressure belt. Due to this geographic location the Alps are exposed to sequences of cyclones and anti-cyclones embedded into the planetary waves (Rossby-waves) forcing the day-to-day weather conditions. The planetary waves, which are induced by the earth's major topographic obstacles (*Schär et al.*, 1998), are perturbed by blocking events stopping the general westerly mean-flow or even changing its direction. In the Atlantic-European region blocking events arise from quasi-stationary high-pressure systems lasting for up to two weeks with a maximum of occurrence during spring and a minimum during summer (*Trenberth et al.*, 2007). They are an important component of intra-seasonal variability. A global pressure oscillation pattern influencing the European climate is the coupled ocean-atmosphere system El Niño/Southern Oscillation (ENSO). Although it is mainly responsible for inter-annual variability in the entire tropical pacific region it has global impacts by changes in jet streams and storm tracks in the mid-latitude (*Trenberth et al.*, 2007). In the Atlantic-European sector ENSO modifies synoptic-scale weather systems and changes the intensity and location of the Atlantic storm track (*Schär et al.*, 1998). Additional variability arises from the interaction between troposphere and stratosphere. The Quasi Biennial Oscillation (QBO) in the tropic stratosphere with an average period of 27 Months modifies the global stratospheric circulation (Brewer-Dobson circulation) and influences the extra-tropical climate. For the Alps a statistically significant QBO signal is found in the monthly rainfall of September and October (*Wanner et al.*, 1997).

On the large-scale (10^3 km to 10^4 km), the Alps are embedded in an area between the Icelandic Low to the northwest, the Azores High to the southwest, the continental Siberian High to the east, and a weak Mediterranean Low to the south during winter. This leads to a large variability of the mean sea level pressure (MSLP) reducing the occurrence of weather patterns of weak pressure gradients in the Alpine region down to ∼16 % (*Schär et al.*, 1998). The strengths and locations of the Icelandic Low and the Azores High are modified by the North Atlantic Oscillation (NAO) on inter-annual and multi-decadal time scales. Although the NAO is active over all seasons it mostly influences synoptic systems (i. e., cyclones, anti-cyclones, and fronts) during winter by altering their frequencies, intensities, and tracks. Usually, most of the cyclones generated in the Atlantic region are impinging the European continent in its north-western part and are moving eastwards forming the Atlantic storm track. In periods with a strongly pronounced NAO the Atlantic storm track is shifted pole-wards and the westerly mean-flow is enhanced and transports more warm and moist maritime air from the Atlantic towards the northern part of the European continent resulting in warmer and wetter winters in Northern and Central Europe (*Thompson and Wallace*, 2001). In Southern Europe, a strong NAO results in cooler and dryer winters (*Thompson and Wallace*, 2001; *Trenberth et al.*, 2007). The NAO is the major winter climate mode, accounting for about one third of the statistically derived inter-annual variability of the mid-tropospheric large-scale flow in the mid-latitudes (*Schwierz et al.*, 2006). In Northern and Central Europe the NAO may account for over 60 % of the climate's variability (*Beniston*, 2006). For example, 56 % of the observed pressure variance in Switzerland can be explained by the behaviour of the NAO (*Beniston and Jungo*,

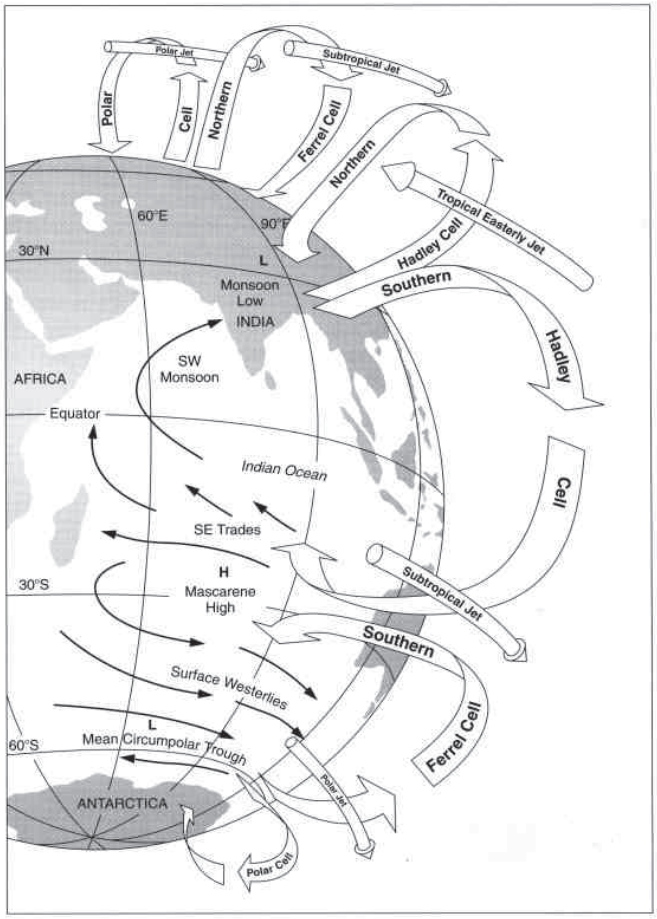

(a)

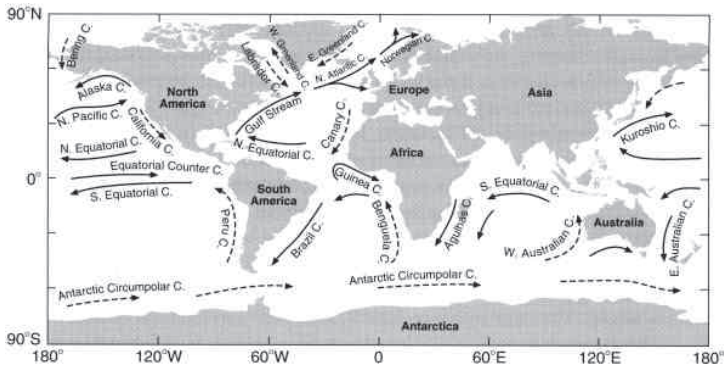

(b)

Figure 1.4: Schematics of planetary circulations from *Washington and Parkinson* (2005). (a) the general circulation. Three basic-cell circulation patterns (i. e., the Hadley Cell, the Ferrel Cell, and the Polar Cell) are shown for the northern hemisphere during summer conditions. The southern Hadley Cell is shifted over more than 20° to the north due to an enhanced continental-wide convection over South-Asia. (b) the major surface ocean currents.

2002). In summer, the Azores High extents to the northeast and becomes the most influencing factor amplified by inter-annual to multi-decadal fluctuations of the NAO, which emphasises persistent high-pressure systems over Northern Europe (*Trenberth et al.*, 2007). In addition, the Atlantic storm track is much weaker pronounced and cyclonic activity is reduced. In the Alpine region, this situation advances the occurrence of weak pressure gradients to a maximum of ∼36 % (*Schär et al.*, 1998) and enforces the development of local climate-related features according to convective weather patterns. Similar situations may appear from blocking events (see above) which are partly related to weak periods of the NAO and partly they are supposed to be induced by the tropospheric-stratospheric exchange (*Trenberth et al.*, 2007). Due to the complexity of the global atmospheric and oceanic circulations potential sources of the NAO's variability are not fully revealed yet, but they include one-way or coupled interactions with the mid-latitude ocean, the tropical ocean, the Indian ocean, and the stratosphere (*Schwierz et al.*, 2006).

1.1.2 On Synoptic and Regional Scales

On scales between 10 km and 10^3 km, the Alpine climate is affected by the mountains' massif itself via retarding and modifying the approaching synoptic systems with respect to the PBL's stability. Most of the cyclones generated over the Atlantic ocean are moving along the storm track into northeastern Europe. When the southern tails of the cyclones' accompanying fronts are impinging and passing the Alps from north and northwest new cyclones may emerge on the lee-side of the Alps. These new cyclones are the result of the Alpine lee cyclo-genesis (cf. Figure 1.5) and are moving eastwards forming a secondary but weaker storm track over the Mediterranean Sea influencing the climate of the east and southeastern part of the Alpine region as well as the entire Mediterranean area (*Schär et al.*, 1998). On average, the lee cyclo-genesis takes place about 65 times per year (*Trigo et al.*, 2002) and is accompanied by numerous flow phenomena on the regional scale: A strong southwesterly flow of warm, moist, and weakly stratified air ahead of the approaching cold front which passes over the Alpine main crest and may develop the South Föhn to the north with a maxima of its occurrence during spring and autumn (*Schär et al.*, 1998; *Weber and Furger*, 2001). As the front moves further, cold air from behind the front is deflected and flows around the western and eastern parts of the Alps pronouncing two strongly stable stratified northerly flows of cold air, the Mistral in the west and the Bora in the east. Finally, when the mass of cold and dry air behind the front grows in height it spills over the Alpine main crest and may generate the North Föhn. Due to the retardation of fronts, the areas downstream are shielded, which results generally in lesser precipitation, weaker winds, and more frequent inversions and fog, especially in winter in cases of high anti-cyclone activity. Although, local phenomena are determined by synoptic phenomena, there is no clear assignment between Föhn, Mistral, Bora, and other characteristic flow patterns, like the Bise (a channelised north-easterly flow in Switzerland), and definite weather patterns (*Weber and Furger*, 2001; *Weber and Kaufmann*, 1998). However, strong flows mostly occur under advective conditions reaching their maximum of occurrence during winter (∼62 %) (*Schär et al.*, 1998). Extreme wind speeds (wind gusts) near the ground with a serious destructive potential (>26.4 m/s, i. e., 10 Bft) are observed when tropical

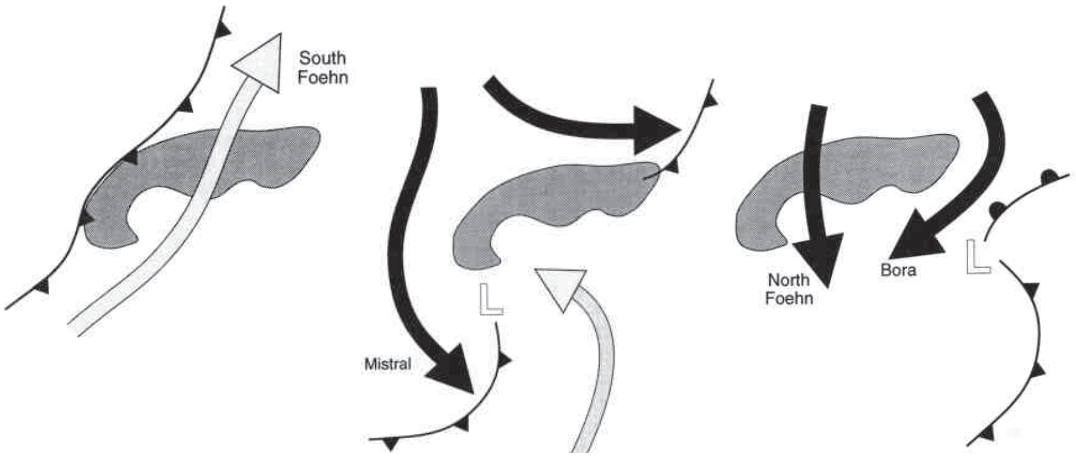

Figure 1.5: Schematic of the Alpine lee-cyclogenesis: (a) an intercepting cold front is deformed and South Föhn results from prefrontal winds, (b) cold-air breaks out into the western Mediterranean Sea (Mistral) and a lee-cyclone is formed, (c) the lee-cyclone progresses eastwards and Bora and North Föhn appear. From *Schär et al.* (1998).

cyclones (i. e., hurricanes) move northwards along the West Atlantic following the Gulf Street and impinge the European continent. *Hart and Evans* (2001) estimate one transitioned tropical cyclone per year over Europe for the 20$^{\text{th}}$ century based on the analysis of cyclone-tracks of the U.S. National Hurricane Center. The German weather service (DWD) counted 25 hurricanes during the period 1990 to 2007 (*Müller-Westermeier, G.*, 2007).

Looking further into details, advective air flows in the Alpine region within a statically stable PBL can mainly be described by two idealised flow regimes (cf. Figure 1.6): the flow-over and the flow-around regime. In the former case, a laminar time-averaged flow of statically stable air impinges an obstacle. The air flow is retarded and lifted but it keeps its laminar structure. The incoming air is lifted along the obstacle's surface and accelerates (Venturi-effect). Right after the obstacle the air falls down until it reaches its original position. Depending on the stability of the stratification the vertical displacement of air induces horizontally and vertically propagating internal gravity waves (cf. Figure 1.7) characterised by their Brunt-Väisälä-frequency (N) (*Etling*, 1996). In the flow around regime, when the velocity of the incoming air flow is slow enough and/or the stratification is more stable the laminar flow breaks down and turbulence (vortex shedding) from dynamic instability (shear instability) occurs where the gravity waves are weaker and the influence on higher levels is smaller. For larger obstacles like the Alps the earth's rotation (Coriolis force) enforces the flow-over regime (*Schär et al.*, 1998). However, the two flow regimes are idealised types and natural air flows are more complex, especially on smaller scales: while the flow-over regime is more pronounced for the Alpine massif, flow-around patterns occur for single mountains. Vortex shedding for the Alps as a hole has not been observed, but single vortices at the western

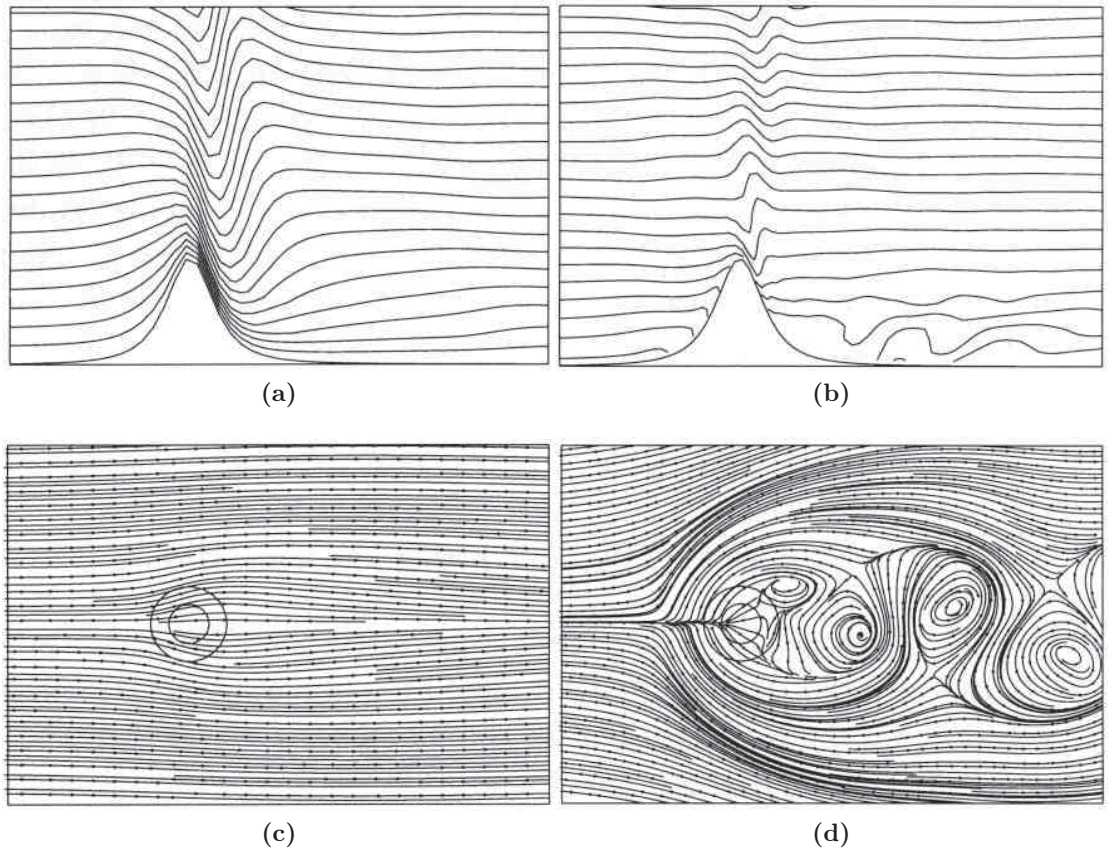

Figure 1.6: Idealised flow patterns from numerical simulations. Panels (a) and (c) show the instantaneous streamlines in a vertical section across a mountain top, panels (b) and (d) show the same features on the surface. Air flows from left to right and shows both, the flow-over (panels (a) and (b)) and the flow-around (panels (c) and (d)) regime. From *Schär et al.* (1998).

edge of the massif have been identified contributing the Alpine lee cyclo-genesis (*Schär et al.*, 1998).

Without disturbances from larger-scale advection, weak pressure gradients which are observed ∼25 % of all days per year (*Steinacker*, 1990), are supporting a diurnal cycle of thermally driven circulations between the Alpine main crest and the adjacent foreland regions (i. e., *"Alpine pumping"*, (*Lugauer and Winkler*, 2005)). Due to the enhanced radiative heating (cooling) of near-surface air layers in the inner Alpine region weak low-level inflows (drainages) are established during daytime (nighttime) based on two topographic effects. First, the terrain provides an elevated source (sink) of heat during the day (night) and second, the volume of air per horizontal area is smaller in the inner Alpine region than in the forelands (i. e., *"volume-effect"* (*Steinacker*, 1984)). Due to this effect the inner Alpine region responses faster to thermal energy gain (loss) and warm (cold) low- (high-) pressure systems are generated during daytime (nighttime) over the Alpine massif. This diurnal cycle of pressure anomalies causes horizontal

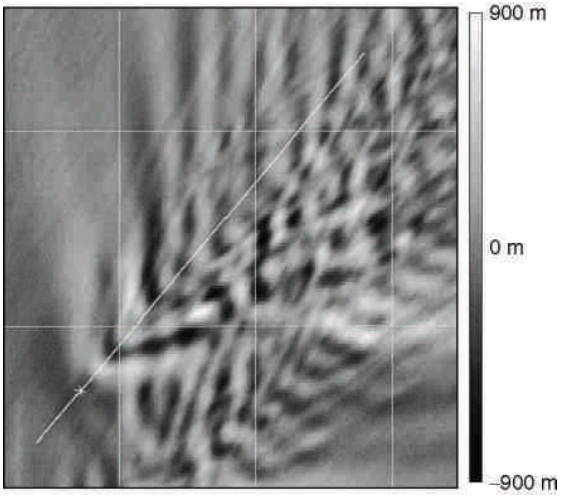

Figure 1.7: Plan view of the vertical displacement of streamlines from atmospheric simulation of the 2 November 1999 in the Alpine region. The small white × marks the location of Mt. Blanc. From *Smith et al.* (2007).

pressure gradients enforcing a diurnal cycle of air circulations. Analysis of observations from 39 surface stations in South Bavaria have shown that on 42 % of all days from April to September between 1996 and 2000 the thermal circulation propagates ∼100 km into the Alpine foreland and shows daily maxima up to 2 m/s during daytime (17:00 UTC) and 1.5 m/s in the morning (07:00 UTC) at selected pre-alpine stations close to the Alpine foothills (*Lugauer and Winkler*, 2005).

In addition, air flows are influenced by the net radiative energy flux (defined as the difference between absorbed incoming and outgoing radiation at the surface) which drives the processes in the PBL by feeding the turbulent fluxes of latent and sensible heat, the heating of the soil, and the melting of snow. *Schär et al.* (1998) report from analysis of observations that the global radiation (i. e., sum of direct and diffuse shortwave radiation) differs between the north and the south of the Alps (with respect to the formation of clouds) and increases with height by ∼0.8 W/m^2 per 100 m. However, since the surface albedo controls the absorption of global radiation, the presence of snow covers in elevated areas substantially reduces absorbed shortwave radiation. Moreover, the long-wave radiation decreases in height with about −3 W/m^2 per 100 m (incoming) and −2 W/m^2 per 100 m (outgoing). Hence, the mean net radiation and in accordance the turbulent heat fluxes of the PBL tends to decrease with height.

1.1.3 On Local Scales

On the subregional (1 km to 10 km) and local scale (<1 km) the effects of the topography and hence the influence on the PBL gets increasingly more important with respect to the terrain's geometry and the earth's surface conditions. Generally, the underlying mechanism which are responsible for deviations between synoptic-scale flow and near surface flow can be divided into:

- **static instability** appears in a static motionless atmosphere from thermal forcing,
- **dynamic instability** appears in a moving atmosphere and is induced by wind shear (i. e., barotropic instability),
- **kinematic terrain effects** modify flow velocities and directions and induce gravity waves due to the terrain's geometry and with respect to the PBL's stability,
- **decoupling through inversion layer** leads to weak thermal valley circulations or stagnant air influenced by the synoptic pressure gradient, and
- **anthropogenic activities** modify the development of inversion layers and induce weak thermal driven circulations based on spatially distributed changes of surface conditions and heat fluxes.

Based on these mechanism numerous flow phenomena occur in complex terrain. The most important are discussed below.

From radiative heating of the surface the PBL becomes statically unstable and convection is induced resulting in decoupled mountain-valley circulations showing a characteristic diurnal cycle (cf. Figure 1.8). The volume-effect, which is responsible for the Alpine pumping may enforce larger heating rates in smaller valley volume, however, *Rotach and Zardi* (2007) adduce dynamic effects of the cross-valley circulation (i. e., subsidence of potentially warmer air from the free atmosphere above the valley and vertical advection) to be the main mechanism for heating up the valley atmosphere. Furthermore, they report that a primary cross-valley circulation due to side-wall heating induces a secondary circulation based on density differences as a result of the centrifugal force of the primary circulation. This secondary flow results into a downslope flow over the sunlit heated surface and upslope flows over cooler (shaded) slopes leading to an asymmetric flow pattern. During nighttime, near surface air parcels are cooled by the surface and hence the air parcels get more dense and subside downslope due to the effect of gravity. *Mahrt* (1982) derived eight classes of stationary slope flows from hydrostatic approximation of the momentum equations for incompressible air with respect to the PBL's stability described by the Froude number (Fr). Usually, the thermal forced circulations are relatively weak: *Weber and Kaufmann* (1998) report mean wind speeds of 2.5 m/s during daytime and 2.0 m/s during nighttime observed 43 m above ground in a two-year period (1991–1992) in a valley close to Basel (Switzerland). In combination with certain synoptic weather conditions and the terrain effects of the Alps, convection may induce tornadoes and other local extreme wind events. *Holzer* (2001) counted 96 tornadoes in Austria (period 1910 to 1998), 63 of them observed during summer, and found a verified maximum wind speed of 93 m/s. While in Germany tornadoes show a spatially homogeneous distribution with a mean annual recurrence density rate between 0.1 $a^{-1}10^{-4}km^{-2}$ and 0.2 $a^{-1}10^{-4}km^{-2}$ (period 1870 to 2000) (*Dotzek*, 2001) the tornadoes in Austria are highly influenced by the Alps: the mean rate of 0.3 $a^{-1}10^{-4}km^{-2}$ is regionally distributed around the eastern foothills of the Alps (1.0 $a^{-1}10^{-4}km^{-2}$ for the greater area around Linz, 1.2 $a^{-1}10^{-4}km^{-2}$ for the southern Vienna Basin, and 0.9 $a^{-1}10^{-4}km^{-2}$ for the Basin of Graz) (*Holzer*, 2001). The genesis of tornadoes in

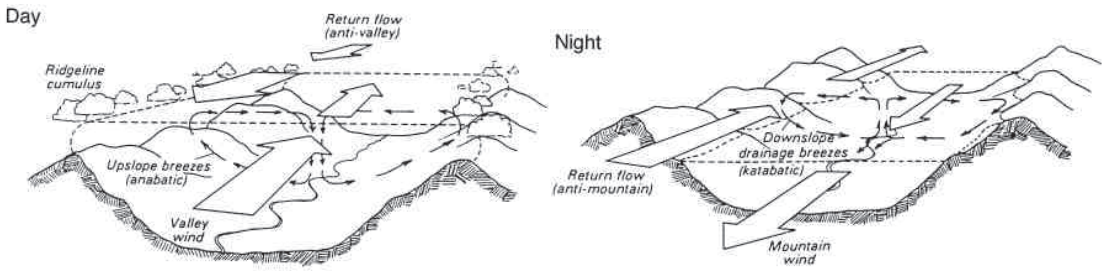

Figure 1.8: Schematic mountain-valley-circtulation during (a) day and (b) night. From *Schär et al.* (1998).

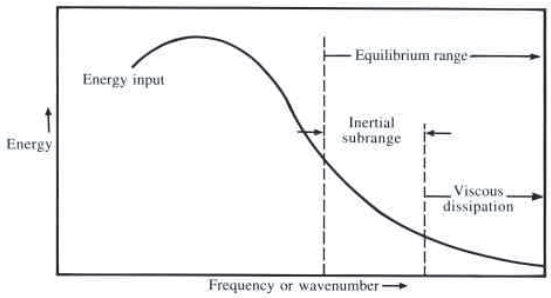

Figure 1.9: Schematic of the turbulent energy cascade. Turbulent kinetic energy is transmitted from larger to smaller wavelengths. Within the inertial subrange turbulent motions are roughly homogeneous, isotropic, inviscid, and self-similar. From *Garratt* (1992).

the Alpine region is hardly investigated. *Holzer* (2001) supposes quasi stationary or stalled cold fronts lying over the eastern Alps and prefrontal squall lines or meso-scale convective systems approaching from the west as responsible synoptic configurations.

Due to barotropic instability (the magnitude of influence of baroclinic instability is 10^2 to 10^3 times smaller than the barotropic instability (*Garratt*, 1992) and is further neglected) any infinitesimal perturbation of an initially laminar flow grows exponentially in time resulting in a cascade of eddies from larger (comparable to the PBL height) to molecular scales where the eddies are eventually dissipated by viscosity (cf. Figure 1.9). Along this cascade (turbulent) kinetic energy is transmitted to smaller scales reducing the mean flow velocity (averaged over a time-period larger than the periodic time of the turbulent eddies). Due to this deceleration (wind shear) the impact of the Coriolis force is reduced and the mean wind directions are turned (Ekman layer). Depending on the PBL's static stability, which is affected by the release (capture) of the heat of phase transformation of water at the surface and within the PBL, the generation of turbulent eddies is enhanced (unstable PBL), supporting convection, or suppressed (stable PBL), decreasing the deviation of the near surface flow from the synoptic flow.

Within the inertial subrange (cf. Figure 1.9) the relationship between mean wind speed and hight above ground is sufficiently described by the Monin–Obukhov Sim-

ilarity Theory in homogeneous and flat terrain. However, observations have shown the break down of this concept in complex terrain (e. g., *Moraes et al.*, 2005). Due to the terrain's geometry additional inhomogeneities of the surface heat fluxes appear. A drastic example pointing out the importance of the terrain's influences are the results of *Rotach et al.* (2008): based observations of the surface energy fluxes on 15 radiation-days during August and October 1999 they have shown that in a narrow valley, the Riviera Valley in southern Switzerland, the daily net radiation is on average $\sim$100 W/m^2 (maximum 700 W/m^2) smaller than the sum over sensible, latent, and ground heat flux, and, therefore, the surface energy budget is not closed.

In the case of an increased static stability the damping-effect of molecular viscosity gets more important and vortex shedding (e. g., Kármán Street) in the averaged flow occurs. Stability also forces an air parcel to flow around an obstacle rather than to flow over it. The flow-around-like pattern is also important for a valley when the incoming flow is not aligned with the valley axis. Depending on the valley geometry, the direction of the incoming flow, and the PBL's stability the flow in the valley completely decouples and is purely driven by the synoptic pressure gradient along the valley. This pressure-driven channelling often occurs in long, straight, and well-defined valleys and has been observed in the upper Rhine Valley and the valleys of the Swiss Middleland (*Weber and Kaufmann*, 1998; *Whiteman and Doran*, 1993). In the case of short and narrow valleys the synoptic flow is simply deflected into an along-valley direction (i. e., forced channelling) (*Whiteman and Doran*, 1993).

The distinctive criterion between the flow-over and flow-around pattern is expressed by the Froude number (Fr). If Fr is smaller than a critical value of 1 the flow-around pattern is pronounced. If Fr is equal to 1 the flow runs through a point of bifurcation and a flow-over pattern occurs accompanied by most intense gravity waves (the natural wavelength of the air is in resonance with the size of the obstacle). In cases where Fr is greater than 1 the flow velocity behind the obstacle becomes larger than the velocity of the gravity wave (supercritical flow) and the gravity wave breaks down and induces turbulence (*Schär et al.*, 1998). If Fr becomes larger than $\sim$1.5 a cavity of reverse flow occurs on the lee-side of the obstacle generating a persistent lee-circulation. E. g., *Jiang and Doyle* (2004), who observed wave breaking for gravity waves (wavelengths 11 km and 6 km to 8 km) via flight-level data of a scanning aerosol backscatter LIDAR (SABL) over the central Alps (the Wildspitze, Austria) on the 21 October 1999, found a lee-side downslope flow (maximum speed $\sim$22 m/s) suddenly transitioning into local wind reversal. In addition, they found a reversal of the energy cascade transmitting energy from smaller wavelengths to larger ones, indicating strong non-linearities during wave breaking. Blocking of air layers beneath the gravity wave, critical layers with reversed wind shear, and hydrolic jumps were found as well during the same observation period (*Smith et al.*, 2007). Numerical simulations have shown that a more structured terrain promotes the breaking of gravity waves and their accompanying phenomena (*Jiang and Doyle*, 2004). Moreover, analysis of natural air flows have shown that the criterion for the flow around pattern depends on the curvature of the obstacle, i. e., the configuration of the terrain. Flow-around has been observed for Fr up to 1.6 (*Pielke*, 2002).

Based on the constraint of mass-conservation a flow impinging a hill is accelerated. Highest velocities occur close to the hill's summit pronouncing a speed-up effect (i. e., difference between the wind speed at the summit and the wind speed of the incoming

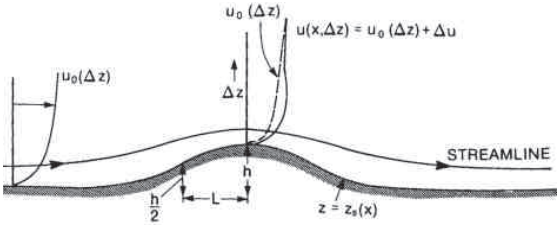

Figure 1.10: Schematic of the speed-up effect. An unperturbed flow with a vertical mean profile of the horizontal wind speed ($u_0(\Delta z)$), which is impinging a gentle hill, is accelerated near the surface (by Δu) with respect to the hill's height (h) and characteristic length (L). From *Taylor et al.* (1987).

unperturbed flow) which decreases in height above the obstacle (cf. Figure 1.10). With respect to the PBL's stability *Weng* (1997) found that a relative speed-up effect for the horizontal wind speed at 8 m above ground is stronger pronounced (∼300 %) during weakly stable conditions than during strongly stable conditions (∼200 %). Moreover, *Hewer* (1998) found negative relative speed-up effects under stable conditions (decelerations) up to −92 % in the submontane areas (downstream and upstream) indicating flow separation. Similar speed-up effects occur in Alpine valleys due to constrictions of the side-walls, i. e., gap-flows. *Mayr et al.* (2007) have investigated gap-flows in the Wipp Valley (Austrian Alps) via Doppler LIDAR observations during a three-month period in 1999. They found speed-up effects of 50 % to 100 % resulting in wind speeds over more than 18 m/s. In the Wipp Valley gap-flows occur ∼70 days per year with a seasonal variability: in winter the PBL is too stable and gap-flows are suppressed; during summer the frontal activity is too less. Gap-flows most frequently occur during spring and autumn with a weak diurnal cycle (preferring nighttime). Typically, gap-flows reach a depths of ∼2500 m. However, they can grow deep enough to affect the air up to or even beyond the tropopause (*Mayr et al.*, 2007).

Inversions caused by radiative cooling, by synoptic and cumulus-induced subsidence or by advection of warmer air results in stagnant air near the surface. In rare circumstances, a large wind shear within the inversion layer may induce internal gravity waves and horizontal roll vortices (*Pielke*, 2002). Depending on cloudiness and stability of the PBL weak thermal circulations appear beneath the inversion layer, which are decoupled from the synoptic flows, but influenced by the synoptic pressure gradient (i. e., *"pressure channelling"* (*Weber and Kaufmann*, 1998). Due to the shielding effect of the Alps south and eastern areas are more affected by inversions. E. g., *Lazar and Podesser* (1999) who summarised numerous investigations of the climate of Graz (an Austrian city located close to the south-eastern part of the Eastern-Alps) and its surrounding report an annual frequency of nighttime inversion up to 90 %, fog events for 100 to 110 days per year strongly influenced by the local topography, and an annual wind speed of 1.3 m/s. Alpine valleys are often capped by inversion as well. However, the process of inversion break up in narrow valleys differs from that in broad valleys or basins leading to persistent inversions even during summer (more often in the southern Alps), whereas stably stratified air is topping a shallow convective mixed PBL throughout the day *Rotach and Zardi* (2007).

Anthropogenic activities lead to numerous complex processes that can be related to the built up of infrastructure and fluxes of energy and matter. The physical effect of infrastructure relates to changes of landscape and alters surface energy and water budgets most directly: e. g., rainwater is quickly removed and is not able to evaporate, or sealed surfaces reduce the moisture availability. Due to changed surface fluxes a new boundary layer, the urban boundary-layer (UBL) (*Mills*, 2007), is formed by the dry, warm, and polluted air over rough urban surfaces. Since many of the air pollutants have distinctive radiative effects the thermal properties of the UBL and radiative exchanges with the surface are modified. In rare circumstances, the relative warmth of city surfaces can induce thermal driven wind circulations (e. g., *"inland sea breezes"* (*Garratt*, 1992)) or prevent from the development of nocturnal inversion. In addition, fluxes of waste heat, materials, and gases are emitted into the atmosphere significantly supporting the formation of urban heat islands. While the exhaust of gases and aerosols can partly easier be quantified, only a few attempts have been made to directly observe the anthropogenic heat fluxes: *Pigeon et al.* (2007), as an example, suggest $\sim$70 W/m^2 during winter and $\sim$15 W/m^2 during summer for the downtown of Toulouse (France) derived from surface energy balance measurements from February 2004 to March 2005.

1.2 Climate Change Effects on Near Surface Winds

Focussing on the Alpine region, climate changes of near surface winds can hardly be detected by analysing wind observations. Due to the strong topographic influences on the PBL (cf. Section 1.1.3) and due to numerous sources of inhomogeneities of wind observations (e. g., changes of the measuring instrument and its site, changes of the surrounding landscape) long-term trends from observed near surface winds are often excluded from actual climate change studies (*Trenberth et al.*, 2007). More often, changes of climate phenomena and climate variables affecting near surface flows are considered. However, *Walter et al.* (2006) report not significant trends for wind speed in Germany (-0.05 m/s; period 1951 to 2001), which change signs and intensify on shorter time scales, i. e., 0.11 m/s for 1961 to 2001, 0.25 m/s for 1971 to 2001, 0.39 m/s for 1981 to 2001, and 0.55 m/s for 1991 to 2001.

The main climate change mechanisms responsible for changes of near surface flows arise from changes of the PBL. Since the PBL is the interfacing layer between the atmosphere and the earth's surface, changes of the PBL are determined by the interplay between changes in large-scale phenomena (atmospheric circulation, synoptic phenomena) and changes in surface conditions, radiation, and surface heat fluxes which are in turn depending on larger-scale phenomena (e. g., precipitation, snow cover, cloudiness, etc.) and on anthropogenic activities (e. g., change of landscape, fluxes of energy, aerosols, and gases). Since the phenomena on their wide range of time and length scales are interacting with each other via a chain of interdependency (cf. Section 1.1), the impacts on single phenomena are partly amplifying and partly compensating the effects of climate change.

Numerous observation-based studies (cf. Section 1.1) have shown that changes of the climate in the Alpine region as a result from changes in atmospheric circulation and synoptic phenomena are highly correlated to changes of the NAO. The NAO *"[...] is*

without question one of the major controlling factors on regional climate in the Alps [...]" (*Beniston and Jungo*, 2002). An observed shift of weather patters since the 1960s enforcing southerly flow configurations during autumn and spring (associated with the lee cyclo-genesis) is correlated with an intensified NAO (*Schär et al.*, 1998). Convective patterns during winter doubled their events from the 1980s to the 1990s while the events of advective patterns where quartered (*Beniston and Jungo*, 2002). Moreover, *Beniston and Jungo* (2002) and *Giorgi et al.* (1997) found that the climate effect of the NAO's variability is stronger pronounced at higher terrain elevations: the processes associated with a strong NAO are increased pressure fields accompanied by compressional warming leading to positive temperature anomalies and a reductions of moisture and precipitation in higher regions. In addition, cloud amount and duration are decreased by a blocking effect of the high pressures fields increasing the sunshine duration and the diurnal warming. *Giorgi et al.* (1997) who analysed temperature records of 36 surface stations in Switzerland (period 1960 to 1994) found a distinctive positive correlation between terrain elevation and the differences of seasonal mean temperatures during winter between phases of a strong and a weak NAO (the anomaly increased from ∼0.8 K at 800 m to ∼2.6 K at 2800 m). However, changes in atmospheric circulations summarised by *Trenberth et al.* (2007) do not show definite significant trends: the NAO reached its maximum during the last 40 years by a drastic increase during the 1960s and is now decreasing to its long-term mean (cf. Figure 1.11). Although there has been considerable work on decadal and longer-term variability of the ENSO, it is still a research question of great importance whether the observed changes of the ENSO are physically linked to global climate change. In the lack of observational data or their substantial uncertainties conclusions about long-term behaviour of the QBO can not be drawn so far. Analysis of blocking events of the westerly winds (period 1948 to 2002) do not show significant long-term trends of the blocking intensity, however, significant decreases in number of events and duration have been found. Additionally, cyclone activity has changed over the last 40 years: significant decrease in mid-latitude cyclone activity and an increase in high-latitude frequency have been observed. Moreover, the storm tracks were shifted pole-wards with increasing storm intensities, but with a decreasing total number of occurrence and *Matulla and von Storch* (2008), who analysed ground-based pressure data, did not find any significant trend in storminess since the late 19$^{\text{th}}$ century over the Atlantic-European sector and Central Europe. However, on the small scale, *Bissoli and J. Grieser* (2007) found higher frequencies of tornadoes in Germany in the years 1998 to 2003 (e. g., in 2003 40 tornadoes have been observed) compared to the period 1950 to 2003, but no shifts of the seasonal cycle and in the intensity distribution.

In accordance to the behaviour of the NAO, which influences the Alpine lee cyclogenesis, the number of Mediterranean cyclones during October to March between 1979 and 1996 does not exhibit a significant trend *Trigo et al.* (2000). However, evidence for a strong correlation between the NAO and the cyclo-genesis cannot be drawn, since the cyclo-genesis mostly occurs during summer *Trigo et al.* (2002), when the NAO is weakest pronounced.

Auer et al. (2007), who homogenised long-term time series of numerous climate variables, found significant changes for air pressure, temperature, precipitation, duration of sunshine, and cloudiness during the 20$^{\text{th}}$ century: the Alpine region as a hole has

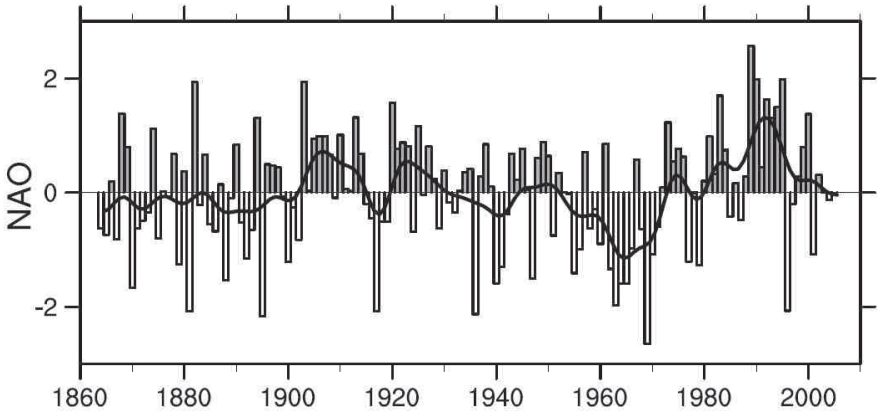

Figure 1.11: Normalised index of the North Atlantic Oscillation (NAO-index) during winter (December to March) from 1864 to 2005. The NAO-index is defined as the difference of the normalised (units of standard deviation) sea level pressure between Lisbon (Portugal) and Stykkisholmur/Reykjavik (Iceland). The average winter sea level pressure data at each station are normalised by dividing each seasonal anomaly by the long-term (1864 to 1983) standard deviation. The smooth black curves shows decadal variations. The individual bar corresponds to the January of the winter season. From *Trenberth et al.* (2007).

warmed twice as much as the northern hemispheric average since the late 19$^{\text{th}}$ century. Since 1950 temperature and air pressure during winter increased more in high regions ($\geq$1500 m above sea level) (2.3 K; 5.8 hPa) than in the low regions (1.6 K; 4.7 hPa). The annual relative humidity decreased in the low regions while it remained on its level in high ones (cf. Figure 1.12). Among non-significant trends, *Auer et al.* (2007) found significant (level of significance $\geq$0.9) regional- and seasonal-depending trends: winter precipitation increased in the north-west quarter of the Alpine region (24 %) during the 20$^{\text{th}}$ century but decreased in low regions ($-$27.3 %) between 1975 and 2000. In summer, the sunshine duration increased more in high regions (15.5 %) than in the low ones (9.8 %) between 1975 and 2000; during winter this ratio is inverted (16.8 % in the high regions and 26.3 % in the low ones). These trends have to be seen in context to the shifts in weather patterns as described by *Beniston and Jungo* (2002) and *Giorgi et al.* (1997).

In addition to the undetermined behaviour of large-scale phenomena and anthropogenic activity, no distinctive trend for near surface wind can be drawn from the observed behaviour of numerous proxy variables. On one hand, the increased temperature and sunshine duration encourage the amount of available energy at the surface which induces additional turbulent fluxes of heat and moisture (*Garratt*, 1992). This could destabilise the PBL and favour flow phenomena related to weak stability (e. g., flow-over regimes, gravity waves and their breaking, speed-up effect, gap-flows, convection, thermal-driven circulations like Alpine pumping and mountain-valley circulations, tornadoes, etc.). On the other hand, assuming a hydrostatic atmosphere one could argue for an increased stability of the PBL on a regional scale due to the stronger temperature trend at higher levels which would suppress turbulence, reduce the effects of barotropic

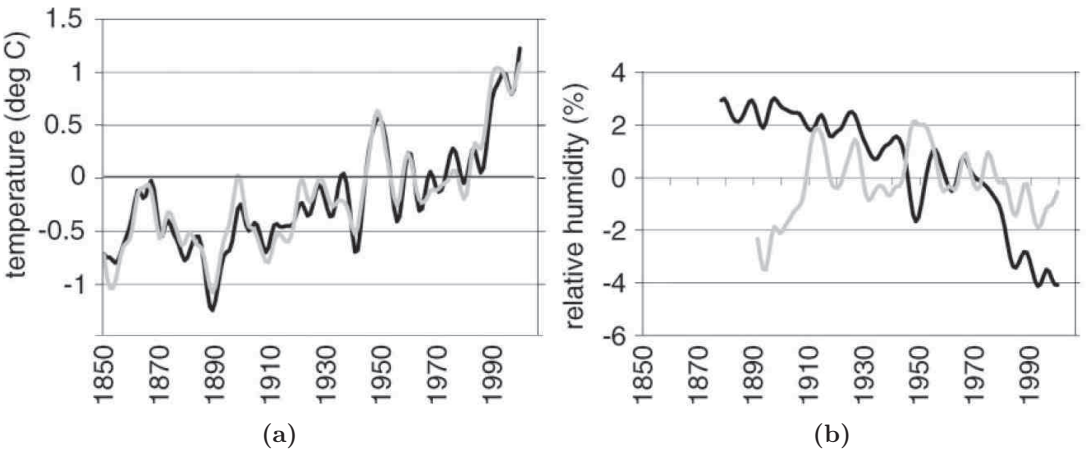

Figure 1.12: Observed elevation-depending climate changes in the Alpine region. (a) Temperature and (b) relative humidity anomalies since 1850. Black, average over observation stations from the northwest and northeast quarter of the Alpine region at low elevations (<1500 m above sea level); gray, average over stations at high elevations (≥1500 m above sea level). Values are 10-year low-pass filtered anomalies to averages from 1901 to 2000 period. From *Auer et al.* (2007).

instability, and favour flow-around regimes. Since opposing effects appear from one source, a distinctive observation-based trend for near surface wind in the Alpine region is not derivable in neither case.

1.3 A Survey of Modern Climate Simulations

In order to approximate the behaviour of the climate system and to quantify its possible evolutions under changing conditions, mathematical models based on the climate variables (cf. Section 1.1) have increasingly been developed and applied during the last decades. One of the most comprehensive techniques, the dynamic modelling approach, is coined by Numerical Weather Prediction (NWP) and relays on solving the mathematical equations of the physical laws governing the atmosphere, hydrosphere, cryosphere, and other climate components and their interactions via discretising the climate system on a grid. It is a general goal of modern climate modelling and NWP to reduce the size of grid spacing (i. e., to increase the resolution) (*Yarnal et al.*, 2001). However, due to the broad spectrum of time and length scales of climate phenomena and the limitations of available computational resources a model's applicability is generally bounded to the scales of those phenomena the model is capable to describe. A more detailed description of modelling approaches for near surface wind and their errors can be found in Section 2.1.

On the global scale, results from 23 coupled Atmosphere-Ocean General Circulation Models (AOGCMs) (∼200 km grid spacing), which are dynamic models capable to describe large-scale phenomena, have contributed the 4$^{\text{th}}$ IPCC Assessment Report (*Solomon et al.*, 2007) to estimate the behaviour of the climate system with respect

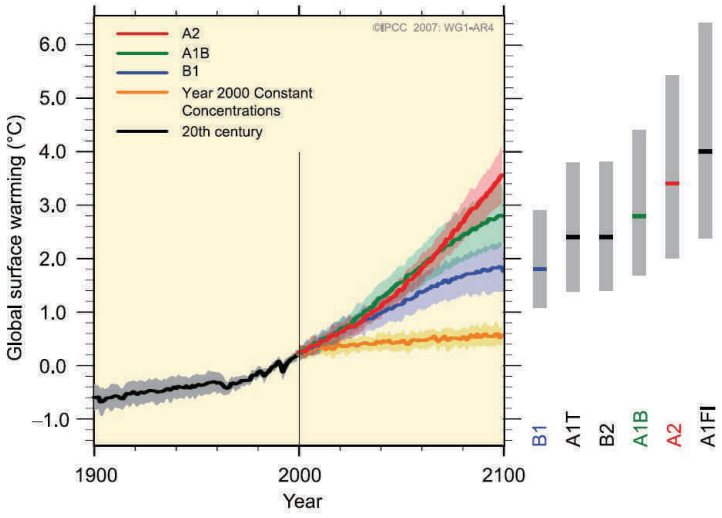

(a)

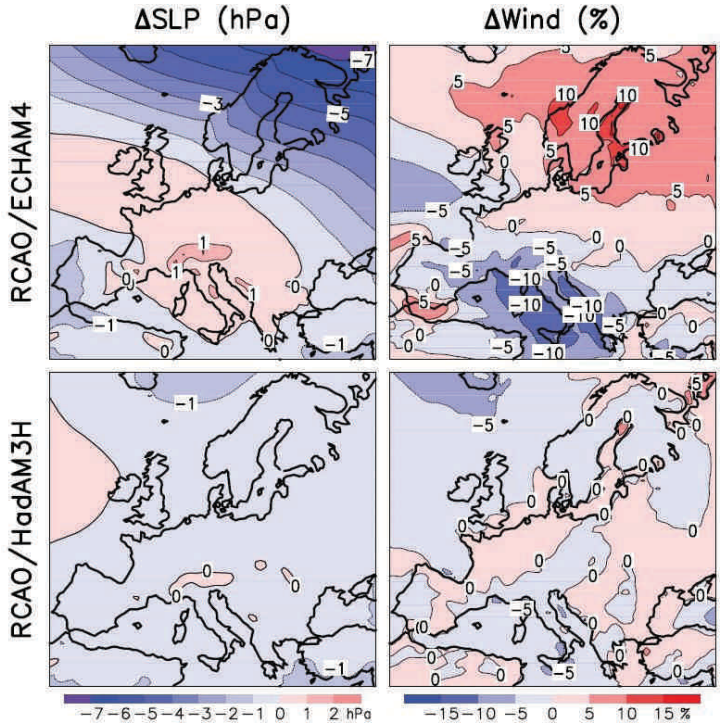

(b)

Figure 1.13: Simulated climate change effects on different scales. (a) Global multi-model averages of surface warming (relative to period 1980 to 1999) and assessed ranges for different scenarios (solid lines); shading denotes the ±1 standard deviation range of individual model annual averages; grey bars at right indicate the best estimate (solid line) and the likely range. From *Solomon et al.* (2007). (b) Changes of annual mean sea level pressure (ΔSLP) and wind speed (ΔWind) (10 m above ground level) from the period 1961 to 1990 to the period 2071 to 2100. The results are based on the scenario A2 and were produced by one RCM (Rossby Centre regional Atmosphere-Ocean model; RCAO) using boundary conditions from two GCM: ECHAM4/OPYC3 (top) and HadAM3H (bottom). From *Rummukainen et al.* (2004) redrawn by *Christensen et al.* (2007).

to numerous future scenarios of greenhouse gases, aerosols, and land cover. These scenarios, e. g., B1, A1T, B2, A1B, A2, and A1FI, refer to the IPCC Special Report on Emission Scenarios (SRES) (*Nakicenovic et al.*, 2000) and can be illustratively marked by their approximated carbon dioxide equivalent concentrations at the end of 2100 of about 600, 700, 800, 850, 1250, and 1550 ppm respectively. Analysis of the models' outputs show scenario-depending increases of the global mean surface temperatures (cf. Figure 1.13a) which are consistent throughout the models. In addition, *Yin* (2005) found a consistent expansion of the Hadley Circulation together with a pole-ward shift of the mid-latitude storm tracks by the end of the 21st century in 15 AOGCMs. However, trends of synoptic activities are more model- than scenario-depending, e. g., *McHugh and Rogers* (2005) found seven out of ten AOGCMs showing an increasing NAO (periods 2070 to 2099 vs. 1961 to 1990). Focussing on Europe, *Pinto et al.* (2007) found in agreement with other studies, e. g., *Leckebusch and Ulbrich* (2004), significant changes in the mid-tropospheric storm tracks in the scenarios A1B, A2, and B1 simulated with one AOGCM (1.875° × 1.875° grid): increasing storm track density of extreme cyclones for several regions of Western Europe, reduction of track density in the Mediterranean region, and a general reduction of the number of cyclones by the end of the 21st century. However, the linkage between cyclone intensities and high near surface wind speeds is highly sensitive against the sample of simulations. *Miller et al.* (2006) found consistent changes throughout 14 AOGCMs for the mean sea level pressure (MSLP) of the winter half-year between early 20th and late 21st century: they show decreases over the poles and increases over the mid-latitudes, associated with the pole-ward shift of the storm tracks in both hemispheres (in agreement with the findings of *Yin* (2005)) and a strengthening of the westerly mean flow in upper levels.

To provide information about climate change on regional scales the results of the global models have further been downscaled via Regional Climate Models (RCMs), which are dynamical models similar to the AOGCMs, or via empirical/statistical methods based on empirical/statistical relationships between large-scale phenomena and local observations. Note that every further downscaling step refines the AOGCMs' results but also has its own shortcomings. This might be of great importance, especially in cases when climate changes are weakly pronounced: e. g., *Pryor et al.* (2005a) found slight increases of the annual mean wind speed over Northern Europe (periods 2071 to 2100 vs. 1961 to 1990; scenario A2) with a RCM (0.44° × 0.44° grid), but found decreases when using empirical/statistical methods (*Pryor et al.*, 2005b). To find robust results multi-model and multi-scenario simulations have been conducted and analysed. The following key-findings affecting near surface wind on regional scales, as they are listed in *Christensen et al.* (2007) and complemented by additional authors, can be summarised:

- The change in the large-scale atmospheric circulation is identified as a key factor considering average and extreme wind speeds.
- Changes in time-averaged gradients of the MSLP over Europe are depending on the used AOGCMs.
- Simulations with an increased north-south MSLP gradient across northern Europe tend to indicate stronger winds in northern Europe and a northward shift in

cyclone activity, which reduces the windiness in the Mediterranean area.

- Several studies have suggested a decrease in the total number of cyclones in the Mediterranean Sea, but in accordance to the driving AOGCM no agreement has been found on whether the number of intense cyclones will increase or decrease.
- Realistic frequencies of high wind speeds were only found in RCMs using a wind gust parametrisation (*Rockel and Woth*, 2007).
- In the Alpine region decreases of the annual wind speed between 0 % and −5 % are projected (2071 to 2100 vs. 1961 to 1990) depending on the used climate model (cf. Figure 1.13b) (*Rummukainen et al.*, 2004).

Focussing on single studies in the Alpine region, divergent climate changes are derived based on the AOGCMs' disagreements: *Räisänen et al.* (2004) obtained changes of the mean annual wind speed between ±4 % (periods 2071 to 2100 vs. 1961 to 1990) on a 50 km grid when driving a RCM by outputs of two AOGCMs (1.875° × 1.25° and 2.8° × 2.8° grid spacing) forced by the scenarios A2 and B2. *Rockel and Woth* (2007), who analysed extreme wind speeds via an ensemble of eight RCMs driven by one AOGCM (1.875° × 1.25° grid spacing; scenario A2) on the same 50 km grid and the same simulation periods, only found significant changes of the 99-percentile of daily mean wind speed in November (−0.2 m/s). *Walter et al.* (2006) used three RCMs to downscale results from an AOGCM (2.8° × 2.8° grid spacing; scenario B2; periods 2070 to 2099 vs. 1960 to 1989) onto a 18 km grid over Europe and found reductions of the annual wind speed up to −0.3 m/s and changes of the monthly wind speed in February and May up to 0.3 m/s and −0.7 m/s, respectively.

2 Methodology

Near surface air flows are partly determined by synoptic weather phenomena and their variability and partly by interactions between the earth's surface and the atmosphere throughout the PBL. In regions with complex topography local near surface flows increasingly decouple from synoptic flows with respect to static and dynamic instabilities, kinematic terrain effects, inversion layers, and anthropogenic activities (cf. Section 1.1.3). In order to generate spatial distributed wind climatologies (i. e., maps of statistic measures of wind speed and wind direction) numeric modelling approaches are trying to capture both, synoptic flows and the decoupling processes. In general, these approaches are based on observation data, especially when most reliable results for simulating the current climate have to be achieved. In the field of climate change research, the requirements are different: first, the focus rather lays on deriving the climate change effect (i. e., the climate change signal) than on generating a climatology for a given climate state and second, observational data are not available.

In the following sub-section, modelling approaches commonly applied in the Alpine region are briefly described and their advantages and shortcomings are discussed. In Section 2.2 a hybrid modelling approach, which is designed to generate highly resolved gridded wind climatologies without the ingestion of observation data, the *"dynamic-diagnostic downscaling method"*, is introduced. The investigation of different variants of this method and their performances in differently complex terrain forms the main part of this study.

2.1 Modelling Approaches in Complex Terrain and Their Performance

In general, fluids can be described by equations derived from a set of conservation principals. The conservation of mass gives the *mass continuity equation* (2.1) in terms of the fluid's density (ρ) and the flow-velocity ($\vec{v}$). The conservation of momentum gives the *momentum equation* (known as *Navier-Stokes equations*) (2.2) with respect to pressure (p), kinematic viscosity (ν), and body forces ($\vec{F}$) (i. e., Coriolis force and gravity). Finally, the conservation of heat gives the *thermodynamic equations* (2.3) in terms of the internal energy (I) and a source-sink term ($\dot{Q}$) for diabatic heating (phase transformation of water and other components, exothermic chemical reactions), radiative fluxes, and diffusion (dissipation of kinetic energy via molecular motion). If the fluid is loaded with moisture and aerosols, the conservation of water and other gaseous matter are considered by *budget equations* (2.4) based on the mass-mixing-ratio (q_n) of each component (n) and their sources and sinks ($\dot{S_{q_n}}$). All together, they form a set of coupled non-linear Partial Differential Equations (PDEs).

$$\frac{\partial \rho}{\partial t} + \nabla \cdot (\rho \vec{v}) = 0 \tag{2.1}$$

$$\frac{\partial \vec{v}}{\partial t} + (\vec{v} \cdot \nabla)\vec{v} = -\frac{\nabla p}{\rho} + \nu \nabla^2 \vec{v} + \vec{F} \tag{2.2}$$

$$\frac{\partial I}{\partial t} + \vec{v} \cdot \nabla I + \frac{p}{\rho} \nabla \cdot \vec{v} = \dot{Q} \tag{2.3}$$

$$\frac{\partial q_n}{\partial t} + \vec{v} \cdot \nabla q_n = \dot{S_{q_n}} \tag{2.4}$$

Following *Ratto et al.* (1994) different model designs can be distinguished according to the physical principles considered and the simplifications made to solve these PDEs. The models can be roughly divided into two general categories: a) *dynamic* (or *prognostic, predictive, primitive equation*) models and b) *diagnostic* (or *kinematic*) models. If dynamic models are driven by data fields with a coarser resolution the process of simulating is called *dynamical downscaling* (*Yarnal et al.*, 2001). As a consequence, the application of diagnostic models on coarser resolved data fields henceforth is called *diagnostic downscaling*. In addition, c) *statistic* and *physical* methods and mixed forms can be found in literature.

2.1.1 Dynamic Models

Dynamic models are the most sophisticated and computationally most expensive methods. They attempt to solve equations (2.1)–(2.4) for a moist and viscous air via advanced numeric methods. Based on assumptions to simplify the governing equations, the models can be further sub-divided. One of the fundamental simplifications is the *hydrostatic* assumption. Thereby, the magnitude of the vertical acceleration ($|dw/dt|$) is assumed to be much less than the magnitude of the vertical pressure gradient force ($|(1/\rho) \cdot \partial p/\partial z|$). This leads to the *hydrostatic equation*

$$\frac{\partial p}{\partial z} = -\rho g \tag{2.5}$$

which can be derived from the vertical component of (2.2). Whether this assumption is valid or not the models are divided into *hydrostatic* and *non-hydrostatic* models, respectively. Unfortunately, however, there is no strong criterion to judge the validity of the hydrostatic assumption, it depends on the meteorological phenomena to be investigated. *Pielke* (2002) concludes from the work of numerous authors that the lower the velocity, the larger the spatial scale, and the higher the hydrostatic stability of the atmosphere the more the hydrostatic assumption is fulfilled. Based on the analysis of internal gravity waves he furthermore summarises that hydrostatic models are only valid for phenomena on horizontal scales larger than 10 km, which implies that surface variations (i. e., mountains) must have horizontal scales of at least 25 km.

The basic numeric concepts to solve equations (2.1)–(2.4) is to discretise any depending variable (φ) of this equations on a grid in space and time. Depending on the model's application different coordinate systems and discretisation techniques are

used. Global models, like the AOGCMs (cf. Section 1.3) or global atmospheric models in NWP, are mostly based on spherical coordinates expanding any depending variable φ in terms of a truncated series of spherical harmonics. Thus, the resolution of the discretisation depends on the truncation of the series. In modern AOGCMs the series is truncated at the 104^{th} term (leading to grid cell sizes of about 80 km $\times$ 120 km in real space), in NWP the resolutions are much higher: e. g., the atmospheric model of the operational forecast system at the European Centre for Medium-Range Weather Forecasts (ECMWF) uses 799 terms ($\sim$25 km grid cells in real space). Higher resolutions may be achieved by Local (or Limited) Area Models (LAMs) or RCMs (cf. Section 1.3), which are applied on geographically limited areas. Thereby, the earth's curvature does not directly affect the coordinate system, and therefore, it is more convenient to use discretisation schemes based on finite differences or finite volumina than on spherical harmonics. To conduct simulations with LAMs or RCMs, lateral boundary conditions (LBCs) throughout the simulation period have to be provided. Usually, these conditions are generated from other models (e. g., AOGCMs) or global observation-based data (re-analysis data).

In order to discretise the time variable (t) *explicit* schemes (e. g., the *leapfrog* scheme) are broadly used. However, technical limitations arise from the *"Courant-Friedrichs-Levi"* (CFL) criterion which couples the time step with the grid space for numerical stability. In contrast, *implicit* schemes are unconditionally stable (e. g., the *Crank-Nicolson* scheme), but they lead to huge equation systems whereas every (space and time) grid cell of the entire simulation period represents one unknown member. In up-to-date models both types of schemes can be found to increase the efficiency: e. g., in the case vertically propagating sound waves are implicitely treated, a bisection of the horizontal grid spacing requires a bisection of the time step and therefore the computational demand is eightfold, if the simulation area stays the same.

A further concept is to average the relations of conservations. Any depending variable (φ) of the discretised PDEs is separated into its grid-volume average ($\overline{\varphi}$) and its sub-grid-scale perturbation (φ'):

$$\varphi = \overline{\varphi} + \varphi'. \tag{2.6}$$

It is convenient to assume that $\overline{\varphi}$ varies much slower in time and space than φ'. The same concept is valid in the description of turbulence, where $\overline{\varphi}$ is known as ensemble mean and φ' is the turbulent perturbation of φ (*Pielke*, 2002). Inserting this scale separation into equations (2.1)–(2.4), time- and volume-averaging them over the dicretisation steps, and following the *Raynolds assumption* (i. e., $\overline{\varphi'} = 0$) separates an averaged part (describing the average behaviour of the system) from a perturbation part, which allows for capturing the sub-grid-scale (or turbulent) fluxes. For example, if $\vec{v}$ consists of the components u, v, and w the fluxes $\overline{w'u'}$ and $\overline{w'v'}$ remain in (2.2). This allows to simulate sub-grid-scale turbulence, if the turbulent fluxes are expressed (i. e., *parameterised*) in terms of given quantities. According to the different types and layers of the PBL (cf. Section 1.1) different parameterisations are used. Differences also arise from the complexity of the mathematical formulae. One of the most commonly used parameterisations is the simple *first order closure* scheme. Here, the turbulent fluxes are derived from an exchange coefficient (K_m) and the vertical gradient of the

average value (2.7):

$$\overline{w'u'} = -K_m \frac{\partial \overline{u}}{\partial z} \qquad \overline{w'v'} = -K_m \frac{\partial \overline{v}}{\partial z} \ . \tag{2.7}$$

If $\overline{V}$ is the magnitude of the horizontal grid-volume averaged flow velocity ($\overline{V} = \sqrt{\overline{u}^2 + \overline{v}^2}$), then equation (2.7) can be written as

$$K_m \frac{\partial \overline{V}}{\partial z} = u_*^2 \ , \tag{2.8}$$

where u_*^2 is known as the *friction velocity* (*Pielke*, 2002). Similar relations can also be found for other quantities with a characteristic vertical profile, e. g., for the potential temperature (θ):

$$\overline{w'\theta'} = -K_\theta \frac{\partial \overline{\theta}}{\partial z} = -u_* \theta_* \ , \tag{2.9}$$

where θ_* is known as the *flux temperature* (*Pielke*, 2002).

Within the surface layer, these approaches (known as *"K-Theory"*) are consistent with the Monin-Obukhov Similarity Theory. In closure schemes of higher order (including higher-order-correlation terms) additional prognostic equations, describing the turbulent fluxes, appear. However, although theoretically more satisfying, comparison studies have shown that well tuned first-order schemes provide an economic and realistic alternative to higher-order schemes (*Pielke*, 2002).

The source-sink terms ($\dot{Q}$ and $\dot{S_{q_n}}$) are parameterised in a different way: instead of closure schemes sophisticated hydrological, chemical, and radiation models are applied. Additionally, to capture biophysical, biogeochemical, and biogeographic (i. e., changes of land cover) influences of vegetation with respect to $\dot{Q}$ and $\dot{S_{q_n}}$ at the surface so-called *soil-vegetation-atmosphere transfer* (SVAT) schemes, which are able to simulate exchanges of energy and moisture between the atmosphere and soil, are implemented in most advanced dynamic models. Nevertheless, parameterisations do not necessarily have to actually simulate the physical processes they are representing in order to be realistic representations of these processes. In fact, *"[...] if the quantitative accuracy of a parameterisation is not sacrificed, then it is desirable to make the parameterisation as computationally simple as possible [...]"* (*Pielke*, 2002).

In general, dynamic models are capable to simulate synoptic processes as well as interactions between the earth's surface and the atmosphere. However, due to the complexity of the governing equations a discretisation error is induced with respect to the size of the grid spacing. Other errors appear from climate phenomena on scales which are not resolved by the grid and which can only partly be captured by sub-grid-scale parameterisations. In addition, because of the concept of averaging (see above) the surface altitude of each grid cell has to be calculated as an area-mean of the real altitudes covered by that grid cell. This leads to a smoothed representation of the orography and important climate phenomena may not be captured well enough: e. g., the flow-over regime is strongly favoured (*Schär et al.*, 1998), which has major impacts on spatial distributions of any climate variable. However, simply increasing the resolution only partly reduces terrain-induced errors, because the parameterisation schemes con-

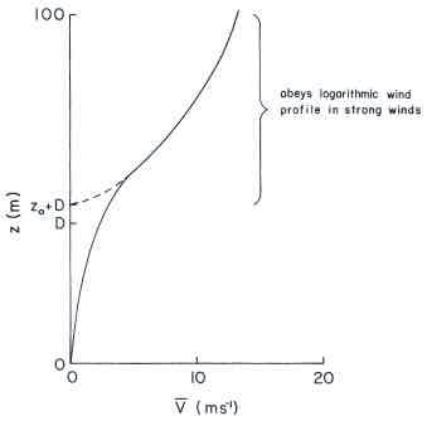

Figure 2.1: Schematic of a mean wind profile (solid line) above and within a dense ground cover. The dashed line represents the expected wind profile if the *zero-plane displacement* (D) is equal to zero. Below D plus the surface roughness length (z_0) the mean horizontal wind speed ($\overline{V}$) exponentially decays. From *Pielke* (2002).

ceptually break-drown when the grid spacing gets too small. Frequent simplifications in the parameterisation schemes inducing considerable errors at small grid spacing are the Monin-Obukhov Theory (cf. Section 1.1.3), the negligence of a vertical displacement of the logarithmic profiles when the ground is covered by high obstacles (e. g., trees or buildings) (cf. Figure 2.1, the negligence of shading effects in mountainous regions, the limitation for radiative fluxes to propagate only in vertical direction, the negligence of angular back-scattering of radiation in valleys, improper representation of the PBL in mountainous regions (cf. Figure 2.2), improper representation of IBLs (*Pielke*, 2002), the negligence of horizontal energy transport and locally unclosed surface energy budgets (*Rotach et al.*, 2008; *Zängl et al.*, 2004), etc.

Additional limitations may arise from the initialisation fields and lateral boundary conditions. For instance, the time step and grid sizes of the boundary conditions have to be small enough to capture the large-scale phenomena which the model is expected to simulate. Similarly, the initialisation fields have to be realistic representations of its variables on the model grid, especially the variables of the soil: *Chen and Dudhia* (2001) have shown that in short-term simulations uncertainties of soil moisture smaller than current accuracy on continental scales (i. e., 10 %) in the initialisation fields lead to significant uncertainties of the surface latent and sensible heat fluxes ($\sim$30 W/m), which have significant impact on any PBL process, especially if the process triggers other processes. On the other hand, deep soil moisture plays an important role in long-term simulations: due to slow hydrological processes anomalies of moisture are lasting in the soil on seasonal and annual time-scales. This may lead to divergent model results in the case of improper initialisation fields (*Seneviratne et al.*, 2006).

Observation data (time series) can be ingested via simple nudging methods, where deviations between modelled and observed values are damped exponentially with respect to the distances of the grid cells from the locations of the observations, or in more

Figure 2.2: Schematic representation of the PBL in (a) a low-resolution numerical model, (b) a high-resolution numerical model, and (c) the PBL as it is found in different boundary-layer studies. From *Rotach and Zardi* (2007).

physically consistent ways, like three- (or four-) dimensional variational data assimilation algorithms (3DVAR, 4DVAR), where initial and lateral boundary conditions are modified until the model errors reach a minimum. Dynamic models may also be driven without any observation data, making them interesting for climate change research.

Because of the high demand of computational resources simulations with dynamic models covering the Alpine region are restricted either to resolutions at the meso-scale or to short-term periods lasting over a couple of days. A study from the former is reported by *Walter et al.* (2006). They conducted simulations of the period 1979–1993 with 4 RCMs without ingestion of observations on an approximately 18 km × 18 km grid over Germany via lateral boundary conditions from a global re-analysis dataset. Comparisons with observations have shown overestimations of all models between 1.0 m/s and 1.5 m/s in the relatively flat southern Germany and underestimations between −0.5 m/s and −2.5 m/s for single grid cells in the German Alps. They relate these model errors to a smoothed representation of the terrain, to improper model representations of the surface roughness, and to observation errors. Studies of short-term simulations report the successful simulation of flow-phenomena on local scale on very highly resolved grids (grid spacing ≤1 km): e. g., *Zängl* (2004) found slight overestimations of the daytime up-valley flow and biases of the maximum wind speed for the nighttime drainage flow ranging between -3.0 m/s and 1.0 m/s in the Inn Valley, Austria; and in the Alpine Rhine Valley, Liechtenstein and Austria, *Zängl and Vogt* (2006) found overestimations of the daytime up-valley flow (2.0 m/s) and the nighttime drainage flow (4.0 m/s) at ∼165 m above ground level. Model errors near the surface in a range of approximately ±5.0 m/s are reported by *Zängl et al.* (2004), when simulating a strong south föhn event in the Wipp Valley, Austria. *Chow et al.* (2006) conducted valley-wind circulation simulations in the Riviera Valley, Switzerland, on 350 m and 150 m grids and found biases between −1.0 m/s and 0.8 m/s for wind speeds and biases between −35.° and 12.0° for wind directions.

To reduce the computational demand and to realise simulations of long periods (decades), dynamic models have been combined with statistical methods since the late 1990ies. The basic concept of this *statistical-dynamical* approach relies on applying the dynamic model only on a few, short-term lasting, characteristic classes of large-scale phenomena (i. e., weather types) instead of the hole simulation period and to reconstruct the entire period from those dynamically modelled classes with respect to their statistical appearance in the original period. Although this method drastically

reduces the demand of computational resources it has at least two conceptual weaknesses: firstly, *Weber and Furger* (2001); *Weber and Kaufmann* (1998) have shown from observations that there is no clear assignment between near surface flow and definite weather types in the Alpine region (even on regional scales, cf. Section 1.1.2) and secondly, the model's results are questionable because of its sensitivity against errors from misleading initialisation fields (especially for soil moisture, see above). Nevertheless, the statistical-dynamical approach has been applied with considerable success: *Fuentes and Heimann* (2000) and *Heimann* (2001) achieved uncertainties of the annual wind speed (period: 1981–1992) of ∼20 % in the Alpine region and on the eastern Adriatic coast on a 20 km grid and *Mengelkamp* (1999) found a remaining model error of -4 % in a moderate complex terrain in Middle-Germany on a highly resolved grid (1 km grid spacing) based on 143 weather-classes for the period 1981–1992.

2.1.2 Diagnostic Models

Diagnostic models are basically designed to simulate topographically influenced air flows in geographically small areas, mostly limited to PBLs under neutral and stable conditions. They omit any time derivative in the continuity (2.1) and momentum equation (2.2) and, as a consequence, the simulation results represent divergence-free steady-state flows. Any dynamic process, like flow splitting, grid resolved turbulence (e. g., vortex shedding), thermal induced circulations, etc. cannot be expected to be found in those models. Furthermore, thermodynamic effects based on diabatic heating (phase transformation of water, exothermic chemical reactions, and anthropogenic activities) as well as radiative fluxes and diffusion do not affect the simulated flow (the equations (2.3) and (2.4) are neglected). However, up-to-date diagnostic models are equipped with empiric parameterisations to handle some of those effects in a simplified manner.

The general approach consists of an initialisation step and an adjustment step. During the former, the models are initialised with an *"initial"* or *"first guess"* wind field ($\vec{v_0}$) which is usually generated from observation data taking into account the PBLs stratification based on Monin-Obukhov Theory. During the latter step, $\vec{v_0}$ is modified by a perturbation wind field ($\vec{v}'$) which represents a topographically induced perturbation of $\vec{v_0}$ and which is assumed to be derivable from the *perturbation velocity potential* (ϕ) (cf. equation (2.10)). Afterwards, the *"adjusted"*, *"final"* or *"reconstructed"* wind field ($\vec{v}$) is calculated from $\vec{v_0}$ and $\vec{v}'$ and automatically satisfies the conservations of momentum and/or mass due to the potential-flow concept.

$$\vec{v}' = \nabla\phi \tag{2.10}$$

Following *Ratto et al.* (1994), diagnostic models can be further subdivided into two groups: a) models based on the analytic solution for the linearised friction-free terrain-induced speed-up effect (cf. Figure 1.10) of a 2-dimensional flow over an idealised hill under neutral condition from *Jackson and Hunt* (1975) (further referred to as *JH-theory*) and b) *kinematic* or *mass-consistent* models purely based on the constraints of mass conservation (2.1). In models of group a) the flow perturbation $\vec{v}'$ in the friction-free case is analytically derived from (2.10) in terms of Fourier and/or Bessel series

spectral space. Within the PBL's surface layer, $\vec{v}'$ is modified to take account for the influences of friction according to the logarithmic wind profile. *Beljaars et al.* (1987) and *Troen and de Baas* (1986) included the momentum equation to apply the spectral approach on 3-dimensional grids with Cartesian coordinate systems and utilised the K-theory to calculate the wind shear. Newer developments are taking account for non-linear terms of the speed-up effect (*Xu and Taylor*, 1994) and utilised Monin-Obukhov Theory for stable stratification (*Weng et al.*, 1997). The models of group a) are conceptually restricted to certain PBL-conditions (neutral and stable stratification) and provide realistic results for hills with a height up to ∼200 m and slopes up to ∼20° (*Beljaars et al.*, 1987; *Dobesch and Kury*, 2006; *Taylor et al.*, 1987). Due to the model's simplifications, the simulation results crucially depend on the quality of the initial wind field ($\vec{v_0}$) and the complexity of the terrain: *Berge et al.* (2006) had to reduce the distances between the observation stations (five anemometers on up to 50 m high masts with up to four years of operation time) from 45 km to less than 3 km in a mountainous and coastal region in Norway in order to reduce the uncertainties of the annual wind speed from ∼25 % to less than 6 %. On the other hand, the demand of computational resources is very low. The models are designed to run on conventional desktop PCs and therefore, they are widely used even in complex terrain outside the model's range of applicability (e. g., mountainous areas in the Alpine region).

Models of group b) rely on the continuity equation (2.1), which reduces to its incompressible form

$$\nabla \vec{v} = 0, \tag{2.11}$$

if the air density (ρ) is assumed to be constant. Furthermore, it is assumed that the flow perturbation $\vec{v}'$ is minimal. This leads to a least-square problem which can be solved by minimising the Lagrangian functional

$$E(\vec{v}, \phi) = \int_V [(\alpha_u^2, \alpha_v^2, \alpha_w^2) \cdot (\vec{v} - \vec{v_0})^2 + \phi \nabla \vec{v}] dV \tag{2.12}$$

throughout the 3-dimensional model volume (V). Here, the perturbation velocity potential (ϕ) appears as the Lagrangian multiplier and α_u, α_v, and α_w are the Gaussian moduli (*Dobesch and Kury*, 2006; *Ratto et al.*, 1994). The flow perturbation $\vec{v}'$ is derivable from its potential via the Euler-Lagrange equations and is given by

$$\vec{v'} = (\frac{1}{2\alpha_u^2}, \frac{1}{2\alpha_v^2}, \frac{1}{2\alpha_w^2}) \nabla \phi. \tag{2.13}$$

Note, if $\alpha_u^2 = \alpha_v^2 = \alpha_w^2 = 1$ equation (2.13) is equal to (2.10). But in general $\alpha_u^2 = \alpha_v^2 = \alpha_1^2 \neq 1$ and $\alpha_w^2 = \alpha_2^2 \neq 1$, which are the weights of the horizontal and vertical adjustments of the velocity components and offer the possibility to take account for the PBL's stability, especially to distinguish between flow-over and flow-around regimes based on the Froude-number (cf. Section 1.1.3 and Figure 1.6) (*Ratto et al.*, 1994). However, to obtain more realistic solutions under nocturnal stable conditions, horizontal and vertical variations of α_1^2/α_2^2 should be taken into account (*Venkatesan et al.*, 1997).

Ratto et al. (1994) point out that, apart from a few models which eliminate ϕ from

(2.13) and obtain a set of uncoupled second-order PDEs for the wind components, most of the mass-consistent models solve a Poisson equation for the perturbation potential which can be derived from (2.13) and (2.11):

$$(1, 1, \frac{\alpha_1^2}{\alpha_2^2})\Delta\phi = -2\alpha_1^2\nabla\vec{v_0}. \tag{2.14}$$

Depending on the selected coordinate system different numerical methods can be found to solve this Poisson equation: in addition to Over-Relaxation and finite Fourier transformation methods summarised in *Ratto et al.* (1994), preconditioned Conjugate Gradient algorithms and Finite Element methods with adaptive grids for terrain-following coordinates are reported from numerous authors (e. g., *Montero et al.*, 1998; *Montero and Sanín*, 2001).

Similar to the JH-theory-based models, the simulation results are highly sensitive to the initial wind field ($\vec{v_0}$): *Gross* (1996), who analysed the applicability of mass-consistent models in the moderate complex terrain of the Upper Rhine Valley via artificially derived observation data from dynamic simulations, showed that between 50 and 100 observation sites per simulation area (∼25 km × 25 km) have to be used in order to obtain realistic flow patterns, if the model is purely driven by observation data. Evaluations of mass-consistent models based on short-term (1–2 days) simulations yielded relative biases of the wind speed for two models between -20 % and 28 % in the Alpine region (500 m grid spacing) (*Desiato et al.*, 1998). In a less complex terrain *Cox et al.* (2005) found mean absolute errors for three models of ∼1.4 m/s on 1 km grids (∼5.8 km average distance between the observation sites).

Due to the numeric methods the demand of computational resources is generally higher compared to the JH-theory-based models. To reduce this demand in the case of climatological studies the models are rather applied on statistical properties (frequency distributions) of available observations than on each observed time slice *Ratto et al.* (1994). This concept uses the linearity of the models' processes, but neglects the physical (spatial) coherence of the flow within the model domain of each single time slice what makes its applicability in the Alpine region questionable. Note, this concept is also broadly applied to JH-theory-based models, like in the European Wind Atlas (*Troen and Petersen*, 1989) which is heavily used in the field of wind engineering.

2.1.3 Statistical and Physical Methods

Statistical methods are neglecting the underlying physical principals and are deriving statistical relations to describe the coherency between statistical quantities of large-scale phenomena (i. e., *pretictors*) and local-scale wind fields (i. e., *predictands*). To generate spatial distributed wind climatologies, these relations are interpolated horizontally. It is most convenient to use simulation results from dynamic models (AOGCMs or RCMs) or representative observations as predictors and local observation data from surface stations as pretictands. Most common methods are based on linear or multi-linear regressions. *Achberger et al.* (2002) compared three linear regression methods driven by the geostrophic wind from an RCM and two observation stations in Northern Europe (Sweden) and found biases between −0.9 m/s and 0.1 m/s in a 10 month simulation

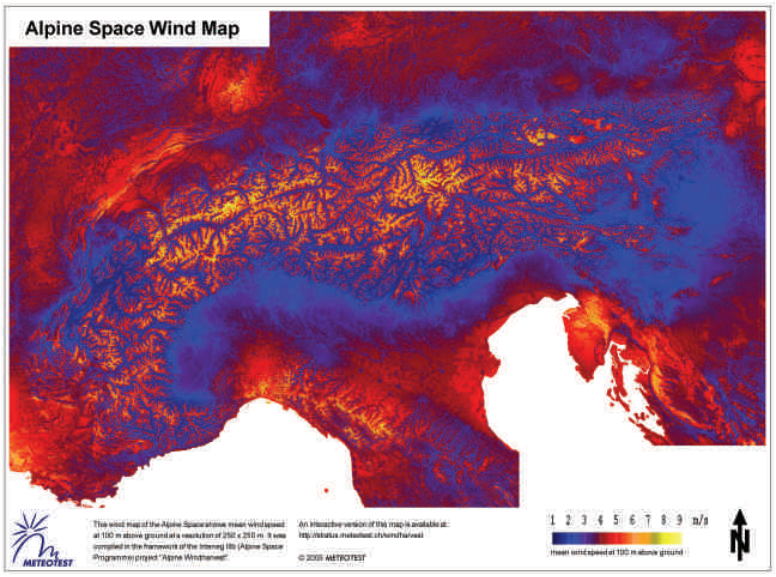

Figure 2.3: Modelled mean annual wind speed 100 m above ground (coloured area [m/s]) of the period 1983–1997 in the Alpine region with 250 m × 250 m grid spacing. From (*Schaffner and Remund*, 2005).

period. *Pryor et al.* (2005b) used multi-linear regressions based on gradients of the sea level pressure and the relative vorticity at 500 hPa from global re-analysis data to derive fitting-parameters of wind speed distributions (i. e., the scale and shape parameter of the Weibull distribution) at 46 surface stations in Sweden. They found an absolute error of 0.1 m/s averaged over all stations for a 21 year simulation (1982–2002). Other techniques are including the Monin-Obukhov Theory and local topographical features prior to the regression step (i. e., the *physical-statistical* method (e. g., *de Rooy and Kok*, 2004)).

Because of the terrain-induced decoupling effects between predictors and predictands (cf. Section 1.1.3) these methods have conceptual shortcomings in the Alpine region. For instance, in an Alpine valley the most frequent flow patterns might be determined by thermal-induced valley circulations with low wind speeds and characteristic regional-scale flows (e. g., Föhn) with high wind speeds. Thus, a resultant frequency distribution would be bi-modal and henceforth challenge any uni-modal-based statistic.

However, one statistical method, which is limited to the interpolation of observed annual wind speeds with respect to complex topography (and neglects any frequency distribution), has been developed during the last decade and is heavily used in the Alps (e. g., *Kunz et al.*, 2004; *Schaffner and Remund*, 2005). Thereby, the observed annual wind speeds are firstly vertically extrapolated to ∼1000 m above ground level to derive an annual large-scale flow above the PBL's surface layer. In a second step this flow is interpolated horizontally onto an aspired highly resolved grid and vertically extrapolated to the corresponding surface altitude at each grid cell with respect to the local surface roughness and geometrical features of the local terrain (via empirically derived correction-terms). This *geo-statistic* method has been successfully applied to

calculate the mean wind speed of the period 1983–1997 in the Swiss territory on a grid with 50 m grid spacing achieving a mean absolute error of 1.5 m/s (*Kunz et al.*, 2004) and over the entire Alpine region on a grid with 250 m grid spacing (cf. Figure 2.3).

2.2 The Hybrid Dynamic/Diagnostic Downscaling Method

2.2.1 Overview

During the Austrian climate research project "Research for Climate Protection – Model Run Evaluation" (reclip:more) (*Loibl et al.*, 2007), which focused on the generation of a highly resolved (10 km × 10 km grid spacing) climate change scenario for the Alpine region primarily based on dynamic models, a hybrid *dynamic-diagnostic* modelling approach was designed to generate highly resolved gridded near surface wind climatologies from long-term simulations (decades) on the 100 m scale.

This approach, published in (*Truhetz et al.*, 2007) and evaluated during a 3 month testbed simulation in the Hohe Tauern region in Austria and in the Eastern Alps by *Gobiet et al.* (2004), was designed a) to be independent from observational data in order to investigate climate change effects purely based on AOGCM simulations, b) to capture both, climate phenomena (and their variability) on large and regional scales as far as possible and the most important terrain-induced effects influencing the local flow (cf. Section 1.1.3) on a sub-diurnal time scale, and c) to be still computationally feasible for long-term simulations. Based on a conceptual idea, as it has already been proposed in air quality studies (e. g., *Barna and Lamb*, 2000; *Chandrasekar et al.*, 2003), the modelling approach consists of two consecutive main steps:

- First, global atmospheric analysis data or atmospheric fields from AOGCMs are dynamically downscaled with the dynamic Mesoscale Model of the 5$^{\text{th}}$ Generation (MM5) (*Dudhia*, 1993) to derive atmospheric fields on a higher spatial and temporal resolution which are physically consistent with the global driving data.

- Second, the a modified version of the diagnostic mass-consistent California Meteorological Model (CALMET) (*Scire et al.*, 2000) is applied on the simulation results of MM5 in order to derive highly resolved divergence-free, stationary flow patterns (cf. Figure 2.4). From statistical analysis of the model output gridded wind climatologies are further calculated.

MM5 is a non-hydrostatic model equipped with a broad spectrum of up-to-date subgrid-scale parameterisations including a SVAT which is capable to simulate climate-related soil processes. It is one of the freely available models, which are believed to generate robust results even in complex terrain, and it is widely used in the field of regional climate modelling (e. g., *Leung et al.*, 2003; *Walter et al.*, 2006). For the Alpine region the following parameterisations were selected for MM5 based on the experiences of dynamic modelling in complex terrain (*Gobiet et al.*, 2006; *Zängl*, 2004; *Zängl et al.*, 2004):

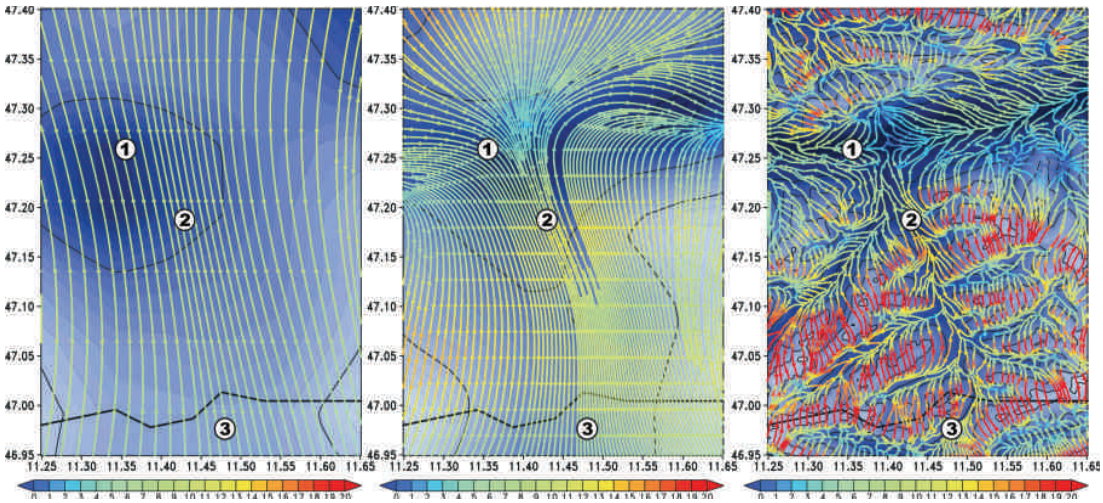

Figure 2.4: Modelled wind field 30 m above ground (coloured stream lines [m/s]) in the Hohe Tauern region (Wipp Valley, Tyrol, Austria). MM5 data representing the 21 Oct 1999 at 00:00 UTC with 15 km grid spacing (left panel) is downscaled via MM5 to 5 km grid spacing (middle panel) and further to 200 m grid spacing (right panel) with CALMET. The sites of the observation stations "Innsbruck-Flugplatz", "Ellboegen", and "Brenner" are marked as (1), (2), (3), respectively.

- an updated cumulus parameterisation with shallow convection (Kain-Fritsch-2) (*Kain*, 2004) in order to better represent the effects of non-precipitating clouds,
- the ETA boundary layer scheme (*Janjic*, 1990, 1994) which introduces a prognostic equation for the turbulent kinetic energy (TKE) and therefore, it is a more properly suited scheme to simulate near surface flows; moreover, it is fairly used when dynamic models are applied in complex terrain (e. g., *Zängl*, 2004; *Zängl et al.*, 2004; *Zängl and Vogt*, 2006),
- a mixed-phase moisture scheme (Reisner-1) (*Reisner et al.*, 1998) including ice-clouds, super-cooled water, and allows for slow melting of snow,
- the Rapid Radiative Transfer Model (RRTM) (*Mlawer et al.*, 1997) which takes into account water vapour, carbon dioxide and ozone and is combined with a cloud-radiation scheme to capture long-wave and short-wave interactions with explicit cloud and clear-air, and
- the NOAH land surface model (*Chen and Dudhia*, 2001) to predict soil moisture and temperature in four layers based on soil conductivity and gravitational flux of moisture as well as canopy moisture and water-equivalent of snow depth.

In addition to the the terrain-induced speed-up effect, CALMET is able to take account for the Froude-effect and for slope flows during day- and nighttime, which are two of the more important effects in the Alpine region (cf. Section 1.1.3). At a glance, after initialising CALMET with interpolated MM5 fields, the initial fields are adjusted by applying the following steps in a sequence:

- generation of vertical velocity components with respect to the geometry of the terrain and the stratification of the PBL (*Liu and Yocke*, 1980) damped by an user-defined factor,
- minimising the divergence until it reaches an user-defined threshold value at each grid cell by adjusting the horizontal wind components (*Goodin et al.*, 1980),
- introduction of slope flows based on the local sensible heat fluxes (*Mahrt*, 1982) and extending up to an user-defined radius of influence,
- adjusting the horizontal velocity components with respect to the Froude-number in order to distinguish between flow-over and flow-around regime, and
- re-adjusting the vertical velocity components to fulfil the incompressible continuity equation.

Nevertheless, from this conceptual down-scaling approach dynamic phenomena, like flow-splitting, vortex shedding, cross-valley circulations, the influences of inversion-layers on near surface flows, turbulence induced increase of wind speeds and extreme events (wind gusts) can only be expected to be found in the simulation results as long as they are captured by the dynamic model.

In addition to the lateral boundary conditions (LBCs) (cf. Section 2.1.1), which have to be prepared for MM5, numerous geo-physical parameters are required for both models in order to generate proper surface boundary conditions (SBCs). The preparation of these parameters in detail as well as the preparation of the surface altitudes are described in Section 3.1. An explanation of the functionality of the geo-physical parameters can be found in Section 2.2.2 for CALMET and in *Dudhia et al.* (2005) and *Chen and Dudhia* (2001) for MM5.

Modifications to the original CALMET code (version 5.53b, level 051216) were made concerning the generation of the initial wind fields, the implementation of the damping factor for numerical stability, and an estimation of snow cover affecting the surface albedo. All modifications are described in detail in Section 2.2.2.

Technically seen, the code of CALMET was transferred from Microsoft Windows®to Linux and prepared for long-term simulations. An interface to establish the connection to MM5 and to conduct grid interpolations was written in FORTRAN90 and compiled into an external library which is linked together with CALMET to reduce the consumption of disk space and to shorten the computational time. In addition, an option was implemented to write out CALMET's simulation results compliant to the NetCDF Climate and Forecast (CF) Metadata Conventions (*Eaton et al.*, 2003).

2.2.2 Technical Description

Looking into details, MM5 discretises the grid-cell-averaged equations (cf. Section 2.1.1) of (2.1)–(2.4) on a staggered Arakawa-Lamb-B grid in a terrain-following σ-pressure-coordinate system (X^{MM5}, Y^{MM5}, σ). The definition of this system from 3-dimensional Cartesian coordinates (x, y, z) and the discretisation into I^{MM5}, J^{MM5}, and K^{MM5} grid-cells with respect to the horizontal and vertical directions are defined by

$$\begin{array}{rclcrcll} X^{MM5}(x) & = & x & & X_i^{MM5} & = & x_i & i = 1, \ldots, I^{MM5} \\ Y^{MM5}(y) & = & y & \mapsto & Y_j^{MM5} & = & y_i & j = 1, \ldots, J^{MM5} \\ \sigma(x,y,z) & = & \frac{p_0^{ref}(z) - p_t^{ref}}{p_s^{ref}(x,y) - p_t^{ref}} & & \sigma_k(x_i, y_j, z_k) & = & \frac{p^{ref}(z_k) - p_t^{ref}}{p_s^{ref}(x_i, y_j) - p_t^{ref}} & k = 1, \ldots, K^{MM5} \end{array} \tag{2.15}$$

where p^{ref} refers to the pressure of a user-given dry hydrostatic reference atmosphere and p_t^{ref} and p_s^{ref} are the p^{ref}-values at the model top and at the surface, respectively. In addition to the top pressure (p_t^{ref}), the reference atmosphere is defined by its reference sea level pressure (p_{slp}^{ref}) and temperature (T_{slp}^{ref}), and the reference temperature lapse rate ($dT^{ref}/d(\ln p^{ref})$). The reference surface pressure (p_s^{ref}) is derived from these constants with respect to the model's surface altitude (h_h^{MM5}) by

$$p_s^{ref} = p_{slp}^{ref} \exp\left(-T_{slp}^{ref} \frac{d(\ln p^{ref})}{dT^{ref}} + \sqrt{\left(T_{slp}^{ref} \frac{d(\ln p^{ref})}{dT^{ref}} \right)^2 - 2g \frac{h_h^{MM5}}{R_d} \frac{d(\ln p^{ref})}{dT^{ref}}} \right) \tag{2.16}$$

with R_d as the gas constant for dry air (287.06 J/kgK).

During model integration MM5 calculates a non-hydrostatic pressure perturbation (p') for each grid cell (i, j, k) so that the actual pressure (p) can be derived from

$$p_{(i,j,k)} = \left(p_{s(i,j,k)}^{ref} - p_t^{ref} \right) \sigma_k + p_t^{ref} + p'_{(i,j,k)}. \tag{2.17}$$

The horizontal components of the velocity ($U_{(i,j,k)}^{MM5}$, $V_{(i,j,k)}^{MM5}$) are located at the 4 corners of each grid cell while the remaining variables are defined at the grid cell's centres (cf. Figure 2.5a). The vertical component of the velocity ($W_{(i,j,k)}^{MM5}$) resides at the top and bottom bounding surfaces between adjacent cells (i. e., full-σ-level) and the remaining variables are located in the cell's middle (i. e., half-*sigma*-level) (cf. Figure 2.5b). To solve the governing equations MM5 uses a second-order leapfrog timestep scheme. Implicit schemes are only applied in 1-dimensional column calculations for vertical sound waves and vertical diffusion, which enhances the model stability and simplifies the parallelisation of the model's code.

Similar to MM5 CALMET operates in a terrain-following coordinate system (X^{CAL}, Y^{CAL}, Z^{CAL}) as well. The definition of this system from 3-dimensional Cartesian coordinates (x, y, z) and the discretisation into I^{CAL}, J^{CAL}, and K^{CAL} grid-cells is defined by

$$\begin{array}{rcrcl} X^{CAL}(x) = x & & X_i^{CAL} = x_i & & i = 1, \ldots, I^{CAL} \\ Y^{CAL}(y) = y & \mapsto & Y_j^{CAL} = y_j & & j = 1, \ldots, J^{CAL} \\ Z^{CAL}(x,y,z) = z - h_t(x,y) & & Z_k^{CAL}(x_i, y_j, z_k) = z_k - h_t(x_i, y_j) & & k = 1, \ldots, K^{CAL} \end{array} \tag{2.18}$$

where h_t refers to the surface altitude in the model domain. Thus, the horizontal (U^{CAL} and V^{CAL}) and vertical (W^{CAL}) velocity components in CALMET's coordinate system are given by

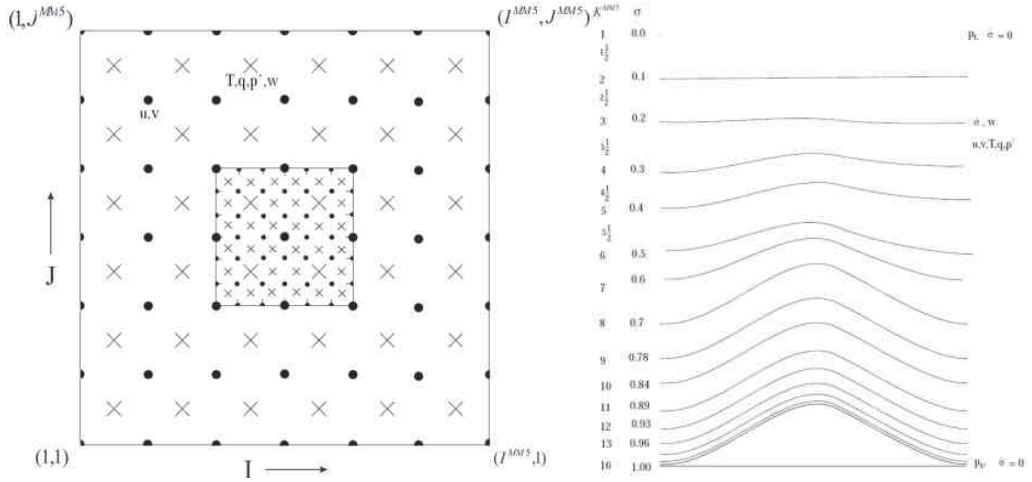

Figure 2.5: Grid definition of the MM5 model. (a) Schematic representation showing the horizontal Arakawa B-grid staggering of the dot (•) and cross (×) grid points. The smaller inner box is a representative mesh staggering for a 3:1 coarse-grid distance to fine-grid distance ratio. (b) Schematic representation of the vertical structure of the model. The example is for 15 vertical layers. Solid lines denote full-sigma levels. From *Dudhia et al.* (2005), modified.

$$\begin{aligned} U^{CAL}(X,Y,Z) &= u(x,y,z) \\ V^{CAL}(X,Y,Z) &= v(x,y,z) \\ W^{CAL}(X,Y,Z) &= w(x,y,z) - u(x,y,z)\frac{\partial h_t}{\partial x} - v(x,y,z)\frac{\partial h_t}{\partial y}. \end{aligned} \tag{2.19}$$

Here, $U^{CAL}_{(i,j,k)}$ and $V^{CAL}_{(i,j,k)}$ are located at the centre of each grid cell (cf. Figure 2.6) and $W^{CAL}_{(i,j,k)}$ at the horizontal bounding surfaces between adjacent cells (i. e., half-k-levels).

To bridge the gap between the two model grids with different coordinate systems, geographic projections (MM5 uses a Lambert Conformal Conic projection, CALMET an Universal Transverse Mercator projection), and grid spacings (CALMET is higher resolved than MM5), and to connect the two models technically in a convenient way the fields of MM5 are interpolated onto CALMET's grid in a double re-gridding step taking account for the orography on the higher resolved grid. The MM5 fields are firstly interpolated onto an intermediate grid with 1 km grid spacing leaving the σ-levels untouched by an MM5-interpolation-tool (*Manning and Haageson*, 1992). Hereby, the fields are interpolated horizontally via bi-linear interpolation and are adjusted regarding to their new altitudes on the 1 km grid. Temperature is adjusted based on the temperature lapse rate of the reference atmosphere and the horizontal wind components via vertical gradients linear in pressure. In addition, the divergence of the vertically averaged horizontal wind field is removed assuming that the correction terms can be derived from a 2-dimensional perturbation velocity potential (cf.Section 2.1.2). Technically seen, the

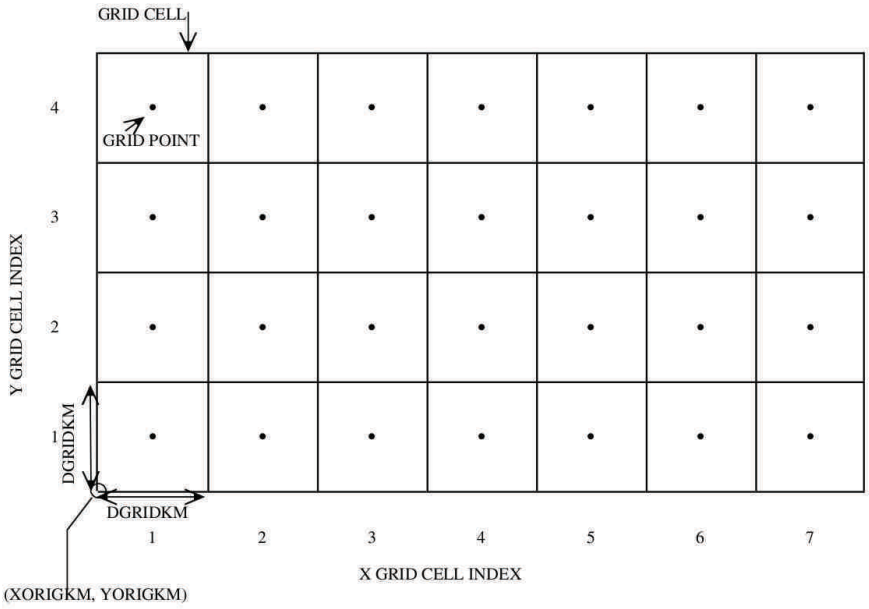

Figure 2.6: Grid definition of the CALMET model. Schematic illustration of the CALMET horizontal grid system for 7 × 4 grid showing the user-defined grid origin (XORIGKM, YORIGKM) and the grid point locations (•). From *Scire et al.* (2000).

interpolation onto the 1 km grid is part of an external library (cf. Section 2.2.1). Secondly, these intermediate fields (1 km grid spacing) are interpolated onto CALMET's grid. Thereby, a cubic-spline method in the vertical direction for the horizontal wind speed is used. This guarantees continuous first derivatives enhancing the numerical stability of CALMET in complex terrain. Wind direction and temperature are interpolated linearly in height above ground. Horizontal wind speeds on CALMET-levels ($|\vec{V}^{CAL}_{0,(k)}|$) beneath the lowest σ-level (at $k = K^{MM5}$) with a height above ground of $Z^{1km}_{(K^{MM5})}$ are extrapolated from the horizontal wind speeds at that level ($|\vec{V}^{1km}_{(K^{MM5})}|$) via the logarithmic wind profile. The original CALMET code is based on a default surface roughness length of 0.5 m. This has been changed and the roughness lengths on the 1 km grid (z_0^{1km}) are used instead for a better representation of local effects:

$$|\vec{V}^{CAL}_{0,(k)}| = |\vec{V}^{1km}_{(K^{MM5})}| \frac{\ln Z^{1km}_{(K^{MM5})} - \ln z_0^{1km}}{\ln Z^{CAL}_{(k)} - \ln z_0^{1km}} \ , \forall \ Z^{CAL}_{(k)} < Z^{1km}_{(K^{MM5})} \ . \tag{2.20}$$

The temperature is extrapolated to the CALMET-levels beneath the lowest σ-level via the dry-adiabatic lapse rate during daytime and via a parameterisation for the nocturnal inversion-layer from *Stull* (1983). Hereby, it is assumed that the reduction of the potential temperature follows an exponential decay in height due to surface cooling. Assuming furthermore that the coefficients of this decay are constant throughout the night, the actual potential temperature at a certain level (Z^{CAL}_k) can be calculated via an exponential extrapolation of the reduction of the potential temperature since sunset

($\Delta\theta^{1km}$) at the lowest two σ-levels ($Z^{1km}_{(K^{MM5})}$ and $Z^{1km}_{(K^{MM5}-1)}$):

$$\theta^{CAL}_{0,(k)} = \theta^{1km}_{(K^{MM5})} + \Delta\theta^{1km}_{(K^{MM5})} \exp\left(\frac{Z^{1km}_{(K^{MM5})} - Z^{CAL}_{(k)}}{Z^{1km}_{(K^{MM5}-1)} - Z^{1km}_{(K^{MM5})}} \ln\frac{\Delta\theta^{1km}_{(K^{MM5})}}{\Delta\theta^{1km}_{(K^{MM5}-1)}}\right) . \quad (2.21)$$

Note this inversion-layer-parameterisation only affects the temperature but not the air flow, flow separation and deflection due to the inversion-layer are therefore neglected.

After the vertical inter- and extrapolations, all fields are interpolated horizontally via an inverse distance method generating the initialisation fields on CALMET's grid. Each variable of the initialisation fields on each CALMET grid cell (φ^{CAL}_0) is calculated from its four nearest-neighbouring cells of the 1 km grid ($\varphi^{1km}_{1,\ldots,4}$) as an weighted average, whereas the weighting factors are represented by the inverse squared distances between the centre of the CALMET cell and the centres of the four surrounding 1 km grid cells ($1/(r^{CAL}_{1km,1,\ldots,4})^2$):

$$\varphi^{CAL}_0 = \frac{\sum_{i=1}^{4} \frac{1}{(r^{CAL}_{1km,i})^2}\varphi^{1km}_i}{\sum_{j=1}^{4} \frac{1}{(r^{CAL}_{1km,j})^2}} . \quad (2.22)$$

Note due to the sequence of interpolations (first vertical, then horizontal) the initialisation fields consist of the intermediate fields which are simply stretched over the CALMET grid (i. e., the fields are not affected by CALMET's orography) and hardly reflect any local topographic effect.

Based on the horizontal initial wind field $\vec{V}^{CAL}_0 = (U^{CAL}_0, V^{CAL}_0)$ the original CALMET version induces vertical wind components with an exponential decay in height regarding to the local terrain slope angles (*Liu and Yocke*, 1980). In Cartesian coordinates the initial vertical velocity at the half-k-levels ($w^{CAL}_{0,(k\pm1/2)}$) is computed as

$$w^{CAL}_{0,(k\pm1/2)} = \begin{cases} (\vec{V}^{CAL}_{0,(k=1)} \cdot \nabla h_t) \exp\left(-B_s Z^{CAL}_{k-1/2}\right) , \text{ if } k = 1 \\ \alpha(\vec{V}^{CAL}_{0,(k=1)} \cdot \nabla h_t) \exp\left(-B_s Z^{CAL}_{k\pm1/2}\right) , \text{ if } k \neq 1 \end{cases} , \quad (2.23)$$

where B_s denotes a stability-depending coefficient and α is a user-defined damping factor (except for the surface-level $(1 - 1/2)$) to tune the terrain-induced speed-up effect. However, since the surface-level is excluded from the damping a discontinuity of the vertical wind component is induced leading to unrealistic results of the divergence-minimisation scheme in complex terrain. To overcome this, the original CALMET code has been modified by applying α on the surface-level as well:

$$w^{CAL}_{0,(k\pm1/2)} = \alpha(\vec{V}^{CAL}_{0,(k=1)} \cdot \nabla h_t) \exp\left(-B_s Z^{CAL}_{k\pm1/2}\right) . \quad (2.24)$$

Usually α ranges between 0.0 and 1.0. Note, any damping factor unequal to 1.0 in principal violates the physical relations.

B_s is derived from the Brunt-Väisälä frequency (N) based on the initial potential temperature (θ_0^{CAL}) or the initial air temperature (T_0^{CAL}) by

$$B_s = \frac{N}{\overline{V}_0^{CAL}} \quad \text{with} \quad \begin{array}{l} N = \sqrt{\frac{g}{\theta_0^{CAL}} \frac{d\theta_0^{CAL}}{dZ^{CAL}}} = \sqrt{\frac{g}{T_0^{CAL}} \left(\frac{dT_0^{CAL}}{dZ^{CAL}} + \frac{g}{c_p} \right)} \\ \overline{V}_0^{CAL} = \frac{\sum_{k=1}^{K^{CAL}} \sqrt{(U_{0,(k)}^{CAL})^2 + (V_{0,(k)}^{CAL})^2} (Z_k^{CAL} - Z_{k-1}^{CAL})}{Z_{K^{CAL}}^{CAL}} \end{array} \tag{2.25}$$

where c_p denotes the specific heat capacity of air (1005.7 J/kgK) and $\overline{V}_0^{CAL}$ is the vertical-averaged horizontal wind speed of the initial field. Under statically neutral ($N \to 0$) and unstable conditions (N is not defined) in CALMET B_s is set to 0.004 1/m. Furthermore, the temperature lapse rates ($d\theta_0^{CAL}/dZ^{CAL}$ and dT_0^{CAL}/dZ^{CAL}) are averaged throughout the model domain.

After transforming w_0^{CAL} into the terrain-following coordinate system via equation (2.19) CALMET applies a two-dimensional divergence-minimisation scheme (*Goodin et al.*, 1980) to the horizontal wind components to fulfil the incompressible continuity equation (2.11). This induces the terrain-depending speed-up effect. Thereby, the adjustments of the wind components are calculated from the divergence at each grid cell ($D_{i,j,k}$):

$$\begin{array}{rcl} U_{new,(i+1,j,k)}^{CAL} & = & U_{(i+1,j,k)}^{CAL} + \frac{-D_{i,j,k}(X_{i+1}^{CAL} - X_i^{CAL})}{2} \\ U_{new,(i-1,j,k)}^{CAL} & = & U_{(i-1,j,k)}^{CAL} - \frac{-D_{i,j,k}(X_i^{CAL} - X_{i-1}^{CAL})}{2} \\ V_{new,(i,j+1,k)}^{CAL} & = & V_{(i,j+1,k)}^{CAL} + \frac{-D_{i,j,k}(Y_{j+1}^{CAL} - Y_j^{CAL})}{2} \\ V_{new,(i,j-1,k)}^{CAL} & = & V_{(i,j-1,k)}^{CAL} - \frac{-D_{i,j,k}(Y_j^{CAL} - Y_{j-1}^{CAL})}{2} \ . \end{array} \tag{2.26}$$

If the divergence is derived from centered difference operators given by

$$D_{i,j,k} = \frac{U_{i+1,j,k}^{CAL} - U_{i-1,j,k}^{CAL}}{X_{i+1}^{CAL} - X_{i-1}^{CAL}} + \frac{V_{i,j+1,k}^{CAL} - V_{i,j-1,k}^{CAL}}{Y_{j+1}^{CAL} - Y_{j-1}^{CAL}} + \frac{W_{i,j,k+1/2}^{CAL} - W_{i,j,k-1/2}^{CAL}}{Z_{k+1/2}^{CAL} - Z_{k-1/2}^{CAL}}, \tag{2.27}$$

an iterative application of this procedure gradually reduces the divergence until a user-defined threshold value (ϵ) is reached throughout the grid. During this procedure the horizontal wind components of the initial field are modified with respect to the terrain fulfilling the continuity equation ($(U_0^{CAL}, V_0^{CAL}) \mapsto (U_1^{CAL}, V_1^{CAL})$). Note, this divergence-minimisation scheme differs from other, more sophisticated methods (e. g., the Lagrangian method, cf. Section 2.1.2), since the vertical wind components are kept constant.

Afterwards, slope flows enforced by sensible heat fluxes are generated based on the

concept of shooting flows from *Mahrt* (1982). The divergence-free wind field is modified by those flows with respect to the terrain geometry ($(U_1^{CAL}, V_1^{CAL}) \mapsto (U_2^{CAL}, V_2^{CAL})$). Following *Mahrt* (1982) slope flows are buoyancy-driven and balanced by surface drag and an entrainment at the top of the slope flow layer. If the flow is assumed to be steady and has a constant depth (d_{sf}), the flow speed (S_{sf}) over a slope with a constant angle α_{sl} can be expressed as

$$S_{sf} = \sqrt[3]{Q_h g r \frac{\sin \alpha_{sl}}{\rho c_p T (C_D + e_c)} (1 - e^{-r/L_e})} \quad \text{with} \quad L_e = \frac{d_{sf}}{C_D + e_c} \tag{2.28}$$

where Q_h is the sensible heat flux, r is the distance from the crest within a user-defined radius r_i, ρ is the air density, C_D is the surface drag coefficient, e_c is an entrainment coefficient at the top of the flow layer, and L_e is an equilibrium length scale at which the flow reaches 80% of its equilibrium speed. In CALMET S_{sf} is calculated for every grid cell based on the initial temperature field, ρ is assumed to be constant, and d_{sf} is set to 5 % of the drop of the elevation from the crest. The values for C_D and e_c are fixed at 0.04, and ρ is assumed to be constant throughout the grid and is set to 1.225 kg/m^3.

During daytime, the sensible heat flux Q_h is calculated from the local energy budget at the surface (*Holtslag and van Ulden*, 1983) in terms of the Bowen-ratio (B), the net horizontal surface radiation (Q^*), the anthropogenic heat flux (Q_f), and the soil heat flux parameter (c_g), which is the ratio between the soil heat flux (Q_g) and the net radiation (Q^*):

$$Q_h = \frac{B}{1+B} \left[Q^* (1 - c_g) + Q_f \right] \ . \tag{2.29}$$

In CALMET B, c_g, and Q_f are kept constant and have to be prepared externally. Following *Holtslag and van Ulden* (1983) the net radiation is derived from the incoming solar short-wave radiation (Q_{SW}), the air temperature at 2 m above ground (T_{2m}), the surface albedo (A) and the cloud cover fraction (C_c) by

$$\begin{aligned} Q^* &= \frac{(1-A) Q_{SW} + c_1 T_{2m}^6 - \sigma_B T_{2m}^4 + c_2 C_c}{1 + c_3} \text{ with} \\ Q_{SW} &= (a_1 \sin \varphi + a_2)(1 + b_1 C_c^{b_2}) \end{aligned} \tag{2.30}$$

and the constant coefficients a_1, a_2, b_1, b_2, c_1, c_2, and c_3 listed in Table 2.1. σ refers to the Stefan-Boltzmann constant (5.674 $\times 10^{-8}$ W/m^{2}K^4) and φ denotes the astronomic solar elevation angle, which is calculated for each grid cell depending on the geographic coordinates and the local time. In CALMET the influences of the terrain on Q_{SW} (i. e., slope angles and orographic shading) are neglected. The cloud cover fraction is calculated from the initialisation field of the relative humidity ($RH_{0,(850)}^{CAL}$) at the 850 hPa level by a simplified relation from *Teixeira* (2001), which was originally designed for global dynamic models in NWP with a coarse resolution, neglecting the influence of liquid water content:

$$C_c = 0.02 \frac{\sqrt{1 + 100(1 - RH^{CAL}_{0,(850)})} - 1}{1 - RH^{CAL}_{0,(850)}} \ . \tag{2.31}$$

During nighttime, stable conditions are assumed and the sensible heat flux Q_h is calculated based on the K-Theory in terms of the friction velocity u_* and the flux temperature θ_* (cf. equation (2.9)):

$$Q_h = -\rho c_p u_* \theta_* \ . \tag{2.32}$$

Note, here ρ is calculated from the initial temperature and pressure reflecting the influence of orography. u_* is computed from θ_*, the horizontal wind speed derived from the divergence-free wind field (U_1^{CAL} , V_1^{CAL}) and the initial temperature (T_0^{CAL}) given on the lowest CALMET level ($k = 1$), and the drag coefficient for neutral conditions (C_{DN}^{CAL}) based on the surface roughness length on CALMET's grid (z_0^{CAL}) following (*Venkatram*, 1980):

$$\begin{aligned}
u_* &= \frac{C_{DN}^{CAL}}{2}(1 + \sqrt{C}) \text{ with} \\
C_{DN}^{CAL} &= \frac{k}{\ln(Z^{CAL}_{(k=1)}) - \ln(z_0^{CAL})} \ , \\
C &= 1 - \frac{4u_0^2}{C_{DN}^{CAL}((U^{CAL}_{1,(k=1)})^2 + (V^{CAL}_{1,(k=1)})^2)} \ , \text{ and} \\
u_0^2 &= \frac{4.7 Z^{CAL}_{(k=1)} g \theta_*}{T^{CAL}_{0,(k=1)}} \ .
\end{aligned} \tag{2.33}$$

The temperature flux θ_* is calculated following *Holtslag and van Ulden* (1983) as the minimum of two estimates, which are based on the cloud cover fraction (C_c) from equation (2.31), the drag coefficient for neutral conditions (C_{DN}^{CAL}) from equation (2.33), the horizontal wind speed, and the initial temperature:

$$\theta_* = \min \left(0.09 \left(1 - \frac{C_c}{2} \right), \frac{T^{CAL}_{0,(k=1)} C_{DN}^{CAL} ((U^{CAL}_{1,(k=1)})^2 + (V^{CAL}_{1,(k=1)})^2)}{18.8 Z^{CAL}_{(k=1)} g} \right) \ . \tag{2.34}$$

In contrast to the original CALMET code, where no snow cover effects are considered, a simple parameterisation of the effect of snow cover on surface albedo is implemented in the following way: the snow heights on the intermediate grid (1 km grid spacing, see above) are transferred to CALMET's grid via the nearest-neighbourhood method. Based on these initial snow heights ($h_{sh,0}^{CAL}$) and the snow-free albedo (A_0) CALMET's surface albedo (A^{CAL}) is calculated from

$$A^{CAL} = \begin{cases} 1.5 A_0 & \forall \ h_{sh,0}^{CAL} > 0.01 \text{ m} \\ A_0 \end{cases} \tag{2.35}$$

Table 2.1: Net radiation constants. From *Holtslag and van Ulden* (1983).

Constant	Value	Unit
a_1	990	$\mathrm{W/m^2}$
a_2	-30	$\mathrm{W/m^2}$
b_1	-0.75	1
b_2	3.4	1
c_1	5.31×10^{-13}	$\mathrm{W/m^2K}$
c_2	60	$\mathrm{W/m^2}$
c_3	0.12	1

Note, the transformation of snow heights from the coarse MM5 grid to the much higher resolved CALMET grid neglects any sub-grid scale effects beyond the MM5 grid.

Based on the local Froude number Fr^{CAL}, derived for each grid cell and defined by

$$Fr^{CAL} = \frac{\sqrt{(U_2^{CAL})^2 + (V_2^{CAL})^2}}{N\Delta h_t} \quad \text{with} \quad \Delta h_t = h_{max} - Z^{CAL} \tag{2.36}$$

where N is the Brunt-Väisälä frequency from equation (2.25) based on the averaged temperature lapse rate, Δh_t is an effective obstacle height, and h_{max} is the highest gridded surface altitude within a user-defined radius of influence (r_i), the horizontal wind components are turned tangentially to the terrain if Fr^{CAL} is smaller than 1 ($(U_2^{CAL}, V_2^{CAL}) \rightarrow (U_3^{CAL}, V_3^{CAL})$).

Note, the slope flows and the Froude-effect are based on the divergence-free wind field (U_1^{CAL}, V_1^{CAL}, W_0^{CAL}) and are generating additional divergence in turn. To remove this divergence the vertical wind components are modified in terms of the re-calculated divergence ($D_{i,j,k}$) from equation (2.27) in a final re-adjustment step:

$$\begin{aligned} W^{CAL}_{2,(i,j,k+1/2)} &= (Z^{CAL}_{k+1/2} - Z^{CAL}_{k-1/2}) D_{i,j,k} + W^{CAL}_{2,(i,j,k-1/2)} \text{ with} \\ W^{CAL}_{2,(i,j,-1/2)} &= W^{CAL}_{0,(i,j,-1/2)} \ . \end{aligned} \tag{2.37}$$

In addition to the user-defined damping factor (α), the threshold value (ϵ), and the radius of influence (r_i) the Bowen-ratio (B), the soil heat flux parameter (c_g), the surface roughness length (z_0^{CAL}), the snow-free surface albedo (A_0), and the surface altitudes have to be prepared on CALMET's grid. On the intermediate 1 km grid the surface roughness lengths (z_0^{1km}) as well as the surface altitudes are required.

3 Improvements of the Wind Downscaling Method

The dynamic-diagnostic downscaling method, introduced in Section 2.2, claims to overcome numerous shortcomings of other modelling approaches. However, several weaknesses arising from limitations and simplifications remain: first, since the results of diagnostic models crucially depend on the quality of their initialisation fields (cf. Section 2.1.2), CALMET's initialisation fields are expected to have a major impact on the quality of the final wind climatologies. Second, possibly improper parameterisations of CALMET and misleading simplifications limiting its potential to simulate stationary flows in the Alpine region can be identified from Section 2.2.2 and summarised as follows:

- the temperature lapse rate and the density of air are kept constant throughout the model domain,
- the calculation of the sensible heat flux is based on externally given constants (i. e., the Bowen ratio and the soil heat flux parameter) and on a cloud cover parameterisation which was designed for global coarsely resolved models in the field of NWP,
- the data fields from the intermediate grid are firstly interpolated vertically and secondly interpolated horizontally which drastically reduces the possibilities to take account for local topography during model initialisation,
- the divergence-minimisation scheme is limited to the horizontal velocity components, and
- the net radiation neglects any orographic effects.

One of the promising options to generate more realistic initialisation fields for CALMET is to increase the resolution of MM5. The validity of this strategy has been indicated by *Truhetz et al.* (2007) who were able to reduce the mean absolute bias of the modelled wind speed (averaged over 6 alpine observation stations) from 1.3 m/s to 0.9 m/s via a reduction of the grid spacing from 10 km to 5 km (simulation-period: September 7 to November 15, 1999). Moreover, the downscaling error tends to be smaller at higher wind speeds ($\geq$15 m/s) indicating that more uncertainties arise at low wind speeds where CALMET's parameterisations should add value. However, a technical limitation of this strategy is given by the exponentially increasing demand of computational resources due to the CFL-criterion (cf. Section 2.1.1). Another possibility to enhance the initialisation fields by inverting the sequence of interpolation and by taking into account for local effects of the topography.

These options as well as some improvements of CALMET's parameterisations are captured by several modifications. According to the general structure of the wind downscaling method, the modifications are related to MM5 and CALMET. Based on a control configuration, referred to as *Av0* (*"A"* refers to the MM5 control setup and *"v0"* to CALMET's control variant from Section 2.2.2) defined in Section 3.1, two variations of the dynamic model (*"B"* and *"C"*) are introduced in Section 3.2. The selection and the description of a limited number of three CALMET improvements (*"v1"*, *"v2"*, and *"v3"*) for further investigation is discussed in Section 3.3. Note, changes of the divergence-minimisation scheme are excluded as well as a re-consideration of CALMET's radiation-scheme, which is investigated by *Bellasio et al.* (2005), who have found promising results for air temperature in the Alpine region.

3.1 The Control Configuration

The control configuration (Av0) was designed to generate realistic flow patterns with 200 m × 200 m grid spacing based on coarsely resolved global driving data (1.125° × 1.125°) in two study regions, the very complex Hohe Tauern region (area 140 km × 70 km, surface altitudes from ∼500 m to 3798 m, the Großglockner) in the Eastern Alps and the relatively flat Vienna Basin (area 120 km × 90 km, surface altitudes from 110 m to 1399 m, the Reisalpe ∼25 km to the south of St. Pölten) in Lower Austria. It consists of two nested dynamic and two diagnostic downscaling steps, one for each study region. During dynamic downscaling the grid spacing of MM5 is reduced from 30 km × 30 km (domain A1) to 10 km (domain A2) (cf. Figure 3.1a), i. e., the 10 km grid is *nested* into the 30 km grid while the simulations of both grids are conducted simultaneously. The simulation results in domain A2 are stored in one-hourly intervals and are interpolated onto two grids with 1 km × 1 km grid spacing (domains A3a and A3b) (cf. Figure 3.1b), defining the intermediate 1 km grids (cf. Section 2.2.2). CALMET in its control variant (v0) is initialised by these intermediate 1 km fields and generates flow patterns on grids with 200 m × 200 m grid spacing for each of the two study regions (cf. Figure 3.1b).

The setup and nesting-strategy for MM5 was defined during reclip:more (*Gobiet et al.*, 2006; *Truhetz et al.*, 2007) to conduct long-term climate simulations in the Alpine region. It was a compromise between favoured larger domains (to generate a climate scenario even for most parts of Europe, domain A1) and the available computational resources. However, it has the advantage to generate more realistic lateral boundary conditions (LBCs) (cf. Section 2.1.1) for the 10 km grid than deriving them from the global driving data: due to the high update rate from MM5's time step in the 30 km grid (i. e., 90 s) dynamic processes (e. g., gravity waves, cf. Section 1.1.2) with velocities up to 1200 km/h are resolved on that grid and hence are transferred to the inner domain (10 km grid) if its LBCs are calculated internally by MM5 during model integration. In contrast, if the LBCs of the 10 km grid is derived from the global driving data, the temporal resolution is limited to the storage interval of the driving data (e. g., 6 h for most global re-analysis datasets and data from GCMs, which limits the resolved velocity to ∼20 km/h if the horizontal grid spacing is 1.125° × 1.125°). Note, the grid spacing of up-to-date and near future long-term climate simulations is still limited

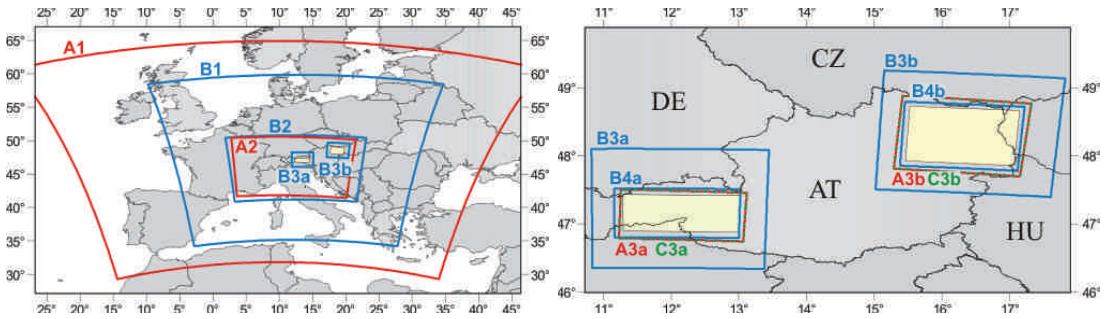

(a) (b)

Figure 3.1: Domain setting of the wind downscaling method and its variants. (a) in the control configuration A (red), the global driving data is dynamically downscaled to 30 km (A1) and to 10 km (A2) and diagnostically downscaled to 200 m grid spacing in the Hohe Tauern region (light green) and the Vienna Basin (light yellow); in variant B (blue), the driving data is dynamically downscaled to 45 km (B1), 15 km (B2), and 5 km grid spacing in both study regions (B3a and B3b). (b) before the diagnostic model is applied, the results of the dynamic downscaling variants (A and B) are interpolated onto 1 km grids (A3a, A3b, and B4a, B4b, respectively); in variant C (green), the result of A2 is dynamically downscaled to 1 km grids (C3a and C3b).

to ∼10 km due to the exponential increase of the demand of computational resources (cf. Section 2.1.1).

The spatial setup of both models as well as all MM5 variations defined in Section 3.2 are shown in Figure 3.1, the model discretisations for the control configuration (Av0) can be taken from Table 3.1. Note, MM5's reference atmosphere (cf. Section 2.2.2) does not reflect any standard atmosphere or mean atmosphere for the model domains: its reference values were left on MM5's internal default values. The top level was selected to be high enough to capture most important processes in the troposphere. CALMET's user-defined constants, i. e., the damping factor (α), the radius of influence (r_i) for the slope-flow parameterisation, and the threshold value for the divergence-minimisation scheme (ϵ) (cf. Section 2.2.2) were empirically estimated by comparing numerous short-term simulations in the Hohe Tauern region with observation data (not shown). Since CALMET's parameterisations are related to processes within the PBL, the top level is placed at 1250 m above ground level (a.g.l.) which includes 98.8% of all PBL heights simulated with MM5 in the Hohe Tauern region during September 7 to November 15, 1999 (*Truhetz et al.*, 2007). The lowest model level is fixed at 10 m (a.g.l.). The setup for the Hohe Tauern region was published by *Gobiet et al.* (2004); *Truhetz et al.* (2007), the setup for the Vienna Basin can be found in *Gobiet et al.* (2007).

In order to generate proper surface boundary conditions (SBCs), MM5 requires numerous geo-physical parameters (e. g., roughness length, heat capacity, albedo, seasonal-depending green vegetation fraction, and several soil parameters like, wilting point, thermal diffusivity, and annual deep soil temperature) as well as the surface altitude. These parameters are based on remotely sensed observations and are available as global

Table 3.1: Discretisations and parameterisations of the control configuration of MM5 and CALMET Av0. MM5 is operated in domains A3a and A3b; these grid are only used for interpolation.

MM5 (version 3.7.4)		Discretisiation	Domain				Reference	
			A1	A2	A3a	A3c	Atmosphere	
cumulus-scheme	Kain-Fritsch-2 shallow conv.	grid cells X I^{MM5}	124	109	145	141	top pressure p_t^{ref} [hPa]	100
PBL-scheme	ETA	grid cells Y J^{MM5}	100	79	85	121	sea-level press. p_{slp}^{ref} [hPa]	1000
moisture-scheme	Reisner-1	grid spacing [km]	30	10	1	1	sea-level temp. T_{slp}^{ref} [K]	275
radiation-scheme	RRTM	model levels K^{MM5}	29	29	29	29	lapse rate $\frac{dT^{ref}}{d(\ln p^{ref})}$ [K]	50
		time steps [s]	90	30	–	–		
		nest-type	one-way	one-way	–	–		

CALMET (version 5.53)		Discretisation	Study region	
			Hohe Tauern	Vienna Basin
damping-factor α [1]	0.1	grid cells X (I^{CAL})	700	600
radius of influence r_i [km]	5	grid cells Y (J^{CAL})	350	450
threshold value ϵ [s^{-1}]	5×10^{-6}	grid spacing [m]	200	200
model top [m]	1250	model levels (K^{CAL})	20	20

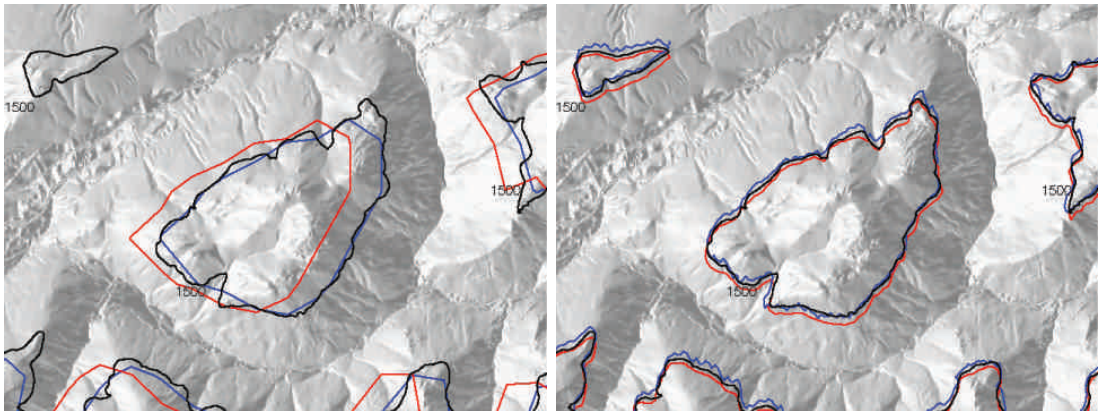

(a) (b)

Figure 3.2: Spatial deviations of different digital elevation models (DEMs). The contour-line at 1500 m altitude (black) derived from a DEM with 10 m × 10 m grid spacing (provided by the Department of the Salzburg State Government, Austria) of a small mountain in the Eastern Alps, the Schwarzberg (47°07'30"N, 13°48'35"E), close to Tamsweg, Austria, is drawn for the DEMs (a) GTOPO30 (red) and SRTM30 (blue) (30" × 30" grid spacing) and (b) uncorrected (red) and corrected (blue) SRTM3 (3' × 3' grid spacing). GTOPO30 has a westerly shift of ∼700 m, SRTM3 a southerly shift of ∼200 m.

terrestrial data fields prepared by the Pennsylvania State University (PSU) and the National Center for Atmospheric Research (NCAR). Hereby, a global digital elevation model (DEM) with a grid spacing of 30 " × 30 " from the U. S. Geological Survey (USGS), called *GTOPO30*, is recommended to be used (*Dudhia et al.*, 2005). However, from plotting contour-lines of GTOPO30 and a new DEM from NASA's Shuttle Radar Topography Mission (SRTM) (*Rabus et al.*, 2003), referred to as *SRTM30*, shows a westerly shift of GTOPO30 of ∼700 m (cf. Figure 3.2a). To reduce misleading geographical representations SRTM30 is used in the dynamic model. The surface roughness lengths and the surface altitudes of the intermediate 1 km grids (cf. Section 2.2.2) are taken from a global PSU/NCAR dataset available on a 30 " grid and SRTM30, respectively.

As explained in Section 2.2.2, CALMET requires the Bowen-ratio (B), the soil heat flux parameter (c_g), the surface roughness length (z_0), the snow-free surface albedo (A_0), and the surface altitude (h_t) on the model grid. Except for the surface altitude, these parameters were taken from literature (*BMU*, 2002; *Hagemann*, 2002; *Pineda et al.*, 2004; *Scire et al.*, 2000) and statically linked to the highly resolved (100 m × 100 m grid spacing) land cover information from the European CORINE land cover data set CLC2000 (*EEA*, 1995), version 8/2005, which was re-sampled to CALMET's 200 m grid via the nearest-neighbourhood method. The linkage between the geo-physical parameters and the land use classes is shown in Table 3.2. The surface altitude was derived from a new global DEM, the SRTM3 with 3" × 3" grid spacing (*Rabus et al.*, 2003). However, this data field is shifted ∼200 m southwards (cf. Figure 3.2b) and contains gaps (cf. Figure 3.3a). The south-shift was simply corrected by moving the

Table 3.2: CORINE land-use categories associated to CALMET's surface roughness length (z_0^{CAL}), snow-free surface albedo (A_0), Bowen ratio (B), and the soil heat flux parameter (c_g). The values are given in their precisions found in literature.

CORINE category (level 3)	z_0^{CAL} [m]	A_0 [1]	B [1]	c_g [1]
continuous urban fabric	2.00	0.173	1.50	0.25
discontinuous urban fabric	1.00	0.173	1.50	0.25
industrial/commercial units	1.00	0.173	1.50	0.25
road and rail networks and associated land	0.20	0.173	1.50	0.25
port areas	0.50	0.173	1.50	0.25
airports	0.10	0.173	1.50	0.25
mineral extraction sites	0.10	0.173	1.50	0.25
dump sites	0.02	0.173	1.50	0.25
construction sites	1.00	0.173	1.50	0.25
green urban areas	0.20	0.173	1.50	0.25
sport and leisure facilities	0.05	0.173	1.50	0.25
non-irrigated arable land	0.05	0.196	1.00	0.15
permanently irrigated land	0.06	0.201	0.50	0.15
rice fields	0.06	0.164	0.50	0.25
vineyards	0.20	0.192	0.50	0.25
fruit trees and berry plantations	0.50	0.165	0.50	0.25
olive groves	0.20	0.165	1.00	0.15
pastures	0.02	0.166	1.00	0.15
annual crops associated with permanent crops	0.25	0.180	1.00	0.15
complex cultivation patterns	0.20	0.181	1.00	0.15
land principally occupied by agriculture with significant areas of natural vegetation	0.20	0.186	1.00	0.15
agro-forestry areas	0.68	0.160	1.00	0.15
broad-leaved forest	1.50	0.153	1.00	0.15
coniferous forest	1.00	0.142	1.00	0.15
mixed forest	1.50	0.145	1.00	0.15
natural grassland	0.02	0.175	1.00	0.15
moors and heathland	0.20	0.162	0.50	0.25
sclerophyllous vegetation	0.47	0.158	0.50	0.25
transitional woodland-shrub	0.50	0.155	1.00	0.15
beaches, dunes and sand plains	0.01	0.170	1.00	0.15
bare rock	0.20	0.181	1.00	0.15
sparsely vegetated areas	0.02	0.204	1.00	0.15
burnt areas	0.10	0.136	1.00	0.15
glaciers and perpetual snow	0.05	0.464	0.50	0.15
inland marshes	0.10	0.151	0.50	0.25
peatbogs	0.10	0.151	0.50	0.25
salt-marshes	0.02	0.151	0.50	0.25
salines	0.20	0.151	0.50	0.25
water courses	0.02	0.078	0.00	1.00
water bodies	0.01	0.078	0.00	1.00
coastal lagoons	0.05	0.078	0.00	1.00
estuaries	0.02	0.078	0.00	1.00
sea and ocean	0.01	0.078	0.00	1.00

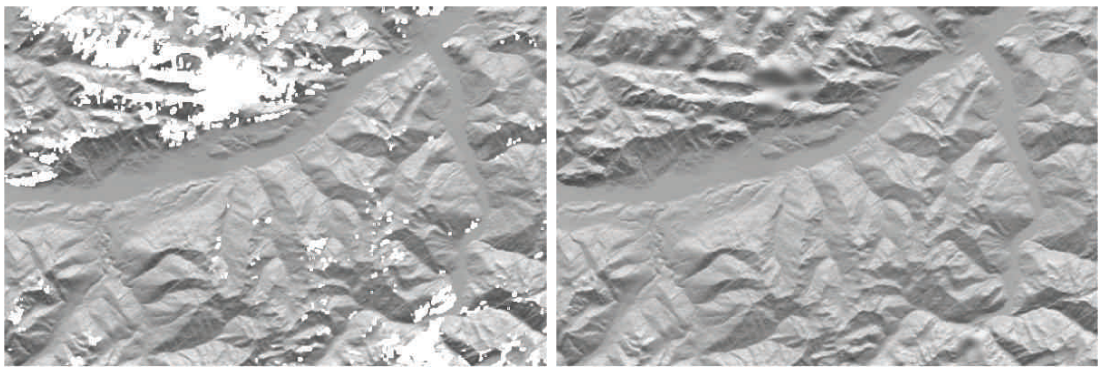

(a) (b)

Figure 3.3: Missing values are filled with spline interpolation techniques leading to smoothing effects. (a) raw and (b) filled SRTM3 data (3' × 3' grid spacing) for a region encompassing a steep mountain-chain to the north of Innsbruck in the Hohe Tauern region, the Nordkette, Tyrol, are shown.

DEM northwards. Additional elevation models and statistical methods were necessary to fill the missing data: a regularised spline interpolation method (*Mitasova and Mitas*, 1993) combined with other DEMs (i. e., the SRTM30 and a DEM with 250 m × 250 m grid spacing provided by the Austrian Research Centers systems research (ARC-sys)) were applied. Finally the DEM was re-sampled to the 200 m grid of the control configuration. The spline interpolation method was very successful in most regions, however, serious smoothing effects in regions with large areas of missing data were not avoidable (cf. Figure 3.3b).

3.2 Variations of the Dynamic Model

To investigate the influence of the resolution of the dynamic model on the resultant wind fields the grid spacing of MM5 is reduced from 10 km, defined in the control configuration (cf. Section 3.1), to 5 km (setup B) and to 1 km (setup C) in both study regions. In order to keep the computational demand on a maintainable level a new type of dynamic downscaling (introduced in Section 3.2.2) is used to reach the 1 km grid.

3.2.1 A Higher Resolved Grid with 5 km Grid Spacing

Setup B consists of three nested MM5 steps increasing the resolution from 45 km × 45 km grid spacing (domain B1) to 15 km × 15 km covering the Alpine region (domain B2) and further to two 5 km × 5 km grids (domain B3a and B3b), one for each study region (cf. Figure 3.1a). Due to the changed geographic setting the intermediate 1 km grids (cf. Section 2.2.2) for the two study regions are changed as well (domain B4a and B4b, cf. Figure 3.1b). The setup was developed during reclip:more. The effects of the

increased resolution of MM5 on down-scaled wind fields in the Hohe Tauern region for a 3 month simulation were published by *Truhetz et al.* (2007).

In addition to the changed discretisation the outermost domain (domain B1) is smaller than in the control configuration (domain A1) and the number of model levels is increased from 29 to 42. To achieve consistency with the control configuration (cf. Section 3.1) and to reduce the complexity of the data-interface between MM5 and CALMET the number of levels is reduced to 29 in the intermediate grids (domain B4a and B4b).

Comparisons of several short-term simulations with radiosonde data indicated that a smaller size of the outermost domain generally tends to better representations of air temperature and humidity mixing ratio on upper-air levels in the inner domains (A2 and B2) (*Gobiet et al.*, 2004; *Truhetz et al.*, 2005). This is related to the degree of freedom: the smaller the number of grid cells the smaller the degree of freedom and therefore the larger the influence of the LBCs. *Gobiet et al.* (2004) and *Truhetz et al.* (2005) derived their LBCs from global re-analysis data which also includes radiosonde data. Therefore, their smaller outer domain led to smaller deviations from radiosondes. This also highlights the importance of the choice of driving data.

The number of levels is increased, because the first part of setup B (domain B1 and B2) is one of the older configurations investigated in reclip:more. It is the first configuration which was used for one-year simulations (*Truhetz et al.*, 2005) and for the first climate simulation (period 1981–1990) for the Alpine region. The simulation results of domain B2 were used to develop empirical/statistical downscaling-methods for temperature and precipitation published in *Themeßl* (2005). Later in reclip:more the number of levels was decreased to 29 due to the higher demand of computational resources and because MM5's accuracy was not sacrificed (*Gobiet et al.*, 2006).

Setup B is summarised in Table 3.3. Note, in addition to the changed geometric setting the cumulus-parameterisation is turned off in the 5 km domains (B3a and B3b). All other parameters stay on their values defined in the control configuration.

3.2.2 Dynamic Initialisation with 1 km Grid Spacing

In setup C the two intermediate 1 +km grids (cf. Section 2.2.2) for the two study regions become two new model domains (domain C3a and C3b, cf. Figure 3.1b) where MM5 is actively operated. These grids are nested into MM5 the innermost domain of the control configuration and are driven by LBCs derived from domain A2. But in contrast to the usual operation of nested domains (e. g., Section 3.1), MM5 is newly initialised in domain C3a and C3b at every stored time-slice found in the output-files of domain A2. In addition, MM5 is iterated only several time-steps while the LBCs are kept constant, i. e., the LBCs are representing a steady state: any depending variable (φ) on the lateral boundaries remains on its value and its according time derivative ($\dot{\varphi}$) is set to zero. Hereby, the wind field is iteratively (i. e., *dynamically*) adopted to the orography. Originally, this procedure was developed in the beginning phase of NWP during the 1970s to generate more realistic initial conditions. It belongs to a special group of initialisation techniques known as *"dynamic initialisation"* (*Pielke*, 2002). *Žagar and Rakovec* (1999) re-named the method to *"dynamic adaptation"* and used it to generate highly resolved surface wind forecasts from coarser NWP data. However, the terminus

Table 3.3: Discretisations and parameterisations of MM5 setup B. The cumulus parameterisation is turned off in domain B3a and B3b. In domain B4a and B4b MM5 is not operated; these grids are only used for interpolation.

MM5 (version 3.7.4)		Discretisiation	Domain						Reference Atmosphere	
			B1	B2	B3a	B3b	B4a	B4b		
cumulus-scheme	Kain-Fritsch-2 shallow conv.	grid cells X I^{MM5}	50	82	40	43	145	141	top pressure p_t^{ref} [hPa]	100
PBL-scheme	ETA	grid cells Y J^{MM5}	50	58	40	37	85	121	sea-level press. p_{slp}^{ref} [hPa]	1000
moisture-scheme	Reisner-1	grid spacing [km]	45	15	5	5	1	1	sea-level temp. T_{slp}^{ref} [K]	275
radiation-scheme	RRTM	model levels K^{MM5}	42	42	42	42	29	29	lapse rate $\frac{dT^{ref}}{d(\ln p^{ref})}$ [K]	50
		time steps [s]	120	40	13.33	13.33	–	–		
		nest-type	one-way	one-way	one-way	one-way	–	–		

dynamic adaptation is broadly used in numerous scientific fields. Even in atmospheric sciences it is loaded by a different meaning: it is associated with changing discretisations during model integration (e. g. *Gopalakrishnan et al.*, 2002) and moving grids (e. g. *Tolman and Alves*, 2005). To avoid confusions, setup C described in this section is henceforth referred to as *"dynamic initialisation"*.

Assuming that steady-state LBCs are leading to steady states in the inner grid cells of the model, where every variable reaches a constant value in time, dynamic processes can be seen as a sequence of steady states. Hereby, local dynamic terrain-induced flow-effects are taken into account as long as they are resolved by the model grid (i. e., the 1 km grids of domains C3a and C3b). Since only a few model iterations are necessary to approximate a steady state the demand of the computational resources is significantly lower than a full model integration. A further reduction of the computational costs can be expected from more efficient model operation, because the time-slices associated with each steady state become independent from each other.

If the physical conservation principals (cf. Section 2.1) are fulfilled and the model represents a steady state, the Divergence Theorem of Gauss (*Holland et al.*, 1993)

$$\int_V (\nabla \cdot \vec{\varphi}) dV = \oint_A (\vec{\varphi} \cdot \vec{n}) dA \tag{3.1}$$

is valid for any depending vectorial variable ($\vec{\varphi}$) (V denotes the volume of the model domain and $\vec{n}$ the outer unit normal vector of the boundary surface A). Unfortunately, this is usually not the case, since LBCs originate from coarser resolutions excluding unresolved phenomena (cf. Section 2.1.1). Additional violations of the Divergence Theorem arise from sources and sinks of diabatic heating, radiative fluxes, and diffusion

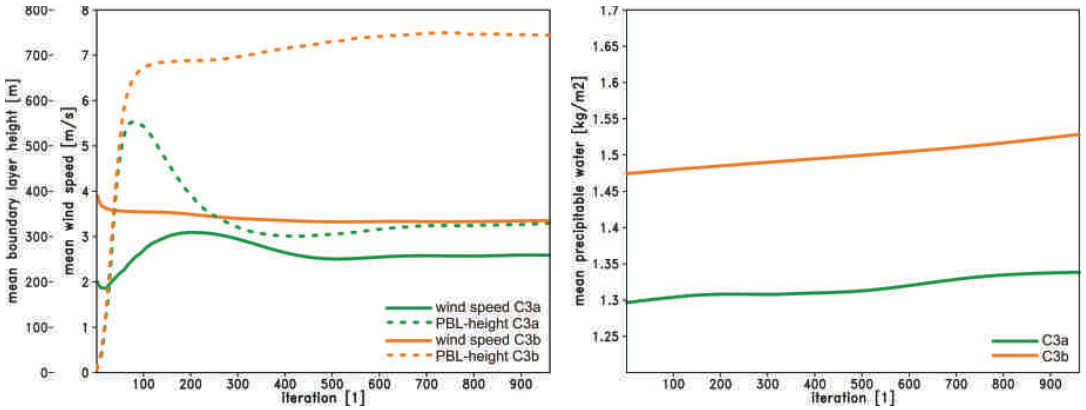

Figure 3.4: Evolution of selected variables in the Hohe Tauern region (domain C3a, green) and in the Vienna Basin (domain C3b, orange) during model iteration driven by steady-state LBCs. Both domains are initialised by results from domain A2 of the control configuration (cf. Section 3.1) referring to June 10, 1999, 10:00 UTC. The simulated domain-averaged quantities of (a) wind speed 10 m a.g.l. (solid line), height of the PBL (dashed line), and (b) precipitable water are shown for each iteration-step.

(cf. Section 2.1) which may be out of equilibrium on a higher resolved grid: for instance, the Alpine pumping (cf. Section 1.1.2) generates a thermally driven diurnal cycle of in-flows ($\oint_A (\vec{v}\cdot\vec{n})dA < 0$) during daytime and out-flows ($\oint_A (\vec{v}\cdot\vec{n})dA > 0$) during nighttime if the boundary surface cuts the flows. However, reducing the number of grid cells and laying the lateral boundaries through flat terrain with homogeneous topography helps to reduce these inconsistencies (cf. Section 3.2.2). To guarantee numerical stability the inconsistencies are additionally damped in a *"nudging"* zone extending up to 7 grid cells from the lateral boundaries (*Dudhia et al.*, 2005).

An impression, how MM5 in dynamic initialisation mode violates the steady-state concept in domain C3a and C3b can be taken from Figure 3.4. The figure shows the evolution of selected variables with respect to MM5's iteration-step (representing a time-step of 3 s) during weakly convective conditions late in the morning on June 10, 1999. On that day the Eastern Alps were influenced by a trough at higher levels over Western Europe which enforced higher-level flows from southwest (*ZAMG*, 1999). The simulated wind speeds and PBL-heights show different spin-up phases in the two study regions with different amplitudes and durations (cf. Figure 3.4a), but they seem to converge to some constant levels indicating the existence of steady-states in the model. During this spin-up the initial state which is derived from domain A2 via interpolation (cf. Section 2.2.2) is iteratively adjusted and the flow-effects of the higher resolved topography are captured. However, the precipitable water (i. e., the vertical integral of humidity mixing ratio weighted by air pressure) increases continuously (cf. Figure 3.4b). Therefore, air moisture is obviously advected through the LBCs and accumulated within the model domains in both study regions ($\oint_A (\vec{v}\cdot\vec{n})dA < 0$) violating the Divergence

Table 3.4: Discretisations and parameterisations of MM5 setup C. It is based on setup A (cf. Section 3.1), but in contrast MM5 is actively operated on the intermediate grids (1 km × 1 km grid spacing) covering the two study regions (domain C3a and C3b). The cumulus-parameterisation is turned off in domain C3a and C3b.

MM5 (version 3.7.4)		Discretisiation	Domain				Reference Atmosphere	
			A1	A2	C3a	C3c		
cumulus-scheme	Kain-Fritsch-2 shallow conv.	grid cells X I^{MM5}	124	109	145	141	top pressure p_t^{ref} [hPa]	100
PBL-scheme	ETA	grid cells Y J^{MM5}	100	79	85	121	sea-level press. p_{slp}^{ref} [hPa]	1000
moisture-scheme	Reisner-1	grid spacing [km]	30	10	1	1	sea-level temp. T_{slp}^{ref} [K]	275
radiation-scheme	RRTM	model levels K^{MM5}	29	29	29	29	lapse rate $\frac{dT^{ref}}{d(\ln p^{ref})}$ [K]	50
		time steps [s]	90	30	3	3		
		iterations	–	–	300	300		
		nest-type	one-way	one-way	one-way	one-way		

Theorem. Since, there is no clearly defined steady-state in the model and hence an unique abort criterion for the iterations concerning all variables can hardly be found, and in order to keep the demand of computational resources on a maintainable level the number of model iterations is limited 300. After the first 300 iterations it is assumed that at least the air flow has completed most of its spin-up phase in most parts of the model domains.

In spite of noticeable uncertainties about the applicability of dynamic initialisation, it is assumed to generate more realistic data fields on the intermediate 1 km grid than the original interpolation-based re-gridding step defined in Section 2.2.2. The parameters of setup C are summarised in Table 3.4.

3.3 Improvements of the Diagnostic Model

In order to focus on the most promising modifications (apart from the divergence minimisation scheme) to overcome CALMET's weaknesses their potential of improvement are discussed. By means of the relative uncertainty arising from each weakness this potential is quantified and its propagation through the model is estimated. For convenience, the superscript "CAL" is omitted in this section.

There are three central parameterisations in CALMET affecting the downscaled wind fields:

- the vertical gradient of the vertical velocity component (dW/dZ) (in CALMET's

terrain-following coordinate system) based on the parameterisation for the initial vertical velocity (w_0) via equations (2.24) and (2.25), given at the lowest model level ($k = 1$) by

$$\frac{dW_{0,(k=1)}}{dZ}\left(Z_{(k=1)}\right) = -\alpha\left(\vec{V}_{0,(k=1)} \cdot \nabla h_t\right) \frac{\sqrt{\frac{g}{\theta_0}\frac{d\theta_0}{dZ}}\exp\left(-\sqrt{\frac{g}{\theta_0}\frac{d\theta_0}{dZ}}\frac{Z_{(k=1)}}{\overline{V}_0}\right)}{\overline{V}_0} \ , \quad (3.2)$$

- the parameterisation of slope-flow velocities (S_{sf}) from

$$S_{sf} = \sqrt[3]{Q_h g r \frac{\sin\alpha_{sl}}{\rho c_p T(C_D + e_c)}(1 - e^{-r/L_e})} \quad \text{with} \quad L_e = \frac{d_{sf}}{C_D + e_c} \quad (3.3)$$

(cf. equation (2.28)), and

- the calculation of the local Froude-number (F_r) based on the horizontal components of the divergence-free wind field (U_2, V_2), given by

$$Fr = \frac{\sqrt{(U_2)^2 + (V_2)^2}}{\sqrt{\frac{g}{\theta_0}\frac{d\theta_0}{dZ}}\Delta h_t} \quad \text{with} \quad \Delta h_t = h_{max} - Z_{(k=1)} \ , \quad (3.4)$$

which is used as a criterion to distinguish between flow-over and flow-around patterns (cf. equation (2.36) and (2.25)).

The uncertainties of these parameters based on uncertainties of their depending variables can conceptually be estimated by partial differentiation: Let $A = A(\varphi)$ be one of the parameters calculated as a function of its depending variable (φ). The uncertainty of A (referred to as $\Delta(A)_\varphi$) is then given by its partial derivative $\partial A(\varphi)/\partial\varphi$ times the uncertainty of φ (referred to as $\Delta\varphi$):

$$\Delta(A)_\varphi = \frac{\partial A(\varphi)}{\partial\varphi}\Delta\varphi \ . \quad (3.5)$$

Hence, the relative uncertainty of A (defined as $\Delta_r(A)_\varphi = \Delta(A)_\varphi/A$) can be expressed in terms of the relative uncertainty of φ (defined as $\Delta_r\varphi = \Delta\varphi/\varphi$) by

$$\Delta_r(A)_\varphi = \underbrace{\left(\frac{\varphi}{A(\varphi)}\frac{\partial A(\varphi)}{\partial\varphi}\right)}_{p}\Delta_r\varphi \ , \quad (3.6)$$

defining a proportionality factor (or sensitivity coefficient) (p) between the relative uncertainties ($\Delta_r(A)_\varphi$ and $\Delta_r\varphi$). If A is a function of multiple variables ($A = A(\varphi_1, \varphi_2, \dots)$), their proportionality factors (p_1, p_2, $\dots$) give the influences of the uncertainty of each variable ($\Delta_r\varphi_1$, $\Delta_r\varphi_2$, $\dots$) on the total uncertainty of A ($\Delta_r(A)$):

$$\Delta_r(A) = \underbrace{\left(\frac{\varphi_1}{A}\frac{\partial A}{\partial \varphi_1}\right)}_{p_1}\Delta_r\varphi_1 + \underbrace{\left(\frac{\varphi_2}{A}\frac{\partial A}{\partial \varphi_2}\right)}_{p_2}\Delta_r\varphi_2 + \dots \ . \tag{3.7}$$

A ranking of the variables to express their importance for the calculation of A may be found by means of the magnitudes of their proportionality factors. If the magnitudes are >1 (<1), the uncertainties are amplified (damped) and hence promising (negligible) improvements are indicated.

Table 3.5 shows the formulae and the expected ranges of numeric values of the proportionality factors (sensitivity coefficients) of CALMET's major parameterisations for the lowest model level ($k = 1$) based on the control configuration (cf. Section 3.1), CALMET's default values (cf. Section 2.2.2), the International Standard Atmosphere (ISA) (*ISO*, 1972), and an observed strongly stable PBL during inversion-breakup (see below). It reflects the vital importance of the initialisation wind field (represented by $\vec{V}_{0,(k=1)}$): uncertainties of $\vec{V}_{0,(k=1)}$ are transmitted without damping, independently from atmospheric conditions. The same is valid for the user-defined damping factor α, and an intermediate (after the application of the divergence minimisation scheme and the slope-flow parameterisation) wind field ($|\vec{V}_2|$) for the Froude-number calculation. Uncertainties of the vertical-averaged initialisation wind field ($\overline{V}_0$) have the similar effects as $\vec{V}_{0,(k=1)}$, however, their magnitudes depend on atmospheric conditions: in the weakly stable ISA ($d\theta_0/dZ \approx 0.0033$ K/m; $N \approx 0.01$ s^{-1}) they are most strongly pronounced, but they have an inverse sign and therefore the uncertainties from $\vec{V}_{0,(k=1)}$ are partly compensated. The magnitudes of the sensitivity coefficients for temperature and its lapse rate are smaller than 1 in most cases: even for the ISA they are limited to 0.5 for CALMET's lowest full-k-level (20 m a.g.l.) (if $\overline{V}_0$ is assumed to be 10 m/s). In exceptional cases under strongly stable conditions with very low wind speeds, the magnitudes of these factors may vanish: e. g., *Whiteman et al.* (2004), who observed a breakup of a strong nighttime inversion in a very narrow Alpine doline, the Grünloch in the Eastern Alps, Austria, during the 3 June 2002, report $d\theta_0/dZ \approx 0.12$ K/m. With their observed mean wind speed of $\sim$0.5 m/s N becomes $\sim$0.052 s^{-1} leading to proportionality factors $\approx$0.0. However, due to the iterative divergence-minimisation scheme (cf. equations (2.26) and (2.27)) the uncertainties of dW_0/dZ do not directly affect the horizontal wind speeds. In general, analytical expressions for the propagation of such uncertainties throughout iterative algorithms are difficult to derive, thus Monte-Carlo methods are usually applied to estimate the overall effect of uncertainties on the simulation results. Since an impression of the importance of the vertical wind component's uncertainties may be taken from Table 3.5 any further investigation of the error propagation by means of Monte-Carlo methods is skipped.

The slope-flow calculation is most sensitive against the distance from the crest (r) (the proportionality factor lies between 1/3 and 2/3, depending on the thickness of the slope-flow and the drag coefficient) and it is lesser sensitive against uncertainties of the sensible heat flux (Q_h), the air density (ρ), and the air temperature (T), since these uncertainties are damped by a factor of 1/3. Since thermal driven slope-flows usually reach velocities $\sim$2.5 m/s (cf. Section 1.1.3), modelled wind fields with low velocities are more affected by improperly simulated slope-flows.

Table 3.5: Sensitivity of selected parameterisations of CALMET (at the lowest model level) expressed in terms of sensitivity coefficients of their variables. Numeric data for the sensitivity coefficients calculated from CALMET's default values, the control configuration *v0* (cf. Section 3.1), the weakly stable International Standard Atmosphere, and a strongly stable PBL during inversion-breakup (see text) are shown. Note, the gradient of the vertical velocity component is calculated prior to the application of the iterative divergence-minimisation scheme (cf. Section 2.2.2).

Parameterisation	**Variable**	**Sensitivity Coefficient**	**Numeric Value [1]**
gradient of the	$\vec{V}_{0,(k=1)}$	1	1.0
vertical velocity	α	1	1.0
component	$\overline{V}_0$	$\frac{Z}{\overline{V}_0}N - 1$	$-1.0, \approx 0.0$
$(dW_{0,(k=1)}/dZ)$	T	$\frac{1}{2}\left(\frac{Z}{\overline{V}_0}N - 1\right)$	$-0.5, \approx 0.0$
	$d\theta_0/dZ$	$\frac{1}{2}\left(1 - \frac{Z}{\overline{V}_0}N\right)$	$0.5, \approx 0.0$
velocity of	Q_h	$1/3$	$1/3$
slope-flow	ρ	$-1/3$	$-1/3$
(S_{sf})	T	$-1/3$	$-1/3$
	d_{sf}	$-\frac{(C_D+e_c)r}{3d_{sf}\left(\exp(\frac{(C_D+e_c)r}{d_{sf}})-1\right)}$	$0.0, \approx -0.025$
	r	$\frac{1}{3}\left[1 + \frac{(C_D+e_c)r}{3d_{sf}\left(\exp(\frac{(C_D+e_c)r}{d_{sf}})-1\right)}\right]$	$1/3, 2/3$
	C_D	$\frac{1}{3}C_D\left[\frac{r}{d_{sf}\left(\exp(\frac{(C_D+e_c)r}{d_{sf}})-1\right)} - \frac{1}{C_D+e_c}\right]$	$0.0, -1/3$
	e_c	$\frac{1}{3}e_c\left[\frac{r}{d_{sf}\left(\exp(\frac{(C_D+e_c)r}{d_{sf}})-1\right)} - \frac{1}{C_D+e_c}\right]$	$0.0, -1/3$
Froude-number	$\lvert\vec{V}_2\rvert$	1	1
(F_r)	T	$\lvert\vec{V}_2\rvert/(2T)$	$0.0, \approx 0.1$
	$d\theta_0/dZ$	$-1/2$	$-1/2$

The Froude-number calculation is most sensitive against flow velocity and temperature lapse rate. However, the impact on the modelled wind fields is expected to be small in general, because the application of the Froude-number-criterion to distinguish between flow-over and flow-around patterns is limited to stable conditions ($d\theta_0/dZ > 0$) and it does only affect the modelled wind direction.

As mentioned at the beginning of Chapter 3, one of CALMET's weaknesses is the potential temperature lapse rate ($d\theta_0/dZ$) which is kept constant throughout the model domain. This seems to neglect any spatial distribution of the stability of the PBL. However, in CALMET uncertainties of $d\theta_0/dZ$ only affect the calculation of dW/dZ and F_r. Since the uncertainties of $d\theta_0/dZ$ are damped by a factor of at most 0.5 (cf. Table 3.5) and may have opposing signs, spatially varying temperature lapse rates are expected to have small impacts on the simulated wind fields. Larger impacts are expected from the air density (ρ) which is currently fixed at 1.225 kg/m^3 during slope-flow calculation and hence does not take account for orographic effects: although the uncertainty of ρ is damped by -1/3 (cf. Table 3.5), ρ is permanently overestimated. Therefore, the velocities of the slope flows are consequently underestimated. Based on the ISA and the model orography, the relative uncertainty of ρ varies between 5 % and 30 % in the Hohe Tauern region leading to underestimations of the slope flows between 1.7 % and 10 % (5.4 % on average). In the Vienna Basin these effects are smaller than 1 % in average due to the lower surface altitudes (cf. Section 3.1). Because of the systematical influence of the improper air density, its calculation is adjusted in Section 3.3.1 defining the first improved version of CALMET, which is selected for further investigations.

The sensible heat flux (Q_h) is also only used for the slope-flow parameterisation. Analogously to the air density the uncertainty of Q_h is damped by a factor of 1/3 (cf. Table 3.5). However, since the calculation of Q_h is based on externally given constants and on a cloud-cover parameterisation which is questionable for meteorological simulations on micro-scale, the magnitude of Q_h's uncertainties may be large and induce significant random errors in the modelled wind fields. Therefore, the calculation of Q_h is re-considered in Section 3.3.2, which defines the second improved version of CALMET.

Since the initialisation fields show the highest proportionality factors (cf. Table 3.5), the third improvement of CALMET is related to an re-considered generation of both, the initial wind fields and the temperature fields. Due to the modifications, described in detail in Section 3.3.3, this improvement enables to fundamentally reduce uncertainties arising from neglected local topographic effects and opens up a broad spectrum of possible future improvements.

3.3.1 Re-Considered Calculation of the Air Density

The re-considered calculation of the air density defines the first CALMET variant, referred to as *v1*. It consists of a simple approximation based on the ideal gas law for dry air to take account for the main orographic effect, i. e., the reduction of pressure and temperature due to an increasing altitude. By calculating the air density from temperature (T^{1km}) and pressure (p^{1km}) on the intermediate 1 km grid of MM5 (cf. Section 2.2.2) the actual weather conditions are taken into account as well. This

orographically affected instantaneous air density (ρ^{1km}) is defined by

$$\rho^{1km} = p^{1km} \frac{R_d}{T^{1km}} \ , \tag{3.8}$$

with the gas constant for dry air ($R_d = 287.04$ J/kgK). It is used to substitute ρ in the slope-flow parameterisation (equation (2.28)). Since the slope-flows are expected to be quite shallow (the spatially varying depth of the flows are limited to 5 % of the drop of the altitude from the crest), the air density of the flow is simply approximated by the air density at 2 m above model surface (any vertical averaging throughout the slope-flow depth is neglected). Thereby, T^{1km} and p^{1km} are extrapolated prior to the application of equation (3.8). The pressure at 2 m is derived from the lowest two σ-levels of MM5 ($Z^{1km}_{(K^{MM5})}$ and $Z^{1km}_{(K^{MM5}-1)}$) via an logarithmic extrapolation:

$$p^{1km}_{(2m)} = p^{1km}_{(K^{MM5})} \exp\left(-\frac{2 - Z^{1km}_{(K^{MM5})}}{Z^{1km}_{(K^{MM5}-1)} - Z^{1km}_{(K^{MM5})}} \ln\left(\frac{p^{1km}_{(K^{MM5})}}{p^{1km}_{(K^{MM5}-1)}} \right) \right) . \tag{3.9}$$

The temperature at 2 m is derived following the same concept as it is used to generate CALMET's initialisation fields from the intermediate 1 km grid (cf. Section 2.2.2): i. e., the dry-adiabatic lapse rate is used during daytime, the parameterisation for nocturnal inversion from *Stull* (1983) is used during nighttime. After $\rho^{1km}_{(2m)}$ is calculated from $p^{1km}_{(2m)}$ and $T^{1km}_{(2m)}$ it is interpolated horizontally via an inverse-distance method onto CALMET's highly resolved grid.

The re-considered calculation of the air density is embedded into the vertical interpolation routines which are performed during the generation of CALMET's initialisation fields.

3.3.2 Re-Considered Calculation of the Sensible Heat Flux

The re-considered calculation of the sensible heat flux defines the second CALMET variant, referred to as *v2*. Hereby, both original approaches from *Holtslag and van Ulden* (1983), the flux-calculation based on the net-radiation and the Bowen-ratio during daytime from equation (2.29) and the calculation based on the flux-temperature during nighttime from equation (2.32), are substituted by a unified calculation based on short- and long-wave radiation and heat fluxes from MM5.

Looking into details, the calculation of the sensible heat flux on CALMET's grid (Q_h) is substituted by solving the energy budget equation at the surface with respect to Q_h:

$$Q_h = Q^* - Q_l - Q_g \ , \tag{3.10}$$

with Q^* as net-radiation, Q_l as latent heat flux, and Q_g as ground heat flux, which is the same starting point as in the original (daytime) approach. However, the original parameterisations for Q^*, Q_l, and Q_g are now substituted by quantities from MM5 interpolated onto the intermediate 1 km grid with respect to some local influence. Q^* (on the CALMET grid) is calculated from MM5's incoming short-wave radiation (direct plus diffuse) (Q^{1km}_{SW}), incoming and outgoing long-wave radiation ($Q^{1km}_{LW} \downarrow$ and $Q^{1km}_{LW} \uparrow$, respectively) (interpolated onto the CALMET grid via the same inverse-distance method

as mentioned in Section 2.2.2), and CALMET's surface albedo (A^{CAL}) from equation (2.35):

$$Q^* = \left(1 - A^{CAL}\right) Q_{SW}^{1km} + Q_{LW}^{1km} \downarrow - Q_{LW}^{1km} \uparrow \ . \tag{3.11}$$

Since MM5 does not comprise the outgoing long-wave radiation in its output-files, $Q_{LW}^{1km} \uparrow$ is calculated from a simple parameterisation described in *Pielke* (2002) based on the incoming long-wave radiation ($Q_{LW}^{1km} \downarrow$), the ground temperature (T_g^{1km}), the surface emissivity (ϵ^{1km}), and the Stefan-Boltzmann constant (σ):

$$Q_{LW}^{1km} \uparrow = \epsilon^{1km} \sigma \left(T_g^{1km}\right)^4 + \left(1 - \epsilon^{1km}\right) Q_{LW}^{1km} \downarrow \ . \tag{3.12}$$

Hereby, ϵ^{1km} is taken from an external table that coarsely reflects the behaviour of an annual cycle by taking account for winter and summer season. This table, as it is implemented in the current version of MM5 (version 3.7.4) (*Dudhia et al.*, 2005), is shown in Table 3.6. It shows the dependency of the surface emissivity from the earth's surface cover defined by a global land-use classification-scheme from the USGS (*Anderson et al.*, 1976)

In addition to the seasonal and land-use-depending variability, ϵ^{1km} is modified by snow-cover following MM5's internal rule: if the simulated water equivalent of snow is larger than 0.0, ϵ^{1km} is set to 0.9, otherwise it remains on its seasonal-depending (snow-free) initial value.

Note in the case CALMET is driven by the dynamic-initialisation-variant of MM5 (domains C3a or C3b with 1 km grid spacing) (cf. Section 3.2.2) Q_{SW}^{1km}, $Q_{LW}^{1km} \downarrow$, and T_g^{1km} are interpolated from domain A2 (10 km grid spacing), because MM5 is not fully operated in domains C3a and C3b and the effect of MM5's hourly re-initialisation on the quality of these variables is not well known due to the general violation of the steady-state-concept (cf. Section 3.2.2).

3.3.3 Altered Interpolation Scheme for Initialisation Fields

As described in Section 2.2.2 the intermediate fields on the 1 km grid are firstly vertically interpolated from their terrain-following σ-levels of MM5 to CALMET's terrain-following height-above-ground-levels. Secondly, they are horizontally interpolated to bridge the gap between the 1 km grid and the higher resolved CALMET grid. This sequence is reversed as described in this chapter, which defines the third CALMET variant, referred to as *v3*.

In this new interpolation scheme the fields from the intermediate 1 km grid are firstly interpolated horizontally. Thereby, horizontal wind speed, wind direction, air temperature, and pressure are interpolated using an inverse-distance method:

$$\varphi_0^{CAL} = \frac{\sum_{i=1}^{4} \frac{1}{r_{1km,i}^{CAL}} \varphi_i^{1km}}{\sum_{j=1}^{4} \frac{1}{r_{1km,j}^{CAL}}} \ , \tag{3.13}$$

where φ_0^{CAL} refers to each variable of the initialisation fields on each CALMET grid

Table 3.6: MM5 surface emissivity (ϵ^{1km}) in terms of a global land-use classification scheme from the USGS (*Anderson et al.*, 1976) with respect to summer (April 15 – October 13) and winter (October 14 – April 14) season. From (*Dudhia et al.*, 2005).

USGS category	ϵ^{1km} [m] summer	ϵ^{1km} [m] winter
urban and built-up land	0.880	0.880
dry-land crop-land and pasture	0.985	0.920
Irrigated Crop-land and Pasture	0.985	0.930
Mixed Dry-land/Irrigated Crop-land and Pasture	0.985	0.920
Crop-land/Grassland Mosaic	0.980	0.920
Crop-land/Woodland Mosaic	0.985	0.930
Grassland	0.960	0.920
Shrub-land	0.930	0.930
Mixed Shrub-land/Grassland	0.950	0.930
Savanna	0.920	0.920
Deciduous Broad-leaf Forest	0.930	0.930
Deciduous Needle-leaf Forest	0.940	0.930
Evergreen Broad leaf Forest	0.950	0.950
Evergreen Needle-leaf Forest	0.950	0.950
Mixed Forest	0.970	0.930
Water Bodies	0.980	0.980
Herbaceous Wetland	0.950	0.950
Wooded Wetland	0.950	0.950
Barren or Sparsely Vegetated	0.900	0.900
Herbaceous Tundra	0.920	0.920
Wooded Tundra	0.930	0.930
Mixed Tundra	0.920	0.920
Bare Ground tundra	0.900	0.900
Snow or Ice	0.950	0.950

cell surrounded by its four nearest-neighbouring values ($\varphi^{1km}_{1,\ldots,4}$) of the 1 km grid in distances of $r^{CAL}_{1km,1,\ldots,4}$. The wind direction (ϕ^{1km}) is interpolated in the same manner, however it is modified to take account for its cyclicality (*Fisher*, 1995):

$$\phi_0^{CAL} = \arctan\left(\frac{\sum_{i=1}^{4} \frac{1}{r^{CAL}_{1km,i}} \sin(\phi_i^{1km})}{\sum_{i=1}^{4} \frac{1}{r^{CAL}_{1km,i}} \cos(\phi_i^{1km})}\right) . \tag{3.14}$$

In addition, the altitudes of the σ-levels, the PBL, and the model surface of the 1 km grid are interpolated by equation (3.13) as well. By means of these variables and the shift from height above ground to altitude topographic effects due to CALMET's highly resolved grid may be taken into account more properly and additional meteorological elements and their temporal variability from MM5 may be introduced. Based on differences in altitude between the CALMET levels and the σ-levels the vertical interpolation is performed in the second step. Temperature, wind speed, and wind direction are inter- and extrapolated in the same way as described in Section 2.2.2: i. e., linear interpolations in altitude for temperature and wind direction between adjacent σ-levels, the cubic-spline interpolation for wind speed, and the daytime/nighttime-depending extrapolation for temperature on altitudes lower than the lowest σ-level. The extrapolation of the wind speed follows the original logarithmic-profile-concept (cf. Section 2.2.2) in an improved manner. It differs in two ways from the original formulae (equation (2.20)): a) CALMET's surface roughness lengths (z_0^{CAL}) are used instead of the roughness lengths on the 1 km grid (z_0^{1km}) and b) the extrapolation is performed on all CALMET levels with a lower altitude than the turbulent surface-layer of the PBL (cf. Figure 1.2). This has the advantage to partly correct the misleading representation of the PBL-height due to the highly resolved orography (cf. Figure 2.2) and to capture the PBL's temporal variability based on the MM5 simulation. Following *Pielke* (2002) the required height of the surface-layer is estimated with 1/10 of the PBL-height. To restrict the effect of the altered interpolation scheme purely on the initialisation fields for wind speed and direction and to achieve conformity with the control-configuration (v0), the vertical temperature lapse rate is averaged over the CALMET grid after initialisation.

4 Evaluation of the Wind Downscaling Method and Its Variants

In order to evaluate the dynamic-diagnostic wind downscaling method (cf. Section 2.2) and its versions defined in Chapter 3 they are driven by LBCs derived from the global re-analysis dataset ERA-40 (*Uppala et al.*, 2004). ERA-40 is the output of a global dynamic model of the ECMWF where worldwide ground-based, air-borne, and remotely sensed observational data have been assimilated via variational algorithms (cf. Section 2.1) during model integration. Due to the high number of assimilated observations ERA-40 is supposed to be the most reliable re-analysis data representing the atmospheric states throughout the period 1957 to 2002.

Based on one-year simulations in the Hohe Tauern region and in the Vienna Basin the downscaling errors and their characteristics are derived by means of model-observation comparisons. This allows to judge each single method improvement step by step and provides insights into the simulation processes and their strengths and weaknesses. In the face of climate change effects on near surface winds the long-term behaviour of the downscaling method and its possible impacts on the climate change signal are investigated by means of a 10-year simulation in the Vienna Basin.

A description of the experimental setup including the concept of evaluation as well as a summary of the statistical measures used to analyse the model errors can be found in the following section. The used observation data, sources of their uncertainties, and the applied method to reduce the number of invalid individual data records in accordance to the observation accuracy are described in Section 4.2. Section 4.3 provides the evaluation results by reviewing the observed model errors in relation to the different downscaling variants. Section 4.4 introduces a method for error correction, and discusses the impact of model errors on climate change effects. A summary of the most important evaluation results, strengths and remaining weaknesses of the wind downscaling method and its variants, conclusions about the added value due to the methods' improvements, a discussion about the methods' applicability with respect to the complexity of the study region's topography, and the most promising combination of the dynamic and diagnostic models for future work can be found in Section 4.5.

4.1 Experimental Setup and Evaluation Strategy

The experimental setup consists of the control configuration Av0 and its variants concerning MM5 (setup B and C) and CALMET (variant v1, v2, and v3) (cf. Figure 3.1 and Chapter 3), which are applied on ERA-40 to generate highly resolved wind fields

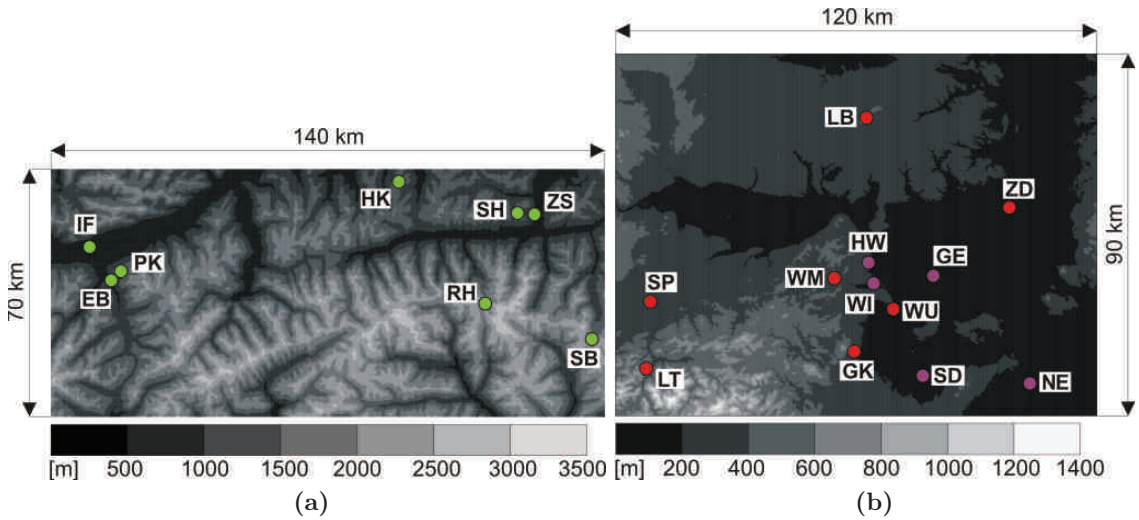

Figure 4.1: Model orography (200 m × 200 m grid spacing) and observation stations (coloured circles; cf. Table 4.1) in the (a) Hohe Tauern region and in the (b) Vienna Basin. The green marked stations are used to evaluate one-year simulations (period: Jan 1 to Dec 31, 1999), the magenta stations are used for the climate simulation (period Jan 1, 1981, to Dec 31, 1990).

(200 m × 200 m grid spacing). These wind fields (representing grid-cell-averaged instantaneous model values, cf. Section 2.2) are compared to observed wind speeds and directions from surface observation stations provided by the Austrian meteorological service, the Central Institute for Meteorology and Geodynamics (ZAMG), and the Institute for Meteorology and Geophysics, University of Innbruck, Austria, (cf. Figure 4.1 and Table 4.1) in order to obtain the error of the wind downscaling method. Thereby, the 3-dimensional modelled air flows are interpolated to the points of the anemometers of the stations via bi-linear (horizontal) and cubic-spline (vertical) interpolation (cf. Section 2.2).

Based on statistical analyses of the downscaling-error the most promising combination of MM5-setups and CALMET-variants is acquired. However, due to the lack of computational resources the simulation period and the number of simulations are limited. In order to capture a broad range of the spectrum of possible weather-phenomena and hence to test the downscaling-methods under numerous different meteorological conditions the simulation periods cover the hole year 1999 (Jan 1, 1999, 00:00 UTC to Dec 31, 1999, 23:00 UTC). As a compromise between the technically available disk-space and the number of simulated weather-phenomena the storage-interval is set to 1 hour. The number of simulations is reduced to 6 by identifying the most promising MM5-setup at first (and keeping CALMET in its control variant v0) and testing the different CALMET-variants driven by this MM5-setup to retrieve the most promising CALMET-variant. As a result the approximately best MM5/CALMET-combination is found.

Furthermore, a climate simulation (period Jan 1, 1981 00:00 UTC to Dec 31, 1990,

Table 4.1: Meta-information of the observation stations in the Hohe Tauern region and the Vienna Basin used to evaluate one-year simulations (period Jan 1 to Dec 31, 1999) and a climate simulation (period Jan 1, 1981, to Dec 31, 1990). Name of station, internal abbreviation (Abbr.), latitude (φ), longitude (λ), surface altitude (Alt.), anemometer height a.g.l. (h), and the World Meteorological Organisation (WMO) identification number are listed (cf. Figure 4.1).

Name of station	Abbr.	φ [°]	λ [°]	Alt. [m]	h [m]	WMO
Hohe Tauern region – one year simulation (period: Jan 1, 1999, 00:00 UTC to Dec 31, 1999, 23:00 UTC)						
Innsbruck-Flugplatz	IF	47.2575	11.3536	579.0	32.0	11120
Patscherkofel	PK	47.2097	11.4617	2247.0	7.0	11126
Hahnenkamm-Ehrenbachhöhe	HK	47.4192	12.3619	1790.0	10.0	11135
Rudolfshütte	RH	47.1339	12.6256	2304.0	10.0	11138
Zell am See	ZS	47.3267	12.7950	766.0	12.0	11144
Schmittenhöhe	SH	47.3297	12.7367	1973.0	12.0	11340
Sonnblick	SB	47.0544	12.9581	3105.0	14.0	11343
Ellbögen	EB	47.1875	11.4294	1080.0	10.0	–
Vienna Basin – one year simulation (period: Jan 1, 1999, 00:00 UTC to Dec 31, 1999, 23:00 UTC)						
Großenzersdorf	GE	48.1994	16.5619	155.0	10.0	11037
Gumpoldskirchen	GK	48.0408	16.2828	218.0	10.0	11082
Leiser Berge	LB	48.5603	16.3719	457.0	25.0	11083
Lilienfeld/Tarschberg	LT	48.0167	15.5833	681.0	10.0	11078
Neusiedl am See	NE	47.9425	16.8578	135.0	18.0	11194
St. Pölten	SP	48.1803	15.6111	285.0	10.0	11028
Wien-Hohe-Warte	HW	48.2486	16.3564	203.0	35.0	11035
Wien-Unterlaa	WU	48.1275	16.4228	200.0	15.0	11040
Zwerndorf	ZD	48.3378	16.8322	146.0	10.0	11085
Vienna Basin – climate simulation (period: Jan 1, 1981, 00:00 UTC to Dec 31, 1990, 23:00 UTC)						
Großenzersdorf	GE	48.1994	16.5619	155.0	10.0	11037
Neusiedl am See	NE	47.9425	16.8578	135.0	18.0	11194
Seibersdorf	SD	47.9767	16.5075	185.0	15.0	11387
Wien-Innere-Stadt	WI	48.1194	16.3672	171.0	52.0	11034
Wien-Hohe-Warte	HW	48.2486	16.3564	203.0	35.0	11035

23:00 UTC) is conducted with the control configuration Av0 for the Vienna Basin and evaluated by means of surface observation stations (cf. Figure 4.1) in order to estimate the long-term behaviour of error statistics, to provide basic information for finding a proper error correction method, and to obtain general information about the impact of the downscaling-error on a climate change signal calculated by the presented wind downscaling method.

Since the major objective of the downscaling method focuses on the generation of wind climatologies a set of (time-independent) statistics neglecting any temporal correlation defines the fundamental basis of the evaluation. This set consists of biases ($\overline{V}_{bias}$, $\overline{\phi}_{bias}$) and frequency distributions for horizontal wind speed and direction (cf. Table 4.2). For the sake of completeness some temporal-correlated (time-dependent) statistics are

Table 4.2: Evaluation statistics for wind vectors $\vec{V}$ based either on horizontal wind components (u,v) or on wind speed ($V = |\vec{V}|$) and direction (ϕ). The statistics are calculated for modelled (index m) and observed (index o) data. Direction-related statistics are adopted from *Fisher* (1995).

Statistic	Formulae
Basic definitions	
Difference (error) of wind speed	$V_d = V_m - V_o$
Difference (error) of wind direction	$\phi_d = \tan^{-1}\left(\frac{\sin(\phi_m-\phi_o)}{\cos(\phi_m-\phi_o)}\right)$
Time-independent statistics	
Mean wind speed	$\overline{V} = \frac{1}{N}\sum_{i=1}^{N} V_i$
Mean wind direction	$\overline{\phi} = \tan^{-1}\left(\frac{\sum_{i=1}^{N}\sin\phi_i}{\sum_{i=1}^{N}\cos\phi_i}\right)$
Standard deviation of wind speed	$s_V = \sqrt{\frac{1}{N-1}\sum_{i=1}^{N}(V_i-\overline{V})^2}$
Standard deviation of wind direction	$s_\phi = \sqrt{-2\ln\left(\frac{1}{N}\sqrt{\left(\sum_{i=1}^{N}\sin\phi_i\right)^2+\left(\sum_{i=1}^{N}\cos\phi_i\right)^2}\right)}$
Standard deviation of wind vector	$s_{\vec{V}} = \sqrt{s_u^2+s_v^2}$ s_u, s_v standard deviations of u and v
Normalised standard deviation of wind vector	$s_{\vec{V},n} = \frac{s_{\vec{V},m}}{s_{\vec{V},o}}$
Mean difference (Bias) of wind speed	$\overline{V}_{bias} = \overline{V}_m - \overline{V}_o = \overline{V}_d$
Difference (Bias) of mean wind direction	$\overline{\phi}_{bias} = \tan^{-1}\left(\frac{\sin(\overline{\phi}_m-\overline{\phi}_o)}{\cos(\overline{\phi}_m-\overline{\phi}_o)}\right)$
Mean of directional differences	$\overline{\phi}_d = \tan^{-1}\left(\frac{\sum_{i=1}^{N}\sin\phi_{d,i}}{\sum_{i=1}^{N}\cos\phi_{d,i}}\right) \neq \overline{\phi}_{bias}$
Time-dependent statistics	
Pearson's correlation coefficient for wind speed	$r_V = \frac{\frac{1}{N-1}\sum_{i=1}^{N}(V_{m,i}-\overline{V}_m)(V_{o,i}-\overline{V}_o)}{s_{V,m}s_{V,o}}$
Correlation coefficient for wind vector	$r_{\vec{V}} = \frac{\frac{1}{N-1}\sum_{i=1}^{N}(u_{m,i}-\overline{u}_m)(u_{o,i}-\overline{u}_o)+(v_{m,i}-\overline{v}_m)(v_{o,i}-\overline{v}_o)}{s_{\vec{V},m}s_{\vec{V},o}}$
Root mean square error for wind vector	$\vec{V}_{rmse} = \sqrt{\frac{1}{N}\sum_{i=1}^{N}(u_{m,i}-u_{o,i})^2+(v_{m,i}-v_{o,i})^2}$
Standard deviation of wind speed differences	$s_{V,d} = \sqrt{\frac{1}{N-1}\sum_{i=1}^{N}(V_{d,i}-\overline{V}_d)^2}$
Standard deviation of directional differences	$s_{\phi,d} = \sqrt{-2\ln\left(\frac{1}{N}\sqrt{\left(\sum_{i=1}^{N}\sin\phi_{d,i}\right)^2+\left(\sum_{i=1}^{N}\cos\phi_{d,i}\right)^2}\right)}$

additionally calculated to provide some insights into the dynamics of the simulated processes. These include the vectorial root mean square error ($\vec{V}_{rmse}$), standard deviations for velocity-related and directional errors ($s_{V,d}$, $s_{\phi,d}$, and $s_{\vec{V},n}$), and velocity-related and vectorial correlation coefficients (r_V and $r_{\vec{V}}$) (cf. Table 4.2). Hereby, $s_{\vec{V},n}$ and $r_{\vec{V}}$ are plotted in a polar-diagram, the Taylor-diagram (*Taylor*, 2001) where the polar-angle is given by $\arccos(r_{\vec{V}})$ and the radius refers to $s_{\vec{V},n}$.

The quality of the frequency distributions for wind speed are expressed in terms of the Kolmogorov-Smirnov statistic (KS_V) which is defined as the maximum of the absolute differences between two cumulative distribution functions ($\mathrm{cdf}_1(V)$, $\mathrm{cdf}_2(V)$) of wind speed (V) (*Press et al.*, 1992):

$$\begin{aligned} KS_V &= \max_{0<V<\infty} |\mathrm{cdf}_1(V) - \mathrm{cdf}_2(V)| \\ &\quad \text{with } KS_V \in [0,1]. \end{aligned} \tag{4.1}$$

From equation (4.1) it can be seen that smaller deviations between two different distributions are indicated by smaller values of KS_V. If modelled and observed distributions are used as $\mathrm{cdf}_1(V)$ and $\mathrm{cdf}_2(V)$, KS_V provides an objective measurement to judge the quality of the model's results. Note KS_V is more sensitive for deviations of $\overline{V}$. To have a similar measurement for the comparison of two distributions of wind direction the Kuiper statistic (KP_ϕ) is used. KP_ϕ is a modified version of the Kolmogorov-Smirnov statistic which is equally sensitive for all data ranges. Therefore, it implicitly takes account for the cyclicity of wind directions. It is defined by (*Press et al.*, 1992):

$$\begin{aligned} KP_\phi &= \max_{0<\phi<360} |\mathrm{cdf}_1(\phi) - \mathrm{cdf}_2(\phi)| + \max_{0<\phi<360} |\mathrm{cdf}_2(\phi) - \mathrm{cdf}_1(\phi)|, \\ &\quad \text{with } KP_\phi \in [0,1]. \end{aligned} \tag{4.2}$$

KP_ϕ has the same property as KS_V: the smaller its value, the smaller the deviations between the two distributions.

In order to judge deviations between modelled and observed distributions and to inter-compare different model configurations the probabilities (P_{KS} and P_{KP} for the Kolmogorov-Smirnov statistic and the Kuiper statistic, respectively) that two distributions are drawn from the same sample (with N values) is given by (*Press et al.*, 1992):

$$\begin{aligned} P_{KS} &= 2\sum_{j=1}^{\infty}(-1)^{j-1}\exp\left(-2j^2\lambda^2\right) \text{ with} \\ \lambda &= \left[\sqrt{\frac{N}{2}} + 0.12 + 0.11\sqrt{\frac{2}{N}}\right] KS_V \end{aligned} \tag{4.3}$$

and

$$\begin{aligned} P_{KP} &= 2\sum_{j=1}^{\infty}(4j^2\lambda^2 - 1)\exp\left(-2j^2\lambda^2\right) \text{ with} \\ \lambda &= \left[\sqrt{\frac{N}{2}} + 0.155 + 0.24\sqrt{\frac{2}{N}}\right] KP_{\phi} \,. \end{aligned} \tag{4.4}$$

To judge whether two values for KS_V (KP_{ϕ}) significantly deviate from each other P_{KS} (P_{KP}) a significance-level of 0.05 is selected which must not be exceeded.

Hypothesis-tests for indicating significant changes in $\overline{V}_{bias}$, $\overline{\phi}_{bias}$, r_V, $s_{V,d}$, and $s_{\phi,d}$ are set aside, because critical core characteristics of the underlying data violate some fundamental assumptions of commonly used tests. In general, wind speeds are non-normally and non-symmetrically distributed. This excludes the application of many parametric tests, like Student's t-test and Fisher's f-test. In addition, the distributions may have different shapes which is a requirement for many non-parametric tests, like the Wilcoxon Rank Sum test (*Sachs and Hedderich*, 2006), or have largely deviating mean values which is a requirement for testing deviations in variances, like the Siegel-Turkey test (*Sachs and Hedderich*, 2006). Other uncertainties preventing from clear evaluation may arise from the limited accuracy of the underlying observational data: multiple bindings between data values and rank numbers may occur due to limited accuracy of observational data and hence may reduce the reliability of non-parametric tests. Tests for significant changes in $\overline{\phi}_{bias}$ and $s_{\phi,d}$ are even more complicated, since the cyclicity of wind direction has to be considered. Parametric circular tests are based on the van Mises distribution, which is the circular analogon of the normal distribution, and non-parametric tests require at least uni-modal distributions (*Fisher*, 1995; *Gaile and Burt*, 1980). Due to the numerous influences which near-surface winds are exposed to (cf. Section 1.1.2 and Section 1.1.3), uni-modally structured distributions of wind directions cannot be expected to be found excluding most of the circular test.

In order to derive station-averaged quantities the station-based statistics are pooled together: biases, Kolmogorov-Smirnov- and Kuiper-statistics are calculated via arithmetic means, standard deviations and the root mean square errors are quadratically averaged, and the correlation coefficients are derived by means of the Fisher-Z Transformation (*Leonhart*, 2004).

4.2 Observation Data and Their Uncertainties

In order to evaluate simulations by means of observations, modelled and observed values have to refer to the same physical quantities. Moreover, processes which the model is unable to capture have to be sorted out from observations as far as possible, otherwise no evidence can be drawn from the evaluation. In the case of the wind downscaling method the representativeness for each specific measuring site has to be fulfilled by both, the observations and the model grid with its limited resolution. The representativeness of an observation is fulfilled when the effects of internal boundary layers (IBL) (cf. Section 1.1, Section 2.1.1) and downstream wakes of obstacles are negligible. In practise, this is achieved when surrounding obstacles are far away from the site and the anemometer is installed high enough. The World Meteorological Organisation (WMO)

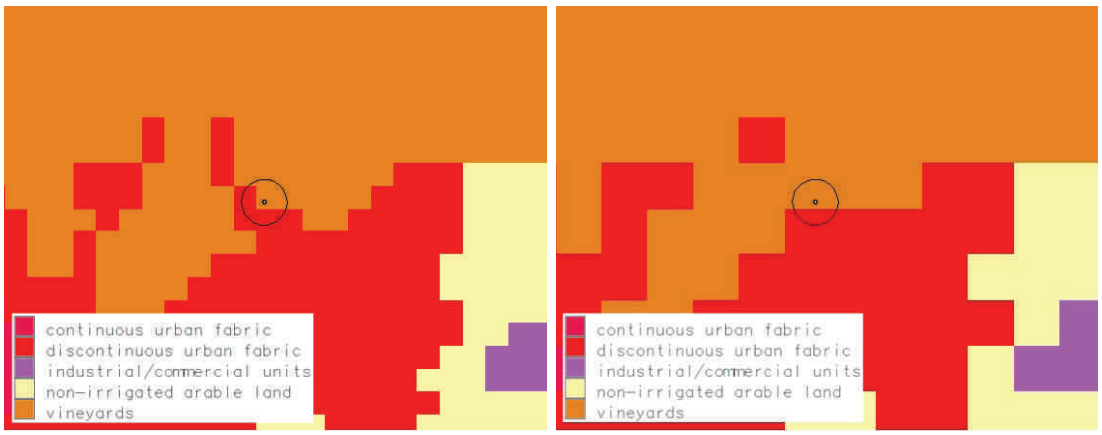

(a) **(b)**

Figure 4.2: Identification of an unrepresentative observation station (black point) in the Vienna Basin (Krems, Lower Austria, 15.6208°E, 48.4183°N) due to topographic inhomogeneities represented by the CORINE land cover data set CLC2000. Changes of CLC2000 occur within a radius of 10 times the anemometer height (i. e., 100 m) on (a) the original CLC2000 grid (100 m × 100 m grid spacing) and on (b) the grid of the diagnostic model (200 m × 200 m grid spacing).

suggests a distance between the anemometer and any obstruction of at least 10 times the obstruction's height for over-land-anemometers (in 10 m a.g.l.) in open terrain as a standard exposure. In cases, where the *"[...] standard exposure is unobtainable, the anemometer might be installed at such a height that its indications should be not too much affected by local obstructions [...]"* (*WMO*, 2006). It is further suggested to place *"[...] the anemometer at a height exceeding 10 m by an amount depending on the effective surface roughness length z_0 of the surroundings: about 13 m if $z_0 = 0.1$ m, and about 19 m if $z_0 = 0.5$ m"*. *Dobesch and Kury* (2006) suggest at least a distance of 150 m to the closest obstacle (for wind speeds >5 m/s), no obstacles closer than 15 times the obstacle's height, and anemometer heights $\geq$20 z_0. The representativeness of the model grid is supposed to be fulfilled when the SBCs (cf. Section 2.2) of the model approximate the natural conditions well enough.

To reduce the effects of both, improper represented observations and misleading SBCs around the observations, the sites with topographic inhomogeneities within a radius of 10 times the anemometer height on the CALMET grids (200 m × 200 m grid spacing) and in nature are excluded from evaluation. Since the SBCs in nature are difficult to obtain due to the influence of changing vegetation (especially when the simulation period lies quite some time in the past) the topographic inhomogeneities are defined by changes of the CORINE land cover data set CLC2000 (cf. Section 3.1) on the model grid and in nature represented by CORINE's full resolution (100 m × 100 m grid spacing) for convenience. Figure 4.2 shows an example of an excluded surface observation due to topographic inhomogeneities.

The technical accuracy of the observation depends on the type of the sensor. Cup

and propeller anemometers are most commonly used and their manufacturers provide accuracies about ±0.2 m/s for averaged wind speeds (10 minutes mean-values) up to 5 m/s, about ±5 % of the observed value above 5 m/s, and about ±2° for wind direction starting from a starting threshold-velocity of 0.5 m/s. However, for most cup and propeller-sensors the response is faster for acceleration than for deceleration tending to overestimate an averaged wind speed. Over-speeding-effects up to 10 % for some designs under turbulent wind conditions are reported by *WMO* (2006). Sonic sensors achieve accuracies about ±1.5 % of the observed value for wind speed, about ±2° for wind direction, and have a starting threshold-velocity of 0.01 m/s. However, these sensors are susceptible to rainy conditions. While single records of the raw observation data are automatically flagged by the data-logger in cases of technical breakdown or special conditions where the sensor's accuracy is heavily affected (e. g., precipitation-events for sonic sensors), some observation-errors in addition to the technical accuracy may remain in the provided data under certain circumstances.

One of the most important observation-errors, which are difficult to detect, is related to the effects of icing. Basically, serious icing of wind observation-sensors appear when super-cooled water-droplets are impinging the surfaces of the sensors and freeze immediately. Hereby, two types of icing are known: wet (dry) icing appears, when the flux of droplets towards the anemometer is larger (smaller) than the freezing rate (*Fikke et al.*, 2007). Results from wind tunnel experiments have shown that the effect of wet icing is much smaller than the effect of dry icing, where the observed wind speed from cup anemometers is slowly (but increasingly) reduced (cf. Figure 4.3). When the anemometer is fully coated with ice and the rotating parts have stopped the data-logger is expected to record no air-movement at all. However, malfunctions of the logger may appear, leading to constant or unrealistic values of the observed velocities. Nowadays, heating systems and icing sensors are installed in actual wind observation stations (if the required power supply is available) to reduce the events of icing and to detect icing periods. However, the reduction of the observed wind speed due to dry icing under harsh conditions is still challenging modern observation techniques (e. g., *Makkonen et al.*, 2001; *Mayr*, 2005).

In addition to the representativeness of observational data, single records of the observed values are sorted out to reduce the effect of observation-errors based on the threshold velocity of the anemometer and the effects of icing. Thereby, observed wind speeds and directions are excluded when the wind speed is ≤0.5 m/s and/or the wind speed is kept constant over at least 3 hours and/or the observations are flagged by the quality control system of the data-provider. However, the reduction-effect of wind speed due to partial dry-icing is not revealed by this sorting method. The observed velocities during winter are therefore supposed to be underestimated.

Any model-observation comparison described in Section 4.1 is based on pairs of modelled and valid observed data coincident in time (i. e., valid 10 minutes mean values recorded in hourly time steps). If an observed value is invalid or missing the according modelled value is set to missing as well. This guaranties comparability between any pair of modelled and observed value and the derived statistical analysis. Since the simulation-periods are covering at least one year, the size of the data sample is quite large and, therefore, the impact of the technical accuracy of each single observation record on the uncertainty of the time-independent statistical analyses plays a minor

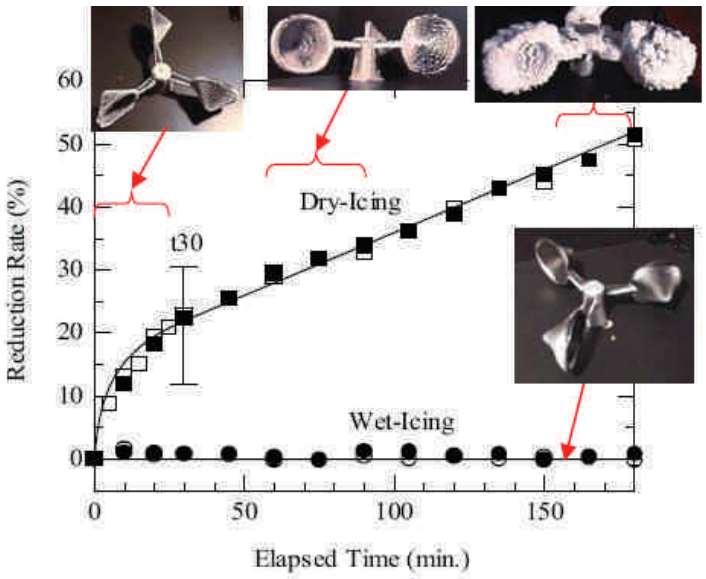

Figure 4.3: Effects of ice accretion on measurements from cup anemometer. During dry icing the observed wind speed is heavily damped (i. e., the reduction rate strongly increases). After 180 minutes of dry icing the observed wind speed is reduced about 50%, while wet icing has nearly no effect. From *Fikke et al.* (2007).

rule. The impact on the time-dependent statistical analyses is ignored, since the main focus of the evaluation lies on frequency distributions of wind speed and direction (cf. Section 4.1). Nonetheless, the technical accuracy leads to a limited number of digits in the observational data records and, hence, it might have considerable impact on non-parametric (rank-based) statistical hypothesis-test (*Sachs and Hedderich*, 2006). However, since the technical accuracy lies within a range of several percentages without systematic characteristic (see above) and the sample size is large, the tests' applicability should not be affected (cf. Section 4.1).

4.3 Performances of the Method and Its Variants

The following three sub-sections provide the main results of the statistical analysis as far as they are necessary for understanding and to keep the traceability of the conclusions drawn in Section 4.5. Additional results can be found in Appendix A.1.

4.3.1 Control Configuration and MM5 Variants

The variety of observed mean wind speeds ($\overline{V}_o$) shown in Table 4.3 and Table 4.4 reflects the strong influence of the topography (exposition and spread of the surface altitude) and the influence of different dominating synoptic-scale weather-patterns in the Hohe Tauern region and the Vienna Basin, respectively: for instance, the speed-up effect (cf. Section 1.1.3) roughly correlates with the altitude in the Hohe Tauern region leading to higher wind speeds at higher stations (e. g., SB is located at 3105 m and

shows 10.2 m/s for $\overline{V}_o$), while in the Vienna Basin the influence of the surrounding land cover (and hence the anemometer height) seems to be stronger pronounced (e. g., the anemometer of LB is located at 25 m a.g.l. and shows 7.5 m/s for $\overline{V}_o$). A similar interpretation of the mean wind direction ($\overline{\phi}_o$) is set aside, because due to diurnal cycles (e. g., the Alpine pumping, cf. Section 1.1.2, and thermal-induced local flows, cf. Section 1.1.3) most of the observed directions are at least bi-modally distributed (cf. Figure 4.4 and Figure 4.5) and the mean direction may lose its evidence. Note the only bi-modal distribution of wind speed is found at EB (cf. Figure 4.4). EB was active during a three-month period in autumn 1999 when Föhn-events (cf. Section 1.1.2) and gap-flows (cf. Section 1.1.3) most frequently occur and hence the distribution can be seen as a result of weak local thermal circulations frequently disturbed by strong gradient-forced synoptic- or regional-scale flows.

The hypothesis-tests applied for each station indicate that all modelled distributions (wind speed and direction) significantly deviate from the observations: the calculated significances shown in Table 4.3 and Table 4.4 are smaller than 0.05.

In general the error statistics of Av0 have smaller values than the statistics for the driving data which are shown in Table 4.5. ERA-40 has larger biases in both study regions and the frequency distributions (in terms of KS_V and KP_ϕ) are improperly captured. Only in exceptional cases the distributions of wind speed (at ZS in Figure 4.4) and directions (at IF in Figure 4.4 and at LT in Figure 4.5) are not improved by Av0. This might have happened for two reasons: first, data from surface and upper-air observations in the Alpine region have been assimilated into ERA-40 (e. g., radiosondes from IF) and second, local wind climatologies may coincidentally agree with large-scale climatologies. General improvements due to the application of Av0 can also be found for the time-dependent statistics, except for $\vec{V}_{rmse}$ and $s_{V,d}$ in the Hohe Tauern region (HK, RH, ZS, SH, and SB). Strong evidences exist that ERA-40's wind speeds are not related to the observations at all ($r_V \leq 0.16$).

For Av0 the averages over all stations show biases of 1.7 m/s and $-2.1°$ in the Hohe Tauern region and 1.5 m/s and 1.7° in the Vienna Basin for wind speed and direction, respectively (cf. Table 4.3 and Table 4.4). These positive biases are shifting the frequency distributions towards higher wind speeds as it can be taken from the station-averaged frequency distributions in Figure 4.6. The frequency distributions per station (in terms of KS_V and KP_ϕ) are more broadly spread in the Hohe Tauern region and the directional distributions are more properly captured in the Vienna Basin, except at LT (cf. Figure 4.5). Most realistic distributions of wind speed are achieved at SB (cf. Figure 4.4) and LB (cf. Figure 4.5), which are two stations less influenced by the surface-layer (cf. Section 1.1): SB is located on a mountain top and LB has an anemometer-height of 25 m (cf.Table 4.1). The directional distribution is captured best at ZD (cf. Figure 4.5), but nonetheless KP_ϕ still significantly deviates from the observation (cf. Table 4.4).

The time-depending statistics show better results in the Vienna Basin: $\vec{V}_{rmse}$, r_V, $s_{V,d}$, and $s_{\phi,d}$ are changed from 7.9 m/s, 0.30, 5.0 m/s, and 82.3° in the Hohe Tauern region to 4.3 m/s, 0.54, 2.4 m/s, and 60.6° in the Vienna Basin, respectively. This behaviour is also reflected in Taylor-diagrams (cf. Figure 4.7) (which have been adopted for the vectorial statistics $s_{\vec{V},n}$ and $r_{\vec{V}}$ in order to combine velocity- and direction-related

Table 4.3: Annual (year 1999) error statistics (cf. Table 4.2) of Av0 (upper panel) and its intermediate dynamic downscaling-step (lower panel) at the stations in the Hohe Tauern region (cf. Table 4.1) along with the ratio of valid data (Val.), the observed mean wind speed ($\overline{V}_o$), and the observed mean wind direction ($\overline{\phi}_o$). Significant deviations from observations (parentheses) and differences between the downscaling-steps (brackets) are indicated by significances < 0.05.

Station Abbr.	Val. [1]	$\overline{V}_o$ [m/s]	$\overline{\phi}_o$ [°]	$\overline{V}_{bias}$ [m/s]	$\overline{\phi}_{bias}$ [°]	KS_V [1]	KP_ϕ [1]	$\vec{V}_{rmse}$ [m/s]	r_V [1]	$s_{V,d}$ [m/s]	$s_{\phi,d}$ [°]
Control configuration Av0 (combined application of MM5 setup A and CALMET v0), 200 m grid spacing											
IF	0.77	2.5	223.1	-0.1	20.6	0.11 (<0.01) [<0.01]	0.24 (<0.01) [<0.01]	4.1	0.13	2.8	99.6
PK	0.56	6.2	346.8	-0.5	-131.3	0.10 (<0.01) [<0.01]	0.47 (<0.01) [<0.01]	8.1	0.58	4.8	88.1
HK	0.91	2.8	264.9	2.5	-20.1	0.36 (<0.01) [<0.01]	0.22 (<0.01) [<0.01]	5.6	0.43	3.9	72.6
RH	0.90	5.4	239.1	2.3	71.1	0.31 (<0.01) [<0.01]	0.31 (<0.01) [<0.01]	9.1	0.16	6.6	78.9
ZS	0.88	1.6	293.7	3.1	-35.3	0.59 (<0.01) [<0.01]	0.42 (<0.01) [<0.01]	6.1	0.02	3.8	102.7
SH	0.95	5.0	244.4	2.8	9.0	0.28 (<0.01) [<0.01]	0.24 (<0.01) [<0.01]	8.0	0.31	5.0	63.5
SB	0.77	10.2	311.6	1.1	-11.9	0.08 (<0.01) [<0.01]	0.21 (<0.01) [<0.01]	12.3	0.40	7.3	70.7
EB	0.15	5.0	136.4	-0.8	-8.2	0.17 (<0.01) [0.08]	0.33 (<0.01) [<0.01]	4.8	0.69	3.0	58.1
ave	0.82	4.7	267.2	1.7	-2.1	0.27	0.30	7.9	0.30	5.0	82.3
Dynamic downscaling-step (MM5 domain A2), 10 km grid spacing											
IF	0.77	2.5	223.1	1.8	20.7	0.35 (<0.01)	0.24 (<0.01)	5.6	0.35	3.0	101.7
PK	0.56	6.2	346.8	-3.0	-174.0	0.23 (<0.01)	0.36 (<0.01)	7.3	0.64	4.8	79.3
HK	0.91	2.8	264.9	1.4	-32.6	0.23 (<0.01)	0.24 (<0.01)	4.3	0.42	2.9	73.1
RH	0.90	5.4	239.1	1.2	26.5	0.24 (<0.01)	0.37 (<0.01)	7.6	0.33	5.6	72.7
ZS	0.88	1.6	293.7	3.5	-36.4	0.63 (<0.01)	0.34 (<0.01)	6.4	0.00	4.0	107.8
SH	0.95	5.0	244.4	-0.4	13.5	0.12 (<0.01)	0.28 (<0.01)	5.8	0.38	3.8	63.2
SB	0.77	10.2	311.6	-2.3	-21.3	0.16 (<0.01)	0.24 (<0.01)	10.8	0.44	6.2	71.6
EB	0.15	5.0	136.4	-0.9	59.0	0.18 (<0.01)	0.67 (<0.01)	6.0	0.70	3.0	55.2
ave	0.82	4.7	267.2	0.5	-4.5	0.28	0.30	7.0	0.37	4.4	81.9

Table 4.4: Same as Table 4.3, but for the Vienna Basin.

Station Abbr.	Val. [1]	$\overline{V}_o$ [m/s]	$\overline{\phi}_o$ [°]	$\overline{V}_{bias}$ [m/s]	$\overline{\phi}_{bias}$ [°]	KS_V [1]	KP_ϕ [1]	$\vec{V}_{rmse}$ [m/s]	r_V [1]	$s_{V,d}$ [m/s]	$s_{\phi,d}$ [°]
Control configuration Av0 (combined application of MM5 setup A and CALMET v0), 200 m grid spacing											
GE	0.95	3.4	297.9	2.1	-3.8	0.35 (<0.01) [<0.01]	0.09 (<0.01) [0.09]	4.6	0.53	2.3	61.5
GK	0.88	2.9	298.2	2.6	-1.3	0.39 (<0.01) [<0.01]	0.21 (<0.01) [<0.01]	4.6	0.50	2.7	61.1
LB	0.23	7.4	222.2	0.3	46.9	0.06 (<0.01) [<0.01]	0.19 (<0.01) [0.12]	7.7	0.51	3.2	65.8
LT	0.96	3.2	256.0	1.9	36.5	0.34 (<0.01) [<0.01]	0.55 (<0.01) [<0.01]	4.6	0.62	2.3	61.4
NE	0.96	3.4	339.2	1.6	-27.6	0.27 (<0.01) [<0.01]	0.16 (<0.01) [<0.01]	4.2	0.50	2.2	62.9
SP	0.94	3.2	252.8	1.8	-7.1	0.29 (<0.01) [<0.01]	0.21 (<0.01) [<0.01]	4.1	0.54	2.4	61.7
HW	0.94	3.5	293.1	1.0	-5.4	0.20 (<0.01) [<0.01]	0.13 (<0.01) [<0.01]	3.6	0.53	2.2	59.9
WU	0.94	4.0	283.3	0.7	3.5	0.16 (<0.01) [0.51]	0.10 (<0.01) [<0.01]	3.7	0.53	2.4	56.4
ZD	0.89	3.8	279.0	1.0	10.1	0.20 (<0.01) [1.00]	0.04 (<0.01) [<0.01]	3.7	0.56	2.2	58.4
ave	0.91	3.5	285.3	1.5	1.7	0.27	0.19	4.3	0.54	2.4	60.6
Dynamic downscaling-step (MM5 domain A2), 10 km grid spacing											
GE	0.95	3.4	297.9	1.0	-1.5	0.20 (<0.01)	0.10 (<0.01)	3.7	0.54	2.0	61.5
GK	0.88	2.9	298.2	1.6	-5.7	0.30 (<0.01)	0.12 (<0.01)	3.7	0.48	2.3	61.0
LB	0.23	7.4	222.2	-1.5	49.0	0.23 (<0.01)	0.20 (<0.01)	7.0	0.50	2.9	66.1
LT	0.96	3.2	256.0	1.1	-9.1	0.22 (<0.01)	0.33 (<0.01)	3.5	0.59	2.0	62.7
NE	0.96	3.4	339.2	2.0	-26.6	0.32 (<0.01)	0.16 (<0.01)	4.5	0.49	2.4	63.3
SP	0.94	3.2	252.8	1.4	3.6	0.25 (<0.01)	0.22 (<0.01)	3.8	0.53	2.2	63.7
HW	0.94	3.5	293.1	2.4	-3.5	0.39 (<0.01)	0.06 (<0.01)	4.6	0.51	2.5	58.8
WU	0.94	4.0	283.3	0.7	11.3	0.17 (<0.01)	0.13 (<0.01)	3.8	0.53	2.3	56.5
ZD	0.89	3.8	279.0	0.9	17.0	0.19 (<0.01)	0.04 (<0.01)	3.7	0.55	2.2	58.0
ave	0.91	3.5	285.3	1.3	-0.6	0.26	0.15	4.1	0.53	2.3	60.9

Table 4.5: Same as Table 4.3 and Table 4.4, but for the ERA-40 dataset in the Hohe Tauern region (upper panel) and the Vienna Basin (lower panel). The statistics are based on the 6 h storage-interval of ERA-40.

Station Abbr.	Val. [1]	$\overline{V}_o$ [m/s]	$\overline{\phi}_o$ [°]	$\overline{V}_{bias}$ [m/s]	$\overline{\phi}_{bias}$ [°]	KS_V [1]	KP_ϕ [1]	$\vec{V}_{rmse}$ [m/s]	r_V [1]	$s_{V,d}$ [m/s]	$s_{\phi,d}$ [°]
ERA-40, Hohe Tauern, 120 km grid spacing											
IF	0.13	2.4	222.8	3.4	28.5	0.51 (<0.01)	0.17 (<0.01)	6.9	0.00	4.1	108.5
PK	0.09	6.2	340.8	-2.2	77.7	0.17 (<0.01)	0.49 (<0.01)	10.0	0.00	6.4	98.5
HK	0.15	2.8	267.5	-1.8	164.4	0.60 (<0.01)	0.43 (<0.01)	3.7	0.00	1.8	106.2
RH	0.15	5.4	238.6	-2.8	-168.5	0.31 (<0.01)	0.48 (<0.01)	8.3	0.10	5.0	128.2
ZS	0.15	1.6	275.3	-0.0	151.9	0.16 (<0.01)	0.41 (<0.01)	2.5	0.00	1.4	168.4
SH	0.16	5.0	242.7	-3.7	-170.0	0.66 (<0.01)	0.41 (<0.01)	6.6	0.03	3.5	111.9
SB	0.13	10.3	311.5	-8.7	127.3	0.85 (<0.01)	0.53 (<0.01)	12.2	0.16	6.3	124.2
EB	0.02	5.1	134.1	-3.6	-57.2	0.53 (<0.01)	0.84 (<0.01)	6.4	0.06	4.1	97.9
ave	0.14	4.7	263.9	-2.3	150.9	0.48	0.43	7.5	0.02	4.3	123.6
ERA-40, Vienna Basin, 120 km grid spacing											
GE	0.16	3.4	299.3	4.3	-46.4	0.49 (<0.01)	0.43 (<0.01)	9.3	0.10	4.9	128.6
GK	0.15	2.9	299.1	3.7	-47.0	0.48 (<0.01)	0.46 (<0.01)	7.9	0.02	4.4	116.7
LB	0.04	7.3	213.0	9.7	49.6	0.69 (<0.01)	0.74 (<0.01)	20.0	0.00	8.4	132.3
LT	0.16	3.2	256.2	1.1	-2.4	0.23 (<0.01)	0.32 (<0.01)	5.3	0.08	3.2	112.3
NE	0.16	3.3	341.4	8.7	-88.0	0.68 (<0.01)	0.50 (<0.01)	14.7	0.16	7.4	156.6
SP	0.16	3.1	249.4	1.7	3.3	0.29 (<0.01)	0.24 (<0.01)	6.0	0.09	3.4	116.6
HW	0.16	3.6	293.1	10.1	-40.2	0.69 (<0.01)	0.38 (<0.01)	15.9	0.08	8.6	127.0
WU	0.16	4.0	283.1	5.3	-28.5	0.49 (<0.01)	0.38 (<0.01)	11.4	0.07	6.1	136.5
ZD	0.15	3.7	281.8	4.7	-29.2	0.47 (<0.01)	0.37 (<0.01)	10.6	0.16	5.5	123.3
ave	0.15	3.5	285.6	5.1	-32.4	0.49	0.39	11.1	0.09	5.8	128.2

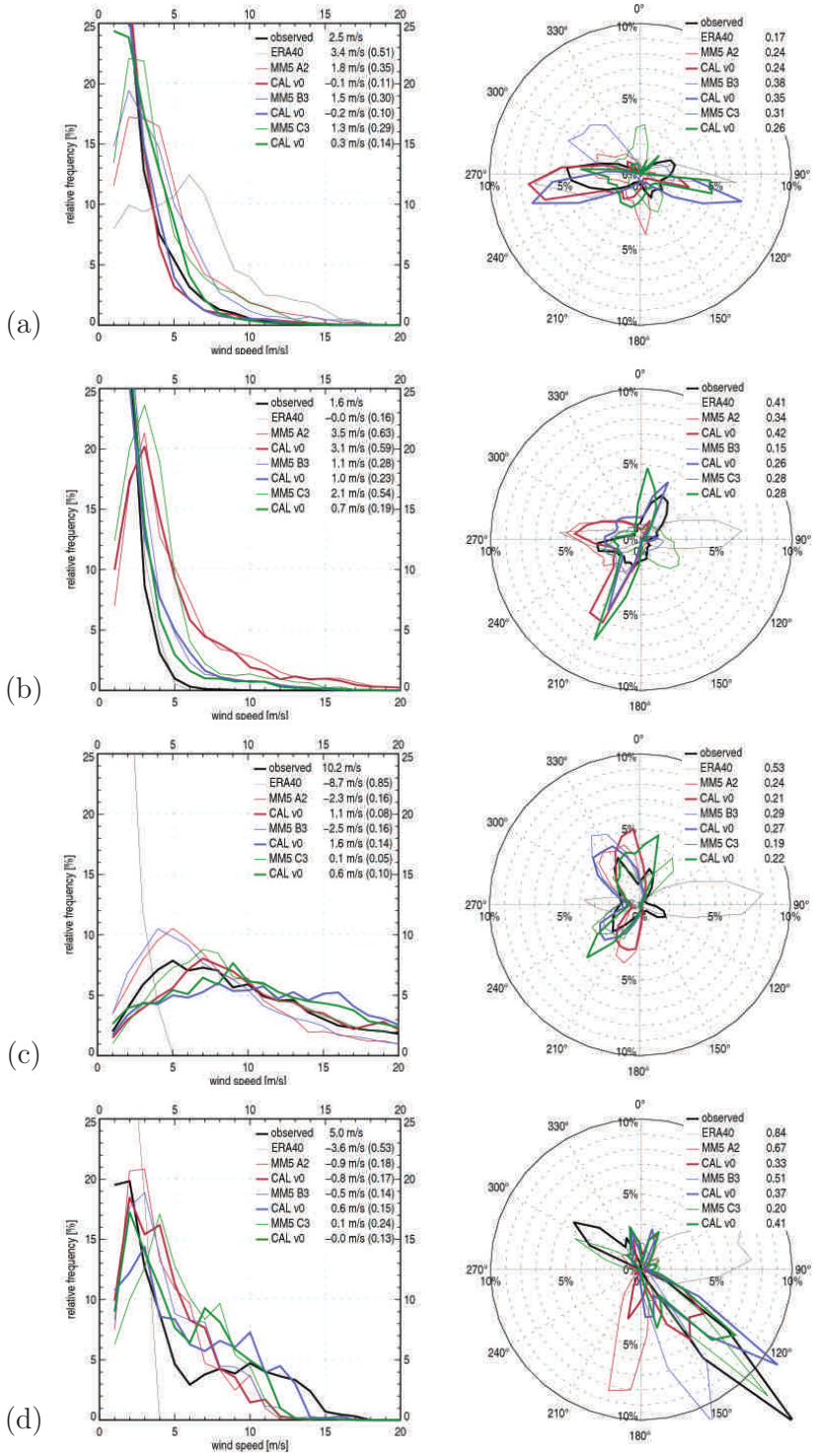

Figure 4.4: Modelled and observed frequency distributions of wind speed (left column) and direction (right column) from the year 1999 in the Hohe Tauern region at stations (a) IF, (b) ZS, (c) SB, and (d) EB (cf. Table 4.1). The observations (thick black lines), the driving data ERA-40 (thin black lines), the MM5 configurations A2, B3, and C3 (thin red, blue, and green lines) which were downscaled by CALMET-variant v0 (thick red, blue, and green lines) are shown. Observed mean values, the models' biases and the quality of the simulated distributions in terms of KS_V (in parentheses) and KP_ϕ are listed in the legends.

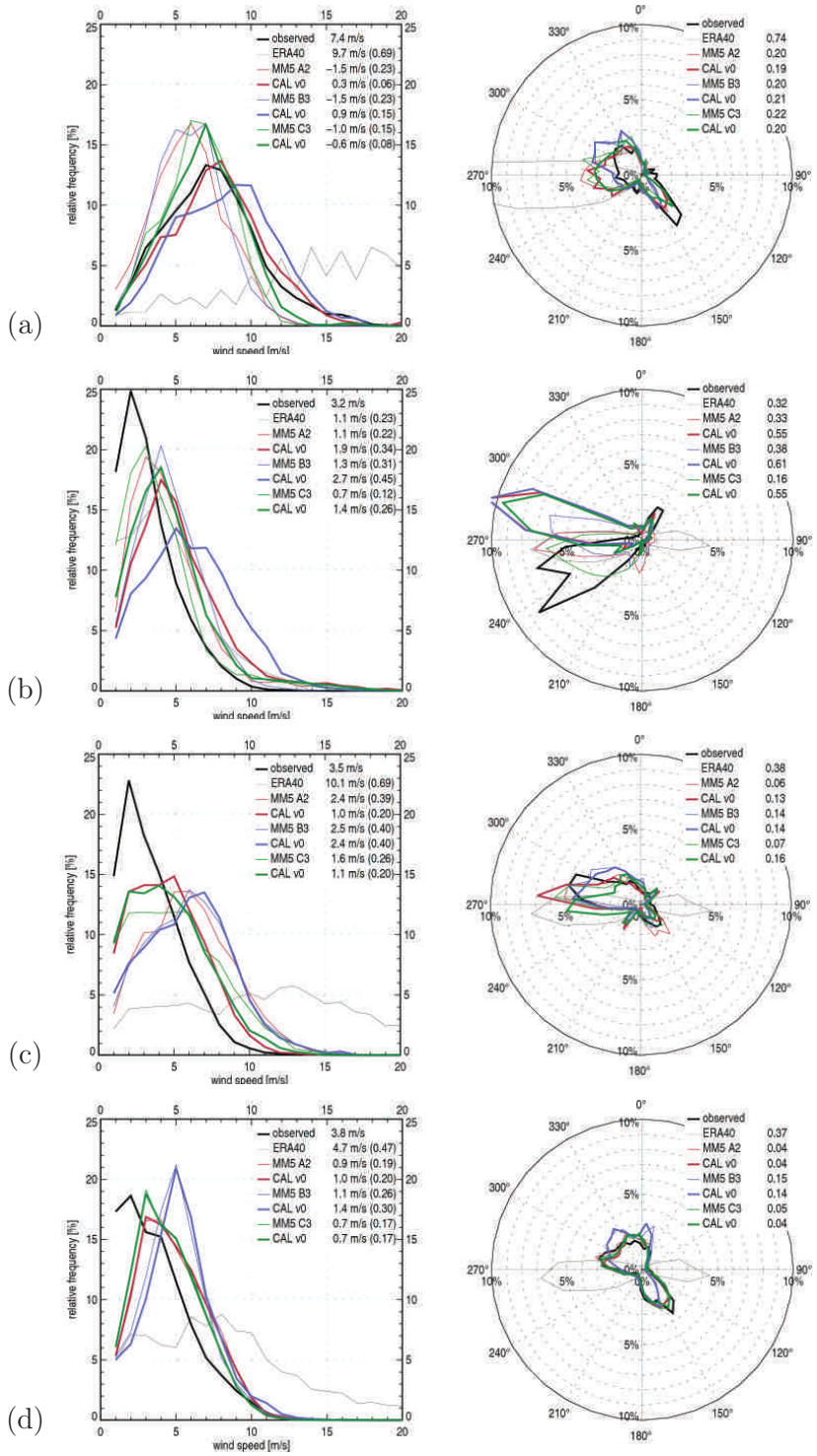

Figure 4.5: Same as Figure 4.4, but for the Vienna Basin at the stations (a) LB, (b) LT, (c) HW, and (d) ZD (cf. Table 4.1).

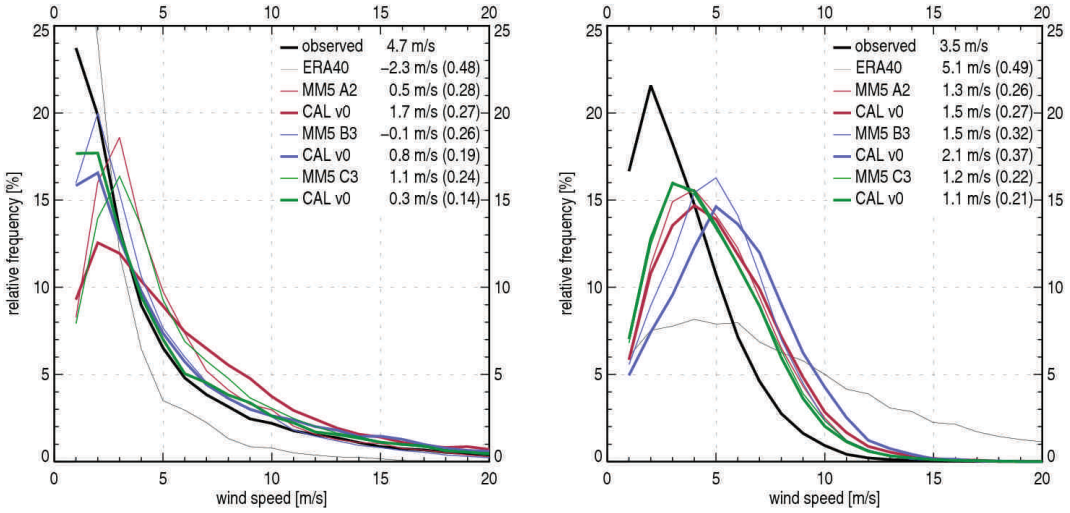

(a) **(b)**

Figure 4.6: Same as Figure 4.4 and Figure 4.5 left column, but averaged over all stations in (a) the Hohe Tauern region and (b) the Vienna Basin (cf. Table 4.1).

quantities): the values for $r_{\vec{V}}$ are higher (the station-averaged $r_{\vec{V}}$ is increased from 0.38 in the Hohe Tauern region to 0.64 in the Vienna Basin) and the values for $s_{\vec{V},n}$ are more densely distributed in the Vienna Basin. The systematic overestimation of wind speeds is reflected by values for $s_{\vec{V},n}$ larger than 1.0, in general.

From comparing the statistics of each single downscaling-step (MM5 and CALMET) of configuration Av0 it cannot be clearly seen that CALMET improves MM5: $\overline{V}_{bias}$, $\overline{\phi}_{bias}$, KS_V, and KP_ϕ are improved at 5 (3), 7 (4), 4 (3), and 5 (2) stations in the Hohe Tauern region (Vienna Basin), if only the significant improvements for KS_V and KP_ϕ are counted. Although the simulated wind fields are much higher resolved and provide much more detail than the wind fields of MM5 domain A2 (cf. Figure 2.4 in Section 2.2.1) the statistics reflect this qualitative improvement in a more subtle manner: apart from $\overline{\phi}_{bias}$ in the Hohe Tauern region, which is reduced from $-4.5°$ to $-2.1°$, the statistics stay at their level or even get worse, but their spread (i. e., the difference between maximum and minimum) across the stations becomes smaller for $\overline{V}_{bias}$, $\overline{\phi}_{bias}$, and $s_{\phi,d}$ in both study regions and for KP_ϕ in the Hohe Tauern region. Looking at the results station by station most notable (and significant) improvements due to CALMET can be found for the distributions of wind speed at IF (KS_V is reduced from 0.35 to 0.11, cf. Figure 4.4) and LB (KS_V is reduced from 0.23 to 0.06, cf. Figure 4.5), and the distribution of wind direction at EB (KP_ϕ is reduced from 0.67 to 0.33, cf. Figure 4.4).

Overviews of the statistics for configuration Bv0, which is distinguished by higher resolved grids (5 km grid spacing) for MM5 (domain B3a and B3b), are provided by Table 4.6 and Table 4.7. But in contrast to the statistic-overviews of Av0 these tables

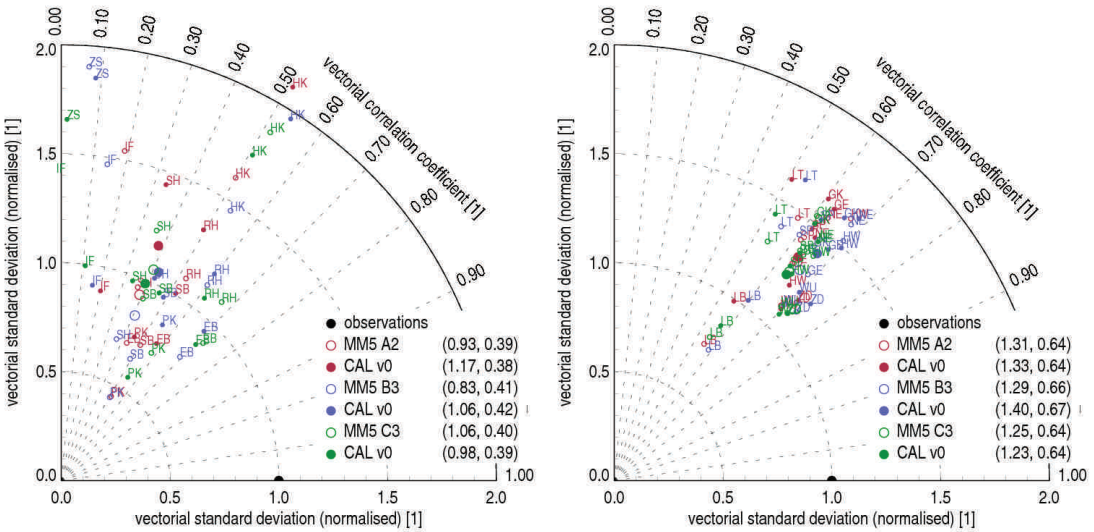

(a) **(b)**

Figure 4.7: Time-dependent vectorial statistics from the year 1999 in (a) the Hohe Tauern region and (b) the Vienna Basin. The MM5 configurations A2, B3, and C3 (red, blue, and green circles) which were downscaled by CALMET-variant v0 (red, blue, and green dots) are shown for each station (small marks) (cf. Table 4.1). Station-averaged (large marks) normalised vectorial standard deviations ($s_{\vec{V},n}$) and vectorial correlation-coefficients ($r_{\vec{V}}$) are listed in the legends.

show the probabilities that the statistics of Av0 and Bv0 are drawn from the same sample. Significant deviations from Av0 are therefore indicated by significances < 0.05.

In general all frequency distributions at all stations in both study regions (cf. Table 4.6 and Table 4.7) and for both downscaling-steps (MM5 and CALMET) significantly change when MM5 is switched to setup B. Improvements of the station-averaged time-independent statistics of Bv0 can be found for $\overline{V}_{bias}$ (reduction to 0.8 m/s), KS_V (reduction to 0.19), and KP_ϕ (reduction to 0.28) in the Hohe Tauern region. However, in the Vienna Basin these statistics get worse: the wind speeds are increasingly overestimated leading to higher biases ($\overline{V}_{bias}$ and $\overline{\phi}_{bias}$ are increased to 2.1 m/s and to 16.7°, respectively) and weaker representations of the frequency distributions (KS_V is increased to 0.37). The averaged time-depending statistics are notably improved by Bv0 in the Hohe Tauern region, too ($\vec{V}_{rmse}$, r_V, and $s_{V,d}$ are changed to 7.1 m/s, 0.41, and 4.1 m/s, respectively), whereas in the Vienna Basin they stay close to the values found for Av0. This behaviour is also reflected by the station-averaged plots (cf. Figure 4.6 and Figure 4.7, where $s_{\vec{V},n}$ is reduced to 1.06 and $r_{\vec{V}}$ is increased to 0.42 in the Hohe Tauern region) and by the station-by-station spread of the statistics. Nonetheless, Bv0 still performs better in the Vienna Basin than in the Hohe Tauern region when the station-averages of $\overline{\phi}_{bias}$, KP_ϕ, $\vec{V}_{rmse}$, r_V, $s_{V,d}$, and $s_{\phi,d}$ are compared.

The underlying mechanisms for this enhanced overestimation of wind speed are difficult to clarify: on one hand the orography is more properly captured by the increased

Table 4.6: Annual (year 1999) error statistics (cf. Table 4.2) of Bv0 (upper panel) and its intermediate dynamic downscaling-step (lower panel) at the stations in the Hohe Tauern region (cf. Table 4.1) along with the ratio of valid data (Val.), the observed mean wind speed ($\overline{V}_o$), and the observed mean wind direction ($\overline{\phi}_o$). Significant deviations from Av0 (parentheses) and differences between the downscaling-steps (brackets) are indicated by significances < 0.05.

Station Abbr.	Val. [1]	$\overline{V}_o$ [m/s]	$\overline{\phi}_o$ [°]	$\overline{V}_{bias}$ [m/s]	$\overline{\phi}_{bias}$ [°]	KS_V [1]	KP_ϕ [1]	$\vec{V}_{rmse}$ [m/s]	r_V [1]	$s_{V,d}$ [m/s]	$s_{\phi,d}$ [°]
Configuration Bv0 (combined application of MM5 setup B and CALMET v0), 200 m grid spacing											
IF	0.77	2.5	223.1	-0.2	-26.7	0.10 (0.03) [<0.01]	0.35 (<0.01) [<0.01]	4.0	0.22	2.5	118.8
PK	0.56	6.2	346.8	-0.1	-149.7	0.05 (<0.01) [<0.01]	0.33 (<0.01) [<0.01]	7.6	0.61	4.9	83.9
HK	0.91	2.8	264.9	2.4	5.9	0.32 (<0.01) [<0.01]	0.12 (<0.01) [<0.01]	5.2	0.44	3.6	64.9
RH	0.90	5.4	239.1	1.2	57.9	0.21 (<0.01) [<0.01]	0.29 (<0.01) [<0.01]	7.1	0.46	5.1	67.9
ZS	0.88	1.6	293.7	1.0	0.5	0.23 (<0.01) [<0.01]	0.26 (<0.01) [<0.01]	3.9	0.10	2.6	101.8
SH	0.95	5.0	244.4	-0.8	36.9	0.17 (<0.01) [<0.01]	0.37 (<0.01) [<0.01]	5.9	0.41	3.9	81.3
SB	0.77	10.2	311.6	1.6	-19.7	0.14 (<0.01) [<0.01]	0.27 (<0.01) [<0.01]	13.2	0.59	5.9	70.5
EB	0.15	5.0	136.4	0.6	-18.3	0.15 (<0.01) [<0.01]	0.37 (<0.01) [<0.01]	4.3	0.69	3.1	53.8
ave	0.82	4.7	267.2	0.8	7.0	0.19	0.28	7.1	0.41	4.1	84.9
Dynamic downscaling-step (MM5 domain B3a), 5 km grid spacing											
IF	0.77	2.5	223.1	1.5	110.7	0.30 (<0.01)	0.38 (<0.01)	5.5	0.18	3.3	123.8
PK	0.56	6.2	346.8	-2.9	-150.5	0.22 (0.05)	0.47 (<0.01)	7.3	0.65	4.7	93.5
HK	0.91	2.8	264.9	1.1	0.2	0.14 (<0.01)	0.18 (<0.01)	3.9	0.43	2.8	64.2
RH	0.90	5.4	239.1	1.9	41.0	0.30 (<0.01)	0.52 (<0.01)	7.7	0.30	5.6	70.1
ZS	0.88	1.6	293.7	1.1	-53.9	0.28 (<0.01)	0.15 (<0.01)	3.9	0.07	2.5	100.8
SH	0.95	5.0	244.4	-2.1	28.9	0.39 (<0.01)	0.31 (<0.01)	5.4	0.41	3.3	90.7
SB	0.77	10.2	311.6	-2.5	-19.4	0.16 (0.01)	0.29 (<0.01)	11.2	0.51	5.8	70.7
EB	0.15	5.0	136.4	-0.5	3.0	0.14 (<0.01)	0.51 (<0.01)	4.1	0.73	2.8	56.3
ave	0.82	4.7	267.2	-0.1	10.0	0.26	0.33	6.6	0.37	4.1	88.4

Table 4.7: Same as Table 4.6, but for the Vienna Basin.

Station Abbr.	Val. [1]	$\overline{V}_o$ [m/s]	$\overline{\phi}_o$ [°]	$\overline{V}_{bias}$ [m/s]	$\overline{\phi}_{bias}$ [°]	KS_V [1]	KP_ϕ [1]	$\vec{V}_{rmse}$ [m/s]	r_V [1]	$s_{V,d}$ [m/s]	$s_{\phi,d}$ [°]
Configuration Bv0 (combined application of MM5 setup B and CALMET v0), 200 m grid spacing											
GE	0.95	3.4	297.9	1.7	12.3	0.34 (<0.01) [<0.01]	0.06 (<0.01) [<0.01]	3.9	0.61	2.0	58.2
GK	0.88	2.9	298.2	2.9	4.7	0.48 (<0.01) [<0.01]	0.19 (<0.01) [<0.01]	4.6	0.57	2.4	58.1
LB	0.23	7.4	222.2	0.9	63.3	0.15 (<0.01) [<0.01]	0.21 (<0.01) [0.72]	7.8	0.62	2.8	60.0
LT	0.96	3.2	256.0	2.7	39.7	0.45 (<0.01) [<0.01]	0.61 (<0.01) [<0.01]	5.1	0.64	2.3	56.2
NE	0.96	3.4	339.2	2.6	-20.4	0.43 (<0.01) [<0.01]	0.15 (<0.01) [<0.01]	4.7	0.54	2.4	57.4
SP	0.94	3.2	252.8	2.0	20.5	0.34 (<0.01) [<0.01]	0.14 (<0.01) [<0.01]	4.2	0.51	2.4	59.7
HW	0.94	3.5	293.1	2.4	9.2	0.40 (<0.01) [0.28]	0.14 (<0.01) [<0.01]	4.5	0.55	2.5	55.3
WU	0.94	4.0	283.3	1.4	26.2	0.29 (<0.01) [<0.01]	0.21 (<0.01) [<0.01]	4.2	0.54	2.4	53.6
ZD	0.89	3.8	279.0	1.4	29.6	0.30 (<0.01) [<0.01]	0.14 (<0.01) [0.01]	3.8	0.55	2.2	54.5
ave	0.91	3.5	285.3	2.1	16.7	0.37	0.21	4.5	0.57	2.3	56.8
Dynamic downscaling-step (MM5 domain B3b), 5 km grid spacing											
GE	0.95	3.4	297.9	1.3	16.1	0.28 (<0.01)	0.07 (<0.01)	3.5	0.61	1.9	58.0
GK	0.88	2.9	298.2	1.7	10.8	0.35 (<0.01)	0.12 (<0.01)	3.5	0.55	2.0	58.7
LB	0.23	7.4	222.2	-1.5	62.9	0.23 (0.21)	0.20 (<0.01)	6.8	0.61	2.6	59.7
LT	0.96	3.2	256.0	1.3	11.5	0.31 (<0.01)	0.38 (<0.01)	3.6	0.60	1.8	56.5
NE	0.96	3.4	339.2	2.5	-18.7	0.42 (<0.01)	0.15 (<0.01)	4.6	0.56	2.3	57.7
SP	0.94	3.2	252.8	1.5	32.2	0.30 (<0.01)	0.23 (<0.01)	3.9	0.48	2.3	61.7
HW	0.94	3.5	293.1	2.5	10.9	0.40 (<0.01)	0.14 (<0.01)	4.6	0.54	2.5	54.3
WU	0.94	4.0	283.3	1.0	29.4	0.25 (<0.01)	0.24 (<0.01)	4.0	0.55	2.3	54.0
ZD	0.89	3.8	279.0	1.1	33.6	0.26 (<0.01)	0.15 (<0.01)	3.7	0.55	2.1	54.6
ave	0.91	3.5	285.3	1.5	17.1	0.32	0.19	4.1	0.56	2.2	57.1

resolution which should lead to improvements in general. On the other hand sub-grid-scale parameterisations may fail at smaller grid spacings due to oversimplifications and conceptual break-downs (cf. Section 2.1.1). Moreover, the number of grid cells in setup B is notably smaller than in setup A and C. Especially, domain B3b consists of 43×37 cells and is therefore strongly influenced by the coarser resolved mother domain B2 (15 km grid spacing). Due to the complexity of the Hohe Tauern region the influence of B2 might be smaller than in the flat Vienna Basin. To clarify the influence of the number of grid cells additional simulations would be necessary. Since the computational resources for this study are limited, further investigations are set aside.

Comparing Bv0 with Av0 station by station (cf. Figure 4.4 and Figure 4.5) the behaviour of the averaged statistics can not be found one by one: at some of the stations the statistics are improved, at others they stay at their level or get worse. Largest improvements can be found at ZS for $\overline{V}_{bias}$, $\overline{\phi}_{bias}$, KS_V, KP_ϕ, $\vec{V}_{rmse}$, and $s_{V,d}$ where the statistics are changed to 1.0 m/s, 0.5°, 0.23, 0.26, 3.9 m/s, and 2.6 m/s, respectively. However, at ZS the modelled and observed wind speeds and directions are nearly decoupled from each other leading to very low correlation-coefficients (r_V is 0.02 for Av0 and 0.10 for Bv0) and large directional standard-deviations of the model errors ($s_{\phi,d}$ is 102.7° for Av0 and 101.8° for Bv0) for both downscaling-variants.

The improvements of MM5's wind fields in the Hohe Tauern region (domain B3a) due to the application of CALMET v0 are similar to those in variant Av0: most statistics stay at their level or get worse, but the spread (i. e., the difference between maximum and minimum) across the stations becomes smaller for $\overline{V}_{bias}$, $\overline{\phi}_{bias}$, $s_{\phi,d}$, and KP_ϕ. In the Vienna Basin $\overline{\phi}_{bias}$ (station-averaged value) is slightly improved, however its spread becomes larger. Improvements for $\overline{V}_{bias}$, $\overline{\phi}_{bias}$, KS_V, and KP_ϕ are found at 6 (1), 3 (6), 6 (1), and 6 (4) stations in the Hohe Tauern region (Vienna Basin). Most notable improvements can be found for the distribution of wind speed at IF (cf. Figure 4.4), PK, HK, and SH. In the Vienna Basin the distributions stay at their levels or get worse (e. g., LT in Figure 4.5).

A comparison of Bv0 with the statistics of ERA-40 (cf. Table 4.5) shows that Bv0 outperforms ERA-40 in both study regions: all station-averaged statistics are improved. However, the quality of the frequency distributions at those stations which Av0 was unable to improve (i. e., IF, ZS, and LT) are only partly improved. The distribution of wind speed at SP gets worse, in addition. The time-dependent statistics in the Hohe Tauern region are more improved by Bv0 than by Av0: $\vec{V}_{rmse}$ has smaller values than ERA-40 at the stations RH, SH, and SB, and $s_{V,d}$ is smaller than ERA-40 at SB as well. Only $s_{V,d}$ at IF becomes larger than ERA-40.

Overviews of the statistics for configuration Cv0, which is distinguished by very highly resolved grids (1 km grid spacing) for MM5 (domains C3a and C3b), are provided by Table 4.8 and Table 4.9 together with the probabilities that the statistics of Cv0 and Av0 are drawn from the same sample. Significant deviations from Av0 can be identified by significances < 0.05.

In the Hohe Tauern region the frequency distributions of Cv0 significantly deviate from the statistics of Av0 in both downscaling-steps (MM5 and CALMET) (cf. Table 4.8. The station-averaged statistics are improved for $\overline{V}_{bias}$, KS_V, KP_ϕ, $\vec{V}_{rmse}$, r_V, and $s_{V,d}$, but $\overline{\phi}_{bias}$ and $s_{\phi,d}$ get worse. In the Vienna Basin the wind speed distribution at WU

Table 4.8: Annual (year 1999) error statistics (cf. Table 4.2) of Cv0 (upper panel) and its intermediate dynamic downscaling-step (lower panel) at the stations in the Hohe Tauern region (cf. Table 4.1) along with the ratio of valid data (Val.), the observed mean wind speed ($\overline{V}_o$), and the observed mean wind direction ($\overline{\phi}_o$). Significant deviations from Av0 (parentheses) and differences between the downscaling-steps (brackets) are indicated by significances < 0.05.

Station Abbr.	Val. [1]	$\overline{V}_o$ [m/s]	$\overline{\phi}_o$ [°]	$\overline{V}_{bias}$ [m/s]	$\overline{\phi}_{bias}$ [°]	KS_V [1]	KP_ϕ [1]	$\vec{V}_{rmse}$ [m/s]	r_V [1]	$s_{V,d}$ [m/s]	$s_{\phi,d}$ [°]
Configuration Cv0 (combined application of MM5 setup C and CALMET v0), 200 m grid spacing											
IF	0.77	2.5	223.1	0.3	-33.1	0.14 (<0.01) [<0.01]	0.26 (<0.01) [<0.01]	4.4	-0.06	3.0	111.9
PK	0.56	6.2	346.8	-2.2	135.7	0.16 (<0.01) [<0.01]	0.29 (<0.01) [<0.01]	7.0	0.66	4.4	84.6
HK	0.91	2.8	264.9	1.4	4.2	0.17 (<0.01) [<0.01]	0.12 (<0.01) [<0.01]	4.7	0.46	3.5	69.9
RH	0.90	5.4	239.1	0.4	-173.9	0.16 (<0.01) [0.01]	0.29 (<0.01) [<0.01]	6.4	0.57	4.4	74.8
ZS	0.88	1.6	293.7	0.7	-23.7	0.19 (<0.01) [<0.01]	0.28 (<0.01) [<0.01]	3.6	0.10	2.3	151.7
SH	0.95	5.0	244.4	0.2	24.0	0.08 (<0.01) [<0.01]	0.28 (<0.01) [<0.01]	6.2	0.38	4.2	73.3
SB	0.77	10.2	311.6	0.6	-5.6	0.10 (<0.01) [<0.01]	0.22 (<0.01) [<0.01]	12.6	0.53	6.1	66.4
EB	0.15	5.0	136.4	-0.0	-35.2	0.13 (<0.01) [<0.01]	0.41 (<0.01) [<0.01]	4.1	0.68	3.0	60.4
ave	0.82	4.7	267.2	0.3	-3.8	0.14	0.25	6.8	0.40	4.1	94.4
Dynamic downscaling-step (MM5 domain C3a), 5 km grid spacing											
IF	0.77	2.5	223.1	1.3	72.0	0.29 (<0.01)	0.31 (<0.01)	5.7	0.31	2.8	113.9
PK	0.56	6.2	346.8	-1.2	116.3	0.08 (<0.01)	0.23 (<0.01)	6.9	0.71	4.1	75.9
HK	0.91	2.8	264.9	2.3	-24.8	0.31 (<0.01)	0.30 (<0.01)	5.3	0.46	3.7	68.5
RH	0.90	5.4	239.1	0.8	28.6	0.17 (<0.01)	0.15 (<0.01)	5.9	0.62	4.2	70.5
ZS	0.88	1.6	293.7	2.1	-149.0	0.54 (<0.01)	0.28 (<0.01)	4.8	0.04	2.8	131.1
SH	0.95	5.0	244.4	1.5	34.0	0.14 (<0.01)	0.46 (<0.01)	7.2	0.44	4.5	65.1
SB	0.77	10.2	311.6	0.1	-9.2	0.05 (<0.01)	0.19 (<0.01)	12.8	0.50	6.2	68.9
EB	0.15	5.0	136.4	0.1	-14.6	0.24 (<0.01)	0.20 (<0.01)	4.0	0.68	3.0	58.2
ave	0.82	4.7	267.2	1.1	25.2	0.24	0.28	7.2	0.45	4.1	87.7

Table 4.9: Same as Table 4.8, but for the Vienna Basin.

Station Abbr.	Val. [1]	$\overline{V}_o$ [m/s]	$\overline{\phi}_o$ [°]	$\overline{V}_{bias}$ [m/s]	$\overline{\phi}_{bias}$ [°]	KS_V [1]	KP_ϕ [1]	$\vec{V}_{rmse}$ [m/s]	r_V [1]	$s_{V,d}$ [m/s]	$s_{\phi,d}$ [°]
Configuration Cv0 (combined application of MM5 setup C and CALMET v0), 200 m grid spacing											
GE	0.95	3.4	297.9	1.2	-4.3	0.23 (<0.01) [>0.99]	0.11 (0.56) [<0.01]	3.9	0.56	2.0	61.4
GK	0.88	2.9	298.2	1.9	0.7	0.29 (<0.01) [<0.01]	0.20 (<0.01) [<0.01]	4.1	0.52	2.6	60.5
LB	0.23	7.4	222.2	-0.6	53.4	0.08 (<0.01) [<0.01]	0.20 (0.15) [<0.01]	7.2	0.52	2.9	65.3
LT	0.96	3.2	256.0	1.4	34.9	0.26 (<0.01) [<0.01]	0.55 (<0.01) [<0.01]	4.1	0.60	2.3	58.6
NE	0.96	3.4	339.2	1.5	-16.7	0.25 (0.02) [0.06]	0.12 (<0.01) [<0.01]	4.1	0.53	2.2	61.7
SP	0.94	3.2	252.8	1.0	3.4	0.17 (<0.01) [<0.01]	0.19 (<0.01) [0.02]	3.4	0.57	2.1	62.3
HW	0.94	3.5	293.1	1.1	-4.2	0.20 (0.01) [<0.01]	0.16 (<0.01) [<0.01]	3.8	0.51	2.4	59.6
WU	0.94	4.0	283.3	0.5	3.2	0.15 (<0.01) [<0.01]	0.09 (0.06) [<0.01]	3.6	0.54	2.3	56.1
ZD	0.89	3.8	279.0	0.7	8.7	0.17 (<0.01) [>0.99]	0.04 (0.21) [0.09]	3.5	0.58	2.1	58.1
ave	0.91	3.5	285.3	1.1	4.4	0.21	0.18	4.0	0.55	2.3	60.0
Dynamic downscaling-step (MM5 domain C3b), 1 km grid spacing											
GE	0.95	3.4	297.9	1.2	-0.7	0.23 (<0.01)	0.10 (<0.01)	3.8	0.56	2.0	61.4
GK	0.88	2.9	298.2	2.2	-5.6	0.33 (<0.01)	0.16 (<0.01)	4.2	0.48	2.6	58.3
LB	0.23	7.4	222.2	-1.0	61.2	0.15 (<0.01)	0.22 (<0.01)	7.2	0.50	2.9	66.2
LT	0.96	3.2	256.0	0.7	4.9	0.12 (<0.01)	0.16 (<0.01)	3.3	0.55	2.2	59.6
NE	0.96	3.4	339.2	1.6	-7.0	0.27 (<0.01)	0.13 (<0.01)	4.1	0.53	2.2	61.3
SP	0.94	3.2	252.8	1.4	4.2	0.24 (0.06)	0.17 (<0.01)	3.7	0.56	2.2	62.3
HW	0.94	3.5	293.1	1.6	-3.1	0.26 (<0.01)	0.07 (<0.01)	4.1	0.50	2.6	58.1
WU	0.94	4.0	283.3	0.7	7.2	0.18 (0.30)	0.10 (<0.01)	3.8	0.54	2.3	56.3
ZD	0.89	3.8	279.0	0.7	13.7	0.17 (<0.01)	0.05 (<0.01)	3.5	0.58	2.1	58.3
ave	0.91	3.5	285.3	1.2	3.2	0.22	0.12	4.0	0.54	2.3	59.7

for MM5 and the distribution of wind direction at GE, LB, WU, and ZD for CALMET do not significantly deviate from those of Av0. However, all station-averaged statistics are slightly improved, except $\overline{\phi}_{bias}$. Among the MM5 variants, Cv0 shows the smallest station-averaged values for $\overline{V}_{bias}$, KS_V, KP_ϕ, and $\vec{V}_{rmse}$ in both study regions: 0.3 m/s, 0.14, 0.25, and 6.8 m/s in the Hohe Tauern region and 1.1 m/s 0.21, 0.18, 4.0 m/s in the Vienna Basin (cf. Figure 4.6). The averaged correlation coefficients (r_V and $r_{\vec{V}}$) lie between those of Av0 and Bv0 and $s_{\vec{V},n}$ is closest to the observations (0.98 in the Hohe Tauern region and 1.23 in the Vienna Basin, cf. Figure 4.7).

Comparing Cv0 with Av0 station by station it can be seen that the station-averaged improvements in both study regions are mostly based on systematic reductions of the downscaling-errors: in the Hohe Tauern region $\overline{V}_{bias}$, KS_V, $\vec{V}_{rmse}$, r_V, and $s_{V,d}$ are improved at 6 stations (only at IF the statistics get worse) and the spreads across the stations are reduced for $\overline{V}_{bias}$, KS_V, and $s_{V,d}$. In the Vienna Basin $\overline{V}_{bias}$, $\overline{\phi}_{bias}$, KS_V, and r_V are reduced at 7 stations, r_V and $s_{\phi,d}$ are reduced at 8 stations. A reduction of the spreads can be found throughout the statistics except for $\overline{V}_{bias}$. Largest improvements can again be found at ZS for $\overline{V}_{bias}$, $\overline{\phi}_{bias}$, KS_V, KP_ϕ, $\vec{V}_{rmse}$, and $s_{V,d}$ where the statistics are changed to 0.7 m/s, $-23.7°$, 0.19, 0.28, 3.6 m/s, and 2.3 m/s, respectively. Hence the frequency distribution of wind speed at ZS is captured best with Cv0 (cf. Figure 4.4). However, the modelled and observed wind speeds and directions at ZS are still decoupled from each other leading to both, the same r_V (0.10) as it was found for Bv0 and the largest standard-deviation of the directional model errors ($s_{\phi,d}$ at ZS is increased to 151.7°). Strong improvements can also be found for PK (KP_ϕ is changed from 0.47 for Av0 to 0.29), HK (KS_V and KP_ϕ are changed to 0.17 and 0.12, respectively), and RH (r_V is increased from 0.16 to 0.57). Note $\overline{\phi}_{bias}$ at RH is strongly increased from 71.1° (Av0) to $-173.9°$, but since the distribution of the wind directions is qualitatively nearly unchanged (KP_ϕ is changed from 0.31 to 0.29) this effect is related to the multi-modal structure of the distribution reducing the evidence of $\overline{\phi}_{bias}$. In the Vienna Basin the improvements are of smaller extent. Largest improvements can be found for $\overline{V}_{bias}$ and KS_V at SP which are changed from 1.8 m/s and 0.29 (Av0) to 1.0 m/s and 0.17, respectively.

Similar to Bv0 the application of CALMET v0 improves $\overline{V}_{bias}$, $\overline{\phi}_{bias}$, KS_V and KP_ϕ of MM5 in the Hohe Tauern region (domain C3a) at 6, 5, 6, and 3 stations (cf. Table 4.8), respectively. Unlike Av0 and Bv0, $\vec{V}_{rmse}$ is reduced at 5 stations leading to a notable reduction of the station-averaged $\vec{V}_{rmse}$ of about -0.4 m/s. In addition, the station-averaged $\overline{V}_{bias}$ is reduced about -0.8 m/s. The spreads of the statistics are quite unaffected, except for KS_V which is strongly reduced due to the improvement of ZS: KS_V is changed from 0.54 (C3a) to 0.19 (v0). This also reduces $\overline{V}_{bias}$ from 2.1 m/s to 0.7 m/s. The time-dependent statistics $\vec{V}_{rmse}$ and r_V are improved at 5 and 3 stations respectively, but the improvements of r_V in Bv0 are not reached. For $s_{\vec{V},n}$ and $r_{\vec{V}}$ no clear improvements can be found on the station-level and the station-averages nearly stay the same (cf. Figure 4.7). In the Vienna Basin $\overline{V}_{bias}$ and KS_V is reduced at 6 stations (Table 4.9), which is much more than for configuration Av0 and Bv0. However, this has only weak consequences for the station-averaged statistics: $\overline{V}_{bias}$ and KS_V are reduced about -0.1 m/s and -0.01, respectively. The large improvements of the frequency distributions (KS_V) at LB and HW found for Av0 (see above) nearly

disappeared: although MM5 captures the distributions in a better way, CALMET is not able to further improve these results. Nevertheless, $|\overline{V}_{bias}|$ is reduced about -0.4 m/s (LB) and -0.5 m/s (HW). Similar to Av0 and Bv0 $\overline{V}_{bias}$, KS_V, KP_ϕ, $\vec{V}_{rmse}$, and $s_{V,d}$ get worse at LT, although r_V is gradually improved. Furthermore, the spread of $\overline{V}_{bias}$ is notably reduced about -0.7 m/s indicating a better characterisation of the downscaling-error due to the application of CALMET v0. This behaviour is also reflected by $s_{\vec{V},n}$ and $r_{\vec{V}}$ in Figure 4.7, where the single stations are more concentrated around their averaged central point, which lies closest to the observations.

Note Cv0 outperforms ERA-40 in all station-averaged statistics in both study regions. But ERA-40's distributions at the critical stations IF, ZS, and LT are still not reached by Cv0 (cf. Figure 4.4 and cf. Figure 4.5), however Cv0 partly reaches the best results at those stations when compared to Av0 and Bv0 (0.19 at ZS and 0.26 at LT for KS_V) and additional degradations are avoided.

From the evaluation results it can be concluded that the MM5 variant C3 provides wind fields which in average fit the observations best with respect to frequency distributions of wind speed and direction in both study regions. It can also be concluded that CALMET v0 is able to further improve MM5's wind fields leading to the best station-averaged results with the smallest station-by-station variability for most of the statistics.

4.3.2 CALMET Improvements

The modified versions of CALMET are driven by the simulation results of the MM5 variant C3 in both study regions.

The time-independent and time-dependent statistics of CALMET variant v1, which is distinguished by a modified calculation of the air-density influencing slope-flows (cf. Section 3.3.1), are nearly identical to those of variant v0 and the hypothesis-test for KS_V and KP_ϕ give possibilities close to 1.00 that the distributions are drawn from the same sample (cf. Table 4.10). Just $\overline{V}_{bias}$ deviates from v0 at 6 stations within the range of $\pm 0.3°$. This behaviour is also depicted by the station-averaged frequency distributions (cf. Figure 4.8) and the Taylor-plots summarising the time-depending statistics (cf. Figure 4.9), although the influence of the re-considered calculation of the air-density on the slope-flow's velocity in the Hohe Tauern region is estimated to lie within a range between 1.7 % and 10 % depending on the altitude (cf. Section 3.3.1). Since in CALMET the slope-flows are modifying the velocities of the underlying (divergence-free) wind fields $\vec{V}_1^{CAL} = (U_1^{CAL}, V_1^{CAL})$ (cf. Section 2.2.2), the relative effects of adjusted slope-flows on the final wind fields are damped based on $|\vec{V}_1^{CAL}|$: wind fields with low velocities are relatively more affected than high velocities. Therefore, considerable impact would be expected at ZS which has the smallest observed mean wind speed (1.6 m/s, cf. Table 4.10) in the Hohe Tauern region. However, ZS is located at the bottom of a deep valley at 766 m (cf. Table 4.1) which reduces the effect of the re-considered air-density calculation.

Due to the lower altitudes in the Vienna Basin the influence of the adjusted air-density on the slope-flow's velocities is expected to be smaller than 1 % (cf. Section 3.3.1) in any case. Moreover, since the orography is flatter than in the Hohe Tauern region

Table 4.10: Annual (year 1999) error statistics (cf. Table 4.2) of Cv1 at the stations in the Hohe Tauern region (upper panel) and the Vienna Basin (lower panel) (cf. Table 4.1) along with the ratio of valid data (Val.), the observed mean wind speed ($\overline{V}_o$), and the observed mean wind direction ($\overline{\phi}_o$). Significant deviations from Cv0 (brackets) are indicated by significances < 0.05.

Station Abbr.	Val. [1]	$\overline{V}_o$ [m/s]	$\overline{\phi}_o$ [°]	$\overline{V}_{bias}$ [m/s]	$\overline{\phi}_{bias}$ [°]	KS_V [1]	KP_ϕ [1]	$\vec{V}_{rmse}$ [m/s]	r_V [1]	$s_{V,d}$ [m/s]	$s_{\phi,d}$ [°]
Configuration Cv1 (combined application of MM5 setup C and CALMET v1), Hohe Tauern region, 200 m grid spacing											
IF	0.77	2.5	223.1	0.3	-33.1	0.14 [>0.99]	0.26 [>0.99]	4.4	-0.05	3.0	111.9
PK	0.56	6.2	346.8	-2.2	135.6	0.15 [>0.99]	0.29 [>0.99]	7.0	0.66	4.4	84.7
HK	0.91	2.8	264.9	1.4	4.0	0.17 [>0.99]	0.11 [>0.99]	4.7	0.46	3.5	70.2
RH	0.90	5.4	239.1	0.4	-173.6	0.16 [>0.99]	0.29 [0.08]	6.5	0.57	4.4	75.1
ZS	0.88	1.6	293.7	0.7	-23.6	0.19 [>0.99]	0.28 [>0.99]	3.6	0.10	2.3	151.8
SH	0.95	5.0	244.4	0.2	24.2	0.08 [>0.99]	0.28 [>0.99]	6.2	0.38	4.2	73.0
SB	0.77	10.2	311.6	0.6	-5.5	0.10 [>0.99]	0.22 [>0.99]	12.6	0.53	6.1	66.4
EB	0.15	5.0	136.4	0.0	-35.1	0.13 [>0.99]	0.42 [0.99]	4.1	0.68	3.0	60.4
ave	0.82	4.7	267.2	0.3	-3.9	0.14	0.25	6.8	0.40	4.1	94.5
Configuration Cv1 (combined application of MM5 setup C and CALMET v1), Vienna Basin, 200 m grid spacing											
GE	0.95	3.4	297.9	1.2	-4.3	0.23 [>0.99]	0.11 [>0.99]	3.9	0.56	2.0	61.4
GK	0.88	2.9	298.2	1.9	0.8	0.29 [>0.99]	0.20 [>0.99]	4.1	0.52	2.6	60.5
LB	0.23	7.4	222.2	-0.6	53.4	0.08 [>0.99]	0.20 [>0.99]	7.2	0.52	2.9	65.3
LT	0.96	3.2	256.0	1.4	35.0	0.26 [>0.99]	0.55 [>0.99]	4.1	0.60	2.3	58.6
NE	0.96	3.4	339.2	1.5	-16.8	0.25 [>0.99]	0.12 [>0.99]	4.1	0.53	2.2	61.7
SP	0.94	3.2	252.8	1.0	3.4	0.17 [>0.99]	0.19 [>0.99]	3.4	0.57	2.1	62.3
HW	0.94	3.5	293.1	1.1	-4.2	0.20 [>0.99]	0.16 [>0.99]	3.8	0.51	2.4	59.7
WU	0.94	4.0	283.3	0.5	3.2	0.15 [>0.99]	0.09 [>0.99]	3.6	0.54	2.3	56.1
ZD	0.89	3.8	279.0	0.7	8.7	0.17 [>0.99]	0.04 [>0.99]	3.5	0.58	2.1	58.1
ave	0.91	3.5	285.3	1.1	4.4	0.21	0.18	4.0	0.55	2.3	60.0

Table 4.11: Same as Table 4.10, but for configuration Cv2.

Station Abbr.	Val. [1]	$\overline{V}_o$ [m/s]	$\overline{\phi}_o$ [°]	$\overline{V}_{bias}$ [m/s]	$\overline{\phi}_{bias}$ [°]	KS_V [1]	KP_ϕ [1]	$\vec{V}_{rmse}$ [m/s]	r_V [1]	$s_{V,d}$ [m/s]	$s_{\phi,d}$ [°]
Configuration Cv2 (combined application of MM5 setup C and CALMET v2), Hohe Tauern region, 200 m grid spacing											
IF	0.77	2.5	223.1	0.3	-34.0	0.13 [0.78]	0.27 [<0.01]	4.4	-0.07	3.0	110.6
PK	0.56	6.2	346.8	-2.1	148.2	0.14 [<0.01]	0.30 [<0.01]	7.1	0.67	4.4	92.4
HK	0.91	2.8	264.9	1.4	5.4	0.16 [<0.01]	0.12 [<0.01]	4.6	0.45	3.4	69.6
RH	0.90	5.4	239.1	0.5	-168.5	0.19 [<0.01]	0.32 [<0.01]	6.4	0.58	4.3	77.2
ZS	0.88	1.6	293.7	0.7	-19.0	0.19 [>0.99]	0.31 [<0.01]	3.6	0.10	2.3	147.7
SH	0.95	5.0	244.4	0.2	21.8	0.08 [0.68]	0.27 [<0.01]	6.3	0.38	4.2	76.0
SB	0.77	10.2	311.6	0.7	-5.8	0.10 [>0.99]	0.22 [0.95]	12.6	0.53	6.1	66.6
EB	0.15	5.0	136.4	0.5	-37.2	0.29 [<0.01]	0.44 [<0.01]	4.3	0.66	3.1	63.8
ave	0.82	4.7	267.2	0.4	-6.8	0.15	0.26	6.8	0.40	4.1	94.6
Configuration Cv2 (combined application of MM5 setup C and CALMET v2), Vienna Basin, 200 m grid spacing											
GE	0.95	3.4	297.9	1.2	-4.3	0.23 [>0.99]	0.11 [>0.99]	3.9	0.56	2.0	61.4
GK	0.88	2.9	298.2	2.0	1.4	0.30 [<0.01]	0.20 [<0.01]	4.1	0.51	2.6	60.6
LB	0.23	7.4	222.2	-0.6	53.5	0.08 [>0.99]	0.20 [>0.99]	7.2	0.52	2.9	65.3
LT	0.96	3.2	256.0	1.5	36.5	0.30 [<0.01]	0.56 [<0.01]	4.1	0.59	2.1	59.3
NE	0.96	3.4	339.2	1.5	-16.2	0.25 [>0.99]	0.12 [>0.99]	4.1	0.53	2.2	61.6
SP	0.94	3.2	252.8	1.0	3.4	0.17 [>0.99]	0.19 [>0.99]	3.4	0.57	2.1	62.3
HW	0.94	3.5	293.1	1.1	-3.5	0.19 [>0.99]	0.17 [0.86]	3.8	0.51	2.4	59.9
WU	0.94	4.0	283.3	0.5	1.5	0.15 [>0.99]	0.09 [>0.99]	3.6	0.54	2.3	56.1
ZD	0.89	3.8	279.0	0.7	8.7	0.17 [>0.99]	0.04 [>0.99]	3.5	0.58	2.1	58.1
ave	0.91	3.5	285.3	1.1	4.6	0.22	0.19	4.0	0.55	2.2	60.1

Table 4.12: Same as Table 4.10, but for configuration Cv3.

Station Abbr.	Val. [1]	$\overline{V}_o$ [m/s]	$\overline{\phi}_o$ [°]	$\overline{V}_{bias}$ [m/s]	$\overline{\phi}_{bias}$ [°]	KS_V [1]	KP_ϕ [1]	$\vec{V}_{rmse}$ [m/s]	r_V [1]	$s_{V,d}$ [m/s]	$s_{\phi,d}$ [°]
Configuration Cv3 (combined application of MM5 setup C and CALMET v3), Hohe Tauern region, 200 m grid spacing											
IF	0.77	2.5	223.1	-0.3	-46.1	0.09 [<0.01]	0.44 [<0.01]	4.1	-0.01	2.8	109.6
PK	0.56	6.2	346.8	-1.4	-106.4	0.09 [<0.01]	0.54 [<0.01]	7.6	0.68	4.3	81.9
HK	0.91	2.8	264.9	2.0	26.3	0.27 [<0.01]	0.27 [<0.01]	5.2	0.50	3.5	69.2
RH	0.90	5.4	239.1	0.1	126.7	0.14 [<0.01]	0.28 [<0.01]	6.2	0.57	4.3	75.1
ZS	0.88	1.6	293.7	0.4	-32.6	0.13 [<0.01]	0.38 [<0.01]	3.2	0.12	2.0	143.3
SH	0.95	5.0	244.4	1.5	37.4	0.13 [<0.01]	0.41 [<0.01]	7.4	0.42	4.7	69.4
SB	0.77	10.2	311.6	2.1	-9.5	0.16 [<0.01]	0.21 [<0.01]	13.8	0.57	6.3	66.8
EB	0.15	5.0	136.4	0.0	-32.2	0.07 [<0.01]	0.36 [<0.01]	4.3	0.70	3.1	63.9
ave	0.82	4.7	267.2	0.7	-1.3	0.15	0.35	7.3	0.43	4.1	91.4
Configuration Cv3 (combined application of MM5 setup C and CALMET v3), Vienna Basin, 200 m grid spacing											
GE	0.95	3.4	297.9	1.2	-0.7	0.23 [0.26]	0.09 [<0.01]	3.8	0.53	2.0	60.9
GK	0.88	2.9	298.2	1.3	0.1	0.21 [<0.01]	0.21 [<0.01]	3.6	0.49	2.5	60.4
LB	0.23	7.4	222.2	0.8	53.5	0.17 [<0.01]	0.20 [0.82]	8.1	0.50	3.2	64.9
LT	0.96	3.2	256.0	0.5	42.3	0.14 [<0.01]	0.58 [<0.01]	3.7	0.60	1.9	60.0
NE	0.96	3.4	339.2	1.1	-17.1	0.20 [<0.01]	0.14 [0.06]	3.8	0.50	2.1	61.7
SP	0.94	3.2	252.8	0.7	6.7	0.12 [<0.01]	0.13 [<0.01]	3.2	0.55	2.0	62.6
HW	0.94	3.5	293.1	1.3	-4.2	0.22 [0.03]	0.14 [0.22]	3.9	0.52	2.4	59.0
WU	0.94	4.0	283.3	0.8	5.1	0.19 [<0.01]	0.08 [0.56]	3.8	0.54	2.4	55.8
ZD	0.89	3.8	279.0	0.7	12.6	0.15 [0.01]	0.05 [0.15]	3.6	0.56	2.2	58.3
ave	0.91	3.5	285.3	0.9	6.7	0.18	0.18	3.9	0.54	2.2	60.1

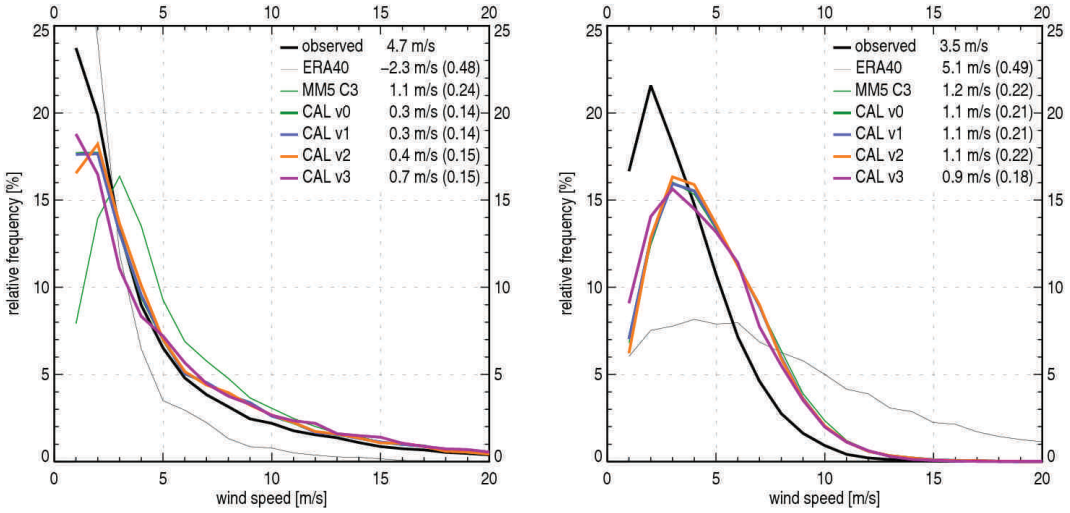

(a) **(b)**

Figure 4.8: Annual station-averaged modelled and observed frequency distributions of wind speed in (a) the Hohe Tauern region and (b) the Vienna Basin. The observations (thick black lines), the driving data ERA-40 (thin black lines), the CALMET-variants v0, v1, v2, and v3 (thick lines in green, blue, orange, and purple, respectively) driven by MM5 C3 (thin green lines) are shown. Observed mean values, the models' biases and the quality of the simulated distributions in terms of KS_V (in parentheses) are listed in the legends.

the slope-flows are much weaker pronounced in general.

Quite unnoticeable changes can also be found for variant v2 (cf. Table 4.11). v2 is characterised by a re-considered calculation of the sensible heat flux affecting the slope-flow parameterisation as well (cf. Section 3.3.2). But in contrast to v1, which only leads to increasing slope flows, changes of the sensible heat fluxes induces both, reductions and accelerations of the flows independently from surface altitude. This results in slightly stronger departures from v0: for KS_V and KP_ϕ significant deviations can be found at 4 and 7 (2 and 1) stations in the Hohe Tauern region (Vienna Basin), respectively. However, those deviations usually range within -0.02 and 0.04 (except EB) leading to gradually increased changes of the station-averaged mean statistics. Only at EB KS_V is increased from 0.13 (v0) to 0.29 which is based on a shift of the bi-modal distribution's first peak towards higher wind speeds (from 2 m/s for v0 and v1 to 4 m/s) (cf. Figure 4.10). Since EB was operating only during a three month period in autumn 1999, this increase of KS_V has only minor effect on the station-averaged distributions (cf. Figure 4.8).

In variant v3 the interpolation sequence for generating CALMET's initialisation fields is altered to take account for a) the actual PBL-height (simulated by MM5 C3) and CALMET's local surface roughness length (z_0^{CAL}) and b) the daytime/nighttime-

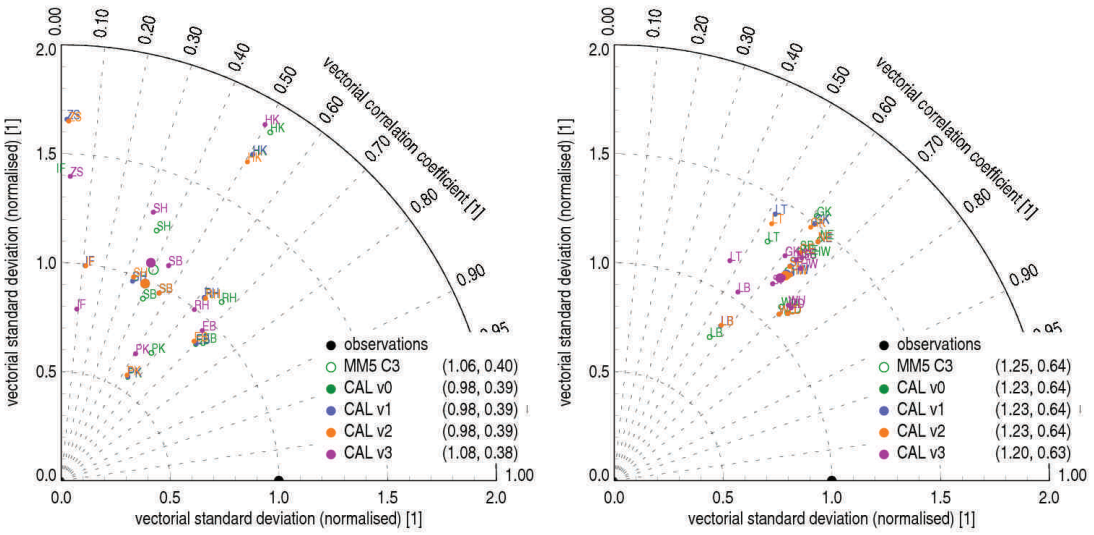

(a) **(b)**

Figure 4.9: Annual time-dependent vectorial statistics in (a) the Hohe Tauern region and (b) the Vienna Basin. The CALMET-variants v0, v1, v2, and v3 (green, blue, orange, and purple dots, respectively) driven by MM5 C3 (green circles) are shown for each station (small marks) (cf. Table 4.1). Station-averaged (large marks) normalised vectorial standard deviations ($s_{\vec{V},n}$) and vectorial correlation-coefficients ($r_{\vec{V}}$) are listed in the legends.

depending temperature-parameterisation for vertical extrapolations (cf. Section 3.3.3). This leads to drastic qualitative improvements in both study regions. The air-flows are much more influenced by local topography resulting in highly structured wind climatologies: e. g., the annual mean wind speed (cf. Figure 4.12) is more dominated by the orography and takes account for local features of the land-cover. Valleys and mountain ridges are stronger pronounced and even small changes of land-cover, like rivers, become visible in the simulation results. These qualitative improvements are partly reflected by the statistics.

In the Hohe Tauern region v3 leads to significant changes for KS_V and KP_ϕ at all stations (cf. Table 4.12). But the improvements of the frequency distributions (at 5 stations for KS_V and at 3 for KP_ϕ) are over-compensated by degradations resulting in increased station-averaged statistics: $\overline{V}_{bias}$, KS_V, KP_ϕ, and $\vec{V}_{rmse}$ are raised from 0.3 m/s, 0.14, 0.25, and 6.8 m/s (v0) to 0.7 m/s, 0.15, 0.35, and 7.3 m/s. The spreads of KS_V, KP_ϕ, and $\vec{V}_{rmse}$ are also slightly increased. A gradually improvement can be found for r_V which is increased from 0.40 (v0) to 0.43 along with a reduction its spread. Most contrary results can be found at PK (cf. Figure 4.10): $\overline{V}_{bias}$ and KS_V are reduced about -0.8 m/s and -0.07, while KP_ϕ and $\vec{V}_{rmse}$ are increased about 0.25 and 0.6 m/s, respectively, which is similar to the statistics at IF (cf. Figure 4.10). Those notable degradations of KP_ϕ are also found at HK, ZS, and SH. However, v2's degradation of KS_V at EB is countermanded and improved leading to its best time-independent

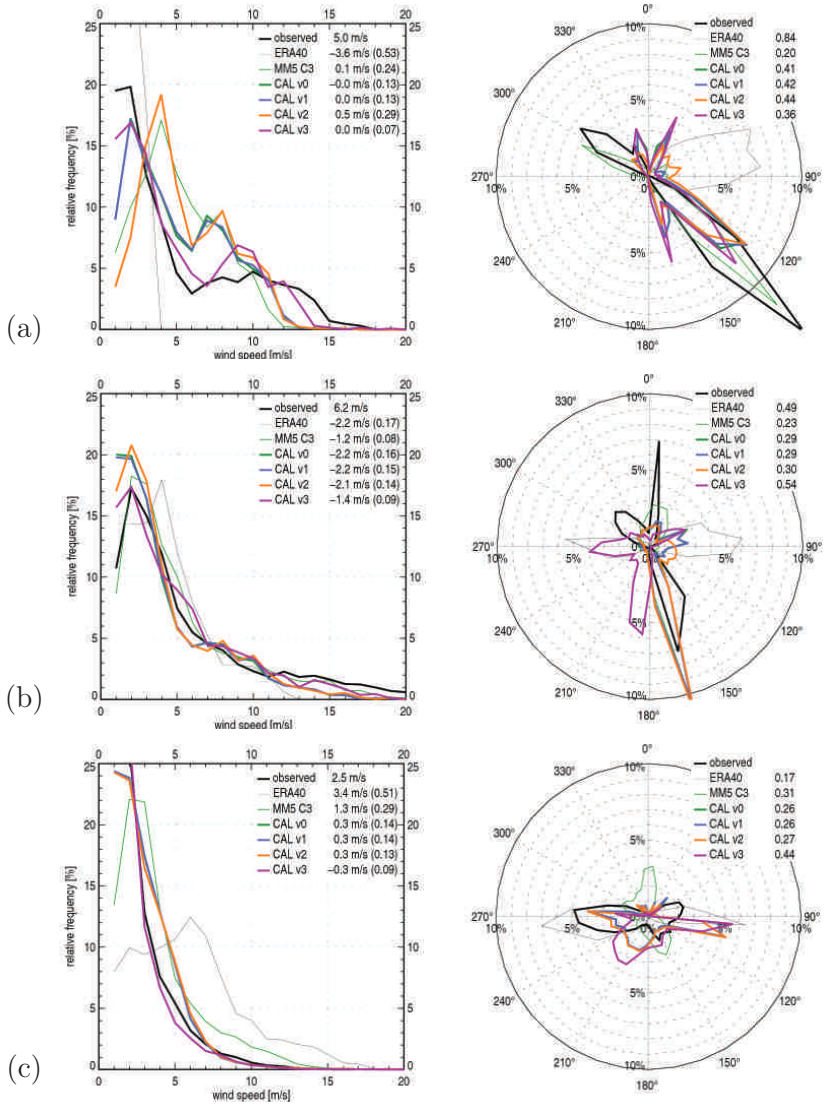

Figure 4.10: Modelled and observed frequency distributions of wind speed (left column) and direction (right column) from Jan 1 to Dec 31, 1999, in the Hohe Tauern region at stations (a) EB, (b) PK, and (c) IF (cf. Table 4.1). Observations (thick black lines), the driving data ERA-40 (thin black lines), MM5 C3 (thin green lines), and the CALMET-variants v0, v1, v2, and v3 (thick lines in green, blue, orange, and purple, respectively) are shown. Observed mean values, the models' biases and the quality of the simulated distributions in terms of KS_V (in parentheses) and KP_ϕ are listed in the legends.

statistics at all (cf. Figure 4.10). Note the contrariness of the time-independent statistics is also reflected by the station-averaged distributions (cf. Figure 4.8) and by the time-dependent vectorial statistics summarised in the Taylor-diagram (cf. Figure 4.9). Due to the compensation of the velocity-related improvements at some scattered stations by direction-related errors no clear changes of $s_{\vec{V},n}$ and $r_{\vec{V}}$ can be deduced in the Hohe Tauern region.

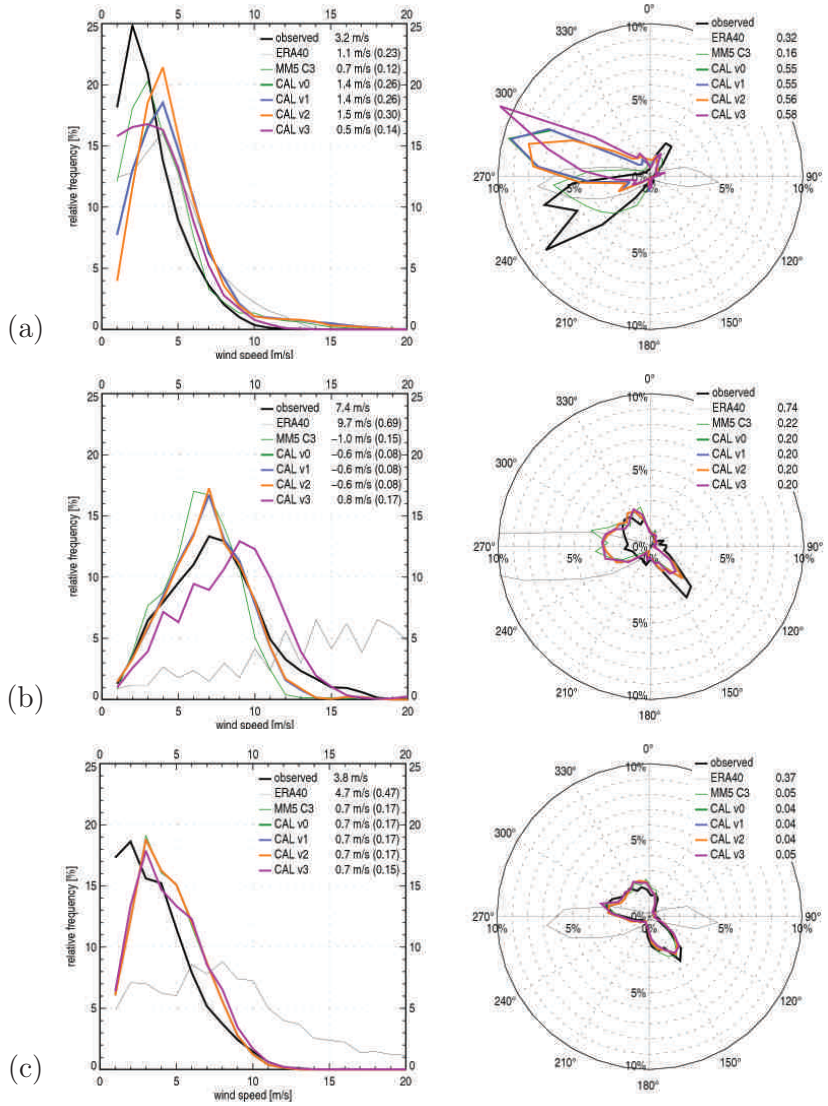

Figure 4.11: Same as Figure 4.10 but for the Vienna Basin at the stations (a) LT, (b) LB, and (c) ZD (cf. Table 4.1).

In the Vienna Basin v3 shows a quite different behaviour: significant changes of KS_V and KP_ϕ can be found at 8 and 4 stations respectively, leading to slightly improved averaged statistics of $\overline{V}_{bias}$ (reduction from v0's 1.1 m/s to 0.9 m/s) and KS_V (reduction from v0's 0.21 to 0.18), which is also depicted in the averaged frequency distributions (cf. Figure 4.8), along with notable reductions of their spreads (from v0's 2.5 m/s to 0.8 m/s and from v0's 0.21 to 0.11) and with a conversion of the single station-by-station velocity-related biases ($\overline{V}_{bias}$) to positive values (cf. Table 4.12). The station-averaged KP_ϕ as well as the time-dependent statistics $\vec{V}_{rmse}$, r_V, $s_{V,d}$ and $s_{\phi,d}$ are nearly left unchanged. Largest improvements can be found at LT where $\overline{V}_{bias}$ is reduced from 1.4 m/s (v0) to 0.5 m/s and KS_V from 0.26 (v0) to 0.14 (cf. Figure 4.11). In contrast, LB shows the largest degradations of the wind speed distribution: KS_V is significantly increased

from 0.08 (v0) to 0.17 and $\overline{V}_{bias}$ is changed from −0.6 m/s to 0.8 m/s (cf. Figure 4.11). Best results for the distributions of wind direction can still be found at ZD even if KP_{ϕ} is (insignificantly) increased from 0.04 (v0) to 0.05 (cf. Figure 4.11). Note the velocity-related improvements along with the minor direction-related changes are also reflected by the vectorial time-dependent normalised statistics $s_{\vec{V},n}$ and $r_{\vec{V}}$ shown in the Taylor-diagram (cf. Figure 4.9): the single marks for the stations are surrounding its slightly improved central point most densely, indicating a notable reduction of the random-part of the downscaling-error.

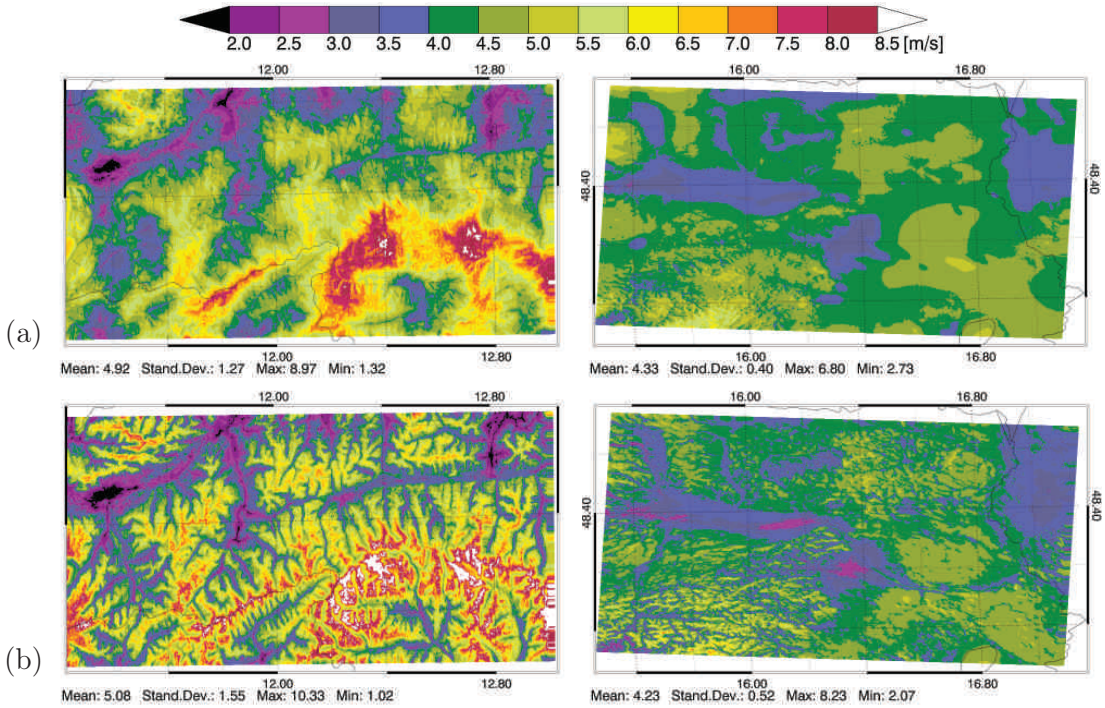

Figure 4.12: Simulated annual wind speed [m/s] at 10 m a.g.l. (period: Jan 1 to Dec 31, 1999) with 200 m × 200 m grid spacing modelled by the CALMET-variants (a) v0 and (b) v3 in the Hohe Tauern region (left column) and in the Vienna Basin (right column) (cf. Figure 4.1). CALMET is driven by MM5 domain C3 (dynamic initialisation) with 1 km × 1 km grid spacing in all cases.

In general, the magnitudes of the station-averaged mean values of the statistics are rather more affected by changes of MM5 than by changes of CALMET in both study regions: e. g., when MM5 is switched to B3 (C3) in the Hohe Tauern region $|\overline{V}_{bias}|$ and KS_V are reduced by −0.9 m/s and −0.1 (−1.4 m/s and −0.1) respectively, but they are increased by 0.4 m/s and 0.01 when CALMET is changed from v0 to v3 (cf. Table 4.13). This highlights the close linkage between the two models and pronounces the strong influence of the initial-fields for the diagnostic model.

Table 4.13: Changes of station-averaged annual statistics (cf. Table 4.2) and their spreads in the Hohe Tauern region and in the Vienna Basin when MM5 is switched from A2 to B3 and C3 and when CALMET is switched from v0 to v3.

Change of configuration	$\overline{V}_{bias}$ [m/s]	$\overline{\phi}_{bias}$ [°]	KS_V [1]	KP_ϕ [1]	$\vec{V}_{rmse}$ [m/s]	r_V [1]	$s_{V,d}$ [m/s]	$s_{\phi,d}$ [°]
Changes of mean values in the Hohe Tauern region								
Av0 → Bv0	-0.9	4.9	-0.08	-0.02	-0.8	0.11	-0.9	2.6
Av0 → Cv0	-1.4	1.7	-0.13	-0.05	-1.1	0.10	-0.9	12.1
Cv0 → Cv3	0.4	-2.5	0.01	0.10	0.5	0.03	0.0	-3.0
Changes of spreads in the Hohe Tauern region								
Av0 → Bv0	-0.7	5.2	-0.24	-0.01	1.1	-0.08	-1.1	20.4
Av0 → Cv0	-0.3	107.2	-0.40	0.03	0.8	0.07	-0.7	46.7
Cv0 → Cv3	-0.1	-76.5	0.09	0.04	1.6	-0.03	0.5	-11.9
Changes of mean values in the Vienna Basin								
Av0 → Bv0	0.6	15.0	0.10	0.02	0.2	0.03	-0.1	-3.8
Av0 → Cv0	-0.4	2.7	-0.06	-0.01	-0.3	0.01	-0.1	-0.6
Cv0 → Cv3	-0.2	2.3	-0.03	0.00	-0.1	-0.01	-0.1	0.1
Changes of spreads in the Vienna Basin								
Av0 → Bv0	-0.3	9.2	0.00	0.04	-0.1	0.01	-0.2	-3.0
Av0 → Cv0	0.2	-4.4	-0.12	0.00	-0.3	-0.03	-0.1	-0.2
Cv0 → Cv3	-1.7	0.5	-0.10	0.02	1.1	0.02	0.4	-0.1

4.3.3 Long-term Simulation with the Control Configuration

As pointed out in Section 4.1 a climate simulation (period Jan 1, 1981 00:00 UTC to Dec 31, 1990, 23:00 UTC) with the control-configuration Av0 (driven by the ERA-40 reanalysis) was conducted for the Alpine region (domain A2) and the Vienna Basin (CALMET study region). The comparison between modelled and observed air-flows at five observation-stations within the Vienna Basin (cf. Table 4.1) shows that Av0 overestimates the wind speeds of this ten-year period in a similar way as in the one-year period (cf. Section 4.3.1): Table 4.14 shows positive biases (between 1.1 m/s and 2.7 m/s) at all stations which is also reflected by the station-averaged frequency distribution (cf. Figure 4.13). Furthermore, the simulation results significantly deviate from the observations at all stations leading to decadal station-averaged statistics for $\overline{V}_{bias}$, $\overline{\phi}_{bias}$, KS_V, and KP_ϕ of 1.7 m/s, 4.0°, 0.29, and 0.14 (cf. Table 4.14), respectively. These results are similar to the one-year statistics. However, the number of stations for the ten-year period is reduced from 10 (one-year period) to 5, because the density of the observation-network of ZAMG was drastically increased later in time (during the nineteen-nineties). In addition, the fraction of valid data (0.68 for the station-average) is notably lower than in the one-year period (0.90). This is partly based on the date when the stations started to operate (e. g., NE started on June 22, 1984), which limits the number of possible data records, and partly based on the less reliability of the older stations. Nevertheless, due to the long simulation period the number of data records is still large enough to obtain statistically significant results: e. g., even if the fraction

Table 4.14: Decadal (period 1981 to 1990) error statistics (cf. Table 4.2) of Av0 (upper panel) and its intermediate dynamic downscaling-step (lower panel) at the stations in the Vienna Basin (cf. Table 4.1) along with the ratio of valid data (Val.), the observed mean wind speed ($\overline{V}_o$), and the observed mean wind direction ($\overline{\phi}_o$). Significant deviations from observations (parentheses) and differences between the downscaling-steps (brackets) are indicated by significances < 0.05.

Station Abbr.	Val. [1]	$\overline{V}_o$ [m/s]	$\overline{\phi}_o$ [°]	$\overline{V}_{bias}$ [m/s]	$\overline{\phi}_{bias}$ [°]	KS_V [1]	KP_ϕ [1]	$\vec{V}_{rmse}$ [m/s]	r_V [1]	$s_{V,d}$ [m/s]	$s_{\phi,d}$ [°]
Control configuration Av0 (combined application of MM5 setup A and CALMET v0), 200 m grid spacing											
GE	0.17	2.8	285.1	2.7	6.3	0.45 (<0.01) [<0.01]	0.10 (<0.01) [<0.01]	4.2	0.59	2.2	53.3
NE	0.59	3.1	338.6	1.8	-28.6	0.31 (<0.01) [<0.01]	0.11 (<0.01) [<0.01]	3.9	0.51	2.2	58.0
SD	0.65	3.0	263.9	2.5	20.9	0.37 (<0.01) [0.23]	0.13 (<0.01) [<0.01]	4.4	0.53	2.5	59.1
WI	0.57	3.3	265.8	1.6	16.1	0.26 (<0.01) [<0.01]	0.10 (<0.01) [<0.01]	3.7	0.56	2.3	54.4
HW	0.93	3.3	280.7	1.1	3.9	0.21 (<0.01) [<0.01]	0.19 (<0.01) [<0.01]	3.4	0.59	2.1	56.4
ave	0.68	3.2	284.6	1.7	4.0	0.29	0.14	3.9	0.56	2.3	56.8
Dynamic downscaling-step (MM5 domain A2), 10 km grid spacing											
GE	0.17	2.8	285.1	1.6	7.9	0.31 (<0.01)	0.12 (<0.01)	3.2	0.60	1.8	53.9
NE	0.59	3.1	338.6	2.1	-27.0	0.36 (<0.01)	0.11 (<0.01)	4.2	0.51	2.3	58.1
SD	0.65	3.0	263.9	2.4	28.7	0.37 (<0.01)	0.13 (<0.01)	4.4	0.52	2.5	59.7
WI	0.57	3.3	265.8	3.1	14.0	0.45 (<0.01)	0.12 (<0.01)	5.0	0.53	2.8	53.7
HW	0.93	3.3	280.7	2.6	4.1	0.39 (<0.01)	0.20 (<0.01)	4.6	0.57	2.5	54.8
ave	0.68	3.2	284.6	2.5	5.7	0.39	0.15	4.5	0.54	2.5	56.3

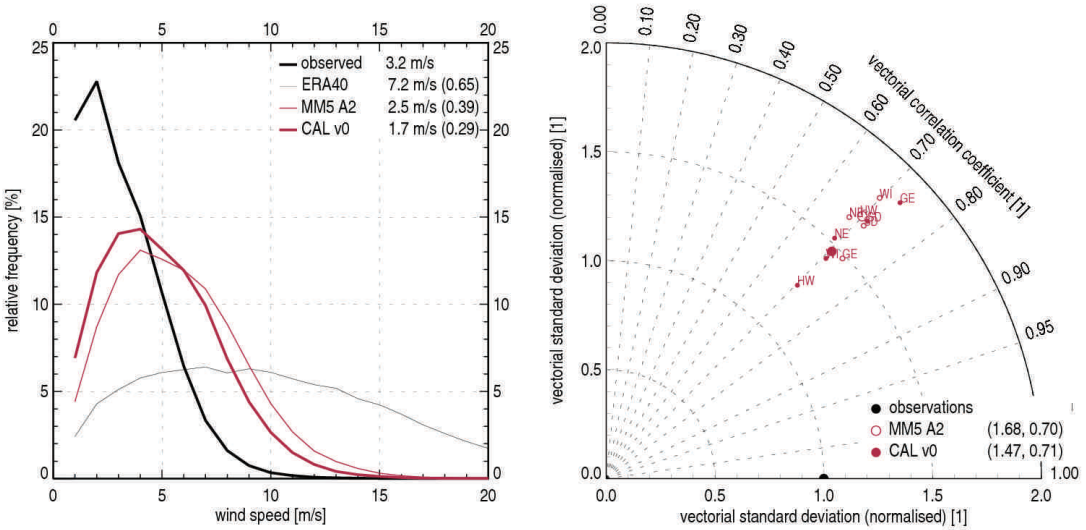

(a) **(b)**

Figure 4.13: Decadal station-averaged modelled and observed (a) frequency distributions of wind speed and (b) time-dependent vectorial statistics in the Vienna Basin. In (a) the observations (thick black line), the driving data ERA-40 (thin black line), the MM5 result A2 (thin red line), and CALMET v0 (thick red line) are shown; observed mean values, the models' biases and the quality of the simulated distributions in terms of KS_V (in parentheses) are listed in the legend. In (b) CALMET v0 (red dots) and MM5 A2 (red circles) are shown for each station (small marks) (cf. Table 4.1); the station-averaged (large marks) normalised vectorial standard deviations ($s_{\vec{V},n}$) and vectorial correlation-coefficients ($r_{\vec{V}}$) are listed in the legend.

of valid data at GE is 0.17 (cf. Table 4.14) the time-series still includes 15287 valid records.

Since $KS_V > KP_\phi$ at all stations the quality of the frequency distribution for wind direction is higher than the quality of the distribution of wind speeds. Due to the systematic overestimation of wind speed the normalised vectorial standard deviations ($s_{\vec{V},n}$) are larger than 1 at all stations (cf. Figure 4.13). However, the representation of wind directions positively influences the vectorial correlation coefficients ($r_{\vec{V}}$): they are higher than the scalar correlation coefficients (r_V), but they are bounded between approximately 0.65 and 0.75.

The distribution of wind speed is captured most properly at HW ($KS_V = 0.21$, Figure 4.14) leading to the smallest values for $\overline{V}_{bias}$, $\vec{V}_{rmse}$, and $s_{V,d}$ (i. e., 1.1 m/s, 3.4 m/s, and 2.1 m/s, respectively, cf. Table 4.14) and the best vectorial time-dependent statistics (cf. Figure 4.13) as well. The worst simulated distribution can be found at GE ($KS_V = 0.45$, Figure 4.14) with a bias ($\overline{V}_{bias}$) of 2.7 m/s which is nearly as large as the observed mean wind speed ($\overline{V}_o = 2.8$ m/s). However, since r_V at GE is quite high (0.59) the departure of the distribution is based on a notable part of a systematic error. Contrarily, the distributions of wind direction show highest quality at GE together with

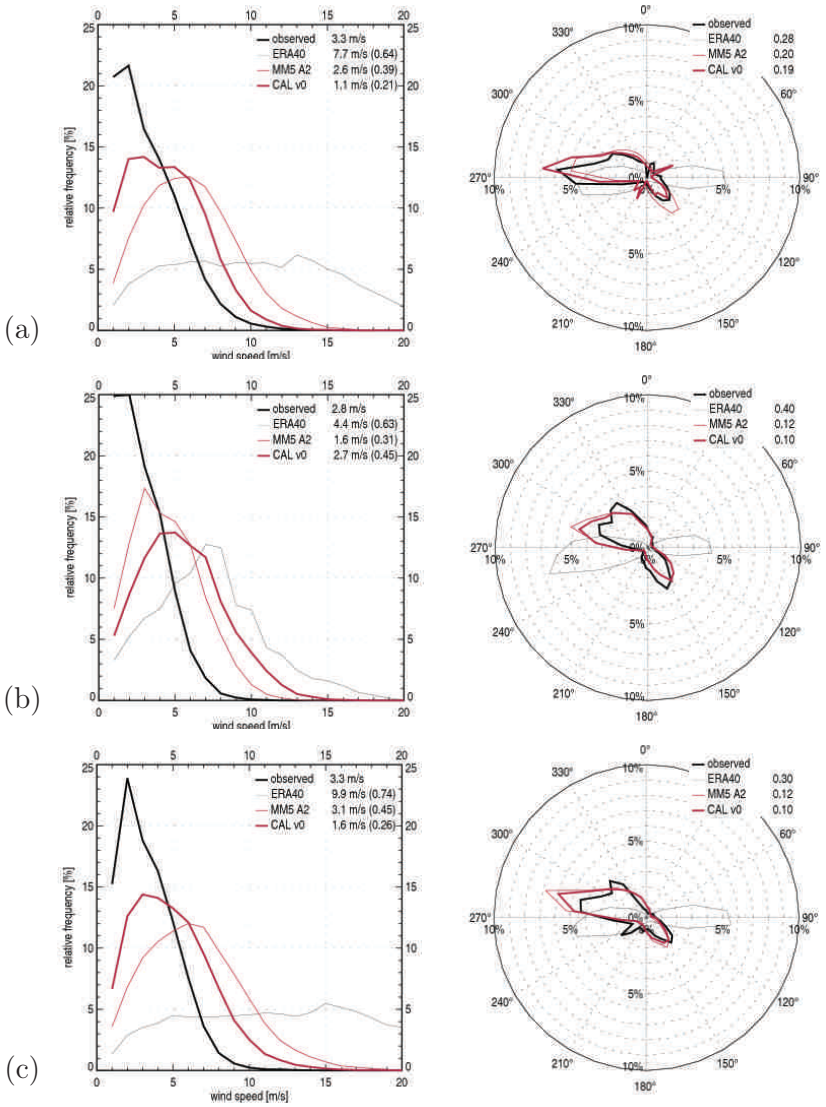

Figure 4.14: Modelled and observed frequency distributions of wind speed (left column) and direction (right column) from Jan 1, 1981, to Dec 31, 1990, in the Vienna Basin at stations (a) HW, (b) GE, and (c) WI (cf. Table 4.1). Observations (thick black lines), the driving data ERA-40 (thin black lines), MM5 A2 (thin red lines), and CALMET-variant v0 (thick red lines) are shown. Observed mean values, the models' biases and the quality of the simulated distributions in terms of KS_V (in parentheses) and KP_ϕ are listed in the legends.

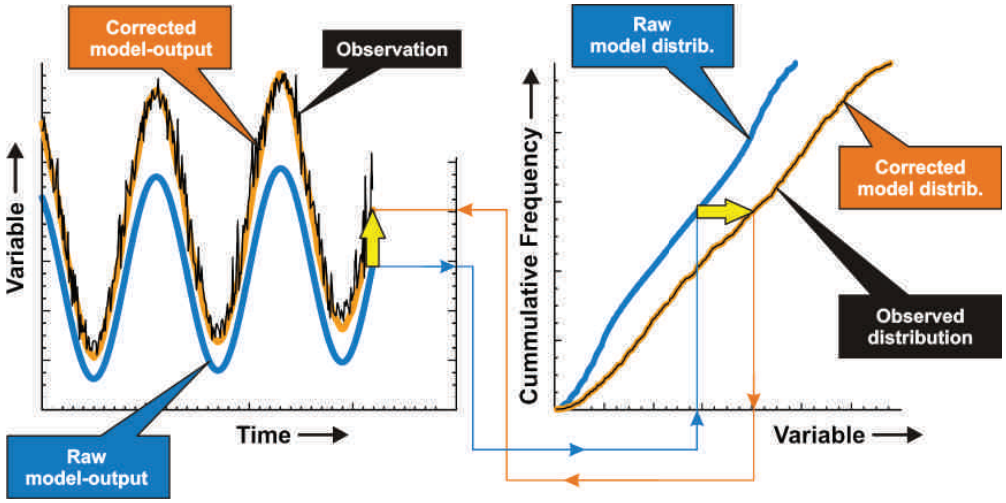

Figure 4.15: Schematic of the quantile mapping method. Raw model output (blue) is corrected (orange) by means of differences (yellow arrow) between modelled and observed (black) cumulative frequency distributions at constant quantiles derived during a training period.

WI ($KP_\phi = 0.10$, Figure 4.14) positively influencing $r_{\vec{V}}$ which reaches an overall value of 0.73 (cf. Figure 4.13).

Improvements for all statistics due to the application of CALMET can be found at three stations on average, but most drastic changes are related to the distributions of wind speed: the station-averaged KS_V is reduced from 0.39 (MM5) to 0.29 according to a reduction of $\overline{V}_{bias}$ from 2.5 m/s (MM5) to 1.7 m/s (cf. Table 4.14 and Figure 4.13) while the other statistics nearly stay at their level. However, the spread of KS_V is increased from 0.14 (MM5) to 0.24, which is based on an enhanced overestimation of wind speeds at GE increasing KS_V from 0.31 (MM5) to 0.45 (cf. Figure 4.14). Strongest improvements of KS_V up to the magnitude of 0.19 can be found at WI and HW along with a reduction of $\overline{V}_{bias}$ about -1.5 m/s. Both, the improvements and the degradations are of similar extend to those of the one-year simulation (cf. Av0 in Section 4.3.1).

Similar to the one-year simulations the ten-year simulation conducted with Av0 outperforms the statistics of the driving data (ERA40) on average and separately for each station (cf. Figure 4.13, Figure 4.14, and Section A.1).

4.4 Error Correction and Its Impact on Climate Simulations

The model-observation comparisons in Section 4.3 clearly show a notable reduction of ERA-40's model errors due to the application of the downscaling method. Nevertheless, significant deviations from observations remain. In order to reduce these remaining errors empirical-statistical methods are available. A review on methods for the preparation of error corrected data from raw model output for local climate im-

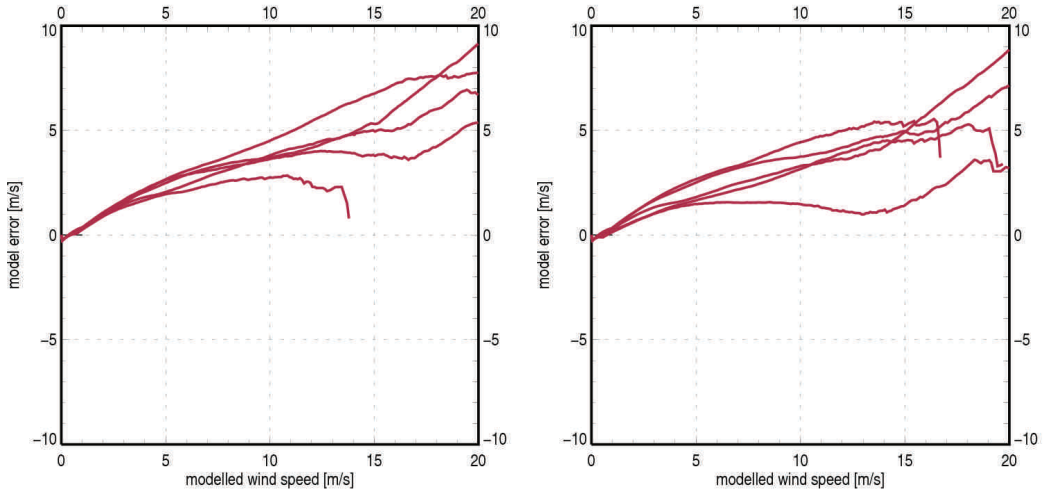

(a) **(b)**

Figure 4.16: Model error of the control configuration Av0 (period 1981 to 1990) as a function of simulated wind speeds at all stations in the Vienna Basin: (a) MM5 domain A2 (10 km grid spacing) and (b) CALMET (200 m grid spacing).

pact studies and the impact of the error correction on the climate change signal can be found in *Themeßl et al.* (2009). Hereby, the methods are flexible enough to bridge the gap between gridded model output and required data (e. g., station-like point-wise time-series) and perform error correction in one step. One of these correction methods, known as *quantile mapping* (QM) (*Wood et al.*, 2004), is an empirical-statistical method which enables to account for errors in the climatological mean (i. e., biases) and in the variability of model variables (e. g. *Piani et al.*, 2009). However, time-dependent statistics, like correlation coefficients between modelled and observed time-series are not improved. But since the focus lies on time-independent statistics (i. e., biases and frequency distributions, cf. Section 4.1) QM provides a feasible error correction technique.

QM derives an error correction function (f_{corr}) based on cumulative frequency distributions of modelled data (cfd_{mod}) from climate simulations of the past (predictors) used as a training period and observational data (cfd_{obs}) (predictands) (cf. Figure 4.15). Hereby, the correction function is defined as difference between predictor and predictand (equivalent to the model error) at constant quantiles. To correct a specific simulated value, its according quantile is derived from cfd_{mod} which is mapped onto cfd_{obs} giving back the corrected value. Note, if QM is applied onto the predictors of the training period all errors of the modelled frequency distributions vanish per construction (the time-dependent errors, like the root mean square error, are not improved).

Assuming the relation between cfd_{mod} and cfd_{obs} (i. e., their differences and hence the correction function f_{corr}) does not change when the predictors are taken from an other period (the application period) than the training period, QM can be used to correct the

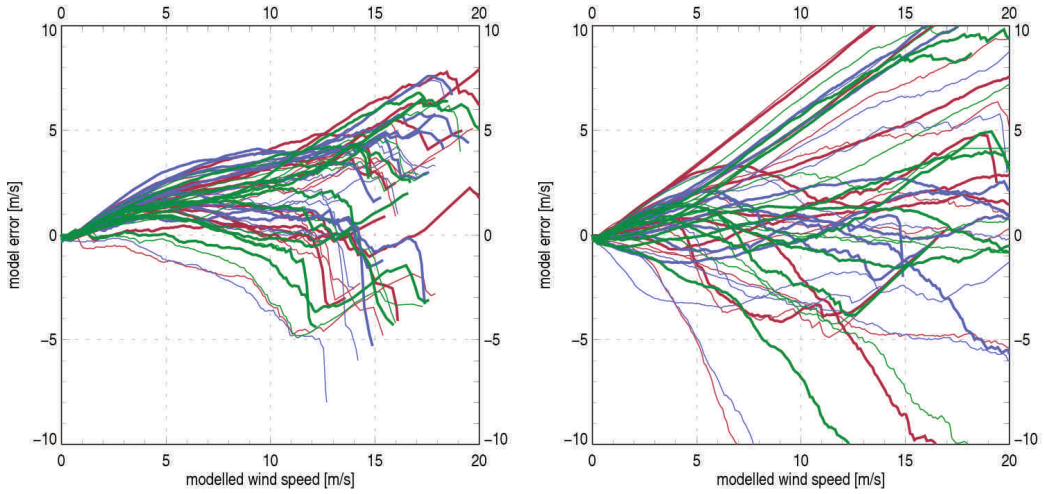

(a) (b)

Figure 4.17: Model errors of CALMET (thick lines) and MM5 (thin lines) of the configurations Av0 (red), Bv0 (blue), and Cv0 (green) (period: Jan 1, 1999, 00:00 UTC to Dec 31, 1999, 23:00 UTC) as a function of simulated wind speeds at all stations in (a) the Vienna Basin and in (b) the Hohe Tauern region.

model errors for this application period. An error corrected climate change signal can be derived, if QM is applied on both simulation periods, the reference period and the scenario period. As long as the model output of the application period lies within the data range of the training period QM gives robust results. Complications arise when the training period does not contain the data range of the application period (e. g., extreme values). In that case the correction function has to be extrapolated which induces extrapolation-errors and, hence, leads to increased uncertainties for extreme values.

Depending on the shape of f_{corr} a climate change signal of a given climate variable (φ) might be significantly affected due to the application of QM. In general, an uncorrected climate change signal ($\Delta\overline{\varphi}$) is defined as the difference between averaged quantities ($\overline{\varphi}$) of a scenario-period ($\overline{\varphi}_{scn}$) and a reference-period ($\overline{\varphi}_{ref}$):

$$\Delta\overline{\varphi} = \overline{\varphi}_{scn} - \overline{\varphi}_{ref} \ . \tag{4.5}$$

Due to the application of $f_{corr}(\varphi)$ as a function of the uncorrected variable on φ each single numeric value of φ is changed ($\varphi \rightarrow \varphi'$):

$$\varphi' = \varphi - f_{corr}(\varphi) \ . \tag{4.6}$$

Since the climate change signal is based on averaged quantities, the behaviour of $f_{corr}(\varphi)$ throughout the averaging-process of φ influences the calculation of the signal. This can easily be seen when $f_{corr}(\varphi)$ is assumed to be linear in φ: if $f_{corr}(\varphi)$ is defined

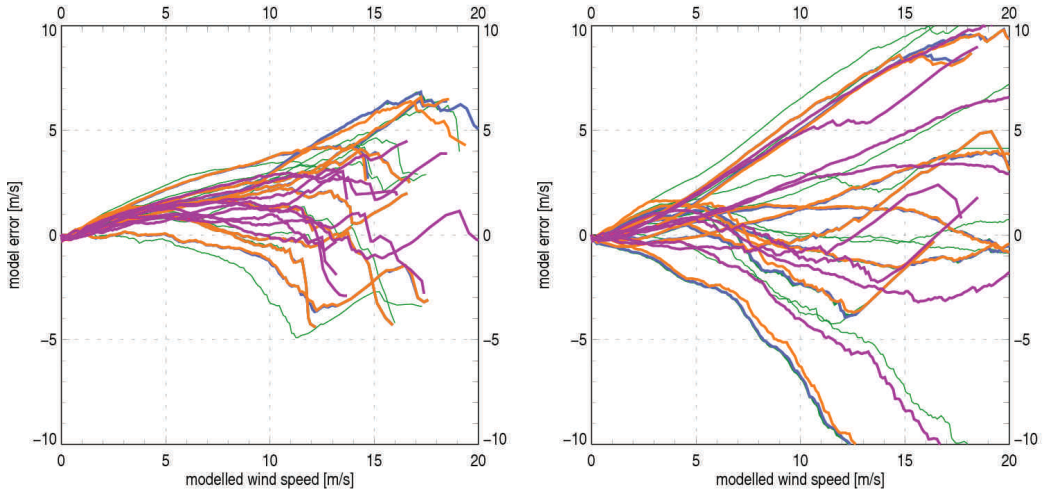

(a) **(b)**

Figure 4.18: Model errors of CALMET (thick lines) and MM5 domain C3 (thin lines) of the configurations Cv0 (green), Cv1 (blue), Cv2 (orange), Cv3 (magenta) (period: Jan 1, 1999, 00:00 UTC to Dec 31, 1999, 23:00 UTC) as a function of simulated wind speeds at all stations in (a) the Vienna Basin and in (b) the Hohe Tauern region.

by a linear equation (with slope k and intercept d)

$$f_{corr}(\varphi) = k \cdot \varphi + d \ , \tag{4.7}$$

and the climate change signal is defined as difference between the arithmetic means of the scenario and reference period, then the corrected climate change signal ($\Delta\overline{\varphi}'$) is given by

$$\Delta\overline{\varphi}' = \overline{\varphi}'_{scn} - \overline{\varphi}'_{ref} = \overline{\varphi}_{scn} - \overline{\varphi}_{ref} - k \cdot (\overline{\varphi}_{scn} - \overline{\varphi}_{ref}) = \Delta\overline{\varphi} \cdot (1 - k) \ , \tag{4.8}$$

where the intercept d vanishes, but the slope k of the correction function remains in the corrected signal. If $k \in]0, 1[$ ($k < 0$) the corrected signal is smaller (larger) than the uncorrected; if $k > 1$ the signal changes its sign.

In the case of the wind downscaling method, the predictors are primarily represented by the simulated time-series of wind speeds (V_m) (hourly basis) of the ERA-40-driven configuration Av0 of the ten-year period (1981 to 1990) in order to correct the downscaling-error of MM5 and CALMET at the sites of the observation-stations in the Vienna Basin (cf. Section 4.3.3). Due to the lack of two-dimensional gridded observational datasets, the predictands are defined as the corresponding station-based observed wind speeds (V_o) (cf. Section 4.1). Investigating the errors of the one-year simulations is a secondary objective in order to gain additional information about the behaviour of the error correction function in the complex Hohe Tauern region.

Table 4.15: Mean derivatives of the error functions ($\partial f_{corr}(V_m)/\partial V_m$) and their spreads for all model configurations in the Vienna Basin and the Hohe Tauern region (period: Jan 1, 1999, 00:00 UTC to Dec 31, 1999, 23:00 UTC).

Configuration	MM5		CALMET	
	spread	mean	spread	mean
Changes of MM5 in the Vienna Basin				
Av0	−0.36 to 0.31	0.13	−0.03 to 0.41	0.21
Bv0	−0.45 to 0.33	0.10	−0.06 to 0.38	0.22
Cv0	−0.43 to 0.36	0.12	−0.28 to 0.39	0.14
Changes of MM5 in the Hohe Tauern region				
Av0	−1.27 to 0.73	−0.09	−0.45 to 0.72	0.13
Bv0	−1.06 to 0.50	−0.15	−0.12 to 0.53	0.11
Cv0	−0.36 to 0.62	0.11	−0.59 to 0.44	0.03
Changes of CALMET in the Vienna Basin				
Cv0	−0.43 to 0.36	0.12	−0.28 to 0.39	0.14
Cv1			−0.28 to 0.39	0.14
Cv2			−0.28 to 0.37	0.13
Cv3			−0.07 to 0.32	0.15
Changes of CALMET in the Hohe Tauern region				
Cv0	−0.36 to 0.62	0.11	−0.59 to 0.44	0.03
Cv1			−0.59 to 0.44	0.03
Cv2			−0.60 to 0.44	0.01
Cv3			−0.37 to 0.51	0.08

Focussing on the ten-year-simulation Av0 overestimates wind speeds at all stations (positive biases, frequency distributions are shifted towards higher wind speeds, cf. Section 4.3.3) in the Vienna Basin. Hence, the correction functions for MM5 (A2) and CALMET (v0) show positive values over all modelled wind speeds (cf. Figure 4.16). Furthermore, the mean first derivative of the correction functions with respect to V_m ($\partial f_{corr}(V_m)/\partial V_m$) for each station lies within a range of 0.19 and 0.97 along with a station-averaged mean of 0.33.

The correction functions for Av0 of the one-year-simulation (cf. Section 4.3.1) show similar characteristics for most of the stations although the number of stations is larger and the stations are broader distributed in space (cf. Section 4.1): the mean derivatives vary in a range between −0.03 and 0.41 along with an averaged mean of 0.21 (cf. Table 4.15 and Figure 4.17) giving positive derivatives for most of the stations. Similar characteristics of the correction functions can also be found for the other configurations (variations of MM5 and modifications of CALMET) (cf. Table 4.15, Figure 4.17, and Figure 4.18). Therefore, following equation (4.8), if a climate change signal within the Vienna Basin is corrected via some linear approximations of these functions it can be expected to be smaller than the uncorrected signal.

Nonetheless, even if the station-wise correction functions show similar characteristics in the Vienna Basin, their spectrum is still quite broad. Therefore, an overall

two-dimensional correction function providing robust and valid results throughout the model grid in oder to correct the simulation within the entire model domain cannot easily be derived and is therefore seen as a promising objective for future investigations. One possible approach could be based on a horizontal interpolation scheme of the station-wise correction functions taking account for different anemometer heights, surface roughness lengths, and orographic features. However, additional observation-stations would be necessary to extract the impacts of these features and to capture their influences on the correction functions in an empirical-statistical way.

In contrast to the Vienna Basin, in the Hohe Tauern region the correction functions of the one-year simulations are much more divergent and show more complex shapes (cf. Figure 4.17, and Figure 4.18): positive and negative values are nearly equally found and the mean first derivatives vary within a range from -0.60 (Cv2) and 0.72 (Av0) (cf. Table 4.15). Figure 4.17, and Figure 4.18 also highlight the stronger pronounced influences of the orography leading to local air-flows deviating from the hybrid dynamic/diagnostic downscaling concept (cf. Section 2.2). Therefore, a general conclusion about the impact on a climate change signal based on the concept of linear approximation (cf. equation (4.8)) cannot be drawn. Moreover, an overall conclusive two-dimensional correction function is difficult to derive from the presented evaluation results. Reliable data from much more observation stations would be necessary to empirically extract the underlying main sources of these large differences between simulation results and observations. At least, shifting (and extending) the simulation period to capture several recent years would offer the possibility to increase the number of stations.

Due to the cyclicity of circular data cumulative distribution functions for wind directions are difficult to derive. A modification of QM to be applicable on wind directions is therefore set aside and addressed to possible future investigations.

4.5 Concluding Remarks

The downscaling-method and its variants have successfully been applied in both study areas, the Hohe Tauern region and the Vienna Basin. The evaluation of the one-year simulations (cf. Section 4.3.1 and Section 4.3.2) and the ten-year climate simulation (cf. Section 4.3.3) has shown that the hybrid dynamic-diagnostic wind downscaling method is a feasible and robust method to generate highly resolved (200 m$\times$200 m grid spacing) climatologies for near surface wind capturing most of the observed relevant features including the multi-modality of observed distributions of wind speed and direction. Although statistically significant deviations from observations generally occur the downscaling method (in any configuration) outperforms the driving data, the re-analysis dataset ERA-40 on average. Only at a few observation-stations the distributions of wind speed (at ZS) and directions (at IF and at LT) are not improved. Since the time series of ERA-40 and the observations are nearly uncorrelated, the ERA-40's outstanding performance in frequency distributions and biases at ZS, IF, and LT is supposed to be based on coincidence.

At a glance, in the Vienna Basin the dynamic as well as the diagnostic model in all configurations (including the ten-year simulation) show positive biases for wind speed

at all stations (except at LB) and the frequency distributions of wind direction are more properly captured than the distributions of wind speed: the station-averaged biases, Kolmogorov-Smirnov statistics, and Kuiper statistics vary between 0.9 m/s and 2.1 m/s (1.1 m/s and 2.5 m/s), 0.18 and 0.37 (0.22 and 0.39), and between 0.14 and 0.21 (0.12 and 0.19) for CALMET (MM5), respectively. In the Hohe Tauern region the distributions of wind speed are more properly captured, but the biases of wind speed show positive and negative values and the statistics have a broader spread: the station-averaged biases, Kolmogorov-Smirnov statistics, and Kuiper statistics vary between 0.3 m/s and 1.7 m/s (-0.1 m/s and 1.1 m/s), 0.14 and 0.27 (0.24 and 0.28), and between 0.25 and 0.35 (0.28 and 0.33) for CALMET (MM5), respectively. In addition to this differences between the two study regions, the time-dependent statistics show improved values in the Vienna Basin when compared to the Hohe Tauern region: the station-averaged root mean square errors, correlation coefficients for wind speed and wind vectors vary between 6.8 m/s and 7.9 m/s (6.6 m/s and 6.2 m/s), 0.30 and 0.41 (0.37 and 0.45), and 0.38 and 0.42 (0.39 and 0.41) in the Hohe Tauern region and between 3.9 m/s and 4.5 m/s (4.0 m/s and 4.5 m/s), 0.53 and 0.57 (0.53 and 0.56), and 0.63 and 0.67 (0.64 and 0.66) in the Vienna Basin for CALMET (MM5), respectively. Improvements due to the application of CALMET depend on the MM5 variant and the observation station, but in general the spreads of the station-by-station statistics are densified indicating a reduction of the random-part of the downscaling-error.

Looking further into details, based on the one-year simulations changes of the resolution of MM5 affect the performance of the downscaling method more than the modifications of CALMET in both study regions (cf. Table 4.13). This highlights the close linkage between the two models and the vital importance of the initial wind fields for diagnostic models. However, smaller grid spacings do not necessarily improve the evaluation statistics (cf. Section 4.3.1): while in the Hohe Tauern region wind-speed-related biases and frequency distributions as well as their spreads are improved, in the Vienna Basin these statistics are only improved by the dynamic initialisation variant of MM5 (setup C). Especially, configuration Bv0 (5 km grid spacing for MM5, cf. Section 3.2.1) shows an enhanced overestimation of wind speed in the Vienna Basin, which is assumed to be based on multiple possible influences (i. e., improper or missing sub-grid-scale parameterisations, domain size/number of grid cells). On average, among the MM5-variants configuration Cv0 approximates the observations best with respect to frequency distributions of wind speed and direction in both study regions. Therefore, the simulations of the CALMET variants were based on MM5 C3.

Focussing on the CALMET variants, significant deviations from variant v0 were only found for variant v3 (altered interpolation scheme based on the height of the PBL from MM5) and to a lesser extend for variant v2 (re-considered sensible heat flux). Variant v3 captures much more topographic features on the highly resolved CALMET-grid and results in more structured climatologies. However, these improvements are only partly reflected by the evaluation statistics: in the Hohe Tauern region v3 gives both, best (at PK) and most worse (at HK) results along with increasing spreads. The distributions of wind speed are partly improved, but distributions of wind direction are notably degraded. In the Vienna Basin both, the time-independent and time-dependent, statistics are more improved leading to best station-averaged results (bias of wind speed is 0.9 m/s and the statistics for the frequency distributions are 0.18) and the

statistics' spreads are strongly reduced indicating a notable reduction of the random-part of the downscaling-error. This enhanced sensibility of CALMET in the complex terrain can be explained by the enhanced sensibility of the divergence-minimisation scheme at steeper slopes (cf. Section 2.2.2) and by the influences of possible misleading representations of the PBL from MM5 (cf. Section 2.1.1) together with the simplified estimation of the surface-layer-height (cf. Section 3.3.3). Due to the flat terrain these effects are reduced in the Vienna Basin. For variant 2, the frequency distributions hardly depart from v0. The Kolmogorov-Smirnov- and Kuiper-statistics deviate within a range between -0.02 and 0.04. Therefore, it can be concluded that CALMET is more sensible for modifications of the initialisation fields than for other modifications. Since variant v3 (driven by MM5 C3) gives most robust results in the Vienna Basin and offers the potential for further improvements also in the Hohe Tauern region via more sophisticated treatment of the PBL it is identified as the most promising combination of MM5 and CALMET.

The ten-year simulation with configuration Av0 in the Vienna Basin (cf. Section 4.3.3) gives similar results as the one-year simulation with Av0. Wind speeds are notably overestimated (station-averaged bias 1.7 m/s) shifting the frequency distributions systematically towards higher velocities (the Kolmogorov-Smirnov statistic gives 0.29 on average) while the distributions of directions are best captured on average (the Kuiper statistic gives 0.14) along with a very small spread of 0.09. These remaining wind-speed-related downscaling errors were corrected via the quantile mapping method, which is based on the observation data. However, these correction functions will affect a climate change signal, if the underlying climate simulations are corrected via this method. Moreover, from the shape of the correction functions and their similarities in the Vienna Basin it can be concluded that a climate change signal of the corrected near-surface wind will be smaller than the signal of the uncorrected one (cf. Section 4.4). Due to a missing long-term simulation and stronger pronounced topographic influences such a general conclusion for the impact of the correction functions on the climate change signal cannot be drawn in the Hohe Tauern region. Due to the lack of two-dimensional gridded observational dataset, the correction functions are currently limited to be applied on the sites of the observation stations.

Summing up, it can be concluded that 1) the steady-state flow concept, which is a primary concept of CALMET and which is further enhanced via the dynamic initialisation procedure of MM5 (variant C, cf. Section 3.2.2), is the most dominant climatological mechanism in the Hohe Tauern region and hence the wind downscaling method generates more realistic frequency distributions of wind speed in this complex terrain, 2) per construction of the wind downscaling method (the steady-state flow concept) wind climatologies in the Hohe Tauern region are mostly forced by synoptic and regional scale processes (cf. Section 1.1.2), while slope flows, the Froude-effect, and other local effects (cf. Section 1.1.3) play a minor climatological role, but are leading to weak (temporal) correlations between modelled and observed flows, 3) the random-part of the downscaling-error is smaller in the Vienna Basin where the wind speed is systematically overestimated, 4) the application of CALMET adds value in general due to the reduction of the station-by-station spreads of the evaluation statistics, 5) the downscaling-errors can be reduced via the quantile-mapping method in order to generate error-corrected wind climatologies, and 6) depending on the shape of the correction

functions climate change signals are affected due to the error correction (i. e., in the Vienna Basin a corrected signal for near surface wind is expected to be smaller than an uncorrected one).

5 A Future Scenario for Near Surface Wind

Within the framework of the project reclip:more long-term climate simulations (periods 1981 to 1990 and 2041 to 2050) (*Gobiet et al.*, 2006; *Truhetz et al.*, 2007) were conducted in order to generate a highly resolved (10 km×10 km grid spacing) climate change scenario for the Alpine region. Hereby, model-output of a GCM, called ECHAM5 (*Roeckner et al.*, 2003) (80 km × 120 km grid spacing), forced by the IPCC emission-scenario IS92a (*Leggett et al.*, 1992) was dynamically downscaled via MM5 following setup A of the wind-downscaling method (cf. Section 3.1). By means of CALMET's control version v0 (cf. Section 3.1) the output of MM5 is further downscaled to generate wind climatologies in the Vienna Basin with 200 m × 200 m grid spacing for current climate (period 1981 to 1990) and the future scenario (period 2041 to 2050). In other words, configuration Av0 of the wind downscaling method is applied on the output of ECHAM5.

Details of the GCM-data can be found in the following Section 5.1. By comparing the simulation results of both periods mean climate change signals of near surface wind are derived for the Alpine region and the Vienna Basin on annual and seasonal basis. These signals along with climate change effects on frequency distributions of wind speed and direction are presented and discussed in Section 5.2. In addition, some main sources of these climate change effects are identified by means of additional analysis of other parameters apart from near surface wind. However, the presented plots are limited to those which are necessary to settle the claim of traceability. The complete plot-series can be found in Appendix A.2. Concluding remarks in Section 5.3 are closing this chapter.

5.1 Driving Data

The driving data, i. e.the LBCs for MM5 domain A1 (cf. Section 3.1), were derived from special ECHAM5-simulations conducted by Martin Wild and Peter Tschuck at the ETH Zürich, Switzerland. In that case ECHAM5 was not coupled to an ocean-model, but it was driven by sea-surface-temperatures simulated by previous ECHAM4-runs instead. Observed greenhouse-gas concentrations were used to generate a reference climate simulation including the period 1981 to 1990 and the IPCC emission scenario IS92a (*Leggett et al.*, 1992) was used to take account for the expected increase of greenhouse gas concentrations during the twenty-first century.

The scenario IS92a is one of the older business-as-usual scenarios of the IPCC introduced in the Third Assessment Report (TAR) (*Houghton et al.*, 2001). Focussing on the future period (2041 to 2050) the increase of the global carbon-dioxide (CO_2) and

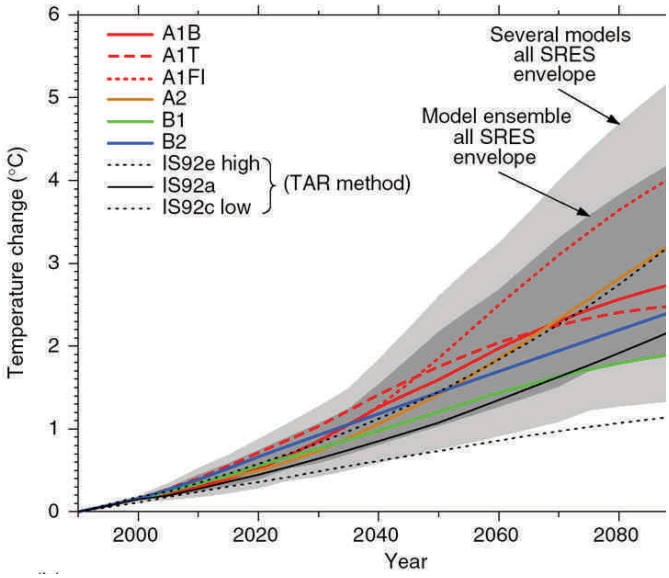

Figure 5.1: Expected change of the global annual mean temperature (2 m a.g.l.) in the 21st century depending on the IPCC greenhouse-gas emission scenario. The scenario IS92a is marked by the black solid line. From *Houghton et al.* (2001), modified.

methane (CH_4) concentrations of IS92a lie between the recent IPCC scenarios SRES A2 and SRES B2 leading to a moderate increase of the global near surface temperature (2 m a.g.l.) (cf. Figure 5.1).

5.2 Climate Change Signals for the Alpine Region and the Vienna Basin

After the application of the wind-downscaling method onto the ECHAM5 model-output climate change signals for wind speed are calculated as differences between two mean values, one referring to the scenario period 2041 to 2050 ($\overline{V}_{scn}$) and one referring to the reference period 1981 to 1990 ($\overline{V}_{ref}$) (cf. equation (4.5) in Section 4.4). Since the application of the error correction method is limited to the points of observation stations and a 2D-correction function is not available yet (cf. Section 4.4), the spatial distributed climate change signals are left uncorrected. Hypothesis-tests are applied on each grid cell to deduct whether the wind speeds of the scenario period significantly differ from those of the reference period and hence whether the derived climate change signals are statistically significant (significance < 0.05) or insignificant (significance ≥ 0.05). For that matter, the samples are de-trended in advance to reduce the effect of internal decadal trends. Furthermore, annual and seasonal mean values for each year of the reference and the scenario period are calculated to reduce the influence of the non-normality of the underlying distributions and hence make simple hypothesis-tests applicable. However, in practise even those mean values do not completely fulfil the constraints of normality. Therefore, the distributions of the annual and seasonal means

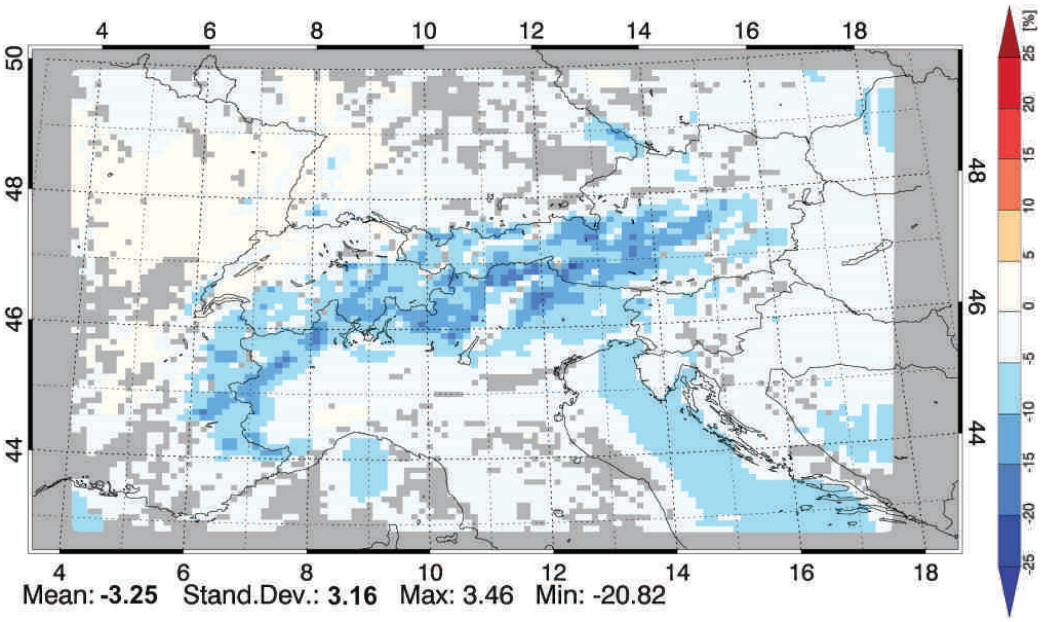

Figure 5.2: Uncorrected relative climatic change of mean annual wind speeds [%] (10 m a.g.l.; periods 1981 to 1990 and 2041 to 2050; emission scenario IS92a) in the Alpine region with 10 km grid spacing from MM5 domain A2 (control configuration, cf. Section 3.1, Figure 3.1). Areas with statistically insignificant signals (significances ≥ 0.05) are grey-shaded and are covering 19.0 % of the model domain.

are tested against normality by means of the Kolmogorov-Smirnov-test (cf. Section 4.1) by substituting cdf_1 or cdf_2 in equation (4.1) with a fitted normal distribution. If the samples are normally distributed, Student's t-test is applied to calculate the significance of the climate change signal, otherwise the significance is derived from the Wilcoxon Rank Sum test. Hypothesis-tests for other climate change signals than for wind speed are set aside.

Significant 2D climate change signals for the mean annual wind speed (10 m a.g.l.) over the Alpine region derived from the dynamic downscaling-step (MM5 domain A2, 10 km grid spacing) are shown in Figure 5.2. The area-fraction of the model-domain covered by statistically significant signals (in the following referred to as *significance-fraction*) is 81.0 %. Especially along the Alpine main crest and in its surrounding plains the signals are significant, negative, and correlated to the surface-altitude leading to spatially distributed decreasing mean annual wind speeds, in general: -3.3 % (-0.2 m/s) averaged over significant and insignificant changes of the entire Alpine region, up to -20.8 % (-1.2 m/s) in mountainous areas, and approximately -5 % in the surrounding plains (cf. Figure 5.2).

Figure 5.3 shows that this general reduction of the annual wind speed is not uniformly distributed over the annual cycle, but the correlation between the climate change signals and the surface-altitude roughly remains. Shifts between the averaged seasons appear along with changes of the significances: during the winter months December, January,

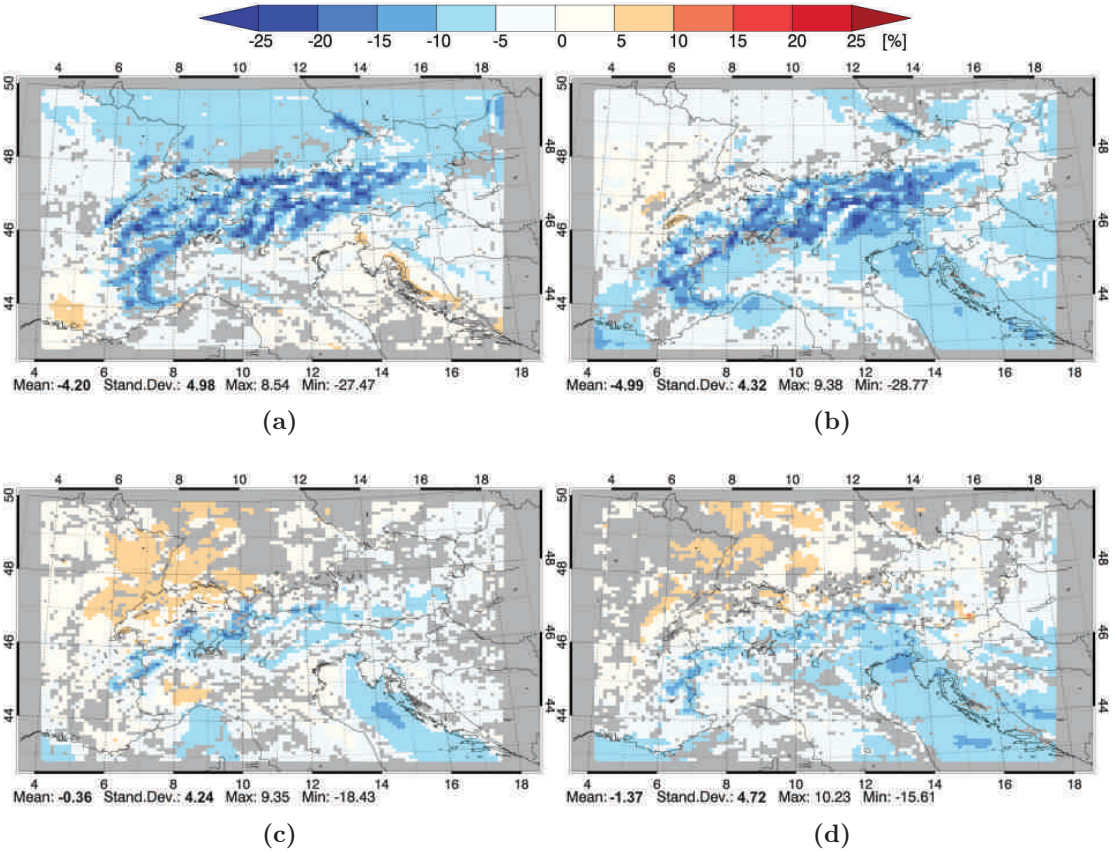

Figure 5.3: Same as for Figure 5.2, but for the seasons (a) DJF, (b) MAM, (c) JJA, and (d) SON. Areas with statistically insignificant signals (grey-shaded) are covering 19.0 %, 12.4 %, 34.0 %, and 33.2 %, respectively.

and February (DJF) and in the months of spring March, April, May (MAM) most drastic reductions up to more than −27 % (−2.5 m/s in DJF and −1.9 m/s in MAM) appear together with significance-fractions >80 %. In the summer months June, July, August (JJA) and in the autumn months September, October, November (SON) the seasonal mean wind speeds are reduced by a maximum of −18.4 % (−1.1 m/s) (JJA) and −15.6 % (−1.0 m/s) (SON), respectively, and the significance-fractions are reduced to ≈ 66 % in both seasons. Especially, in Upper Austria and in the Vienna Basin the significances are very weak during JJA. However, significant increases of the wind speeds up to 10 % (≈ 0.4 m/s) are found north-west to the Alps in south-eastern Germany, northern parts of Switzerland, and some eastern parts of France during JJA and SON, while slight reductions between −5 % (−0.3 m/s) and −7 % (−0.4 m/s) are found over the Adriatic Sea throughout the seasons MAM, JJA, and SON.

Focussing on the Vienna Basin shown in Figure 5.4 and hence on the results of the combined dynamic-diagnostic downscaling method, the wind speeds (10 m a.g.l.) are decreasing as well. However, the climate change signals are much weaker pronounced than in the Alps and the correlation to the surface-altitude is not that obvious: the mean

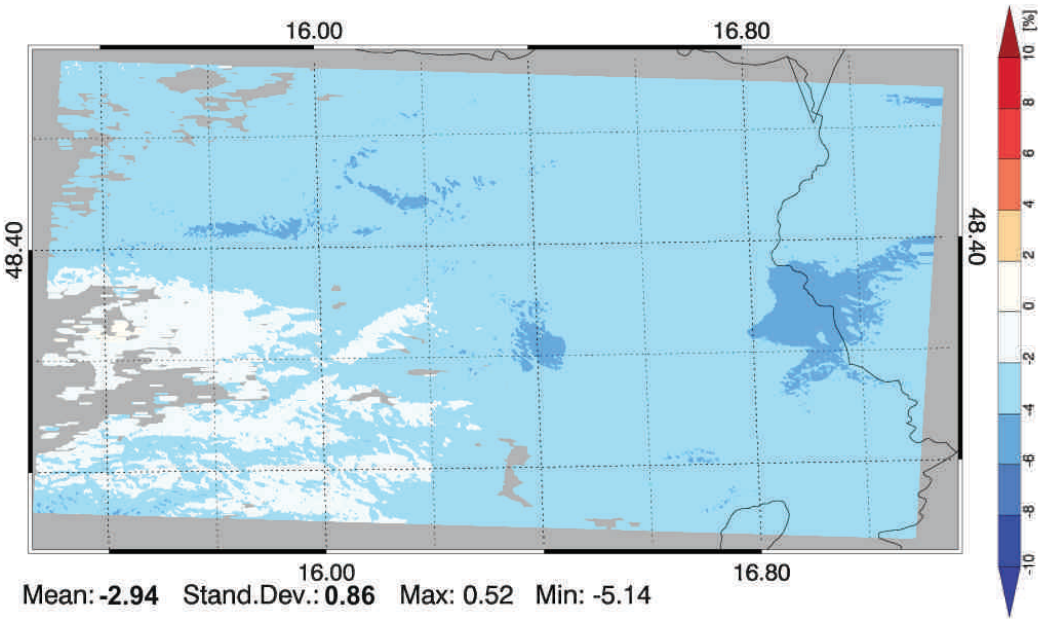

Figure 5.4: Uncorrected relative climatic change of mean annual wind speeds [%] (10 m a.g.l.; periods 1981 to 1990 and 2041 to 2050; emission scenario IS92a) in the Vienna Basin with 200 m grid spacing from the control configuration Av0 (cf. Section 3.1, Figure 3.1). Areas with statistically insignificant signals (significances ≥ 0.05) are grey-shaded and are covering 13.7 % of the model domain.

annual wind speed is reduced by −2.9 % (−0.2 m/s) on average, partly up to −5.1 %, along with a significance-fraction of 86.3 %. Similar to the behaviour in the Alps notable seasonal variability of the climate change signals can be found in Figure 5.5: strongest reductions appear in DJF and MAM with up to −9 % (−0.7 m/s and −0.4 m/s, respectively), where the significance-fractions are 95.3 % (DJF) and 79.7 % (MAM), while weakly increasing wind speeds up to 6 % (0.3 m/s) are found for SON with a significance-fraction of 70.5 %. During JJA the fraction of significant signals is drastically reduced to 37.1 %, preventing the signals from domain-wide interpretation, but in areas with significant signals the mean wind speed is reduced by up to −5.2 % (−0.2 m/s).

In addition to the 2D climate change signals (see above), point-wise signals for wind speed and direction are derived at the sites of the five long-lasting observation stations in the Vienna Basin introduced in Section 4.4 (cf. Figure 4.1 and Table 4.1). Since the correction functions for wind speed were derived in Section 4.4 (cf. Figure 4.16), the climate change signals for wind speed are corrected at these sites. By means of the Kolmogorov-Smirnov-test and the Kuiper-test (cf. Section 4.1) significances of departures between the distributions of the reference and the scenario period are calculated in order to indicate significant changes of the distributions.

Corrected and uncorrected frequency distributions from the reference and scenario simulation averaged over all station sites are shown in Figure 5.6: on average, the uncorrected climate change signals give a significant overall reduction of −0.2 m/s

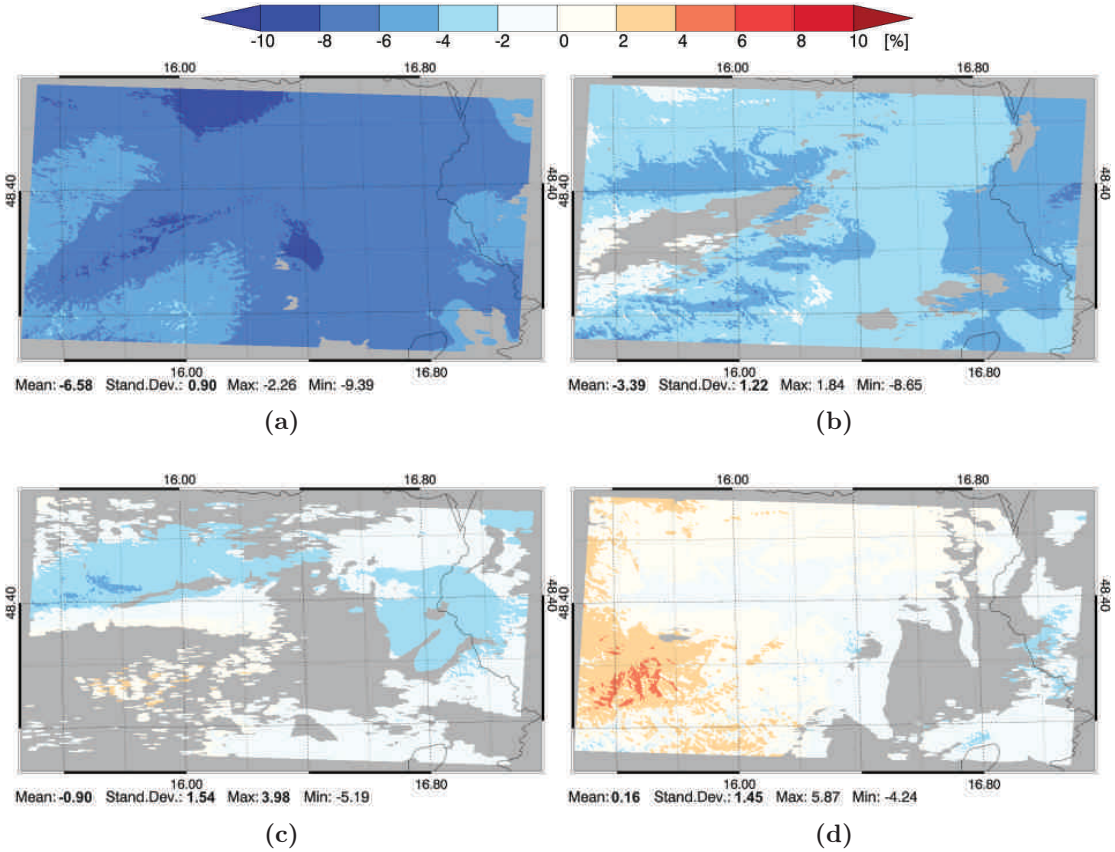

Figure 5.5: Same as for Figure 5.4, but for the seasons (a) DJF, (b) MAM, (c) JJA, and (d) SON. Areas with statistically insignificant signals (grey-shaded) are covering 4.7 %, 20.3 %, 62.9 %, and 29.5 %, respectively.

(−3.7 %) for wind speeds shifting the frequency distributions of the scenario simulation towards lower velocities. Concerning wind directions, enhancements of the westerly winds from directions between 270° and 300° are detected on average (cf. Figure 5.6).

As it was expected from the shape of the correction functions (cf. Section 4.4) the velocity-related signal is dampened due to the application of the error correction method: the station-averaged signal of the mean annual wind speed is significantly reduced to −0.1 m/s (−2.9 %) (cf. Figure 5.6). Therefore, the error correction method has significant impact on the climate change signal.

Looking at each station site separately, the averaged climate change signals from Figure 5.6 can also be found: the wind speeds are reduced, the westerly winds are enhanced, and the error correction functions significantly modify the climate change signals. At the investigated station sites the error correction approximately halves the magnitude of the climate change signal, e. g., at station GE the signal for wind speed is reduced from −0.2 m/s to −0.1 m/s (cf. Figure 5.7; frequency distributions for all stations can be found in Section A.2).

Comparing the 2D climate change signals of the dynamic (cf. Figure 5.2 and Fig-

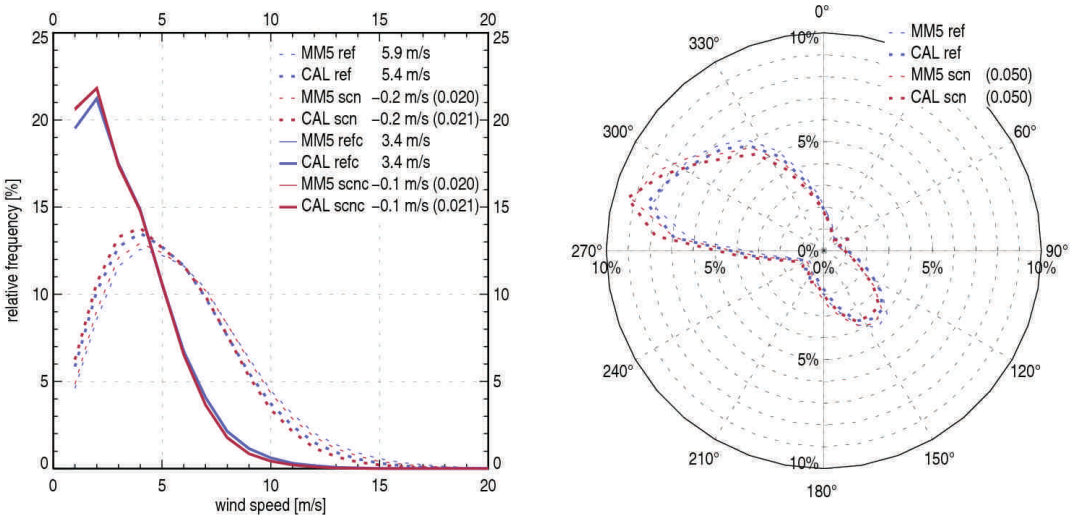

Figure 5.6: Station-averaged frequency distributions of (a) corrected (solid lines) and uncorrected (dashed lines) wind speeds and (b) uncorrected wind directions from the reference period 1981 to 1990 (index "ref") and the scenario period 2041 to 2050 (index "scn") modelled by both downscaling-steps: MM5 domain A2 (thin lines) and CALMET variant v0 (thick lines). The legend in (a) shows uncorrected and corrected (index "c") mean annual wind speeds for the reference simulations (ref/refc) and the scenario simulations (scn/scnc). The averaged statistics of the (a) Kolmogorov-Smirnov-test and (b) Kuiper-test comparing the distributions of the scenario with the reference period are listed in the legends (in parentheses).

ure 5.3) and the combined dynamic-diagnostic downscaling steps (cf. Figure 5.4 and Figure 5.5) in the Vienna Basin and comparing the two downscaling-steps by means of the point-wise signals at the station sites (cf. Figure 5.6 and Figure 5.7), the strong dependency of the diagnostic model from its initialisation fields is highlighted again: the changes of the annual wind speeds have the same magnitudes, and the frequency distributions have similar shapes, even if the 2D signals of the combined dynamic-diagnostic downscaling method are more structured and influenced by the highly resolved model-topography.

As pointed out in Section 1.3 climate change effects on near surface winds are related to changes of synoptic-scale processes as well as to changes of smaller-scale processes within the PBL. Both influences are difficult to analyse, since they depend on changes of the general circulations (e. g., shifts of the atmospheric circulation-cells, changes of the NAO) and on changes of short-term weather patterns (e. g., number, intensity, and tracks of cyclones). However, some evidence for changes of synoptic-scale processes is indicated by changes of the spatial distribution of the mean (referring to average large-scale processes) and the standard deviation (referring to short-term synoptic-scale

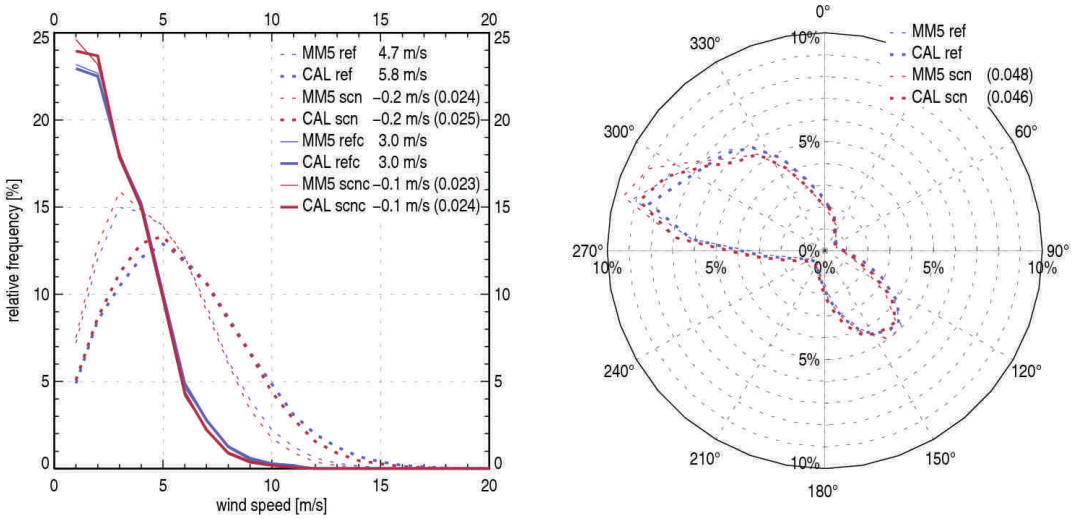

(a) **(b)**

Figure 5.7: Same as for Figure 5.6, but for station GE.

conditions) of the sea-level pressure (derived from 6-hourly pressure fields): Figure 5.8 shows largest seasonal changes of both variables during DJF and JJA. In DJF, when the PBL is more stable stratified, the mean sea-level pressure is increased in Northern, Eastern, and Central Europe by up to 3.7 hPa resulting in a more stagnant atmosphere over Central Europe and hence to a reduction of gradient-forced air-flows over the Alps on synoptic-scales on average. Due to the orography-induced speed-up effect (cf. Section 1.1.3 and Section 2.1.2) this reduction of synoptic air-flows is stronger pronounced in the Alps and explains the observed large reduction of wind speed in the scenario simulation (see above). On the other hand, the standard deviation of the sea-level pressure is increased by up to 0.8 hPa to the south of the Alps an in South-Eastern Europe (cf. Figure 5.8) indicating an increased short-term variability leading to increased regional frontal winds in this area (e. g., increased wind speeds along the Dalmatian coast line in Figure 5.3).

During the other seasons the relations become more complex, because of the increasing influence of thermal processes, like convection. Especially during JJA (cf. Figure 5.9) the seasonal sensible heat fluxes are increased by up to 40.7 W/m^2 in the Alps, but also in the Po Basin, in northern Italy, and in the south of France. However, this increased heat fluxes result in regionally different effects on the PBL: Figure 5.9 shows that the seasonal mean temperature lapse rate (approximated by the air temperature and the geo-potential height between the 700 hPa level and 2 m a.g.l. for convenience) is decreased by −1.9 K/km in JJA in the Alps, while in the Po Basin the lapse rate is nearly left unchanged. Since a reduction of the lapse rate indicates a de-stabilisation of the PBL, convective flow patterns are supposed to occur more frequently at the expense of flow patterns under neutral and stable conditions. Since neutral and stable conditions are favouring higher wind speeds, e. g., the orography-induced speed-up ef-

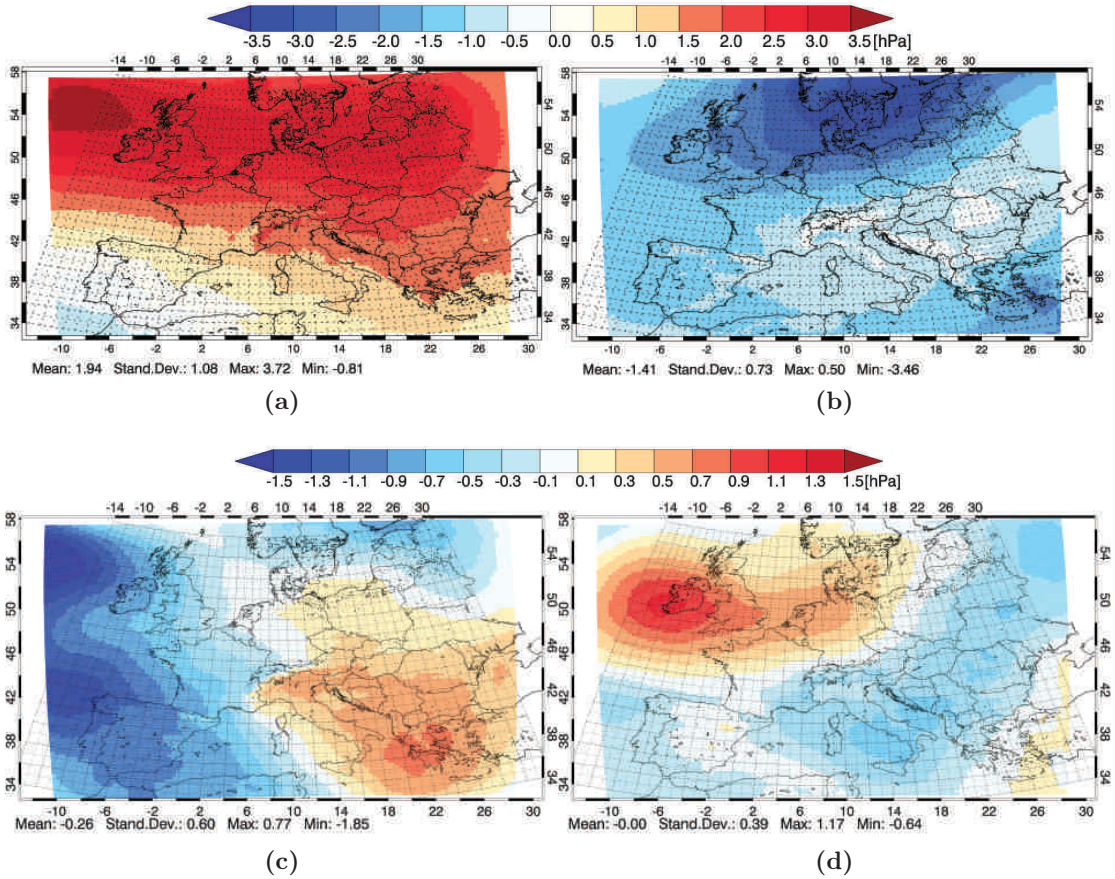

Figure 5.8: Uncorrected climatic change of seasonal mean (upper row) and standard deviation (lower row) of sea-level-pressure [hPa] (periods 1981 to 1990 and 2041 to 2050; emission scenario IS92a) over Europe with 30 km grid spacing from MM5 domain A1 (control configuration, cf. Section 3.1, Figure 3.1) for the seasons (a) (c) DJF and (b) (d) JJA.

fect (cf. Section 1.1.3 and Section 2.1.2) or gravity waves (cf. Section 1.1.2), lower wind speeds are expected to be found under unstable conditions.

Seasonal and regional variability is also reflected by the changes of the near surface temperature (2 m a.g.l.), which shows highest temperature-increases of up to 3.7 °C during JJA (cf. Figure 5.9) in the inner Alps.

By comparing the changes of the heat fluxes, temperatures, and lapse rates the relation between the reduction of wind speed during JJA in the inner Alps (cf. Figure 5.3) and changes of the PBL becomes phenomenologically obvious.

The reduction of the wind speeds in the Alps during MAM (cf. Figure 5.3) is related to both, changes of the surface energy budget and changes of synoptic-scale processes. The increase of the sensible heat fluxes together with the reduction of the stability of the PBL is weaker pronounced and shifted to geographic regions at lower altitudes (see Appendix A.2, Figure A.19 and Figure A.20, respectively). In addition, changes of synoptic-scale processes, similar to those found for DJF, are indicated by changes of the

sea-level pressure as well (see Appendix A.2, Figure A.17 and Figure A.18). Therefore, in MAM multiple overlapping effects exist preventing from detailed explanation of the climate change effects for near surface wind.

Due to the complexity of the processes unique assignments between causes and effects requires further investigations. First indications can be taken from changes of snow-cover and moisture availability at the surface. These seem to play important parts within this context: for instance, in the scenario simulation the snow-cover in JJA completely vanishes by the end of August in the inner Alps (while it partly remains in the reference simulation) (not shown) resulting in erratic decrease of surface albedo and hence in increase of the surface energy budget due to enhanced absorption of incoming radiation during daytime (cf. equations (3.10) and (3.11) in Section 3.3.2). This concept based on a changing snow-cover is supported by the behaviour of the sensible heat fluxes and the temperature lapse rates during MAM, since geographic regions at lower altitudes are affected.

In contrast to the inner Alps, in the Po Basin, northern Italy, and southern parts of France the increase of sensible heat fluxes only appears during JJA (cf. Figure 5.9 and Appendix A.2, Figure A.19) and does not affect the temperature lapse rate (cf. Figure 5.9 and Appendix A.2, Figure A.20) and hence the seasonal wind speeds are hardly changed (cf. Figure 5.3). Additional analysis of the simulation results indicate that there is no change in the surface albedo in these regions (not shown) and hence the increase of the sensible heat flux has to be achieved at the expense of the latent and/or ground heat fluxes and/or by changes of the incoming radiation (cf. equation (3.10) and (3.11) in Section 3.3.2). Since the stability of the PBL is hardly affected, reductions of the latent heat flux based on a temperature-forced drying-out of the soil and hence a reduction of the moisture availability at the surface are supposed to be the cause for preventing near surface wind from large changes. However, in order to clarify the relationships and to draw general robust conclusions about the future behaviour of near surface wind further investigations are required.

5.3 Concluding Remarks

The wind-downscaling method has successfully been applied to the model-output of a GCM (ECHAM5) and generated air-flows in the Alpine region (10 km × 10 km grid spacing) and the Vienna Basin (200 m × 200 m grid spacing) of the periods 1981 to 1990 and 2041 to 2050 (emission scenario IS92a) sampled in hourly time-slices. Based on these wind fields climate change signals for near surface wind (10 m a.g.l.) consisting of changes of mean wind speeds (2D maps) and point-wise frequency distributions of wind speeds and direction were derived and investigated with respect to their statistical significance.

The results show decreasing annual wind speeds along with a significantly pronounced annual cycle of the climate change signal for near surface wind in the Alpine region. Notable significant increases of the seasonal wind speeds occur north-west to the Alps during JJA and SON, while the wind speeds are generally decreasing in mountainous areas throughout the year. From additional analyses of the climate change signals of sea-level pressure, sensible heat flux, temperature, and temperature lapse rate derived

from the dynamic model three main sources for the observed behaviour of wind speed can be identified:

- **changes of synoptic- and large-scale processes** are reducing horizontal pressure gradients, particularly during DJF under stable conditions,
- the **orography-induced speed-up effect** amplifies reductions of wind speeds in mountainous areas under neutral and stable conditions, particularly during DJF, and
- **interactions between the atmosphere and the earth's surface** are mostly affecting the stability of the PBL during MAM and JJA leading to regionally different climate change effects of near surface wind. De-stabilisations based on temperature-forced reductions of the snow-cover are reducing mean wind speeds.

In accordance to the limitations of the diagnostic step of the downscaling-method the climate change signals for near surface wind (i. e., changes of annual and seasonal wind speeds) are strongly correlated to those of the dynamic step in the Vienna Basin. However, they are more structured due to the influence of the higher resolved topography (200 m grid spacing).

From the presented frequency distributions of the scenario and the reference simulation, which were corrected by means of error correction functions (cf. Section 4.4) applied at the sites of observation-stations, furthermore conclusions can be drawn:

- annual wind speeds are significantly reduced and hence the frequency distributions are condensed to lower wind speeds,
- westerly winds are slightly enhanced,
- due to the error correction functions' shape their application approximately halves the magnitude of the climate change signal of annual wind speeds, and
- the strong dependency of the diagnostic downscaling step from its initialisation fields and hence from the dynamic downscaling step remains in the climate change signals.

Concerning the interpretation of the presented climate change signals one has to be aware that these effects are based on one greenhouse-gas emission-scenario (IS92a), one GCM (ECHAM5), one RCM (MM5), and one diagnostic model (CALMET). Since uncertainties are induced by each model (including the GCM), the evidence of the signals and hence the drawn conclusions are limited to this specific configuration. Especially, the GCM's uncertainties of changes of atmospheric large-scale circulations and changes of the NAO prevent from a clear interpretation of the presented climate change signals of near surface wind: since different GCMs show different evolutions of the NAO (cf. Section 1.3), which is dominating the synoptic-scale weather-processes in the Alpine region at most during wintertime, the seasonal shift of the mean wind speed needs further investigations, in particular, a study of the sensitivity to the GCM.

However, the observed notable reduction of the seasonal wind speed during MAM and JJA in the inner Alps is also based on local changes of the snow-cover forced by rising (background) temperatures provided by the driving GCM. Since increasing temperatures are a more conformal result of up-to-date GCMs (cf. Section 1.3), there exists strong evidence for the reduction of wind speeds during MAM and JJA in the inner Alps to be a robust model-independent climate change effect.

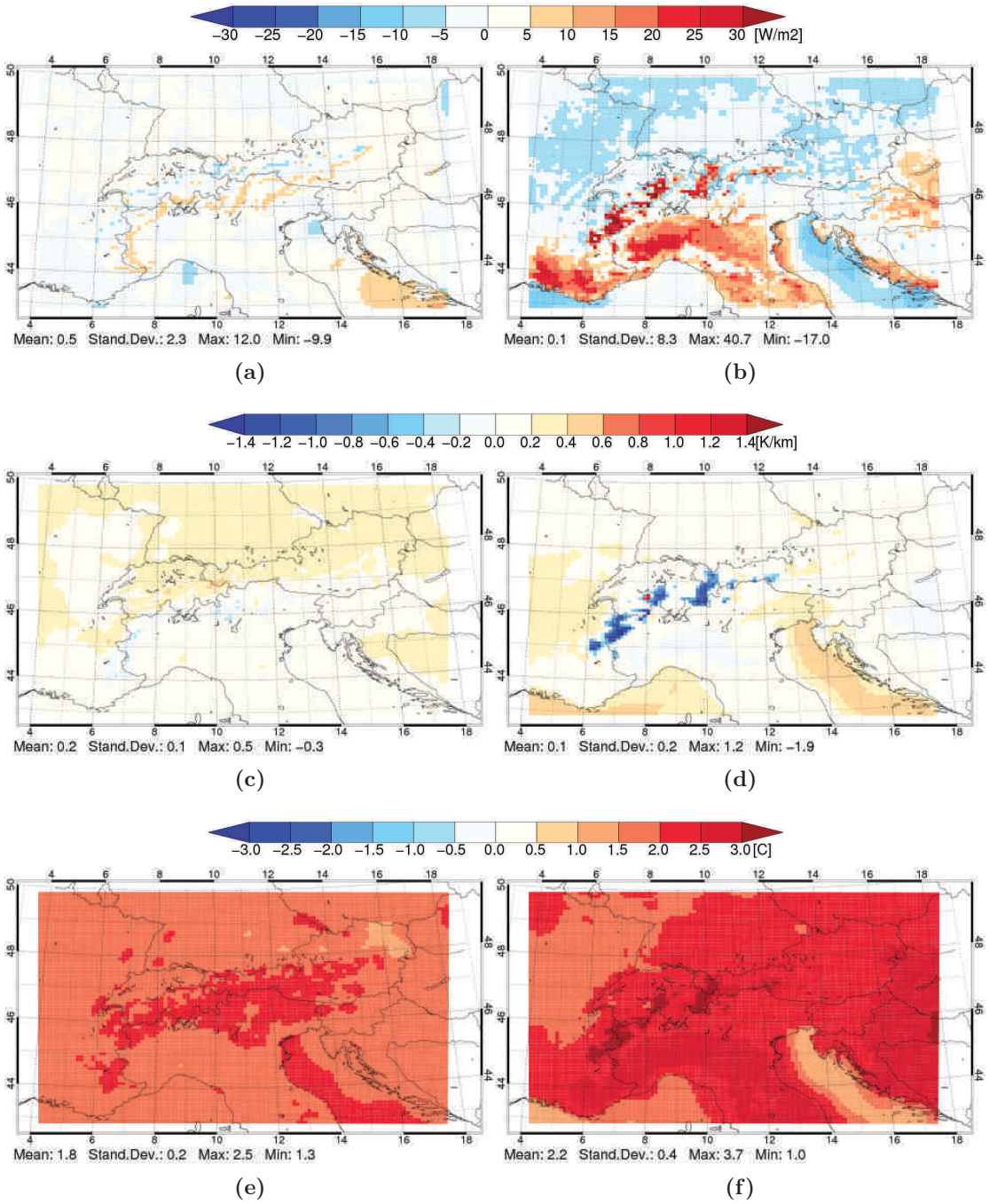

Figure 5.9: Uncorrected climatic change of seasonal sensible heat flux [W/m^2] (first row), temperature lapse rate [K/km] (second row), and temperature (2 m a.g.l.) [°C] (third row) (periods 1981 to 1990 and 2041 to 2050; emission scenario IS92a) in the Alpine region with 10 km grid spacing from MM5 domain A2 (control configuration, cf. Section 3.1, Figure 3.1) for the seasons DJF (left column) and JJA (right column).

Conclusions

The main objective of this thesis was to investigate the applicability of the steady-state flow concept for generating highly resolved wind climatologies on the 100 m scale in the European Alpine region. For that purpose the hybrid dynamic-diagnostic downscaling method based on the sequential application of the dynamic model MM5 (covering the entire Alpine region with 10 km $\times$ 10 km grid spacing) and the diagnostic model CALMET (200 m $\times$ 200 m grid spacing) has been introduced and successfully applied to the Hohe Tauern region and to the Vienna Basin. In order to improve the downscaling method and to identify dominant climatological mechanisms, several modifications of both models have been designed and evaluated by means of one-year simulations and observational data from 17 surface stations. In addition, a ten-year climate simulation in the Vienna Basin has been evaluated. Wind gusts and extremes were set aside.

From the evaluation results it can be concluded that the wind downscaling method and its variants generate realistic wind climatologies reflecting the orographic speed-up effect and the multi-modal characteristics of observed frequency distributions for wind speed and direction. Although statistically significant deviations from the observations occur, the downscaling method and its variants outperforms the driving reanalysis data ERA-40. It can be further concluded, that the steady-state flow concept together with the orographic speed-up effect are the most dominant climatological mechanisms. The quality of the generated wind climatologies is mostly affected by the ability to capture synoptic- and regional-scale processes, while unresolved or misrepresented small-scale processes like slope flows, the Froude effect, orographic-induced turbulence, inversion layers, and anthropogenic activities are reducing the temporal correlations between modelled and observed flows. In the Vienna Basin the steady-state flow concept is more valid than in the Hohe Tauern region, leading to both higher temporal correlations between modelled and observed flows and an enhanced systematic overestimation of wind speed. In general, highly structured climatologies capturing a broad spectrum of local variability do not necessarily show the smallest model errors. More complex modelling approaches do also require higher accuracy in the driving data and in the external parameters in order to tap their full potential.

Based on the ERA-40 driven simulations statistical error correction functions for wind speed have been derived via the quantile-mapping method in order to generate error-corrected wind climatologies. Depending on the shape of these correction functions climate change signals are differently affected: if the slope of a correction function is positive and smaller than one, a corrected signal is expected to be smaller than an uncorrected signal. This is the case in the Vienna Basin. In the Hohe Tauern region the correction functions are too broadly spread to draw a coherent conclusion.

The second objective was to identify simulation-independent climatological main processes affecting near surface wind under changing climate. For that purpose the downscaling method has been successfully applied to the output of a GCM (ECHAM5) to generate wind climatologies covering the Alpine region (10 km × 10 km grid spacing) and the Vienna Basin (200 m × 200 m grid spacing). Climate change signals for near surface wind derived from these climatologies (periods 1981 to 1990 and 2041 to 2050, IPCC scenario IS92a) show decreasing annual wind speeds throughout the Alpine region. This reduction correlates to the orography and reaches highest magnitudes along the Alpine main crest. The correlation to the orography is strongest pronounced in winter (DJF) and is weakened along the annual cycle. In JJA and SON the Alps act as a climate change barrier with increasing (decreasing) wind speeds in the Northwest (Southeast). The magnitude of these signals is approximately halved by the application of the statistical error correction functions.

Based on the annual cycle of the climate change signal for wind speed and on additional analyses of sea-level pressure, sensible heat flux, air temperature (2 m a.g.l.), and temperature lapse rate derived from the output of the dynamic model three main conclusions can be drawn:

- Changes of synoptic- and large-scale processes are affecting horizontal pressure gradients and hence gradient-forced synoptic- and regional-scale air flows, particularly during DJF.
- The orography-induced speed-up effect amplifies changes of wind speeds in mountainous areas under neutral and stable conditions.
- Interactions between the atmosphere and the earth's surface are mostly affecting the stability of the PBL and lead to regionally varying climate change effects of near surface wind.

Since different GCMs show different evolutions of synoptic- and large-scale processes no robust general conclusion about the future behaviour of near surface wind can be drawn from the presented climate change signals. These signals are based on one emission-scenario (IS92a), one GCM (ECHAM5), one RCM (MM5), and one diagnostic model (CALMET). However, since there is a broad agreement about temperature increase and since atmosphere-surface interactions are locally affecting near surface winds there exists strong evidence for a robust model-independent reduction of the wind speed during MAM and JJA in the inner Alps based on the temperature-forced reduction of the snow-cover. Since the snow-cover and the speed-up effect are correlated to surface altitude it can be further expected to find larger reductions of the wind speed in higher resolved climate simulations.

In order to draw general robust conclusions about the future behaviour of near surface wind, multi-model ensemble simulations based on multiple emission-scenarios have to be investigated in future research activities. Since diagnostic models are strongly related to their initialisation fields, these investigations might be limited to dynamic models, as long as numeric quantifications of the climate change signals on highly resolved grids are not of interest in those activities.

Bibliography

Achberger, C., M. Ekström, and L. Bärring (2002), Estimation of local near-surface wind conditions – comparison of WASP and regression based techniques, *Meteorol. Appl.*, *8*, 211–221, doi:10.1017/S1350482702002062.

Allison, I., N. L. Bindoff, R. A. Bindschadler, P. M. Cox, N. de Noblet, M. H. England, J. E. Francis, N. Gruber, A. M. Haywood, D. J. Karoly, G. Kaser, C. L. Quéré, T. M. Lenton, M. E. Mann, B. I. McNeil, A. J. Pitman, S. Rahmstorf, E. Regnot, H. J. Schellnhuber, S. H. Schneider, S. C. Sherwood, R. C. J. Somerville, K. Steffen, E. J. Steig, M. Visbeck, and A. J. Weaver (2009), *The Copenhagen Diagnosis: Updating the World on the Latest Climate Science*, ISBN 978-0-9807316-1-3, 64 pp., University of New South Wales, Climate Change Research Centre, Sydney, Australia, available at: http://www.copenhagendiagnoses.com/ (November 2009).

AMS (2000), AMS Glossary of Meteorology, available at: http://amsglossary.allenpress.com/glossary (April 2008).

Anderson, J. R., E. E. Hardy, J. T. Roach, and R. E. Witmer (1976), A Land Use And Land Cover Classification System For Use With Remote Sensor Data, Geological Survey Professional Paper 964, *Tech. rep.*, United States Geological Survey (USGS), Washington, USA, available at: http://pubs.er.usgs.gov/usgspubs/pp/pp964 (October 2008).

Auer, I., R. Böhm, A. Jurkovic, W. Lipa, A. Orlik, R. Potzmann, W. Schöner, M. Ungerböck, C. Matulla, K. Briffa, P. Jones, D. Efthymiadis, M. Brunetti, T. Nanni, M. Maugeri, L. Mercalli, O. Mestre, J. M. Moisselin, M. Begert, G. Müller-Westermeier, V. Kveton, O. Bochnicek, P. Stastny, M. Lapin, S. Szalai, T. Szentimrey, T. Cegnar, M. Dolinar, M. Gajic-Capka, K. Zaninovic, Z. Majestorovic, and E. Nieplova (2007), HISTALP - historical instrumental climatological surface time series of the Greater Alpine Region, *Int. J. Climatol.*, *27*, 17–46, doi:10.1002/joc.1377.

Barna, M., and B. Lamb (2000), Improving ozone modeling in regions of complex terrain using observational nudging in a prognostic meteorological model, *Atmos. Env.*, *34*, 4889–4906.

Barry, G. R., and A. M. Carleton (Eds.) (2001), *Synoptic and Dynamic Climatology*, Routledge, London, United Kingdom and New York, USA.

Beljaars, A. C. M., J. L. Walmsley, and P. A. Taylor (1987), A mixed spectral finite-difference model for neutrally stratified boundary-layer flow over roughness changes and topography, *Bound.-Layer Meteorol.*, *38*, 273–303.

Bellasio, G. M., R., J. S. Scire, M. G. Longoni, R. Bianconi, and N. Quaranta (2005), Alogorithms to account for topographic shading effects and surface temperature dependence on terrain elevation in diagnostic meteorological models, *Bound.-Layer Meteorol.*, *114*(3), 595–614.

Beniston, M. (2006), Mountain weather and climate: A general overview and a focus on climatic change in the Alps, *Hydrobiologia*, *562*, 3–16, doi:10.1007/s10750-005-1802-0.

Beniston, M., and P. Jungo (2002), Shifts in the distributions of pressure, temperature and moisture and changes in the typical weather patterns in the Alpine region in response to the behavior of the North Atlantic Oscillation, *Theor. Appl. Climatol.*, *71*, 29–42.

Berge, E., F. Nyhammer, L. Tallhaug, and Ø. Jacobsen (2006), An Evaluation of the WAsP Model at a Coastal Mountainous Site in Norway, *Wind Energ.*, *9*, 131–140, doi:10.1002/we.191.

Bissoli, P., and M. W. J. Grieser, N. Dotzek (2007), Tornadoes in Germany 1950–2003 and their relation to particular weather conditions, *Global and Planetary Change*, *57*, 124–138, doi:10.1016/j.gloplacha.2006.11.007.

BMU (2002), *Erste Allgemeine Verwaltungsvorschrift zum Bundes-Immissionsschutzgesetz, Technische Anleitung zur Reinhaltung der Luft (TA Luft), Gemeinsames Minsterialblatt (GMBl.) 25–29*, 511–605 pp., Bundesministerium für Umwelt, Naturschutz und Reaktorsicherheit (BMU), Berlin, Germany.

Chandrasekar, A., C. R. Philbrick, R. Clark, B. Doddridge, and P. Georgopoulos (2003), Evaluating the performance of a computationally efficient MM5/CALMET system for developing wind field inputs to air quality models, *Atmos. Env.*, *37*, 3267–3276.

Chen, F., and J. Dudhia (2001), Coupling an Advanced Land Surface-Hydrology Model with the Penn State-NCAR MM5 Modeling System. Part I: Model Implementation and Sensitivity, *Mon. Weather Rev.*, *129*(4), 569–585.

Chow, F. K., A. P. Weigel, R. L. Street, M. W. Rotach, and M. Xue (2006), High-Resolution Large-Eddy Simulations of Flow in a Steep Alpine Valley. Part I: Methodology, Verification, and Sensitivity Experiments, *J. Appl. Meteorol. Climatol.*, *45*(1), 63–86.

Christensen, J. H., B. Hewitson, A. Busuioc, A. Chen, X. Gao, I. Held, R. Jones, R. Kolli, W.-T. Kwon, R. Laprise, V. M. Rueda, L. Mearns, C. Menéndez, J. Räisänen, A. Rinke, A. Sarr, and P. Whetton (2007), Regional climate projections, in *Climate Change 2007: The Physical Science Basis. Contribution of Working Group I to the Fourth Assessment Report of the Intergovernmental Panel on Climate Change*, edited by S. Soloman, D. Qin, M. Manning, Z. Chen, M. Marquis, K. B. Averyt, M. Tignor, and H. L. Miller, Cambridge University Press, Cambridge, United Kingdom and New York, NY, USA.

Cox, R. M., J. Sontowski, and C. M. Dougherty (2005), An evaluation of three diagnostic wind models (CALMET, MSCIPUF, and SWIFT) with wind data from the Dipole Pride 26 field experiments, *Meteorol. Appl.*, *12*, 329–341, doi:10.1017/S1350482705001908.

de Rooy, W. C., and K. Kok (2004), A Combined Physical–Statistical Approach for the Downscaling of Model Wind Speed, *Wea. Forecasting*, *19*, 485–495.

Desiato, F., S. Finardi, G. Brusasca, and M. G. Morselli (1998), TRANSALP 1989 experimental campaign – I. Simulation of 3D flow with diagnostic wind field models, *Atmos. Env.*, *32*(7), 1141–1156.

Dobesch, H., and G. Kury (2006), Basic meteorological concepts an drecommendations fort he exploitation of wind energy in the atmospheric boundary layer, *Österreichische Beiträge zu Meteorologie und Geophysik*, *38*, 1–118.

Dotzek, N. (2001), Tornadoes in Germany, *Atmos. Res.*, *56*, 233–251.

Dudhia, J. (1993), A Nonhydrostatic Version of the Penn State-NCAR Mesoscale Model: Validation Tests and Simulation of an Atlantic Cyclone and Cold Front, *Mon. Weather Rev.*, *121*(5), 1493–1513.

Dudhia, J., D. Gill, K. Manning, W. Wang, and C. Bruyere (2005), *PSU/NCAR Mesoscale Modeling System, Tutorial Class Notes and User's Guide: MM5 Modeling System Version 3*, National Center for Atmospheric Research (NCAR), Boulder, USA, available at: http://www.mmm.ucar.edu/mm5/documents/tutorial-v3-notes.html (August 2008).

Eaton, B., J. Gregory, B. Drach, K. Taylor, and S. Hankin (2003), *NetCDF Climate and Forecast (CF) Metadata Conventions, Version 1.0*, National Center for Atmosperic Research (NCAR), Hadley Centre, Lawrence Livermore National Laboratory (LLNL), National Oceanic and Atmospheric Administration (NOAA), available at: http://cf-pcmdi.llnl.gov (August 2008).

EEA (1995), CORINE Land Cover – European Environment Agency Report, *Tech. rep.*, European Environment Agency (EEA), Copenhagen, Denmark, available at: http://www.eea.europa.eu (August 2008).

Etling, D. (1996), *Theoretische Meteorologie: Eine Einführung*, Vieweg Verlag, Braunschweig, Wiesbaden, Germany.

Fikke, S., G. Ronsten, A. Heimo, S. Kunz, M. Ostrozlik, P.-E. Persson, J. Sabata, B. Wareing, B. Wichura, J. Chum, T. Laakso, K. Säntti, and L. Makkonen (2007), Cost 727: Atmospheric icing on structures, measurements and data collection on icing: State of the art, *Tech. Rep. No. 75*, Bundesamt für Meteorologie und Klimatologie, MeteoSwiss, Zurich, Switzerland, available at: http://www.meteotest.ch/cost727/media.html (October 2008).

Fisher, N. I. (1995), *Statistical analysis of circular data*, 277 pp., Cambridge University Press, Cambridge, UK and New York, USA.

Fuentes, U., and D. Heimann (2000), An Improved Statistical-Dynamical Downscaling Scheme and its Application to the Alpine Precipitation Climatology, *Theor. Appl. Climatol.*, *65*, 119–135.

Gaile, G. L., and J. E. Burt (1980), *Directional Statistics*, Concepts and Techniques in Modern Geography, No. 25, 22 pp., Quantitative Methods Research Group (QMRG) of the Royal Geographical Society and the Institute of British Geographers, available at: http://www.qmrg.org.uk/ (April 2009).

Garratt, J. R. (1992), *The atmospheric boundary layer*, Cambridge University Press, Cambirdge, UK and New York, USA.

Giorgi, F., J. W. Hurrell, M. R. Marinucci, and M. Beniston (1997), Elevation Dependency of the Surface Climate Change Signal: A Model Study, *J. Climate*, *10*, 288–296.

Gobiet, A., H. Truhetz, and G. Kirchengast (2004), reclip:more: research for climate protection – model run evaluation, report project year 1, *Tech. Rep. for ARC No. 1/2004*, Institute for Geophysics, Astrophysics, and Meteorology (IGAM), University of Graz, Graz, Austria, available at: http://www.wegcenter.at/reloclim/publikationen/ (April 2008).

Gobiet, A., H. Truhetz, and A. Riegler (2006), A climate scenario for the alpine region, reclip:more project year 3, wegcenter progress report, *Tech. rep.*, Wegener Center for Climate and Global Change (WegCenter), University of Graz, Graz, Austria, available at: http://www.wegcenter.at/reloclim/publikationen/ (April 2008).

Gobiet, A., G. Kirchengast, L. Manney, M. Borsche, C. Retscher, and G. Stiller (2007), Retrieval of temperature profiles from CHAMP for climate monitoring: intercomparison with Envisat MIPAS and GOMOS and different atmospheric analyses, *Atmos. Chem. Phys.*, *7*(13), 3519–3536.

Goodin, W. R., G. J. McRae, and J. H. Seinfeld (1980), An objective analysis technique for constructing three-dimensional urbal-scale wind fields, *J. Appl. Meteor.*, *19*(1), 98–108.

Gopalakrishnan, S. G., D. P. Bacon, N. N. Ahmad, Z. Boybeyi, T. J. Dunn, M. S. Hall, Y. J. Lee, P. C. S. Lee, D. E. Mays, R. V. Madala, A. Sarma, M. D. Turner, and T. R. Wait (2002), An Operational Multiscale Hurricane Forecasting System, *Mon. Weather Rev.*, *130*(7), 1830–1847.

Gross, G. (1996), On the applicability of numerical mass-consistent wind field models, *Bound.-Layer Meteorol.*, *77*, 379–394.

Hagemann, S. (2002), An improved land surface parameter dataset for global and regional climate models, MPI Rport 336, *Tech. rep.*, Max Planck Institute for Meteorology (MPI), Hamburg, Germany, available at: http://www.mpimet.mpg.de/en/wissenschaft/publikationen/reports.html (August 2008).

Hantel, M. (2001), Klimatologie, in *Bergmann - Schaefer: Lehrbuch der Expermintalphysik: Erde und Planeten*, edited by W. Raith, Walter de Gruyter, Berlin, Germany, New York, USA.

Hart, R. E., and J. L. Evans (2001), A Climatology of the Extratropical Transition of Atlantic Tropical Cyclones, *J. Climate*, *14*(4), 546–564.

Heimann, D. (2001), A model-based wind climatology of the eastern Adriatic coast, *Meteorol. Z.*, *10*(1), 5–16, doi:10.1127/0941-2948/2001/0010-0005.

Hewer, F. E. (1998), Non-linear numerical model predictions of flow over an isolated hill of moderate slope, *Bound.-Layer Meteorol.*, *87*, 381–408.

Holland, B., R. Macek, and J. Carrafiello (Eds.) (1993), *Advanced Engineering Mathematics – Erwin Kreyszig*, ISBN 0-471-59989-1, 7^{th} ed., 1428 pp., John Wily & Sons, Inc., New York, USA.

Holtslag, A. A. M., and A. P. van Ulden (1983), A simple scheme for daytime estimates of the surface fluxes from routine weather data, *J. Climate App. Meteor.*, *22*(4), 517–529.

Holzer, A. M. (2001), Tornado climatology of Austria, *Atmos. Res.*, *56*, 203–211.

Houghton, J. T., Y. Ding, D. J. Griggs, M. Noguer, P. J. van der Linden, X. Dai, K. Maskell, and C. A. Johnson (Eds.) (2001), *Working Group I: The Scientific Basis. Contribution of Working Group I to the Third Assessment Report of the Intergovernmental Panel on Climate Change*, p. 881, Cambridge University Press, Cambridge, United Kingdom and New York, NY, USA.

ISO (1972), Standard Atmosphere, International Standard 2533, available at: `http://www.iso.org/iso/home.htm` (September 2008).

Jackson, P. S., and J. C. R. Hunt (1975), Turbulent wind flow over a low hill, *Q. J. R. Meteorol. Soc.*, *101*, 929–955.

Janjic, Z. I. (1990), The step-mountain coordinate: Physical package, *Mon. Weather Rev.*, *118*(17), 1429–1443.

Janjic, Z. I. (1994), The step-mountain eta coordinate model: Further development of the convection, vscous sublayer, and turbulent closure schemes, *Mon. Weather Rev.*, *122*(5), 927–945.

Jiang, Q., and J. D. Doyle (2004), Gravity Wave Breaking over the Central Alps: Role of Complex Terrain, *J. Atmos. Sci.*, *61*, 2249–2266.

Kain, J. S. (2004), The Kain-Fritsch convective parameterization: An Update, *J. Appl. Meteor.*, *43*(1), 170–181.

Kunz, S., F. Dällenbach, B. Schaffner, H. Buser, H.-R. Henz, and D. R. Soguel (2004), *Konzept Windenergie Schweiz, Grundlagen für die Standortwahl von Windparks*, 37 pp., Bundesamt für Energie (BFE), Bundesamt für Umwelt, Wald und Landschaft (BUWAL), Bundesamt für Raumentwicklung (ARE), Bern, Switzerland, available at: http://www.bfe.admin.ch/themen/00490/00500/index.html?lang=de&dossier_id=00728 (August 2008).

Lazar, R., and A. Podesser (1999), An urban climate analysis of Graz and its significance for urban planning in the tributary valleys east of Graz (Austria), *Atmos. Env.*, *33*, 4195–4209.

Leckebusch, G. C., and U. Ulbrich (2004), On the relationship between cyclones and extreme windstorm events over Europe under climate change, *Global and Planetary Change*, *44*, 181–193, doi:10.1016/j.gloplacha.2004.06.011.

Leggett, J., W. J. Pepper, and R. J. Swart (1992), Emissions scenarios for the IPCC: an update, in *Climate Change 1992: The Supplementary Report to the IPCC Scientific Assessment*, edited by J. T. Houghton, B. A. Callander, and S. K. Varney, pp. 68–95, Cambridge University Press, Cambridge, United Kingdom and New York, NY, USA.

Leonhart, R. (2004), *Lehrbuch Statistik – Einstieg und Vertiefung*, 496 pp., Verlag Hans Huber, Bern, Göttingen, Germany, and Toronto, Seattle, USA.

Leung, L. R., Y. Qian, and X. Bian (2003), Hydroclimate of the Western United States Based on Observations and Regional Climate Simulation of 1981–2000. Part I: Seasonal Statistics, *J. Climate*, *16*(12), 1892–1911.

Liu, M. K., and M. A. Yocke (1980), Siting of wind turbine generators in complex terrain, *J. Energy*, *4*(1), 10–16.

Loibl, W., A. Beck, M. Dorninger, H. Formayer, A. Gobiet, and W. Schöner (2007), Kwiss-program reclip:more, research for climate protection - model run evaluation, *Tech. rep.*, Austrian Research Centers GmbH – ARC systems research division, Vienna, Austria, available at: http://systemsresearch.arcs.ac.at/SE/projects/reclip/ (April 2008).

Lugauer, M., and P. Winkler (2005), Thermal circulation in South Bavaria – climatology and synoptic aspects, *Meteorol. Z.*, *14*(1), 15–30, doi:10.1127/0941-2948/2005/0014-0015.

Mahrt, L. (1982), Momentum Balace of Gravity Flows, *J. Atmos. Sci.*, *39*, 2701–2711.

Makkonen, L., P. Lehtonen, and L. Helle (2001), Anemometry in Icing Conditions, *J. Atmos. Oceanic Technol.*, *18*(9), 1457–1469.

Manning, K. W., and P. L. Haageson (1992), *Data ingest and objective analysis for the PSU/NCAR mesoscale modeling system: Programs DATAGRID and RAWINS, NCAR Technical Note TN-376+IA*, National Center for Atmospheric Research (NCAR), Boulder, USA, available at: http://www.mmm.ucar.edu/mm5/documents/dgraw-doc.html (August 2008).

Matulla, C., and H. von Storch (2008), The evolution of storminess since 1880 along Canada's East, Northern and Central Europe [abstract], in *Klima, Klimawandel und Auswirkungen (10. Österreichischer Klimatag), 13.03. – 14.03.2008*, University of Natural Resources and Applied Life Sciences, Vienna, Austria.

Mayr, G. (2005), *Workpackage 6: Wind potential and wind measurements*, Report No. 6 for the EU Interreg IIIB Alpine Space Programme No. A/I-2/3.1/5, 26 pp., Alpine Windharvest Partnership Network, Institute for Meteorology and Geophysics, University of Innbruck, Austria, available at: http://alpinespace.org/alpinewindharvest.html (August 2008).

Mayr, G. J., L. Armi, A. Gohm, G. Zängl, D. R. Durran, C. Flamant, S. Gaberšek, S. Mobbs, A. Ross, and M. Weissmann (2007), Gap flows: Results from the Mesoscale Alpine Programme, *Q. J. R. Meteorol. Soc.*, *133*, 881–896, doi:10.1002/qj.66.

McHugh, M. J., and J. C. Rogers (2005), Multi-model representation of the North Atlantic Oscillation in the 20th and 21st centuries, *Geophys. Res. Lett.*, *32*, L21,713, doi:10.1029/2005GL023679.

Mengelkamp, H.-T. (1999), Wind Climate Simulation over Complex Terrain and Wind Turbine Energy Output Estimation, *Theor. Appl. Climatol.*, *63*, 129–139.

Miller, R. L., G. A. Schmidt, and D. T. Shindell (2006), Forced annular variations in the 20th century Intergovernmental Panel on Climate Change Fourth Assessment Report models, *J. Geophys. Res.*, *111*, D18,101, doi:10.1029/2005JD006323.

Mills, G. (2007), Cities as agents of global change, *Int. J. Climatol.*, *27*, 1849–1857, doi:10.1002/joc.1604.

Mitasova, H., and L. Mitas (1993), Interpolation by regularized spline with tension: I. theory and implementation, *Math. Geol.*, *25*(6), 641–655.

Mlawer, E. J., S. J. Taubman, P. D. Brown, M. J. Iacono, and S. A. Clough (1997), Radiative transfer for inhomogeneous atmospheres: RRTM, a validated correlated-k model for the longwave, *J. Geophys. Res.*, *102*(D14), 16,663–16,682.

Montero, G., and N. Sanín (2001), 3-D modelling of wind field adjustment using finite differences in a terrain conformal coordinate system, *J. Wind Eng. Ind. Aer.*, *89*, 471–488.

Montero, G., R. Montenegro, and J. M. Escobar (1998), A 3-D diagnostic model for wind field adjustment, *J. Wind Eng. Ind. Aer.*, *74–76*, 249–261.

Moraes, O. L. L., O. C. Acevedo, G. A. Degrazia, D. Anfossi, R. da Silva, and V. Anabor (2005), Surface layer turbulence parameters over a complex terrain, *Atmos. Env.*, *39*, 3103–3112, doi:10.1016/j.atmosenv.2005.01.046.

Müller-Westermeier, G. (2007), Beschreibung und klimatologische Bewertung des Orkantiefs "Kyrill", Available at: http://metportal.dwd.de/ (April 2008).

Nakicenovic, N., J. Alcamo, G. Davis, B. de Vries, J. Fenhann, S. Gaffin, K. Gregory, A. Grübler, T. Y. Jung, T. Kram, E. L. L. Rovere, L. Michaelis, S. Mori, T. Morita, W. Pepper, H. Pitcher, L. Price, K. Riahi, A. Roehrl, H.-H. Rogner, A. Sankovski, M. Schlesinger, P. Shukla, S. Smith, R. Swart, S. van Rooijen, N. Victor, and Z. Dadi (2000), *Special Report on Emissions Scenarios*, Cambridge University Press, Cambridge, United Kingdom and New York, NY, USA.

Orlanski, I. (1975), Rational subdivision of scales for atmospheric processes, *Bull. Amer. Meteorol. Soc.*, *56*(5), 527–530.

Piani, C., J. O. Haerter, and E. Coppola (2009), Statistical bias correction for daily precipitation in regional climate models over Europe, *Theor. Appl. Climatol.*, doi: 10.1007/s00704-009-0134-9.

Pielke, R. A., Sr. (2002), *Mesoscale Meteorological Modeling*, International Geophysics Series, Vol. 78, 2^{nd} ed., Academic Press, San Diego, California, USA.

Pigeon, G., D. Legain, P. Durand, and V. Masson (2007), Anthropogenic heat release in an old European agglomeration (Toulouse, France), *Int. J. Climatol.*, *27*, 1969–1981, doi:10.1002/joc.1530.

Pineda, N., O. Jorba, J. Jorge, and J. M. Baldasano (2004), Using NOAA AVHRR and SPOT VGT data to estimate surface parameters: application to a mesocale meteorological model, *Int. J. Remote Sensing*, *25*(1), 129–143.

Pinto, J. G., U. Ulbrich, G. C. Leckebusch, T. Spangehl, M. Reyers, and S. Zacharias (2007), Changes in storm track and cyclone activity in three SRES ensemble experiments with the ECHAM5/MPI-OM1 GCM, *Climate Dyn.*, *29*, 195–210, doi: 10.1007/s00382-007-0230-4.

Press, W. H., S. A. Teukolsky, W. T. Vatterling, and B. P. Flennery (1992), *Numerical Recipes in FORTRAN 77 – The Art of Scientific Computing*, Cambridge University Press, Cambridge, UK and New York, USA.

Pryor, S. C., R. J. Barthelmie, and E. Kjellström (2005a), Potential climate change impact on wind energy resources in northern Europe: analyses using a regional climate model, *Climate Dyn.*, *25*(7/8), 815–835, doi:10.1007/s00382-005-0072-x.

Pryor, S. C., R. J. Barthelmie, and E. Kjellström (2005b), Empirical downscaling of wind speed probability distributions, *J. Geophys. Res.*, *110*(D19109), doi:10.1029/ 2005JD005899.

Rabus, B., M. Eineder, A. Roth, and R. Bamler (2003), The shuttle radar topography mission – a new class of digital elevation models acquired by spaceborne radar, *ISPRS J. Photogramm.*, *57*(4), 241–262, doi:10.1016/S0924-2716(02)00124-7.

Ratto, C. F., R. Festa, and C. Romeo (1994), Mass-consistent models for wind fields over complex terrain: The state of the art, *Environ. Software*, *9*, 247–268.

Reisner, J., R. J. Rasmussen, and R. T. Bruintjes (1998), Explicit forecasting of supercooled liquid water in winter storms using the MM5 mesoscale model, *Q. J. R. Meteorol. Soc.*, *124*(548), 1071–1107.

Rockel, B., and K. Woth (2007), Extremes of near-surface wind speed over Europe and their future changes as estimated from an ensemble of RCM simulations, *Clim. Change*, *81*, 267–280, doi:10.1007/s10584-006-9227-y.

Roeckner, E., G. Bauml, L. Bonaventura, R. Brotkopf, M. Esch, M. Giorgetta, S. Hagemann, I. Kirchner, L. Kornblueh, E. Manzini, A. Rhodin, U. Schulzweida, and A. Tompkins (2003), The Atmospheric General Circulation Model ECHAM5. Part 1: Model Description, MPI Report 349, *Tech. rep.*, Max Planck Institute for Meteorology (MPI), Hamburg, Germany, available at: http://www.mpimet.mpg.de/en/wissenschaft/publikationen/reports.html (August 2008).

Rotach, M. W., and D. Zardi (2007), On the boundary-layer structure over highly complex terrain: Key findings from MAP, *Q. J. R. Meteorol. Soc.*, *133(625)*, 937–948, doi:10.1002/qj.71.

Rotach, M. W., M. Andretta, P. Calanca, A. P. Weigel, and A. Weiss (2008), Boundary layer characteristics and turbulent exchange mechanisms in highly complex terrain, *Acta Geophysica*, *56*(1), 194–219, doi:10.2478/s11600-007-0043-1.

Rummukainen, M., S. Bergström, G. Persson, J. Rhode, and M. Tjiernström (2004), The Swedish Regional Climate Modelling Programme, SWECLIM: A Review, *Ambio*, *33*, 176–182.

Räisänen, J., U. Hansson, A. Ullerstig, R. Döscher, L. P. Graham, C. Jones, H. E. M. Meier, P. Samuelsson, and U. Willen (2004), European climate in the late twenty-first century: regional simulations with two driving global models and two forcing scenarios, *Climate Dyn.*, *22*, 13–31, doi:10.1007/s00382-003-0365-x.

Sachs, L., and J. Hedderich (2006), *Angewandte Statistik – Methodensammlung mit R*, 702 pp., Springer-Verlag, Berlin, Heidelberg, Germany.

Savelyev, S. A., and P. A. Taylor (2005), Internal boundary layers: I. Height formulae for neutral and diabatic flows, *Bound.-Layer Meteorol.*, *115*, 1–25.

Schaffner, B., and J. Remund (2005), *Workpackage 7: Alpine Space Wind Map, Modelling Approach*, Report No. 7-2 for the EU Interreg IIIB Alpine Space Programme No. A/I-2/3.1/5, 30 pp., Alpine Windharvest Partnership Network, Meteotest, Bern, Switzerland, available at: http://stratus.meteotest.ch/windharvest (August 2008).

Schwierz, C., C. Appenzeller, H. C. Davis, M. A. Liniger, W. Müller, T. F. Stocker, and M. Yoshimori (2006), Challenges posed by and approaches to the study of seasonal-to-decadal climate variability, *Clim. Change*, *79*, 31–63, doi:10.1007/s10584-006-9076-8.

Schär, C., T. D. Davies, C. Frei, H. Wanner, M. Widmann, M. Wild, and H. C. Davies (1998), Current Alpine Climate, in *Views from the Alps: Regional Perspectives on Climate Change*, edited by P. Cebon, U. Dahinden, H. C. Davies, D. M. Imboden, and C. C. Jaeger, Massachusetts Institute of Technology (The MIT Press), Cambridge, United Kingdom and Massachusetts, USA.

Scire, J. S., F. R. Robe, M. E. Fernau, and R. J. Yamertino (2000), *A User's Guide for the CALMET Meteorological Model (Version 5)*, 332 pp., Atmospheric Studies Group (ASG), Lowell, Massachusetts, USA, available at: http://www.src.com/calpuff/download (August 2008).

Seneviratne, S. I., R. D. Koster, G. Zhichang, P. A. Dirmeyer, E. Kowalczyk, D. Lawrence, P. Liu, C.-H. Lu, D. Mocko, K. W. Oleson, and D. Verseghy (2006), Soil Moisture Memory in AGCM Simulations: Analysis of Global Land-Atmosphere Coupling Experiment (GLACE) Data, *Journal Hydrometeorol.*, *7*(6), 1090–1112.

Smith, R. B., J. D. Doyle, Q. Jiang, and S. A. Smith (2007), Alpine gravity waves: Lessons from the MAP regarding mountain wave generation and breaking, *Q. J. R. Meteorol. Soc.*, *133*, 917–936, doi:10.1002/qj.103.

Solomon, S., D. Qin, M. Manning, Z. Chen, M. Marquis, K. B. Averyt, M. Tignor, and H. L. Miller (Eds.) (2007), *Climate Change 2007: The Physical Science Basis. Contribution of Working Group I to the Fourth Assessment Report of the Intergovernmental Panel on Climate Change*, p. 996, Cambridge University Press, Cambridge, United Kingdom and New York, NY, USA.

Steinacker, R. (1984), Area-height distribution of a valley and its relation to the valley wind, *Beiträge zur Physik der Atmosphäre*, *57*, 64–71.

Steinacker, R. (1990), Eine ostalpine Strömungslagenklassifikation, available at: http://www.univie.ac.at/IMG-Wien/weatherregime/ (April 2008).

Stull, R. B. (1983), A heat-flux history length scale for the nocturnal boundary-layer, *Tellus A*, *35*(3), 219–230.

Stull, R. B. (1988), *An Introduction to Boundary Layer Meteorology*, Kluwer Academic Publishers, Dordrecht, Germany, Bosten, USA, and London, United Kingdom, 680 pp.

Taylor, K. E. (2001), Summarizing multiple aspects of model performance in a single diagram, *J. Geophys. Res.*, *106*(D7), 7183–7192.

Taylor, P. A., P. J. Mason, and E. F. Bradley (1987), Boundary-layer flow over low hills, *Bound.-Layer Meteorol.*, *39*, 107–132.

Teixeira, J. (2001), Cloud Fraction and Relative Humidity in a Prognostic Cloud Fraction Scheme, *Mon. Weather Rev.*, *129*(7), 1750–1753.

Themeßl, M. (2005), *Downscaling of Temperature and Precipitation in the Alpine Region Hohe Tauern, Master's thesis, Scientific Report No. 5-2005*, ISBN 3-9502126-2-0, 122 pp., Wegener Center Verlag, Graz, Austria, available at: http://www.uni-graz.at/igam7www/igam7www_forschung/igam7www_reloclim/igam7www_reloclim_publikationen.htm (April 2008).

Themeßl, M., A. Gobiet, and A. Leuprecht (2009), Empirical-statistical downscaling and error correction of daily precipitation from a Regional Climate Model in the Alpine region (submitted), *Int. J. Climatol.*

Thompson, D. W. J., and J. H. Wallace (2001), Regional Climate Impacts of the Northern Hemisphere Annular Mode, *Science*, *293*(5527), 85–89.

Tolman, H. L., and J. H. G. M. Alves (2005), Numerical modeling of wind waves generated by tropical cyclones using moving grids, *Ocean Modell.*, *9*(4), 305–323, doi:10.1016/j.ocemod.2004.09.003.

Trenberth, K. E., P. D. Jones, P. Ambenje, R. Bojariu, D. Easterling, A. Klein Tank, D. Parker, F. Rahimzadeh, J. A. Renwick, M. Rusticucci, B. Soden, and P. Zhai (2007), Observations: Surface and atmospheric climate change, in *Climate Change 2007: The Physical Science Basis. Contribution of Working Group I to the Fourth Assessment Report of the Intergovernmental Panel on Climate Change*, edited by S. Soloman, D. Qin, M. Manning, Z. Chen, M. Marquis, K. B. Averyt, M. Tignor, and H. L. Miller, Cambridge University Press, Cambridge, United Kingdom and New York, NY, USA.

Trigo, I. F., T. D. Davies, and G. R. Bigg (2000), Decline in Mediterranean rainfall caused by weakening of Mediterranean cyclons, *Geophys. Res. Lett.*, *27*(18), 2913–2916.

Trigo, I. F., G. R. Bigg, and T. D. Davies (2002), Climatology of Cylcogenesis Mechanisms in the Mediterranean, *Mon. Weather Rev.*, *130*(3), 549–569.

Troen, I., and A. F. A. de Baas (1986), A Spectral Diagnostic Model for Wind Flow Simulation in Complex Terrain [abstract], in *EWEC'86. Proceedings. Vol. 1. European Wind Energy Association. Conference and Exhibition, 7 – 9 October 1986*, edited by W. Palz and E. Sesto, pp. 243–249, European Wind Energy Association, Rome, Italy.

Troen, I., and E. Petersen (1989), *European Wind Atlas*, RisøNational Laboratory, Roskilde, Denmark.

Truhetz, H., A. Gobiet, and G. Kirchengast (2005), reclip:more research for climate protection – model run evaluation, WegCenter Report #2 project year 2 (Nov 2004 – Oct 2005), *Tech. Rep. for ARC No. 1/2005*, Wegener Center for Climate and Global Change (WegCenter), University of Graz, Graz, Austria, available at: http://www.wegcenter.at/reloclim/publikationen/ (April 2008).

Truhetz, H., A. Gobiet, and G. Kirchengast (2007), Evaluation of a dynamic-diagnostic modelling approach to generate highly resolved wind fields in the Alpine region, *Meteorol. Z.*, *16*(2), 191–201, doi:10.1127/0941-2948/2007/0192.

Uppala, S., P. Kållesberg, A. Hernandez, S. Saarinen, M. Fiorino, X. Li, K. Onogi, U. Andrea, and V. D. C. Bechtold (2004), ERA-40: ECMWF 45-years reanalysis of the global atmosphere and surface conditions 1957–2002, *Tech. Rep. , ECMWF Newsletter – No. 101*, European Centre for Medium Range Weather Forecasts (ECMWF), Reading, UK.

Venkatesan, R., M. Möllermann-Coers, and A. Natarajan (1997), Modelling Wind Field and Pollution Transport over a Complex Terrain Using an Emergency Dose Information Code SPEEDI, *J. Appl. Meteorol.*, *36*, 1138–1159.

Venkatram, A. (1980), Estimating the Monin-Obukhov Length in the Stable Boundary-Layer for Dispersion Calculations, *Bound.-Layer Meteorol.*, *19*(4), 481–485.

Walter, A., K. Keuler, D. Jacob, R. Knoche, A. Block, S. Kotlarski, G. Müller-Westermeier, D. Rechid, and W. Ahrens (2006), A high resolution reference data set of German wind velocity 1951–2001 and comparison with regional climate model results, *Meteorol. Z.*, *15*(6), 585–596, doi:10.1127/0941-2948/2006/0162.

Wanner, H., R. Rickli, E. Salvisberg, C. Schmutz, and M. Schüpp (1997), Global Climate Change and Variability and its Influence on Alpine Climate - Concepts and Observations, *Theor. Appl. Climatol.*, *58*, 221–243.

Washington, W. M., and C. L. Parkinson (2005), *An Introduction to Three-Dimensional Climate Modeling*, 2^{nd} ed., University Science Books, Sausalito California, USA.

Weber, R. O., and M. Furger (2001), Climatology of near-surface wind patterns over Switzerland, *Int. J. Climatol.*, *21*, 809–827, doi:10.1002/joc.667.

Weber, R. O., and P. Kaufmann (1998), Relationship of Synoptic Winds and Complex Terrain Flows during the MISTRAL Field experiment, *J. Appl. Meteorol.*, *37*, 1486–1496.

Weng, W. (1997), Stably stratified boundary-layer flow over low hills: a comparison of model results and field data, *Bound.-Layer Meteorol.*, *85*, 223–241.

Weng, W., L. Chang, and P. A. Taylor (1997), Modelling stably stratified boundary-layer flow over low hills, *Q. J. R. Meteorol. Soc.*, *123*, 1841–1866.

Whiteman, C. D., and J. C. Doran (1993), The Relationship between Overlaying Synoptic-Scale Flows and Winds within a Valley, *J. Appl. Meteorol.*, *32(11)*, 1669–1682.

Whiteman, C. D., B. Pospichal, S. Eisenbach, P. Weihs, C. B. Clements, R. Steinacker, E. Mursch-Radlgruber, and M. Dorninger (2004), Inversion Breakup in Small Rocky Mountain and Alpine Basins, *J. Appl. Meteorol.*, *43(8)*, 1069–1082.

WMO (2006), Guide to Meteorological Instruments and Methods of Observation, *Tech. Rep. 8 (Preliminary Seventh Edition)*, Secretariat of the World Meteorological Organization, Geneva.

Wood, A. W., L. R. Leung, V. Sridhar, and D. P. Lettenmaier (2004), Hydrologic implications of dynamical and statistical approaches to downscaling climate model outputs, *Clim. Change*, *62(1–3)*, 189–216.

Xu, D., and P. A. Taylor (1994), A non-linear extension of the mixed spectral finite difference model for neutrally stratified turbulent flow over topography, *Bound.-Layer Meteorol.*, *49*, 177–186.

Yarnal, B., A. C. Comrie, B. Frakes, and D. P. Brown (2001), Developments and prospects ini synoptic climatology, *Int. J. Climatol.*, *21*, 1923–1950, doi:10.1002/joc.675.

Yin, J. H. (2005), A consistent poleward shift of the storm tracks in simulations of 21st century climate, *Geophys. Res. Lett.*, *32*, L18,701, doi:10.1029/2005GL023684.

Žagar, M., and J. Rakovec (1999), Small-scale surface wind prediction using dynamic adaptation, *Tellus*, *51 A*(4), 489–504.

ZAMG (1999), Witterungsverlauf juni 1999, *Tech. rep.*, Central Institute for Meteorology and Geodynamics (ZAMG), Vienna, Austria, available at: http://www.zamg.ac.at/klima/klima_monat/wetterlagen (April 2008).

Zervos, A., C. Kjaer, S. Azau, J. Scola, and J. Quesada (2009), Pure Power – Wind energy targets for 2020 and 2030, *Tech. rep.*, European Wind Energy Association (EWEA), Brussels, Belgium, available at: http://www.ewea.org/index.php?id=178 (Janury 2010).

Zängl, G. (2004), A reexamination of the valley wind system in the Alpine Inn Valley with numerical simulations, *Meteorol. Atmos. Phys.*, *87*, 241–256, doi:10.1007/s00703-003-0056-5.

Zängl, G., and S. Vogt (2006), Valley-wind charateristics in the Alpine Rhine Valley: Measurements with a wind-temperature profiler in comparison with numerical simulations, *Meteorol. Z.*, *15*(2), 179–186, doi:10.1127/0941-2948/2006/0110.

Zängl, G., A. Gohm, and G. Geier (2004), South foehn in the Wipp Valley – Inssbruck region: Numerical simulations of the 24 October 1999 case (MAP-IOP 10), *Meteorol. Atmos. Phys.*, *86*, 213–243, doi:10.1007/s00703-003-0029-8.

List of Abbreviations

3DVAR, 4DVAR	Three-/four-dimensional variational data assimilation
ARC-sys	Austrian Research Centers systems research
AOGCM	Atmosphere-Ocean General Circulation Model
CALMET	California Meteorological Model
CFL criterion	Courant-Friedrichs-Levi criterion
DEM	Digital elevation model
DJF	Winter season (December, January, February)
DKRZ	Deutsches Klimarechenzentrum
DWD	Deutscher Wetterdienst
ECHAM4	Global Climate Model from Max-Planck Institute for Meteorology (version 4)
ECHAM5	Global Climate Model from Max-Planck Institute for Meteorology (version 5)
ECMWF	European Centre for Medium-Range Weather Forecasts
ENSO	El Niño/Southern Oscillation
ERA-40	ECMWF reanalyses (40 years time span)
GCM	General Circulation Model in NWP / Global Climate Model in climate research
HadAM3H	Hadley Center Atmospheric Model
IBL	Internal Boundary-layer
IPCC	Intergovernmental Panel on Climate Change
ISA	International Standard Atmosphere
JJA	Summer season (June, July, August)
LAM	Local (Limited) Area Model
LBC	Lateral boundary condition
LIDAR	Light detection and ranging
MAM	Spring season (March, April, May)
MM5	PSU/NCAR Mesoscale Model of the 5^{th} Generation
MPI-M	Max-Plack Institute for Meteorology

MSLP	Mean sea level pressure
NAO	North Atlantic Oscillation
NCAR	National Center for Atmospheric Research
NWP	Numerical Weather Prediction
OPYC3	Ocean General Circulation Model from DKRZ
PBL	Planetary Boundary-Layer
PDE	Partial Differential Equation
PSU	Pennsylvania State University
QM	Quantile Mapping
QBO	Quasi Biennial Oscillation
RCAO	Rossby Centre Regional Atmosphere-Ocean Model
RCM	Regional Climate Model
SABL	Scattering Aerosol Backscatter LIDAR
SBC	Surface boundary condition
SON	Autumn season (September, October, November)
SRES	IPCC Special Report on Emission Scenarios
SRTM	Shuttle Radio Topography Mission
SVAT	Soil-vegetation-atmosphere transfer
UBL	Urban Boundary-Layer
USGS	United States Geological Survey
UTC	Universal Time Coordinated
WMO	World Meteorological Organisation
ZAMG	Zentralanstalt für Meteorologie und Geodynamik

List of Figures

A Appendix

This Appendix provides detailed results from evaluating the different variants of the wind-downscaling method introduced in Chapter 3. Appendix A.1 shows modelled frequency distributions of wind speed and direction from the periods Jan 1, to Dec 31, 1999, and Jan 1, 1981, to Dec 31, 1990, and compares them with observational data collected from surface stations in the Vienna Basin and in the Hohe Tauern region (cf. Section 4.1, Table 4.1). In addition, uncorrected modelled annual wind speeds (Jan 1, to Dec 31, 1999) with 200 m grid spacing for both study regions generated by the control configuration Av0 and the variants Cv0, Cv1, Cv2, and Cv3 (cf. Section 3.2.2 and Section 3.3) can be found in Appendix A.1 in order to document the mode of operation of the wind-downscaling method in general and to show the influence of the different variants of the diagnostic downscaling step.

Furthermore, Appendix A.2 shows corrected and uncorrected frequency distributions of wind speed and direction located at the sites of the observation stations in the Vienna Basin (cf. Table 4.1) from climate simulations of the reference-period Jan 1, 1981, to Dec 31, 1990, and the scenario-period Jan 1, 2041, to Dec 31, 2050. The distributions are derived from applying the method's control configuration Av0, consisting of MM5 setup A as dynamic downscaling step and CALMET variant v0 as diagnostic downscaling step, onto the output of the GCM ECHAM5 forced by observed greenhouse-gas concentrations (reference-period) and the business-of-usual emission scenario IS92a (scenario-period). In addition, uncorrected 2D-plots of mean seasonal changes of air temperature, sensible heat flux, temperature lapse rate, mean sea-level pressure, and standard deviation for sea-level pressure of the MM5 domain A2 (10 km grid spacing) covering the Alpine region are given to provide some insight into the complex interrelationships between different sources for the simulated climate change effects for near surface wind.

A.1 Evaluation Results

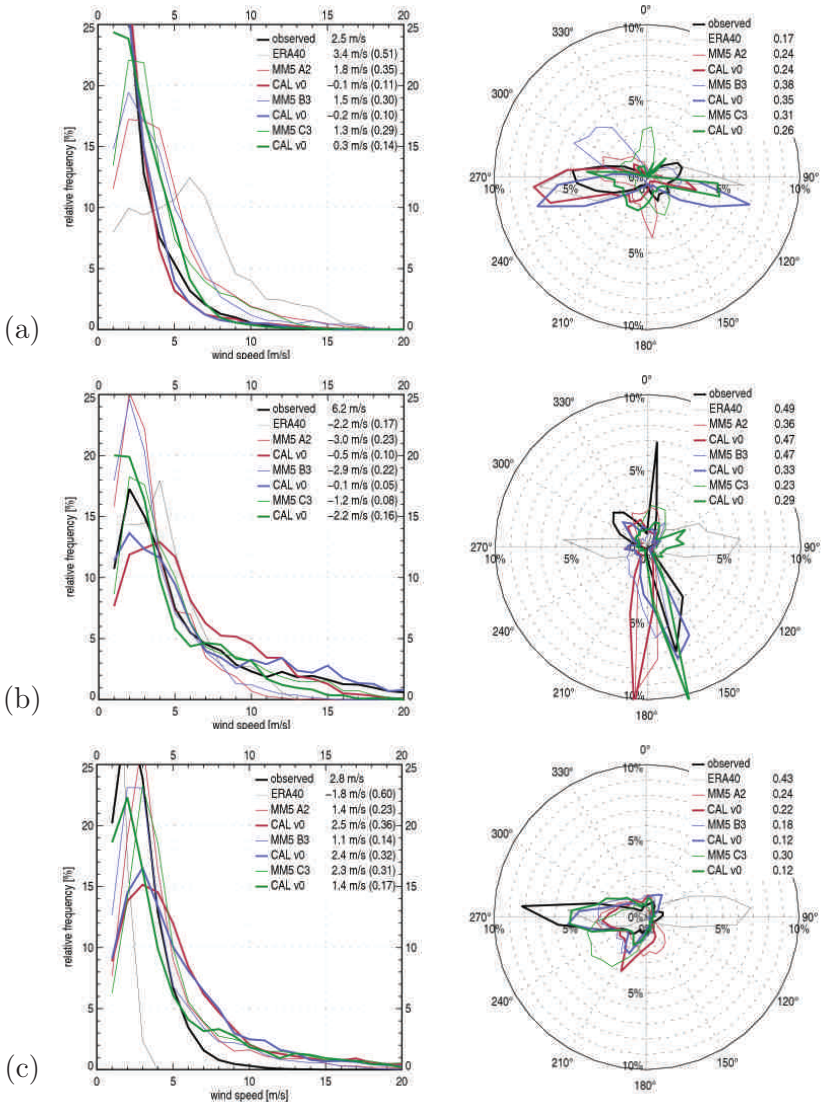

Figure A.1: Modelled and observed frequency distributions of wind speed (left column) and direction (right column) from Jan 1 to Dec 31, 1999, in the Hohe Tauern region at stations (a) IF, (b) PK, and (c) HK (cf. Table 4.1). Observations (thick black lines), ERA-40 (thin black lines), MM5 domains A2, B3, and C3 (thin red, blue, and green lines) downscaled by CALMET v0 (thick red, blue, and green lines) are shown. Observed mean values, biases, and the quality of the simulated distributions in terms of KS_V (in parentheses) and KP_ϕ are listed in the legends.

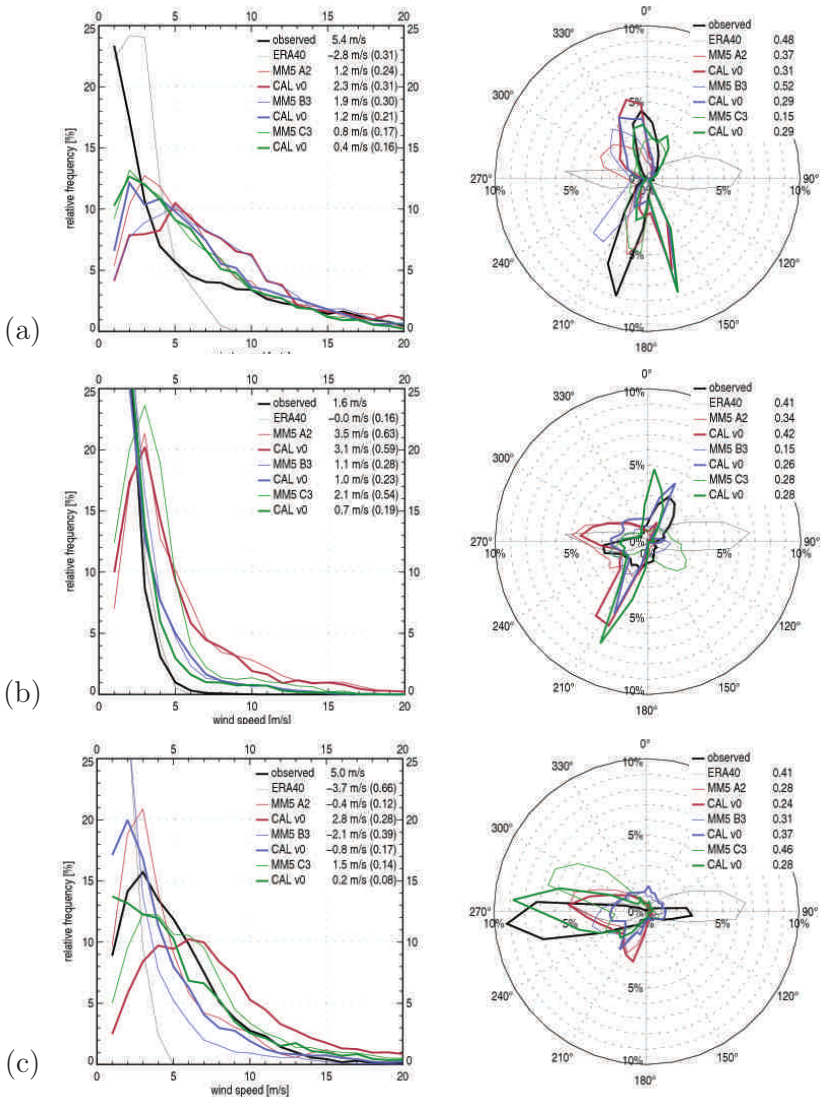

Figure A.2: Same as Figure A.1 but for the stations (a) RH, (b) ZS, and (c) SH, (c) SB, and (d) EB (cf. Table 4.1).

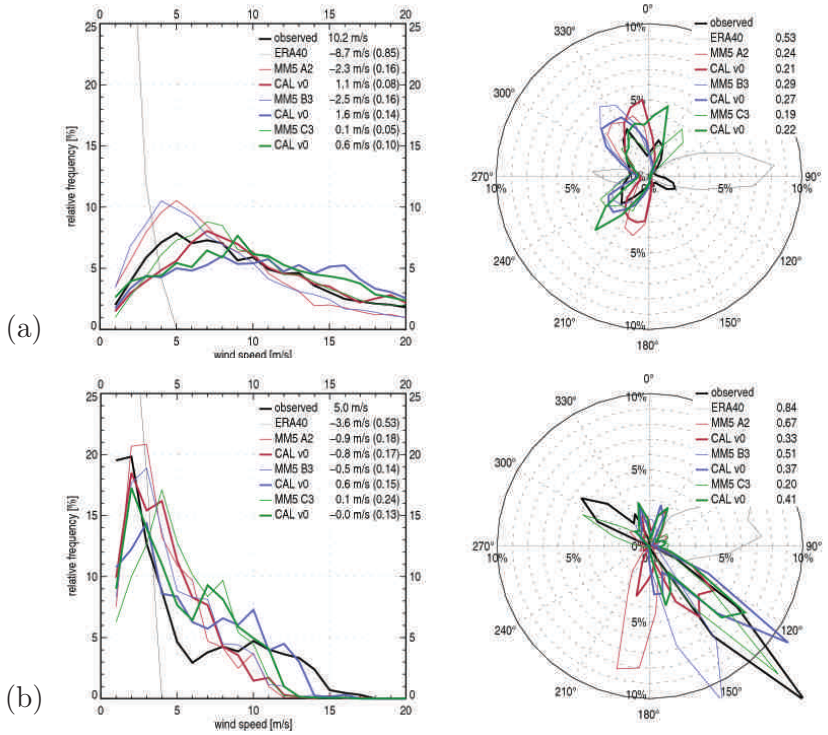

Figure A.3: Same as Figure A.1, but for the stations (a) SB and (b) EB (cf. Table 4.1).

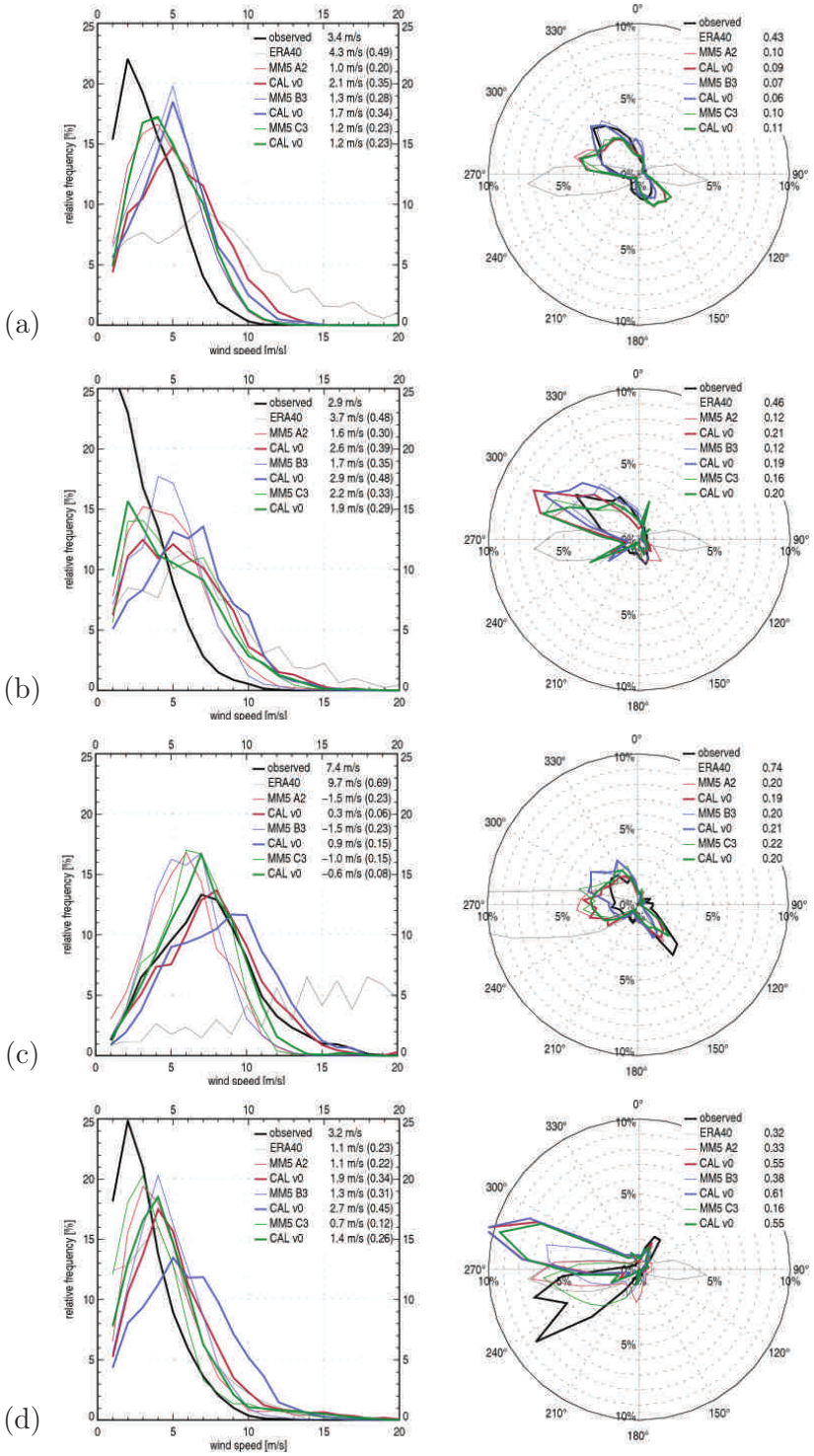

Figure A.4: Modelled and observed frequency distributions of wind speed (left column) and direction (right column) from Jan 1 to Dec 31, 1999, in the Vienna Basin at stations (a) GE, (b) GK, (c) LB, and (d) LT (cf. Table 4.1). The observations (thick black lines), the driving data ERA-40 (thin black lines), the MM5 configurations A2, B3, and C3 (thin red, blue, and green lines) which were downscaled by CALMET-variant v0 (thick red, blue, and green lines) are shown. Observed mean values, the models' biases and the quality of the simulated distributions in terms of KS_V (in parentheses) and KP_ϕ are listed in the legends.

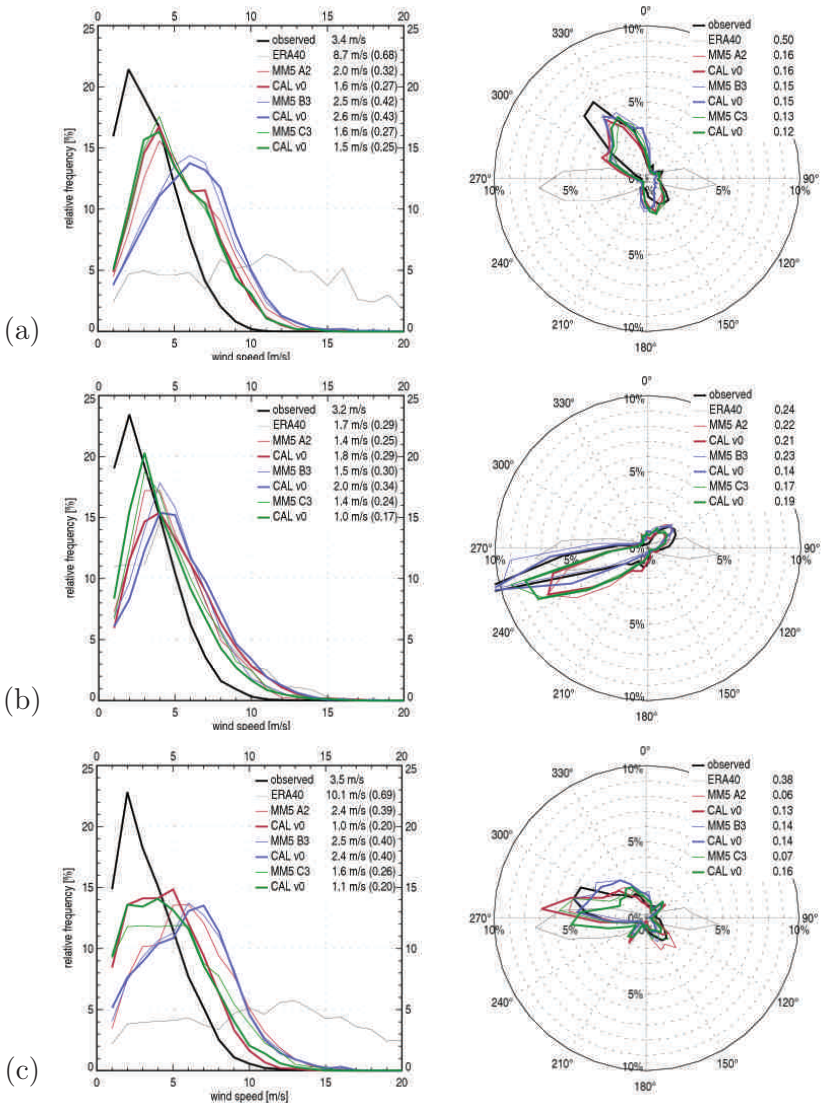

Figure A.5: Same as Figure A.4, but for the stations (a) NE, (b) SP, and (c) HW (cf. Table 4.1).

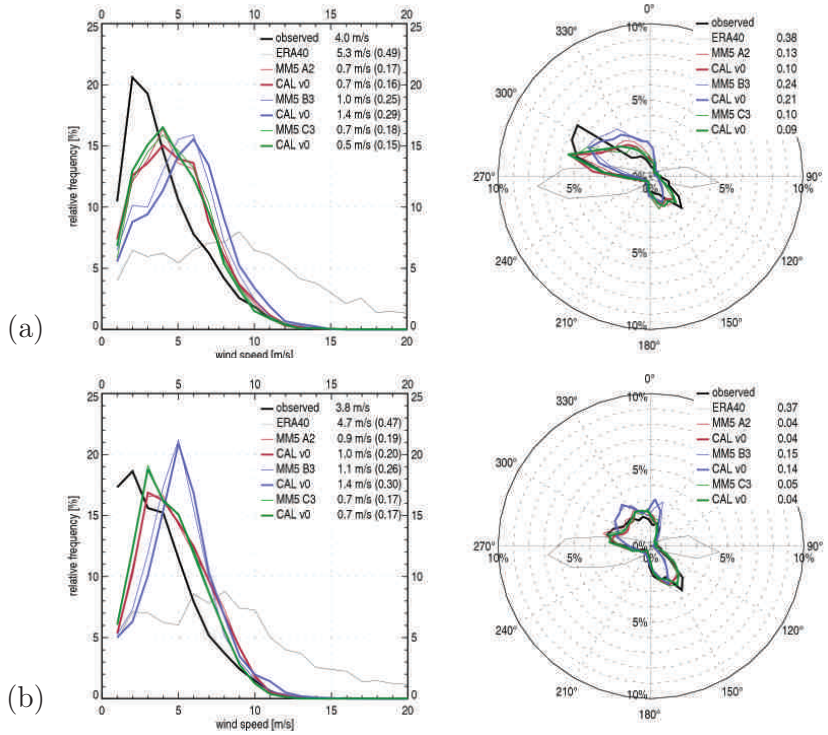

Figure A.6: Same as Figure A.4, but for the stations (a) WU and (b) ZD (cf. Table 4.1).

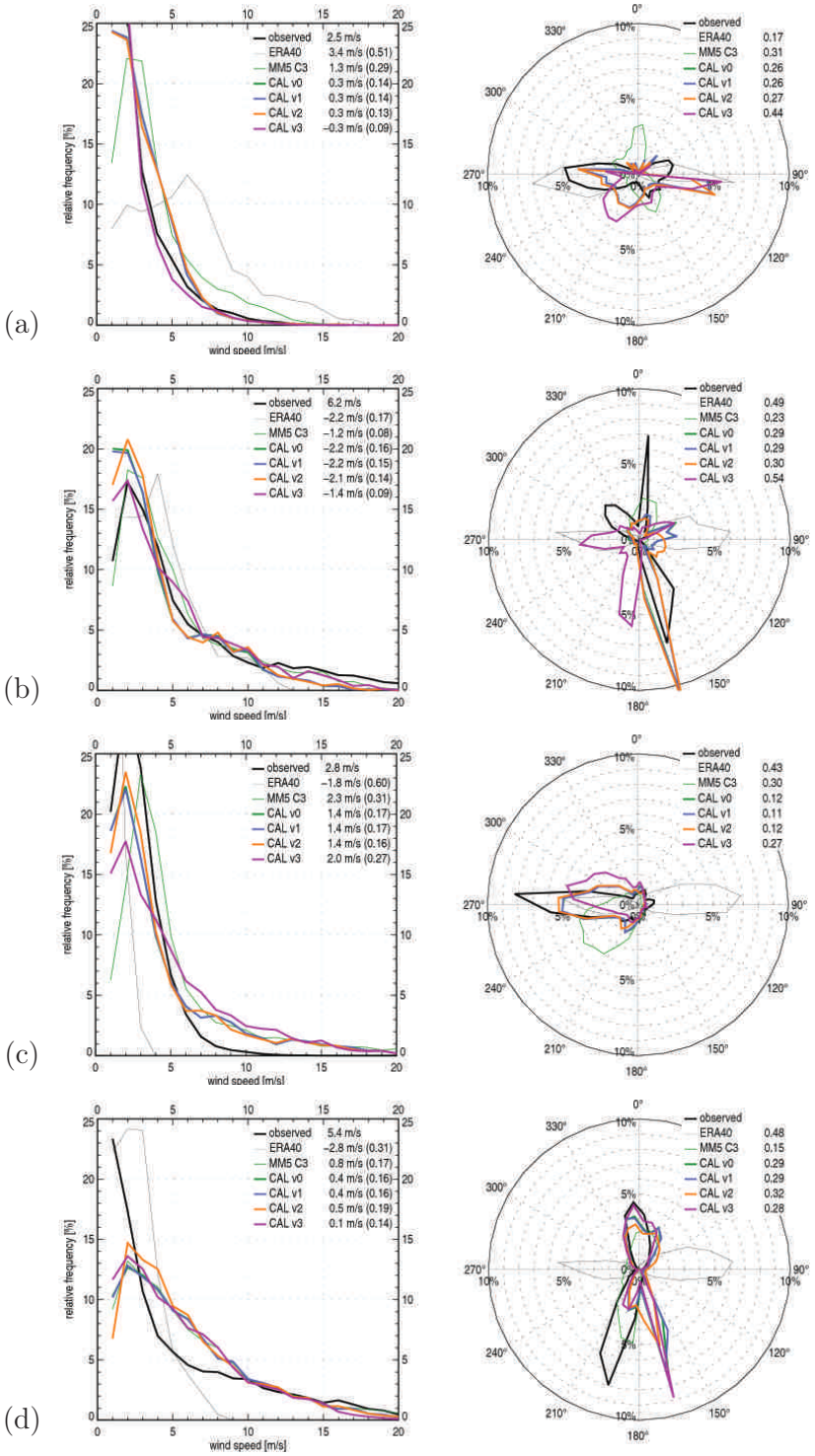

Figure A.7: Modelled and observed frequency distributions of wind speed (left column) and direction (right column) from Jan 1 to Dec 31, 1999, in the Hohe Tauern region at stations (a) IF, (b) PK, (c) HK, and (d) RH (cf. Table 4.1). Observations (thick black lines), the driving data ERA-40 (thin black lines), MM5 C3 (thin green lines), and the CALMET-variants v0, v1, v2, and v3 (thick lines in green, blue, orange, and purple, respectively) are shown. Observed mean values, the models' biases and the quality of the simulated distributions in terms of KS_V (in parentheses) and KP_ϕ are listed in the legends.

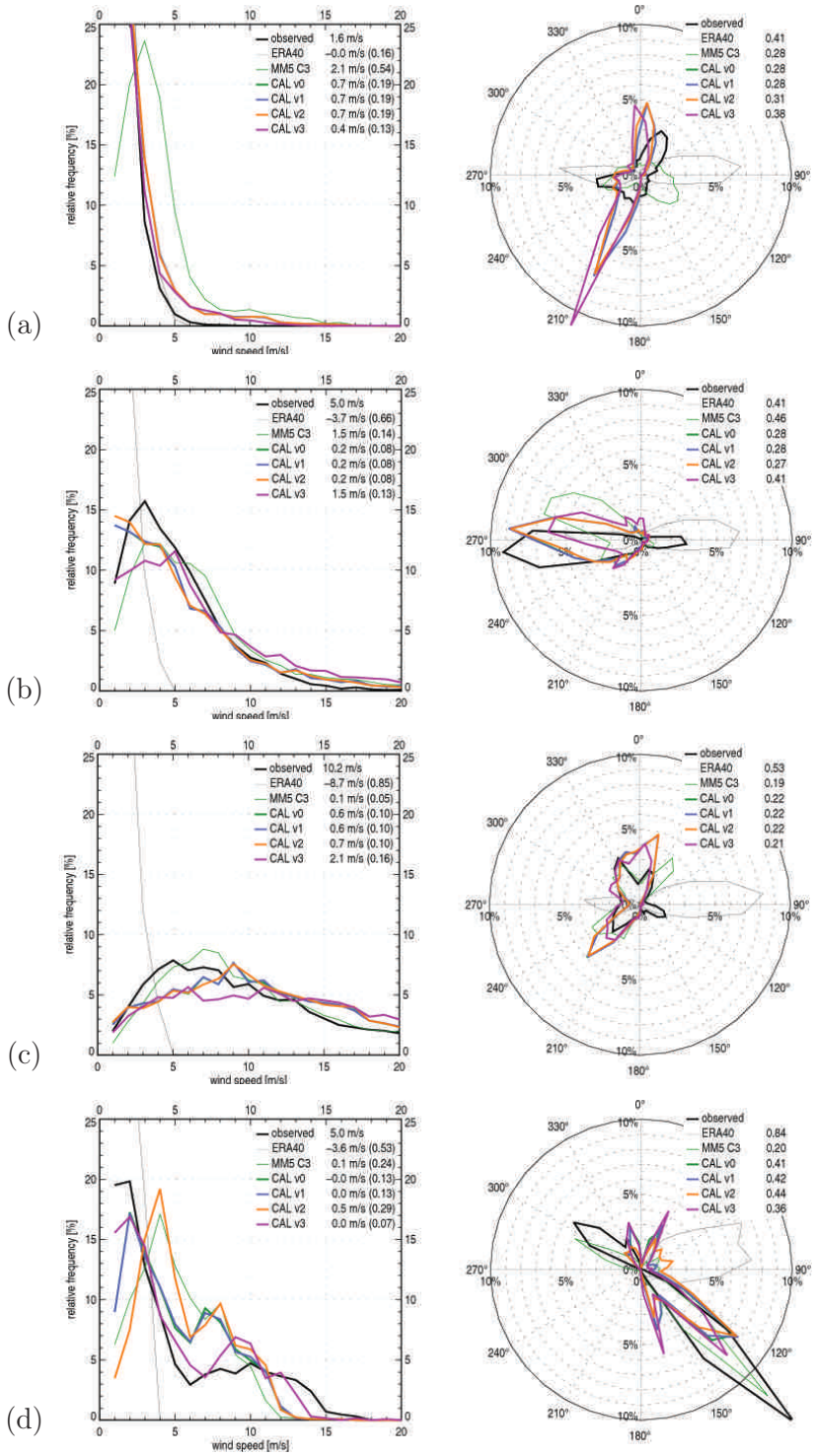

Figure A.8: Same as Figure A.7, but for the stations (a) ZS, (b) SH, (c) SB, and (d) EB (cf. Table 4.1).

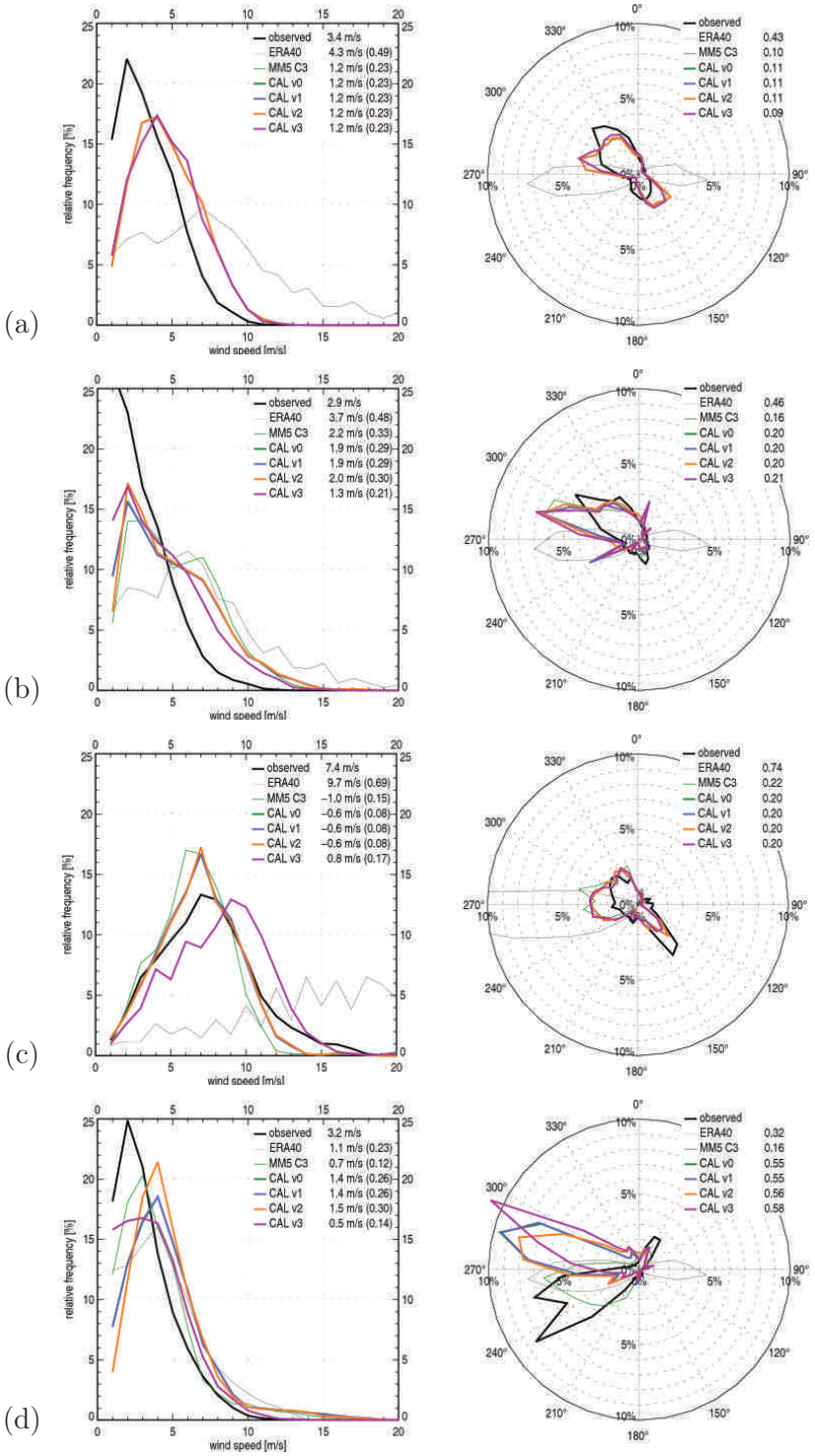

Figure A.9: Modelled and observed frequency distributions of wind speed (left column) and direction (right column) from Jan 1 to Dec 31, 1999, in the Vienna Basin at stations (a) GE, (b) GK, (c) LB, and (d) LT (cf. Table 4.1). Observations (thick black lines), the driving data ERA-40 (thin black lines), MM5 C3 (thin green lines), and the CALMET-variants v0, v1, v2, and v3 (thick lines in green, blue, orange, and purple, respectively) are shown. Observed mean values, the models' biases and the quality of the simulated distributions in terms of KS_V (in parentheses) and KP_ϕ are listed in the legends.

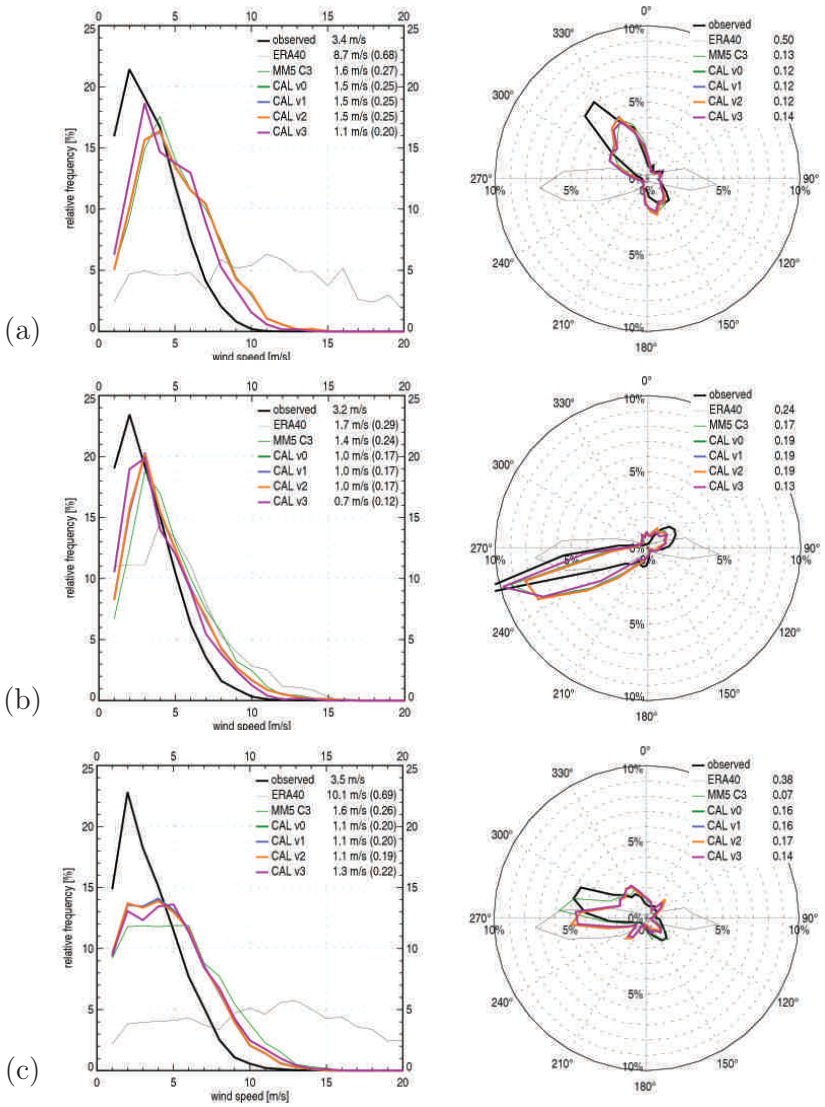

Figure A.10: Same as Figure A.9 but for the stations (a) NE, (b) SP, and (c) HW (cf. Table 4.1).

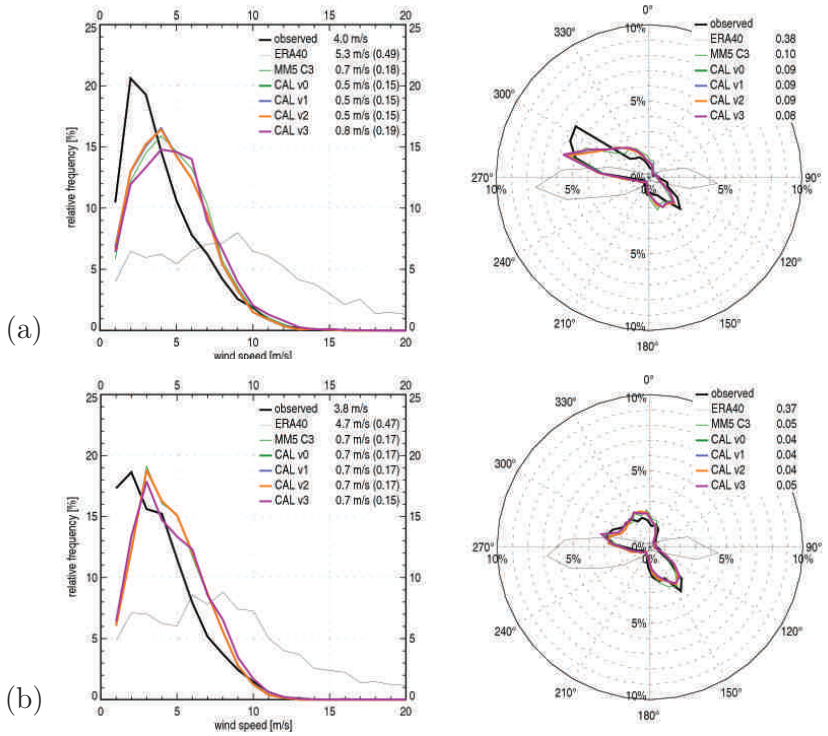

Figure A.11: Same as Figure A.9, but for the stations (a) WU and (b) ZD (cf. Table 4.1).

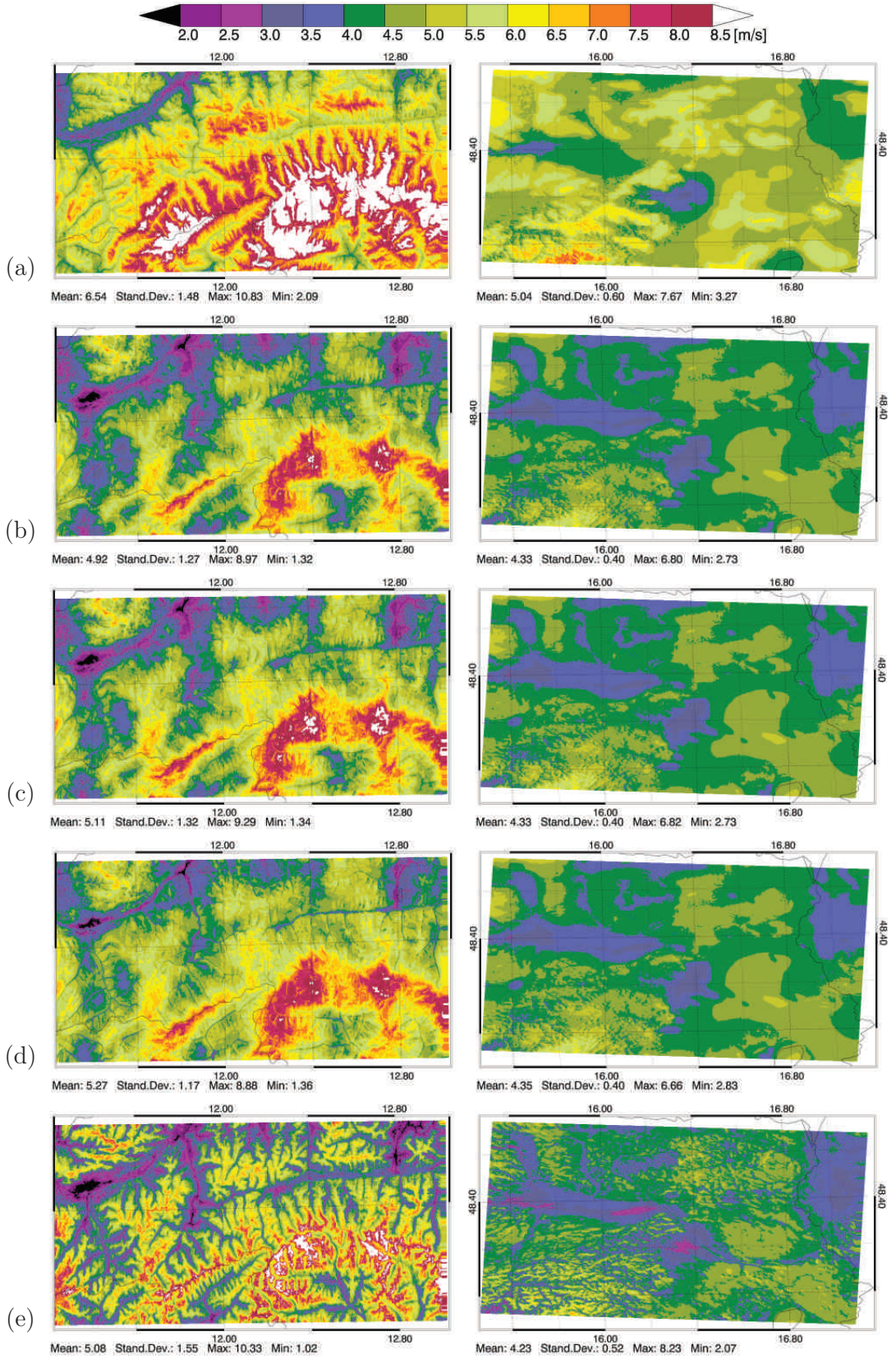

Figure A.12: Simulated annual wind speed [m/s] at 10 m a.g.l. (period: Jan 1 to Dec 31, 1999) with 200 m × 200 m grid spacing modelled by the variants (a) Av0, (b) Cv0, (c) Cv1, (d) Cv2, and (e) Cv3 in the Hohe Tauern region (left column) and in the Vienna Basin (right column).

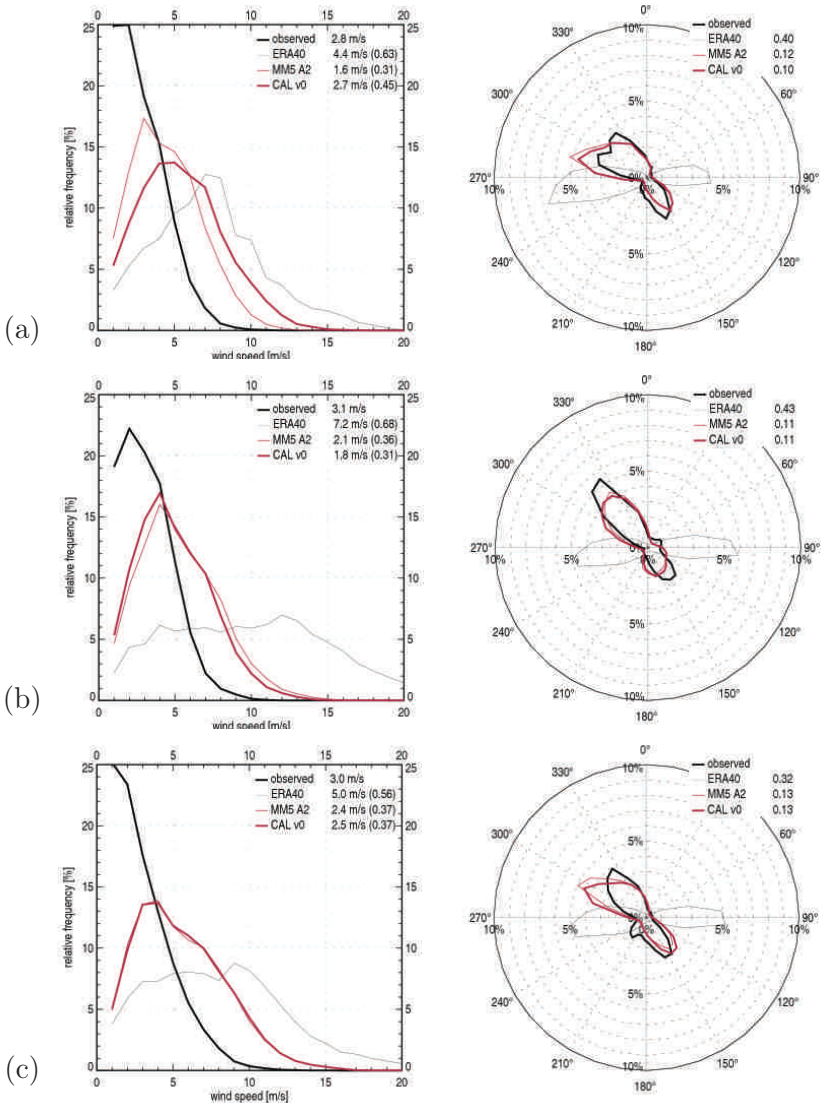

Figure A.13: Modelled and observed frequency distributions of wind speed (left column) and direction (right column) from Jan 1, 1981, to Dec 31, 1990, in the Vienna Basin at stations (a) GE, (b) GK, and (c) SD (cf. Table 4.1). Observations (thick black lines), the driving data ERA-40 (thin black lines), MM5 A2 (thin red lines), and CALMET v0 (thick red lines) are shown. Observed mean values, the models' biases and the quality of the simulated distributions in terms of KS_V (in parentheses) and KP_ϕ are listed in the legends.

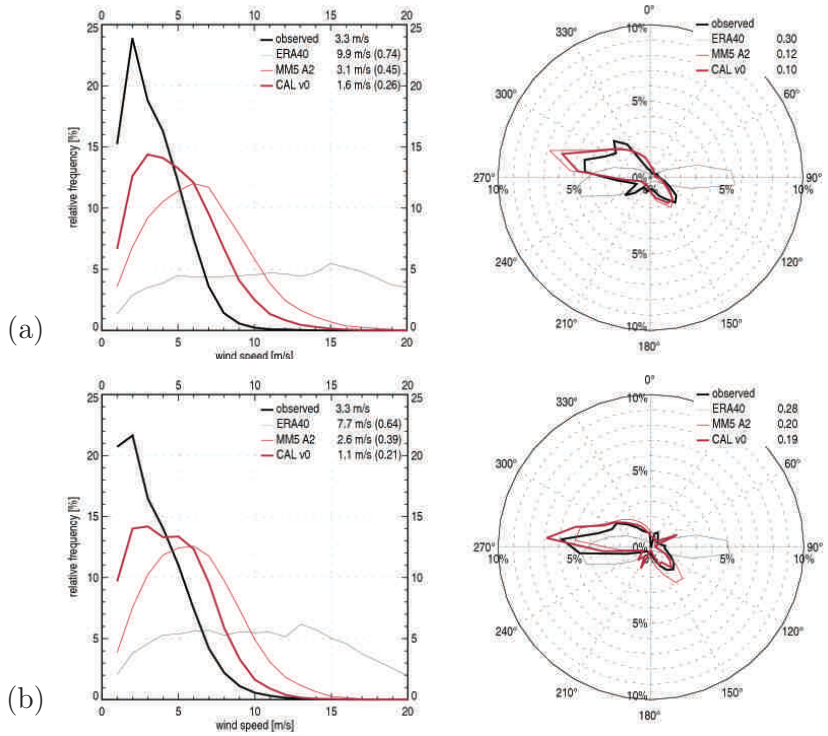

Figure A.14: Same as Figure A.13 but for the stations (a) WI and (b) HW (cf. Table 4.1).

A.2 Climate Change Signals

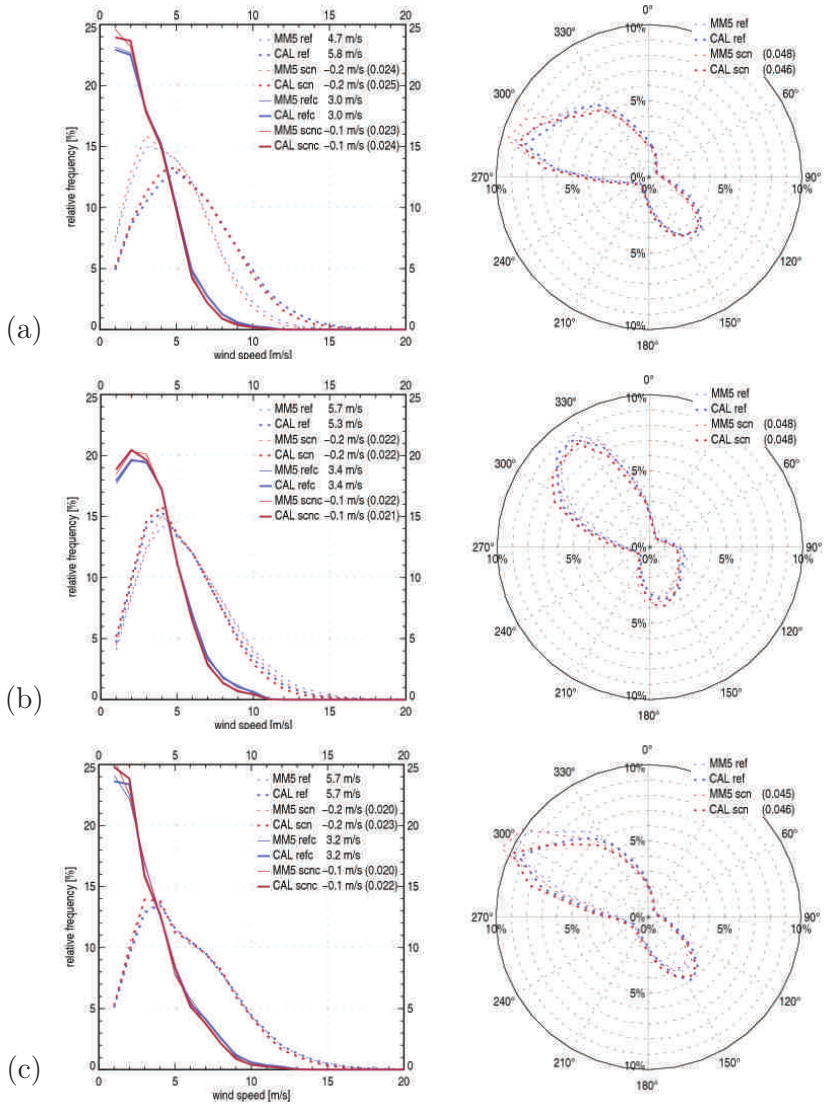

Figure A.15: Frequency distributions of corrected (solid lines) and uncorrected (dashed lines) wind speeds (left column) and directions (right column) from the reference-period 1981 to 1990 (index ref) and the scenario-period 2041 to 2050 (index scn) modelled by both downscaling-steps: MM5 domain A2 (thin lines) and CALMET variant v0 (thick lines) in the Vienna Basin at stations (a) GE, (b) GK, and (c) SD (cf. Table 4.1). The legends in the left column show (corrected and uncorrected) mean annual wind speeds from the reference-simulations and their changes due to the scenario-simulations. The statistics of the Kolmogorov-Smirnov-test (left column) and Kuiper-test (right column) comparing the distributions of the scenario- with the reference-period are listed in the legends as well (in parenthesis).

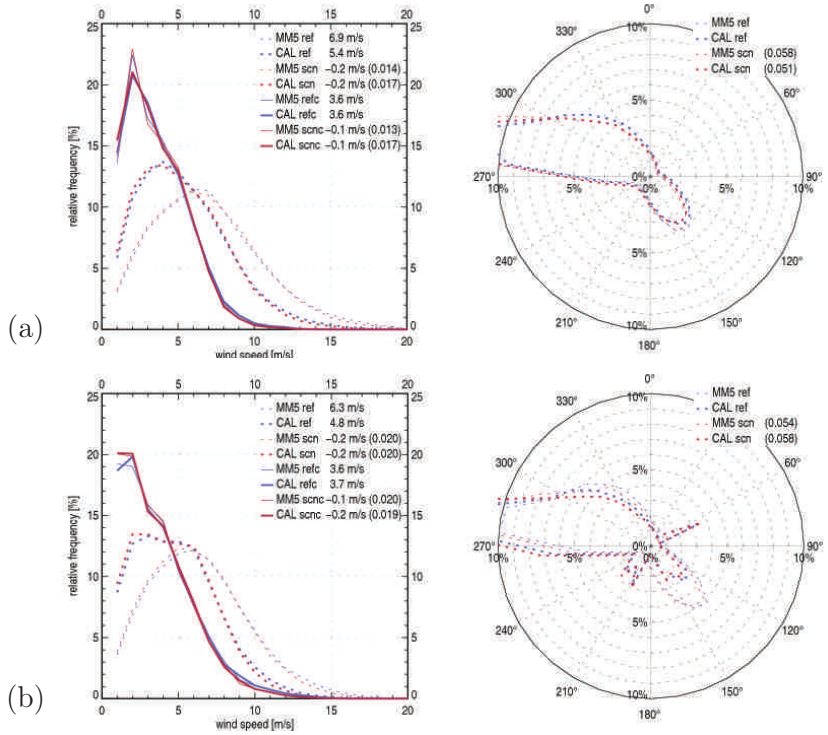

Figure A.16: Same as Figure A.15 but for the stations (a) WI and (b) HW (cf. Table 4.1).

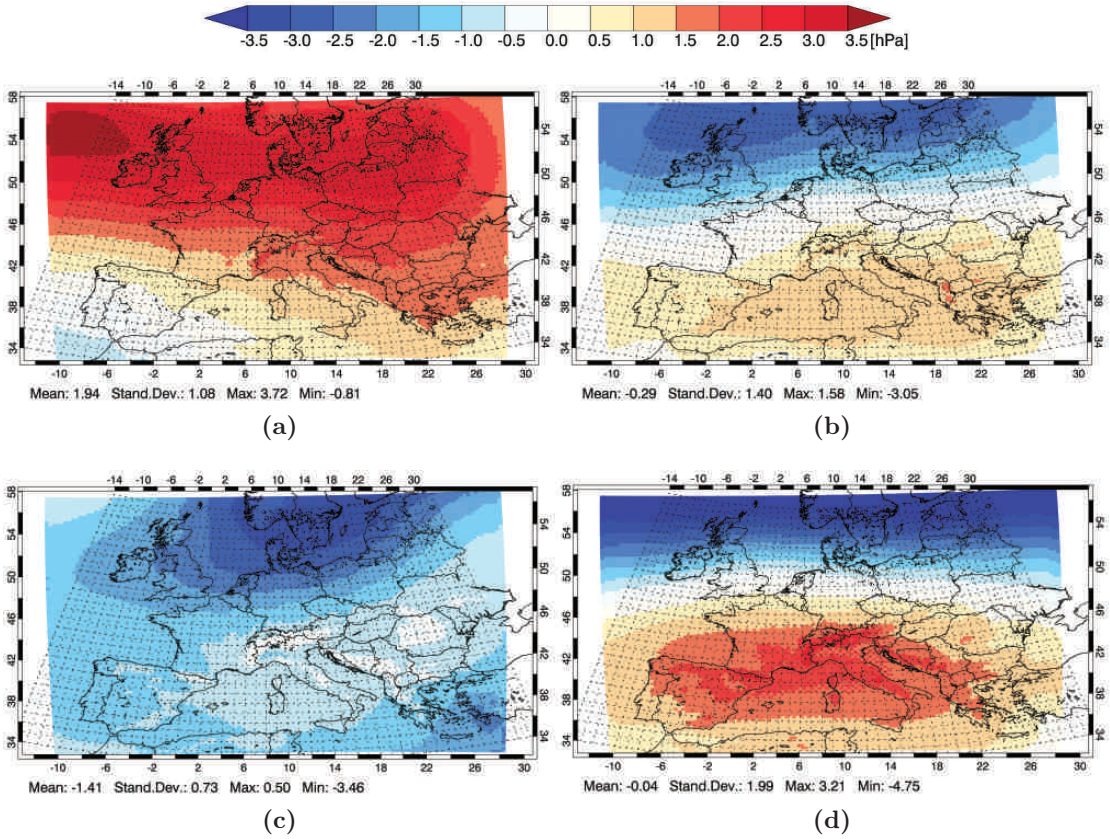

Figure A.17: Uncorrected climatic change of seasonal mean sea-level-pressure [hPa] (periods 1981 to 1990 and 2041 to 2050; emission scenario IS92a) over Europe with 30 km grid spacing from MM5 domain A1 (control configuration, cf. Section 3.1, Figure 3.1) for the seasons (a) DJF, (b) MAM, (c) JJA, and (d) SON.

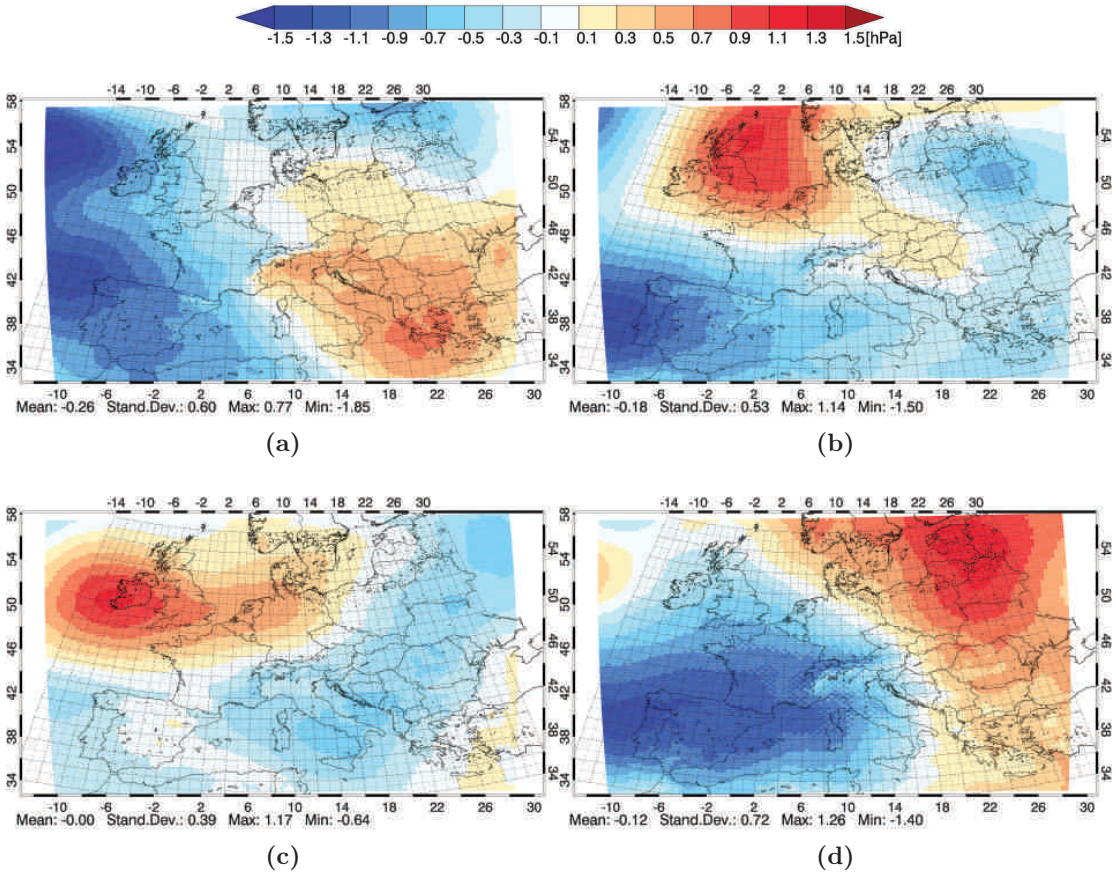

Figure A.18: Same as for Figure A.17, but for seasonal standard deviation of sea-level pressure [Pa].

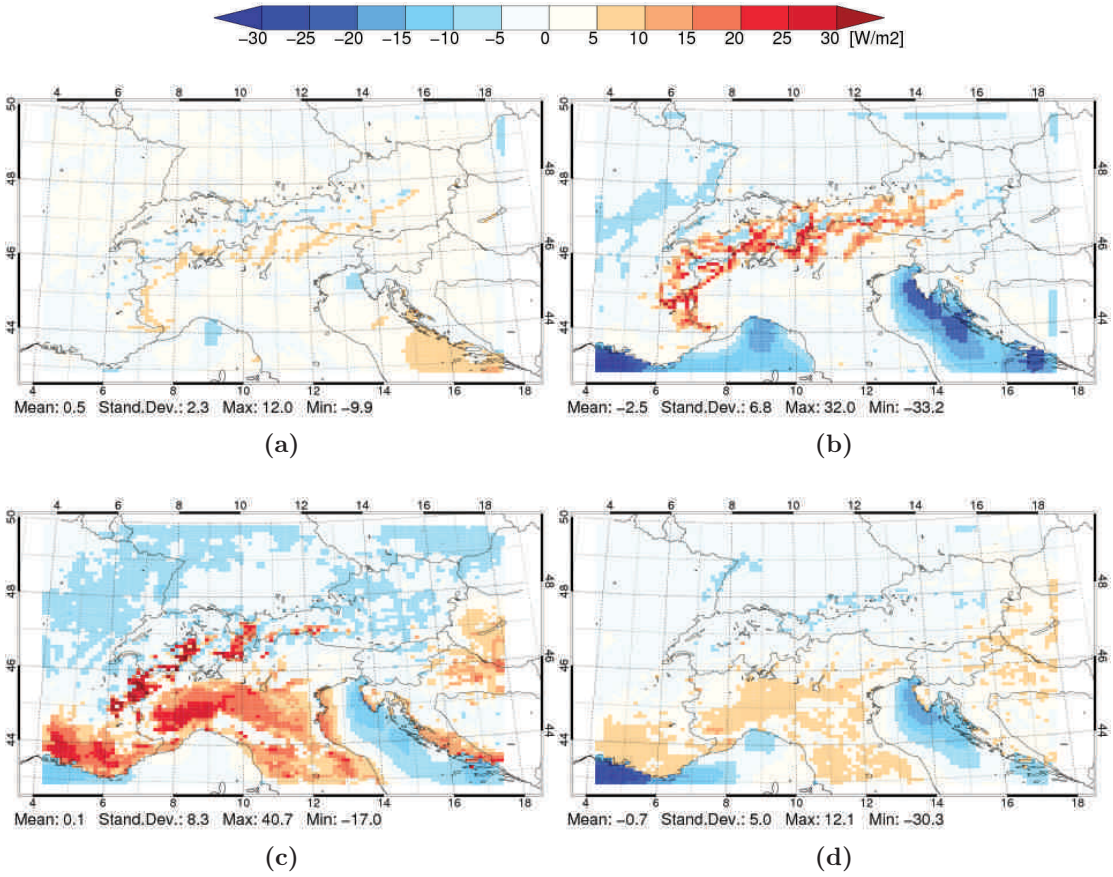

Figure A.19: Uncorrected climatic change of seasonal mean sensible heat flux [W/m^2] (periods 1981 to 1990 and 2041 to 2050; emission scenario IS92a) in the Alpine region with 10 km grid spacing from MM5 domain A2 (control configuration, cf. Section 3.1, Figure 3.1) for the seasons (a) DJF, (b) MAM, (c) JJA, and (d) SON.

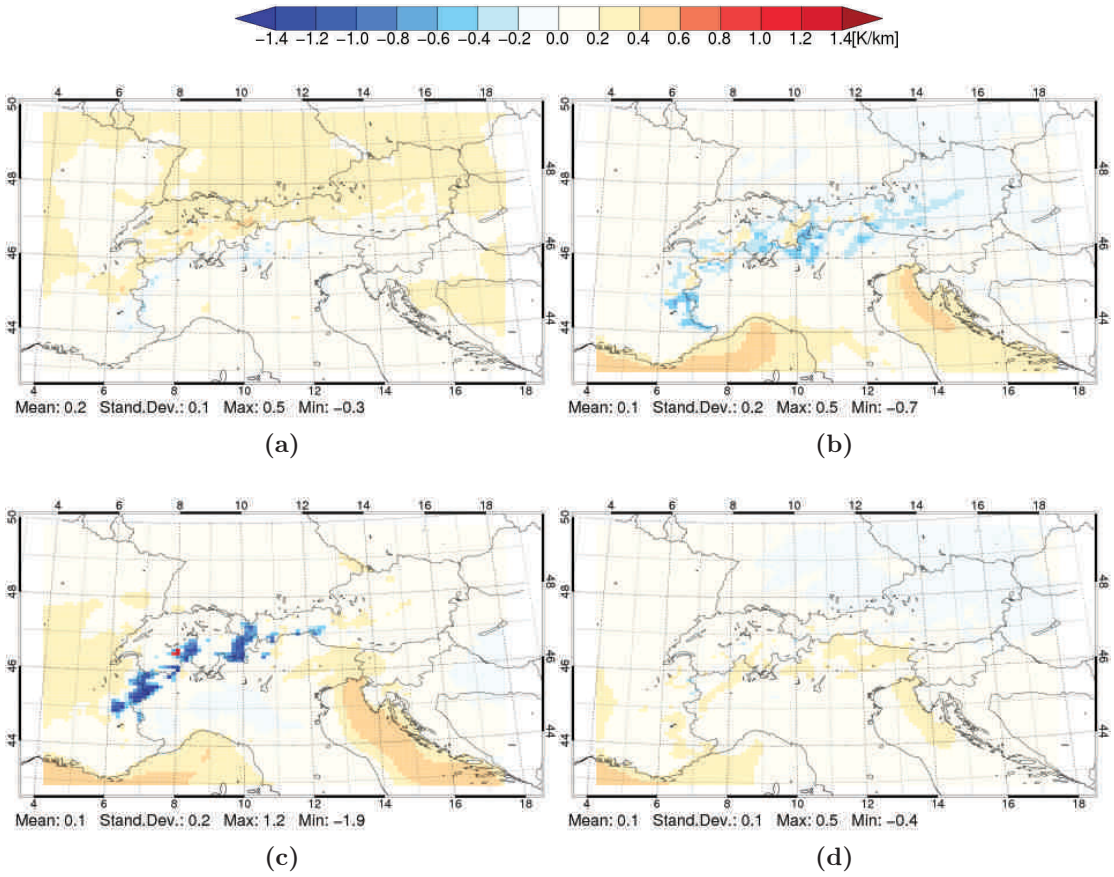

Figure A.20: Same as for Figure A.19, but for seasonal mean temperature lapse rate [K/km].

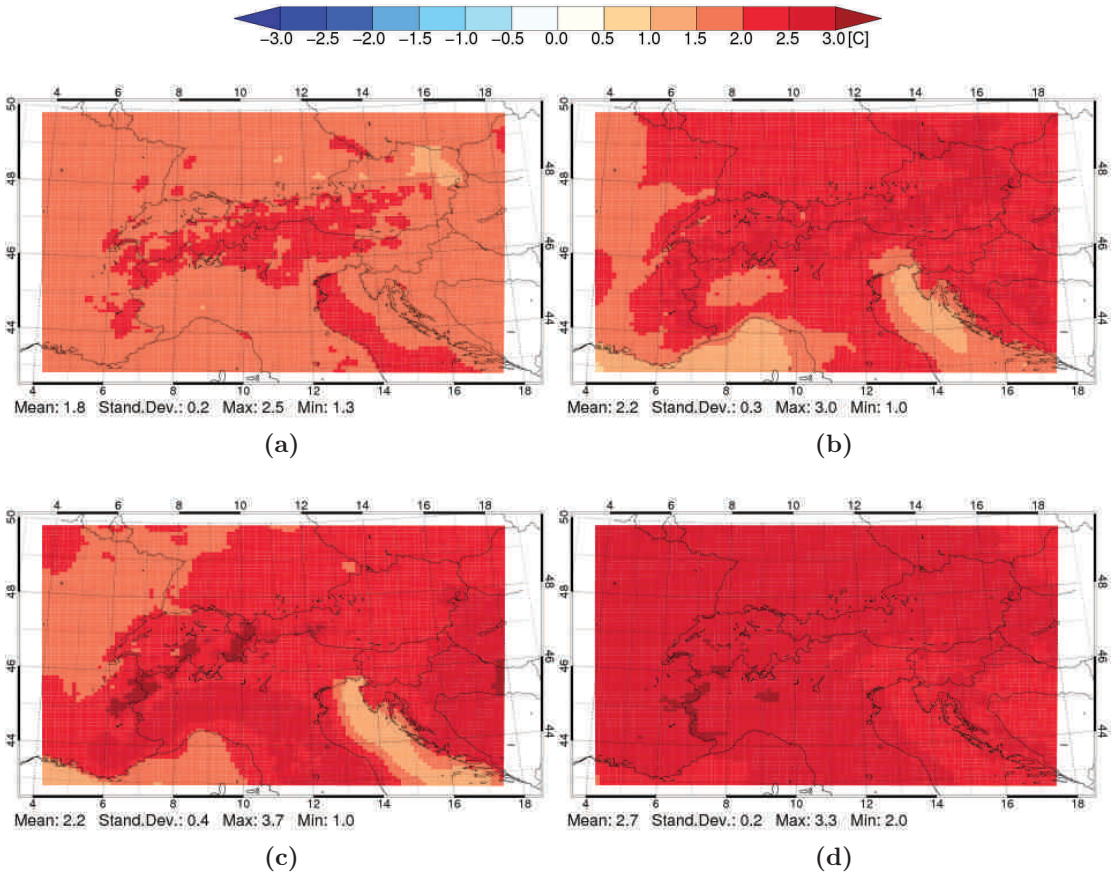

Figure A.21: Same as for Figure A.19, but for seasonal mean temperature (2 m a.g.l.) [°C].

Abstract:
The present thesis focuses on investigating and improving a hybrid dynamic-diagnostic downscaling method for near surface wind, which enables to provide wind climatologies over complex topography on the 100 m scale. A second objective is to conduct climate simulations and to identify climatological main processes affecting the long-term behaviour of averaged near surface wind conditions in the European Alpine region under increasing greenhouse-gas concentrations.
Several variants of the method were applied in two study regions, the Hohe Tauern region and the Vienna Basin. Comparisons with observations show that the steady-state flow concept and the orographic speed-up effect are the most dominant climatological mechanisms. The quality of the modelled climatologies is mostly affected by the ability to capture synoptic- and regional-scale processes.
The method has been applied to the output of the climate model ECHAM5 (periods 1981 to 1990 and 2041 to 2050, IPCC scenario IS92a). The climate change signals show decreasing annual wind speeds and it can be concluded that a) changes of synoptic- and large-scale processes are affecting local gradient-forced air flows, b) the orographic speed-up effect amplifies changes in mountainous areas, and c) interactions between the atmosphere and the earth's surface lead to regionally varying climate change effects. There exists strong evidence for a robust model-independent reduction of seasonal (winter, summer) wind speeds in the inner Alps.

Zum Inhalt:
Das Ziel der vorliegenden Arbeit ist die Untersuchung einer kombinierten dynamischen-diagnostischen downscaling Methode für bodennahen Wind, welche es ermöglicht Windklimatologien in komplexer Topographie auf der 100 m Skala zu erstellen. Ein zweites Ziel ist die Durchführung von Klimasimulationen zur Identifikation klimatologischer Prozesse, die das Langzeitverhalten von mittleren Windverhältnissen in den Europäischen Alpen bei steigenden Treibhausgaskonzentrationen bestimmen.
Mehrere Varianten der Methode wurden in den Hohen Tauern und dem Wiener Becken eingesetzt. Vergleiche mit Beobachtungsdaten zeigen, dass die Konzepte der Stationären Strömung und der Strömungsüberhöhung die dominantesten Klimamechanismen sind. Die Qualität der Windklimatologien wird hauptsächlich von der Fähigkeit, synoptische und regionale Prozesse abzubilden, beeinflusst.
Die Methode wurde auf eine Klimasimulation des Modells ECHAM5 (Perioden 1981 bis 1990 und 2041 bis 2050, IPCC Szenario IS92a) angewandt. Die Klimaänderungssignale zeigen rückläufige Jahreswindgeschwindigkeiten und es kann gefolgert werden, dass a) Änderungen der synoptischen und regionalen Prozesse lokale gradientenbedingte Strömungen beeinflussen, b) die Strömungsüberhöhung Änderungen im Gebirge verstärken und c) Wechselwirkungen zw. Atmosphäre und Erdoberfläche zu regional unterschiedlichen Effekten führen. Unabhängig von der Wahl der Modelle werden saisonale (Frühling, Sommer) Windgeschwindigkeiten in den Alpen zurückgehen.

Wegener Center for Climate and Global Change
University of Graz
Leechgasse 25
A-8010 Graz, Austria
www.wegcenter.at
ISBN 978-3-9502940-0-2